



HAL
open science

Modeling questions for numerical simulations of aeronautical combustors

Adrien Chatelier

► **To cite this version:**

Adrien Chatelier. Modeling questions for numerical simulations of aeronautical combustors. Fluids mechanics [physics.class-ph]. Université Paris Saclay (COmUE), 2019. English. NNT : 2019SACLC061 . tel-02294255

HAL Id: tel-02294255

<https://theses.hal.science/tel-02294255>

Submitted on 23 Sep 2019

HAL is a multi-disciplinary open access archive for the deposit and dissemination of scientific research documents, whether they are published or not. The documents may come from teaching and research institutions in France or abroad, or from public or private research centers.

L'archive ouverte pluridisciplinaire **HAL**, est destinée au dépôt et à la diffusion de documents scientifiques de niveau recherche, publiés ou non, émanant des établissements d'enseignement et de recherche français ou étrangers, des laboratoires publics ou privés.

Modeling questions for numerical simulations of aeronautical combustors

Thèse de doctorat de l'Université Paris-Saclay
préparée à CentraleSupélec

Ecole doctorale n°579 Sciences mécaniques et énergétiques, matériaux et géosciences (SMEMAG)
Spécialité de doctorat : Énergétique

Thèse présentée et soutenue à Gif-sur-Yvette, le 26 juin 2019, par

ADRIEN CHATELIER

Composition du Jury :

Thierry Schuller Professeur, IMFT (UMR 5502)	Président
Christophe Duwig Professeur, KTH	Rapporteur
Bruno Renou Professeur, CORIA (UMR 6614)	Rapporteur
Éléonore Riber Chercheur sénior, CERFACS	Examineur
Dirk Roakerts Professeur, TU Delft	Examineur
Francis Dupoirieux Ingénieur de recherche, ONERA	Examineur
Benoît Fiorina Professeur, CentraleSupélec (EM2C - UPR 288)	Directeur de thèse
Nicolas Bertier Ingénieur de recherche, ONERA	Encadrant

Remerciements

Ça y est, c'est la fin du voyage. Il m'aura fallu 1756 jours pour arriver à l'écriture de ces remerciements, soit 4 ans, 9 mois et 22 jours. Ce voyage m'a poussé dans mes retranchements et je n'y serais pas arrivé seul. Je souhaite donc par ces quelques mots maladroits témoigner ma reconnaissance à toutes ces personnes qui de près ou de loin m'ont permis d'aller au bout de cette thèse.

Je tiens tout d'abord à remercier les membres du jury qui ont accepté de lire mon manuscrit et de participer à ma soutenance : Thierry en tant que président, Professeurs Duwig et Renou pour leur rapport sur mon manuscrit et leurs questions, Madame Riber, Professeur Roakerts et Francis pour leurs questions durant la soutenance.

Deux personnes sont à l'origine de cette thèse et je voudrais les remercier pour leur confiance tout au long du périple. Nicolas est le premier à m'avoir fait confiance pour le stage de fin d'étude et m'a permis de progresser en combustion. C'est grâce à lui que j'en suis là aujourd'hui. Il m'a fait comprendre l'importance du travail en équipe et de la bienveillance. Benoît m'a appris quant à lui l'importance de présenter et de parler de son travail.

J'ai passé une bonne moitié de la thèse au laboratoire EM2C et j'y ai rencontré des gens exceptionnels qui m'ont soutenu en toute situation. Il me faut tout d'abord souligner l'apport essentiel de Renaud et Chaï qui m'ont mis le pied à l'étrier sur YALES2 (et merci à l'équipe du CORIA - Vincent, Ghislain, Pierre ...- pour ce super code !), tout en étant infiniment patients ! Je tiens aussi à remercier Bene, qui a su trouver les mots justes dans les moments les plus difficiles. J'ai passé des moments incroyables dans le bien nommé "bureau des champions" avec Pedro (le plus fort !) et Aurélien. La "team Benoît" était tout aussi importante grâce à Melody, Cédric et Giampaolo. Je remercie aussi tous les autres doctorants (liste non exhaustive !) : Keke (tu dois encore me supporter en plus !), Pedro R, Erwan, Thea, Leo, Macole, Gizem, Maria, Nicolas M, Robin, Livia, Amanda, Abi, Augustin, Renaud G, Davy, Lorella, David, Roxane, Arthur, Constantin, Yacine, Thibault G, Paul... Merci aussi aux permanents : Aymeric V, Jean-Michel, Sébastien T, Nathalie, Noï, Brigitte, Thomas, Sébastien D...

L'autre moitié s'est passée à l'ONERA, avec de très bons moments vécus au 5ème étage du beau centre de Châtillon (et surtout en dehors !). Merci à mes compagnons d'infortune du DEFA puis du DMPE : Quentin, Valentin, Nicolas R, Nicolas D (un vrai frère !), Bastien, Pierre, vous pouvez le faire ! J'ai une reconnaissance toute particulière pour Aymeric, qui m'a permis de comprendre une petite partie de CEDRE, ce n'est pas une mince affaire ! J'ai aussi eu la chance de travailler avec les permanents : Luc-Henry, Pascale, Emmanuel, Dominique, Jean-Michel, Lionel et tous les autres !

La thèse n'était bien sûr qu'une étape et je n'ai pas attendu la fin pour commencer la suite (un défi de plus). J'ai maintenant la chance de travailler sur des projets uniques grâce à Christophe, Didier et Eric, merci pour votre confiance ! Entre FEP/A et le CofEx, j'ai trouvé une équipe unique avec (entre autres) : Etienne (le gremlin !), Pierre, Antoine B, JB, Simon, Kevin C, Marco, Romain, Louis, Alexandre, Quentin, Nicolas, Baptiste, Sébastien, Romain (merci pour ton soutien !), Aurélien, Marie, Rémi mais aussi Emmanuel, Guillaume, Antoine D et tous les autres.

Enfin, je veux remercier les personnes qui ne m'ont pas perdu de vue malgré les années : les Svenska Vänner, les ENSTA, le clan des 1st...

Pour terminer ces remerciements, rien n'aurait été possible sans le soutien constant, indéfectible, inestimable de mes parents, mon frère et mes grands-parents.

Abstract

The design of aeronautical combustion chambers requires a precise balance between the different physical phenomena involved, such as flame-turbulence interaction, heat losses, flame dynamics or fuel evaporation and mixing. Numerous numerical tools exist in the literature to predict these kinds of turbulent reacting flows.

The unsteady turbulence models, for example LES (Large Eddy Simulation), represent an excellent compromise for the prediction of the mixing in realistic configurations. The tabulated chemistry approach is an attractive trade-off between computation cost and accuracy for predicting the structure of flames.

In this thesis, advanced turbulence and tabulated chemistry models are applied to complex configurations in order to assess their ability to predict the structure of turbulent flames.

The prediction of the FDF (Flame Describing Function) by the F-TACLES (Filtered TABulated Chemistry for Large Eddy Simulations) model is compared to experimental data for a non-adiabatic premixed swirled flame. The FDF is well predicted for a wide range of frequencies and two velocity fluctuation levels. The origin of the discrepancies is analyzed.

The first application of the F-TACLES model in a two-phase burner is proposed. The chosen burner is the KIAI spray jet flame, recently studied at CORIA. A detailed comparison with the experiments is performed and shows that F-TACLES is able to predict the correct flame shape.

The ZDES (Zonal Detached Eddy Simulation) model is studied in a realistic aeronautical injector, the TLC configuration. In cold conditions, the ZDES is validated against velocity measurements and compared to LES results. In reacting conditions, the prediction of temperature profiles in the combustion chamber is greatly improved in the ZDES.

Keywords: Large Eddy Simulation; Zonal Detached Eddy Simulation; Turbulent combustion; Tabulated chemistry; Flame dynamics; F-TACLES model; Two-phase flame.

Résumé

La conception de chambres de combustion aéronautiques requiert un compromis entre les différents phénomènes physiques présents, comme les interactions entre la flamme et la turbulence, les pertes thermiques, la dynamique de flamme ou l'évaporation du carburant et son mélange. De nombreux outils numériques existent dans la littérature pour prédire ce genre d'écoulements réactifs turbulents.

Les modèles de turbulence instationnaires, par exemple LES (Large Eddy Simulation), sont un excellent compromis pour la prédiction du mélange dans des configurations réalistes. L'approche de chimie tabulée représente un équilibre attrayant entre coût de calcul et précision pour la prédiction de structure de flamme.

Dans cette thèse, des modèles de turbulence avancés et de chimie tabulée sont appliqués à des configurations complexes afin d'évaluer leur capacité à prédire la structure de flammes turbulentes.

La prédiction de la FDF (Flame Describing Function) par le modèle F-TACLES (Filtered TABulated Chemistry for Large Eddy Simulations) est comparé à des données expérimentales pour une flamme swirlée, prémélangée et non-adiabatique. La FDF est bien prédite pour une large plage de fréquences et deux niveaux de fluctuations de vitesse. L'origine des différences est analysée. La première application du modèle F-TACLES à un brûleur diphasique est proposée. Le brûleur choisi est la flamme jet diphasique KIAI, récemment étudié au CORIA. Une comparaison détaillée avec l'expérience est faite et montre que F-TACLES est capable de prédire la bonne forme de flamme.

Le modèle ZDES (Zonal Detached Eddy Simulation) est étudié dans la configuration TLC, un injecteur aéronautique réaliste. En non-réactif, la ZDES est validée par rapport aux mesures de vitesse expérimentales et comparée à des résultats de LES. En conditions réactives, la prédiction des profils de température dans la chambre de combustion est grandement améliorée en ZDES.

Mots-clés : Large Eddy Simulation ; Zonal Detached Eddy Simulation ; Combustion turbulente ; Chimie tabulée ; Dynamique de flamme ; Modèle F-TACLES ; Flamme diphasique.

Synthèse

L'objectif général de cette thèse était de fournir des informations sur les questions de modélisation rencontrées dans les simulations de chambres de combustion aéronautiques. Le cadre principal pour les choix numériques était l'utilisation de la chimie tabulée avec des modèles turbulents instationnaires. Deux axes ont été choisis pour étudier les choix de modélisation : la capacité à retrouver les propriétés de la flamme dans des conditions non adiabatiques ou diphasiques et l'influence du modèle de turbulence sur la topologie de l'écoulement dans une géométrie complexe. Pour chaque axe, les simulations ont été comparées aux bases de données expérimentales existantes. Ces comparaisons ont conduit aux réalisations suivantes.

Réalisations majeures

Étude des performances du modèle F-TACLES dans des configurations complexes

La thèse de [Mercier \(2015\)](#) a conduit à l'extension du modèle F-TACLES aux écoulements non adiabatiques. Les défis pour cette thèse étaient de déterminer si le modèle F-TACLES était capable de :

- prédire la forme correcte d'une flamme non adiabatique,
- récupérer la dynamique de la flamme grâce à la fonction de description de la flamme (FDF),
- prédire la forme d'une flamme diphasique.

Dans le brûleur EM2C, alimenté avec un mélange $\text{CH}_4/\text{H}_2/\text{air}$, il a été montré dans [Mercier et al. \(2016a\)](#) que F-TACLES était capable de prédire la forme correcte de la flamme pour deux niveaux d'enrichissement en H_2 conduisant à une forme de flamme en M pour une quantité supérieure et une forme de flamme en V pour une quantité inférieure. Cette différence s'explique par les pertes de chaleur dans la zone de recirculation externe qui ont conduit à l'extinction de la flamme dans cette région. En cas d'enrichissement élevé, le front de flamme externe est toujours présent en raison de la quantité de H_2 alors que ce front de flamme disparaissait à mesure que la quantité de H_2 diminuait dans le mélange. Le nouveau formalisme F-TACLES, prenant en compte les pertes de chaleur, était nécessaire pour retrouver la forme correcte de la flamme. Malgré ces

résultats, il a été montré dans cette thèse qu'il existait un front de flamme externe résiduel dans la zone de recirculation externe. Cela a été attribué à l'absence des effets d'étirement sur le front de flamme dans le modèle F-TACLES.

Pour le même brûleur, dans des conditions pulsées, la comparaison des FDF a montré des résultats prometteurs en ce qui concerne les expériences, présentés dans [Chatelier et al. \(2019\)](#). Le gain et la phase de la FDF ont été comparés entre simulations et expériences pour plusieurs fréquences et deux niveaux de fluctuations de vitesse. Les amplitudes de gain et de phase correctes ont été trouvées dans les Simulations aux Grandes Échelles (SGE) pour les deux niveaux. Une comparaison détaillée entre les moyennes de phase de

- l'émission expérimentale d' OH^* et le dégagement de chaleur des SGE,
- champs de vitesse expérimentaux PIV et SGE et
- probabilité de présence de gaz brûlés chauds

a été proposé pour deux niveaux de fluctuations de vitesse et de fréquences. Les simulations ont démontré la prédiction précise de la dynamique de la flamme, qui dépend de la fréquence.

Cependant, certains écarts ont été identifiés dans la prédiction de gain, en particulier pour une fréquence, où une baisse de gain trouvée dans les expériences n'a pas été reproduite par les simulations. Une analyse plus poussée a montré que la résolution du maillage ou le modèle de plissement de la flamme à l'échelle de la grille n'étaient pas à l'origine de la mauvaise prédiction du gain. Les effets d'étirement qui ne sont pas inclus dans le modèle F-TACLES se sont avérés être la cause la plus probable de cet écart.

L'analyse des performances du F-TACLES dans un écoulement diphasique a conduit à la simulation du brûleur KIAI. D'excellents résultats ont été trouvés dans la prédiction de la forme de la flamme dans des conditions diphasiques, comme présenté dans [Chatelier et al. \(2019\)](#). La structure de la flamme et sa hauteur de stabilisation ont été récupérées par les SGE. Comme dans les expériences, deux structures de flammes différentes sont apparues: un front de flamme interne prémélangé très plissé et un front de flamme externe de diffusion. La comparaison avec les diagnostics expérimentaux a mis en évidence la capacité du solveur YALES2 à prédire la vitesse et la stratification correctes du spray, ainsi que la bonne topologie de l'écoulement pour le gaz.

Cependant, des problèmes sont apparus pour la température de phase liquide, qui n'étaient pas liés au modèle F-TACLES. Les hypothèses du modèle d'évaporation étaient responsables de l'écart entre les expériences et les simulations.

Analyse de l'intérêt de ZDES pour les géométries complexes

La thèse de [Boucher \(2015\)](#) a étudié une configuration complexe représentative d'un véritable injecteur aéronautique, appelé TLC. Il a été constaté que dans

des conditions réactives, les simulations conduisaient à une prédiction incorrecte du champ de température dans la chambre. Dans cette thèse, l'objectif était de :

- déterminer la capacité du modèle LES à récupérer la topologie de l'écoulement correcte sans combustion,
- examiner l'intérêt du ZDES pour cette géométrie complexe avec et sans combustion.

Le choix de la configuration TLC pour l'application finale de cette thèse a été motivé par la complexité de sa géométrie et la présence de tous les phénomènes étudiés précédemment dans cette thèse. La présence de trois systèmes \tilde{A} swirl et d'un système de refroidissement représente un réel défi pour les codes CFD, même dans des conditions non réactives. En outre, le carburant liquide est injecté avec deux méthodes différentes, ce qui pose de nombreuses questions de modélisation concernant la description du spray dans les simulations. La combinaison de tous ces paramètres avec des diagnostics au coeur de l'écoulement fait de la configuration TLC un cas intéressant pour la validation des approches de modélisation dans des configurations complexes.

Les résultats présentés dans cette thèse ont montré que le LES et le ZDES étaient capables de prédire la topologie d'écoulement correcte sans combustion. La discrétisation des couches limites dans la ZDES n'a pas entraîné de différences majeures, mais a permis une analyse fine des propriétés de l'écoulement à proximité des parois. La capacité du modèle ZDES à capturer des structures de couche limite complexes a été démontrée sur cette configuration.

Dans les conditions de réaction, malgré la même topologie d'écoulement et la même modélisation de la combustion turbulente, il a été démontré que la différence de traitement des couches limites conduisait à deux distributions de spray différentes. Le spray provenant de l'injection multipoint traversant la couche limite dans le ZDES était sensible aux fluctuations de vitesse se produisant près des parois des swirles, alors que les particules dans la SGE étaient beaucoup moins dispersées en raison de la cellule unique de la couche limite.

La dispersion accrue du spray dans la ZDES a entraîné une distribution complètement différente de la vapeur de carburant dans la chambre de combustion par rapport à la SGE. En conséquence, le champ de température résultant dans la chambre s'est révélé très différent entre les deux simulations. Dans la ZDES, les gaz chauds ne se trouvaient pas dans la zone de recirculation centrale tandis que dans le SOI, ils restaient dans une grande partie de la région centrale de la chambre. La comparaison avec les données expérimentales a montré que le ZDES donnait la meilleure prédiction de la température dans la chambre.

Perspectives

Les conclusions précédentes soulèvent les perspectives suivantes:

- Afin de retrouver la forme et la dynamique correctes de la flamme, la prise en compte des effets d'étirement sur la structure de la flamme semble nécessaire. La formulation actuelle du modèle F-TACLES n'est pas en mesure d'inclure cet effet et une extension supplémentaire pourrait être intéressante.
- Même si l'application du modèle F-TACLES aux flammes diphasiques est prometteuse, l'étude d'autres configurations diphasiques est nécessaire pour identifier les limites de la formulation actuelle. Par exemple, le brûleur KIAI existe dans une version avec swirl et confinée qui présente une structure de flamme complètement différente (Santiago et al. (2016)). Il a été étudié numériquement par Shum-Kivan (2017) et constituerait un excellent candidat pour l'évaluation du modèle F-TACLES dans des écoulements diphasiques.
- La modélisation de la phase liquide dans cette thèse n'a pas été au centre des préoccupations, mais les nouvelles données expérimentales sur la configuration KIAI ont montré que la température des gouttelettes avait été mal prédite par les simulations. L'étude de \mathcal{C}^{TM} autres modèles d'évaporation est nécessaire pour corriger ces résultats.
- L'utilisation de ZDES dans des conditions réactives a conduit à des résultats inattendus. Il serait intéressant d'étudier l'impact de la modélisation de la phase dispersée sur le champ de température, par exemple en ajoutant un modèle de fragmentation secondaire.
- En raison de la complexité de la configuration TLC, de nombreux aspects des problèmes de modélisation n'ont pas été explorés dans cette thèse:
 - Une convergence en maillage serait nécessaire pour valider complètement les approches ZDES et LES dans des conditions froides et réactives afin de déterminer si les résultats sont sensibles à la résolution du maillage.
 - L'influence de l'écoulement dans le plénum sur la topologie d'écoulement global n'a pas été étudiée. L'accent pourrait être mis sur l'écoulement autour du bras d'injection de carburant. En outre, une étude de l'influence de l'entrée sur les résultats (par exemple à travers les propriétés du champ de vitesse injecté) est une question intéressante.
 - La modélisation de l'injection du spray était plutôt simple, avec seulement plusieurs injecteurs numériques pour l'injection multipoint. Des simulations supplémentaires sont nécessaires pour étudier l'influence de la méthode d'injection sur les résultats.

Contents

Abstract	iii
Résumé	v
Synthèse	vii
Introduction	1
I Turbulent combustion modeling: application of tabulated chemistry models to complex configurations	11
1 Turbulent combustion modeling	13
1.1 Governing equations	13
1.2 Flow solvers	15
1.3 Turbulence modeling	16
1.4 Combustion modeling	22
2 Application of the F-TACLES model to the EM2C burner in steady and pulsed conditions	31
2.1 Objectives of this chapter	32
2.2 Experimental setup	33
2.3 Simulations in steady conditions	38
2.4 Simulations in pulsed conditions	54
3 Application of the F-TACLES model to the CORIA spray burner	81
3.1 Context of the study and objectives	82
3.2 Experimental configuration	83
3.3 Numerical Setup	84
3.4 Results and analysis	87
3.5 Conclusion	105
II Prediction of turbulent reactive flows in complex geometries: application of the ZDES approach to a realistic aero-	

nautical geometry	107
4 Validation of the ZDES approach to the TLC configuration in non-reacting conditions	109
4.1 Context of the study	110
4.2 Objectives of the chapter	110
4.3 The TLC configuration	111
4.4 Simulations	114
4.5 Results and analysis	115
4.6 Conclusion	134
5 Comparison of the LES and ZDES approaches to the TLC configuration in reacting conditions	141
5.1 Goal of this chapter	142
5.2 The TLC configuration	142
5.3 Simulations	144
5.4 Results and analysis	145
5.5 Conclusion	162
Conclusion	163
References	181

Introduction

Challenges for the design of aeronautical combustion chambers

Modern aircrafts are equipped with turbofans. A generic architecture of a turbofan is presented in Fig. 1. The fan is designed to ingest the incoming air that will enter the core engine or bypass it. In the core engine, the air pressure is increased by the compressor. It then enters the combustion chamber where fuel is burned. The generated hot gases enter the turbine that will in turn drive the compressor. The nozzle is the final part of the turbofan, where the hot gases are accelerated.

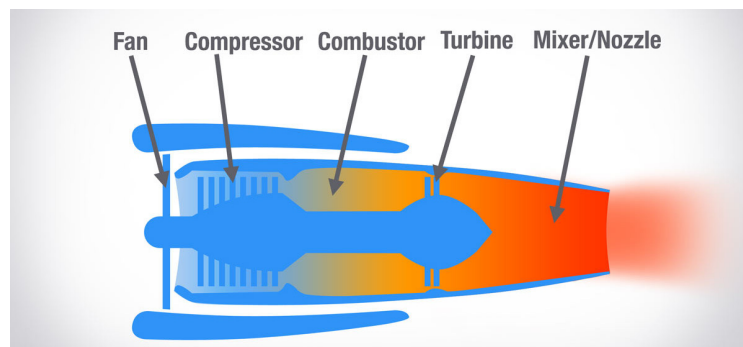


Figure 1: *Turbofan generic architecture, adapted from Cutler (2019).*

The principle of an aeronautical combustor is presented in Fig. 2. Manufacturers face numerous difficulties, especially regarding the combustion processes. Engines must burn the fuel efficiently for a wide range of pressure, temperature and air flow rate. The first challenge is to ensure that the ignition of the engine is possible for a given environment. In the event of a flameout, the regulation system of the engine must also be able to re-ignite it as fast as possible, even at high altitudes, where the pressure and the temperature are different from the ones encountered at sea level.

Another major topic in the design of an engine is the respect of the environmental norms that prescribe maximum levels pollutant emissions. As these norms are more and more demanding over the years, in order to attain the goals of the

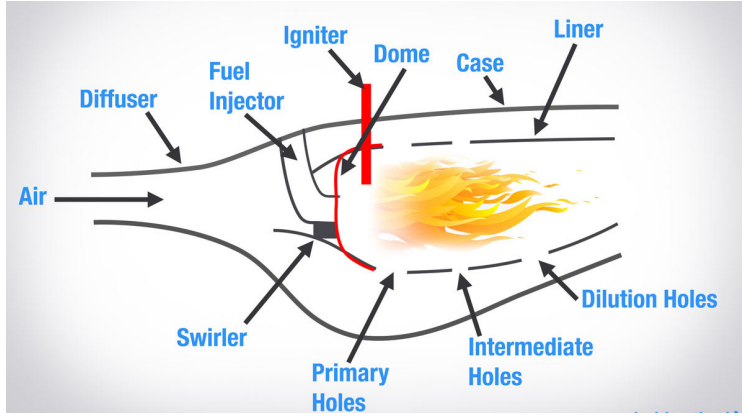


Figure 2: *Aeronautical combustor principle, adapted from Cutler (2019).*

international community in terms of pollution reduction, manufacturers must be able to control actively the various pollutants that are generated by the combustion. This is achieved by controlling the combustion regime, as in lean conditions the emissions of NO_x are decreased for instance.

Also, aircraft engines must be able to operate for up to 100,000 flight hours. This longevity can only be achieved if the mechanical structure of the engine is preserved. Because of the combustion, the turbine, located after the chamber suffers from thermo-mechanical constraints that must be controlled. This means that the gases exiting the combustion chamber must be as homogeneous as possible in order to avoid hot spots on the structure.

Finally, the current designs of aeronautical injectors involve multiple choices in fuel injection and air paths. The fuel is injected through various devices which enable a precise control of its distribution, depending on the engine operating point (taxi, take-off, cruise...). The control of the recirculation zones shape and size is performed thanks to swirlers, which impose a rotating motion to the flow and facilitate the stabilization of flames in the shear layers. The combination of different swirler types (axial or radial inlets, axial or radial outlets, varying number or angles of the swirling vanes...) permits a fine control of the flow. Therefore, this high level of complexity in the geometry of aeronautical injectors leads to a complex flow topology, including flow separation. The origin of the detachment can be related to different causes: a change of curvature in the geometry or an adverse pressure gradient for example.

All of the topics presented above represent a constraint for the design of aeronautical combustion chambers. They can lead to different technological solutions which may be opposed. The design of an engine revolves around optimizing each parameter while satisfying each constraint.

Major physical phenomena involved in aeronautical combustion chambers flows

Flows in aeronautical combustion chambers are fully turbulent. Turbulent motion is essential since it enhances the mixing between fuel and air in the combustion chamber. However, the control of turbulent flows is extremely difficult, especially the undesired phenomena that can occur in complex geometries, such as massive flow separation. This kind of phenomenon can have a direct impact on the performance on the engine, for example by increasing the pressure drop.

The injection of liquid fuel in the combustion chamber through various means represents a major design topic. The efficiency of the combustion in the chamber is directly linked to its ability to evaporate and burn the fuel as completely as possible. The choice of the position of the liquid fuel injectors must address two opposed issues: it must be able to quickly evaporate the fuel, but it also has to prevent the ignition of the fuel/air mixture in undesired zones for safety reasons.

The flame stabilization represents a crucial topic for the design of combustion chambers. The existence of flame anchoring on a wall requires mechanical studies to prevent the destruction of the engine. The answer to that issue can be the introduction of dedicated devices to enhance the cooling of the engine. It can be the increase in thickness of the material where the flame touches the wall or the use of air cooling with perforated plates. But these choices can also have an impact on the extinction of the flame. By introducing high heat losses, the efficiency of the engine can be affected.

The flame dynamics result from the coupling between heat release and flow modulations. If the flame dynamics are not controlled, thermoacoustic instabilities can appear in the combustion chamber. The triggering of these instabilities is one of the most critical aspect of the design of the engine and must be prevented to ensure the safety of the engine. Numerous parameters can influence both the frequency and the intensity of the instabilities, such as the operating point (equivalence ratio, distribution of the fuel injection) or the external conditions (air and wall temperatures).

In this thesis, we chose four physical phenomena that will be studied specifically:

- Turbulent flow
- Two-phase combustion
- Flame stabilization
- Flame dynamics

They represent some of the typical phenomena that are involved in the operation of aeronautical combustion chambers. A brief description of each one is proposed below.

Numerical approaches to predict turbulent combustion in realistic configurations

The four major physical phenomena studied in this thesis are presented above. This section aims at presenting the state of the art of the numerical approaches for each of these phenomena.

Turbulence modelling

In order to simulate aeronautical injectors and even whole combustion chambers, manufacturers can now afford Large Eddy Simulations (LES) as a numerical tool (Piomelli and Chasnov (1996); Piomelli (1999); Sagaut (2006)). This approach, by resolving the most energetic structures of the flow, presents a lot of benefits for predicting accurately the flow dynamics and the mixing between species (which is essential in combustion). The unresolved scales, also called "subgrid" scales, have to be modeled to represent the phenomena that have a length scale below the resolution of the LES filter. Numerous subgrid scale models are available in the literature, for example by assuming an eddy-viscosity for the unresolved Reynolds stresses (Smagorinsky (1963); Germano et al. (1991); Nicoud and Ducros (1999); Nicoud et al. (2011a)). They are usually used along with wall laws to recover the proper friction at the walls in attached boundary layers. The simulations that use this approach are called WM-LES, for Wall Modelled Large Eddy Simulations, as opposed to WR-LES, for Wall Resolved Large Eddy Simulations, where the mesh is refined in the proper directions to capture the boundary layer dynamics. In this thesis, for the sake of clarity, WM-LES is simplified to LES.

LES was applied with success to simple combustion chambers equipped with a single swirler such as the PRECCINSTA experiment (Lartigue et al. (2004)), the Cambridge stratified swirl burner (Mercier et al. (2015a), Brauner et al. (2016), Proch et al. (2017), Turkeri et al. (2019)) in gaseous flow or the MERCATO setup (Sanjosé et al. (2010)) in two-phase conditions. The flow topology in these configurations is mostly fixed by a singularity in the geometry, namely a sudden expansion. This kind of simple geometries is usually well characterized by experiments which enables an accurate validation of the LES. The configurations representative of real aeronautical injectors are much more complex: the geometry is intricate, the flow almost always contains two phases (generally a liquid fuel and gaseous air), the Reynolds is usually high, the range of time and space scales is wide because of the various phenomena involved (turbulence, combustion, spray dynamics and evaporation...) and the operating pressure is subject to significant variations (from few to tenths of bars). There are very few studies in which simulations are validated against detailed experiments, because the experimental data are scarce and the predominant phenomena are coupled and difficult to simulate under realistic conditions. Several examples exist that shows the interest of LES for predicting

the ignition sequence (Boileau et al. (2008); Philip et al. (2014), Barré et al. (2014)) or the flow inside a helicopter combustion chamber (Auzillon et al. (2013)). Other advanced simulations exist in the literature where additional effects are taken into account, such as heat transfer and radiation (Berger et al. (2015)). However, the comparison with experiments is often either limited or absent, making the validation of the flow topology predicted by LES difficult or impossible.

A known difficulty for LES is that close to the walls, the most energetic turbulent structures of the flow are very thin and would be extremely expensive to resolve due to mesh constraints. In this region, the mesh has to be refined in the streamwise direction to retrieve the structures responsible for the friction (namely the quasi-streamwise vortices and "hairpin" structures (Robinson (1991); Schlichting and Gersten (2016))). The combined use of wall laws and adapted subgrid scale models can improve the results, but the near-wall turbulence often needs to be described properly to retrieve correctly the flow detachment.

To tackle the problem of wall treatment and to overcome the limits of LES usual modeling, hybrid methods were developed. They combine a URANS (Unsteady Reynolds Averaged Navier Stokes) treatment of the boundary layer to resolve the near-wall dynamics and LES away from the walls to capture the mixing. An example of a hybrid method is the Detached Eddy Simulation (DES) (Spalart et al. (1997)). In this work, its principle is the modification of the original Spalart-Allmaras one-equation RANS model to evolve toward a Smagorinsky-type model for the turbulent viscosity far from the walls. It was improved with the Delayed Detached Eddy Simulation (DDES) (Spalart et al. (2006)), to overcome some difficulties with the previous formulation, such as Grid Induced Separation or Model Stress Depletion.

The Zonal Detached Eddy Simulation (ZDES) approach, developed by Deck (2012), is a DES-type model and brings flexibility in the choices of modeling. The ZDES model was applied with success to non-reacting configurations such as academic configurations (Deck et al. (2014); Weiss and Deck (2013)), landing gears (de la Puente et al. (2014)) or in reacting conditions on backward facing steps (Sainte-Rose et al. (2008)) or nozzles (Sainte-Rose et al. (2012)).

Combustion chemistry

Flame stabilization and pollutant formation requires a fine description of the combustion kinetics (Rutland (2011), Pope (2013)). Numerous methods exist in the literature to model the combustion chemistry (for instance for kerosene combustion see Dagaut and Cathonnet (2006)).

Four major ways can be used: detailed, global, analytically reduced or tabulated chemistry. Each represents a trade-off between an accurate description of the chemical processes and their cost. Detailed chemistry requires a large amount of computation power for the chemistry alone because of the number of species and

reactions. Therefore it is not usable in complex configurations. For industrial applications, global chemistry is one of the most applied models. It is designed to recover the basic properties of a flame (for example laminar flame velocity or final composition). Examples for kerosene are proposed in [Franzelli et al. \(2010\)](#) and [Choi \(2011\)](#). These approaches are attractive for their cost, but in situations where additional properties are required (pollutant emissions or detailed chemistry effects such as preferential diffusion), they are not designed to recover them. That is why the development of analytically reduced schemes has grown over the years ([Montgomery et al. \(2002\)](#), [Luche et al. \(2004\)](#), [Zettervall et al. \(2016\)](#), [Jaravel et al. \(2017\)](#)) with specific targets for the reduction.

Finally, tabulated chemistry methodologies have been developed during the last decades to account for detailed chemistry effects at a reduced CPU cost ([Fiorina et al. \(2015\)](#); [Oijen et al. \(2016\)](#)). Among them, the Filtered Tabulated Chemistry for LES (F-TACLES), has been especially developed to incorporate complex chemistry effects in an LES formalism ([Fiorina et al. \(2010a\)](#)). It consists in tabulating the chemical ingredients needed by the LES in a filtered lookup table. F-TACLES has been applied to complex gaseous turbulent flames such as stratified ([Auzillon et al. \(2012a\)](#)) and non-adiabatic ([Mercier et al. \(2014a\)](#); [Mercier et al. \(2016a\)](#)) configurations. The suitability of F-TACLES to turbulent spray flames simulations has however never been addressed, which is one of the objectives of this thesis.

Heat losses modelling

In many combustors operating in the lean premixed combustion regime, the flame is stabilized by a swirling flow. By promoting recirculation zones composed of burnt gases, flame stabilization is enhanced over a wide range of operating conditions ([Huang and Yang \(2009a\)](#)). The flow structure in a combustor equipped with a swirling injector is very complex ([Gupta et al. \(1984\)](#)) and either M or V flame shapes can be observed. The shape taken by the flame then affects the temperature field in the burnt gases at the outlet of the combustion chamber and pollutant emissions. Experiments and simulations indicate that the topology of swirling flames is highly sensitive to fuel composition ([Kim et al. \(2010\)](#); [Terhaar et al. \(2014\)](#); [Guiberti et al. \(2015\)](#)) and heat transfer to the combustion chamber walls ([Guiberti et al. \(2015a\)](#); [Nogenmyr et al. \(2013\)](#); [Tay Wo Chong et al. \(2009\)](#); [Proch and Kempf \(2015\)](#); [Donini et al. \(2013\)](#)). Simulations of the stabilization regimes of these flames are very challenging as numerous physical phenomena such as the combustion chemistry, flame interactions with turbulence and heat losses have to be taken into account.

In this way, modeling efforts are continuously conducted to improve the description of detailed chemistry effects in turbulent combustion simulations ([Fiorina et al. \(2015\)](#)). In particular, Large Eddy Simulations (LES) turbulent com-

bustion models based on tabulated chemistry have been recently improved by several groups to account for the influence of heat transfer on the flame stabilization process (Trisjono et al. (2014); Ketelheun et al. (2013); Mercier et al. (2014b)). These numerical strategies have been targeted on the same Turbulent Stratified Flame (TSF) experiments conducted at the Technical University of Darmstadt (TUD) (Kuenne et al. (2012)). A joined comparative study between simulations and experimental data shows that while each adiabatic computations predict a flame anchored on the burner lip, all non-adiabatic simulations agree on a flame lift-off of one half pilot diameter (Fiorina et al. (2015)). These last results lead to a better agreement with experimental measurements of temperature and species concentrations (Fiorina et al. (2015)). However, being unconfined and non-swirled, the TSF configuration validates only partially the ability of a turbulent combustion model to capture flame stabilization process in a gas turbine like combustor. To achieve the validation, complementary experimental configurations, more representative of combustion chamber with a swirling flow are required.

Tay Wo Chong et al. (2009) analyzed numerically the influence of heat losses on the shape taken by the flame in a confined swirled non-adiabatic combustor. They accounted for heat losses in Reynolds Averaged Navier-Stokes (RANS) simulations to reproduce the V flame shape observed through chemiluminescence imaging experiments. However, as accurate measurements of the thermal boundary conditions and flame shape were not available in this study, the comparisons between simulations and experiments remained qualitative. Proch and Kempf (2015) modelled the effects of heat losses in a model gas turbine combustor where it was shown that non-adiabatic computations allow a better prediction of the flame shape and length in comparisons to adiabatic simulations. In this study, the wall temperatures were not measured and a fixed temperature of $T = 1000$ K was imposed for all the combustor walls. Nogenmyr et al. (2013) imposed realistic measured temperature profiles in the non-adiabatic LES of a reduced-scale confined burner. However, temperature measurements were not realized on the same burner geometry and with the same fuel as in the simulation.

Flame dynamics

Simulations of the response of swirling flames to flow modulations motivate research efforts from many groups (Tay-Wo-Chong et al. (2012); Iudiciani and Duwig (2011); Palies et al. (2011); Krediet et al. (2012); Tay-Wo-Chong and Polifke (2013); Hermeth et al. (2014); Bauerheim et al. (2015); Han and Morgans (2015)) and the progress made are reviewed in Poinot (2017), Huang and Yang (2009b) and Candel et al. (2014).

By explicitly computing the unsteady interactions between the largest struc-

tures of the flow field and the flame, Large Eddy Simulation (LES) is one attractive strategy to determine the Flame Transfer Function (FTF) in practical conditions. Subgrid scale models are required to capture key quantities, such as the flame thickness or the flame wrinkling, which are not fully resolved on practical meshes (Poinsot and Veynante (2005); Pitsch (2006)). As recently illustrated in a collaborative study performed in the framework of the TNF workshop (Fiorina et al. (2015)), LES turbulent combustion models designed for turbulent premixed combustion yield good predictions of the mean statistical flame properties such as the flame front position, the temperature field, or the species mass fractions.

Studies about the ability of LES turbulent combustion strategies to retrieve flame dynamics properties and in particular its frequency response to flow modulations remain however scarce. Among the few investigations conducted, a series of studies (Tay Wo Chong et al. (2010); Tay Wo Chong and Polifke (2013)) focused on the impact of flame confinement and thermal boundary conditions on the FTF of a premixed swirling flame. They used the LES compressible code AVBP from ?? (a) with a Dynamic Thickened Flame Model (Legier et al. (2000)). A broadband frequency perturbation method was followed to determine the FTF in the simulations (Tay Wo Chong et al. (2010)). Numerical results for the cold flow field were first compared to velocity measurements. The calculated heat release distribution was also compared to an image of the OH* light distribution measured in the combustor for steady flow injection conditions. It was then shown that the broadband forcing technique allows to well reproduce the measured FTF for vanishingly small perturbation levels. No detailed comparisons of the flame motions with experiments were however carried out in these studies. An interesting conclusion is that heat losses to the walls need to be taken into account to retrieve qualitatively the flame shape observed in experiments and its FTF (Komarek et al. (2008); Chong et al. (2009); Keppeler et al. (2012); Tay Wo Chong and Polifke (2013)). The same team recently studied the combined effects of heat losses and strain rate (Tay Wo Chong et al. (2016); Tay Wo Chong et al. (2017)) and found as in Guiberti et al. (2015b) and Mercier et al. (2016b) that they strongly alter the way the flame is stabilized. These authors however did not have access to detailed experimental data for velocity and temperature fields in their combustor.

Han and Morgans (2015) also chose LES to recover the FDF of a lean premixed turbulent flame stabilized in the wake of a bluff body. The incompressible solver Code_Saturne with Flame Surface Density (Boger et al. (1998)) and Fureby's fractal approach for flame wrinkling (Fureby (2005)) are used in these simulations. Heat losses at the walls were not considered in this study and there is no swirl imparted to the flow. The simulations qualitatively retrieve the FDF for different perturbation levels and frequencies. Simulations led to under-prediction of the FDF gain, but a fairly good agreement for the FDF

phase lag. These authors also provide a qualitative comparison between the simulated flame motions and results from experiments (Balachandran et al. (2005)) based on phase averaged analysis of the flame surface density data for different forcing frequencies. Suggestions are given for interpretation of the differences observed between experiments and simulations. A closer look of the results shown in Han and Morgans (2015) reveals that the flame dynamics is not well reproduced by the simulations close to the solid boundaries. Large differences with experiments are observed for the flame shape calculated at the flame base and flame tip. There are also no detailed comparisons with experiments for the response of the flow field to the pulsations.

It is also found in other studies that heat losses to solid boundaries modify the acoustic response of laminar flames, and in particular alter the FTF gain (Kedia et al. (2011); Mejia et al. (2015); Kedia and Ghoniem (2015)). This is mainly attributed to changes of the flame response at its anchoring location.

Despite its significance, the influence of heat losses on the FTF has not been studied to find the physical phenomena that are involved.

Objectives of this thesis

The objectives of this thesis revolve around the four physical phenomena presented above.

The first objective is to assess the ability of numerical simulations to reproduce experimental results and identify their current limitations. Two main aspects are considered: the flame dynamics of non-adiabatic flames and the stabilization of spray flames. The validation of the simulations is based on detailed comparisons between experimental diagnostics and their corresponding quantity in the simulations.

The second objective is to compare different approaches for turbulence modeling and provide recommendations for the simulations of complex configurations. The design of the mesh is addressed carefully and its influence on the simulation results is discussed, especially in a two-phase flow context.

Organization of this manuscript

The central theme of this thesis is the study of tabulated chemistry models in configurations representative of aeronautical combustion chambers. This thesis is divided in two parts and five chapters:

- **Part I** focuses on the turbulent combustion modeling and the application of the F-TACLES model to two challenging configurations.

Chapter 1 presents the turbulent combustion modeling framework of this thesis.

Chapter 2 details the study of a non-adiabatic combustor in steady and pulsed conditions and how the F-TACLES formalism performs in these conditions.

Chapter 3 focuses on the first application of the F-TACLES formalism in two-phase combustion.

- **Part II** presents the numerical study of a realistic aeronautical injector.

Chapter 4 proposes a validation of the ZDES turbulence approach in non-reacting conditions for a realistic aeronautical injector.

Chapter 5 shows the performance of LES and ZDES approaches with tabulated chemistry in reacting conditions for this injector.

Part I

Turbulent combustion modeling: application of tabulated chemistry models to complex configurations

Chapter 1

Turbulent combustion modeling

This chapter focuses on the presentation of the turbulent combustion modeling framework. It presents the governing equations and the models used. It is centered around the tabulated chemistry models for the combustion and the LES and ZDES formalism for the turbulence.

1.1 Governing equations

1.1.1 Flow governing equations

The filtered equations for mass, species, momentum and total energy solved by a flow solver are written in Eqs. 1.1,1.2,1.3 and 1.4. The equation for mass conservation reads:

$$\frac{\partial \bar{\rho}}{\partial t} + \nabla \cdot (\bar{\rho} \tilde{\mathbf{u}}) = 0, \quad (1.1)$$

where $\bar{\rho}$ is the filtered density and $\tilde{\mathbf{u}}$ the filtered velocity (\bar{x} denoting the Reynolds filtering operator and \tilde{x} the Favre or density-weighted filtering operator of the quantity x). The equation for species reads:

$$\begin{aligned} \frac{\partial \bar{\rho} \tilde{Y}_i}{\partial t} + \nabla \cdot (\bar{\rho} \tilde{\mathbf{u}} \tilde{Y}_i) &= \nabla \cdot (\bar{\mathbf{D}}_i) + \tilde{\omega}_i \\ &+ \nabla \cdot \left[\bar{\rho} (\widetilde{\mathbf{u} Y_i} - \tilde{\mathbf{u}} \tilde{Y}_i) \right], \end{aligned} \quad (1.2)$$

where \tilde{Y}_i is the filtered mass fraction, $\bar{\mathbf{D}}_i$ the filtered diffusive flux and $\tilde{\omega}_i$ the filtered source term of the specie i . The equation for momentum is written as:

$$\begin{aligned} \frac{\partial \bar{\rho} \tilde{\mathbf{u}}}{\partial t} + \nabla \cdot (\bar{\rho} \tilde{\mathbf{u}} \otimes \tilde{\mathbf{u}}) &= \nabla \cdot (\bar{\boldsymbol{\tau}} - \bar{p} \mathbf{I}) + \bar{S}_m \\ &+ \nabla \cdot \left[\bar{\rho} (\widetilde{\mathbf{u} \otimes \mathbf{u}} - \tilde{\mathbf{u}} \otimes \tilde{\mathbf{u}}) \right], \end{aligned} \quad (1.3)$$

where $\bar{\tau}$ is the filtered viscous stresses tensor, \bar{p} the filtered pressure, \mathbf{I} the identity tensor and \bar{S}_m the filtered momentum volume sources, which are neglected here. Finally, the equation for total energy reads:

$$\begin{aligned} \frac{\partial \bar{\rho} \tilde{e}_t}{\partial t} + \nabla \cdot (\bar{\rho} \tilde{e}_t \tilde{\mathbf{u}}) &= \nabla \cdot (\overline{\mathbf{D}_{e_t}}) + \nabla \cdot [(\bar{\tau} - \bar{p} \mathbf{I}) \tilde{\mathbf{u}}] \\ &+ \nabla \cdot [\overline{\rho e_t \mathbf{u} - (\tau - p \mathbf{I}) \mathbf{u}}] \\ &+ \nabla \cdot [-\bar{\rho} \tilde{e}_t \tilde{\mathbf{u}} + (\bar{\tau} - \bar{p} \mathbf{I}) \tilde{\mathbf{u}}] + \bar{S}_{e_t}, \end{aligned} \quad (1.4)$$

where \tilde{e}_t is the filtered total energy, $\overline{\mathbf{D}_{e_t}}$ the filtered total energy flux and \bar{S}_{e_t} the filtered total energy volume source term, neglected here.

The filtering operation introduces terms that need to be closed. The filtered diffusion and energy fluxes are approximated with a simple gradient assumption. The term $\tau_t = \bar{\rho} (\widetilde{\mathbf{u} \otimes \mathbf{u}} - \tilde{\mathbf{u}} \otimes \tilde{\mathbf{u}})$ is closed depending of the chosen turbulence approach. The turbulence approaches used in this thesis are presented in Sec. 1.3.

1.1.2 Dispersed phase governing equations

The dispersed phase is described in this thesis with a Lagrangian point-force approach, which is two-way coupled to the gaseous phase. The following transport equations are solved for each numerical droplet, that represents an ensemble of physical droplets:

$$\frac{d\mathbf{x}_p}{dt} = \mathbf{u}_p \quad (1.5)$$

$$m_p \frac{d\mathbf{u}_p}{dt} = m_p (\mathbf{u}_p - \mathbf{u}) \frac{3C_D Re_p \rho \nu}{4\rho_p d_p^2} \quad \text{with } Re_p = \frac{d_p |\mathbf{u}_p - \mathbf{u}|}{\nu} \quad (1.6)$$

where \mathbf{x}_p is the particle position, \mathbf{u}_p the particle velocity, \mathbf{u} the gas velocity, m_p the particle mass, C_D the drag coefficient, ν the kinematic viscosity, ρ_p the particle density and Re_p the particle Reynolds number.

The evaporation of the spray is modelled with the classical approach derived by Spalding (1953). The droplet mass transfer equation reads:

$$\dot{m}_p = -\pi d_p \rho \mathcal{D} Sh \log(1 + B_M) \quad (1.7)$$

where d_p is the particle diameter, \mathcal{D} is the diffusion coefficient, Sh the Sherwood number and B_M the Spalding mass number.

The other droplet parameters are derived by integrating either the droplet mass or energy equations. Droplet temperature T_p and diameter d_p are obtained by solving the following set of equations:

$$\frac{dT_p}{dt} = -\frac{1}{\tau_p} \left(T_p - \left(T_\infty - \frac{L_v B_T}{C_{p,1/3}} \right) \right) \quad (1.8)$$

$$\frac{dd_p^2}{dt} = -\frac{2Sh\mu_{1/3} \log(1 + B_M)}{\rho_p Sc} \quad (1.9)$$

$$\tau_p = \frac{\rho_p d_p^2}{6} \frac{Sc}{Sh \cdot \mu_{1/3}} \frac{C_{p,k}}{C_{p,1/3}} \frac{B_T}{\log(1 + B_M)} \quad (1.10)$$

where τ_p is the thermal characteristic time of the Spalding model, T_∞ the gas temperature in the far field, L_v the latent heat of vaporization of the fuel, B_T the Spalding thermal number, $C_{p,1/3}$ the heat capacity at a classical reference state assuming a one third/two third equilibrium between the far field and the droplet surface, $\mu_{1/3}$ the dynamic viscosity at the same reference state and Sc the Schmidt number.

For analysis purposes in Chapters 3 and 5, the Stokes number is introduced and defined as:

$$Stk = \frac{t_0 u_0}{l_0} \quad (1.11)$$

where t_0 is the relaxation time of the particle, u_0 the fluid velocity around the particle and l_0 a characteristic length of the flow. t_0 is defined as:

$$t_0 = \frac{\rho_p d_p^2}{18\mu_g} \quad (1.12)$$

where ρ_p is the density of the particle, d_p its diameter and μ_g the dynamic viscosity of the gas surrounding the particle.

1.2 Flow solvers

Two flow solvers are used in this thesis: YALES2 and CEDRE. The choice of the solver depends on the configuration. For low Mach-number applications, YALES2 is adapted while CEDRE is able to treat compressible flows.

1.2.1 YALES2

The simulations presented in Chapters 2 and 3 are performed using the low Mach-number cell-vertex flow solver YALES2 (Moureau et al. (2011a)).

A centered fourth-order finite volume scheme is used for spatial discretization. The time integration relies on a low-Mach number projection method for variable density flows. The time integration of convective terms is performed using the TRK4 fourth-order scheme (Kraushaar (2011)).

1.2.2 CEDRE

The simulations presented in Chapters 4 and 5 are performed with the finite-volume cell-centered CHARME solver for the gaseous phase and the Lagrangian SPARTE solver for the liquid dispersed phase. They both belong to the CEDRE platform for numerical simulations in energetics, developed at ONERA (Reffloch et al. (2011)).

The finite-volume CHARME solver solves compressible reacting flows on unstructured meshes (made of any type of polyedra). The spatial discretization is based on the use of a second order MUSCL (Monotonic Upwind Scheme for Conservation Laws) scheme, with Roe-like upwind fluxes and a Van-Leer limiter. Time integration is performed with an implicit second order Runge-Kutta scheme, along with a GMRES (Generalized Minimal RESidual method) resolution of the linear system.

The SPARTE solver computes the transport of particles following a Lagrangian approach. The time integration is explicit.

1.3 Turbulence modeling

1.3.1 The Boussinesq hypothesis

To close the momentum equation, the tensor $\tau_t = \bar{\rho} (\widetilde{\mathbf{u} \otimes \mathbf{u}} - \tilde{\mathbf{u}} \otimes \tilde{\mathbf{u}})$ is modelled with the Boussinesq hypothesis:

$$\tau_t = \mu_t \left[\nabla \tilde{\mathbf{u}} + (\nabla \tilde{\mathbf{u}})^T - \frac{2}{3} (\nabla \cdot \tilde{\mathbf{u}}) \mathbf{I} \right], \quad (1.13)$$

where μ_t is a quantity homogeneous to a dynamic viscosity. The closure of μ_t depends on the choice of the turbulence model. Two models for μ_t based on LES and ZDES concepts are used in this thesis and described in Sec. 1.3.2 and 1.3.3 respectively.

1.3.2 LES approach

The first approach for turbulence used in this thesis is the LES, which decomposes the flow into a resolved part (the most energetic structures) and modelled subgrid scales. μ_t (see Eq. 1.13) is closed as a subgrid scale viscosity. Two subgrid scale viscosity are used in this thesis.

In Chapters 2 and 3, the SIGMA model (Nicoud et al. (2011a)) is used to model μ_{sgs} :

$$\mu_{sgs} = \bar{\rho} \left(C_\sigma \widehat{\Delta} \right)^2 \mathcal{D}_\sigma \text{ with } \mathcal{D}_\sigma = \frac{\sigma_3(\sigma_1 - \sigma_2)(\sigma_2 - \sigma_3)}{\sigma_1^2}, \quad (1.14)$$

where σ_1 , σ_2 and σ_3 are the singular values of the velocity gradient tensor, $\widehat{\Delta}$ the filter size and $C_\sigma = 1.35$ the constant of the SIGMA model.

In Chapters 4 and 5, μ_{sgs} is modelled following Smagorinsky (1963):

$$\mu_{sgs} = \bar{\rho} \left(C_S \widehat{\Delta} \right)^2 \sqrt{2\widetilde{S} : \widetilde{S}}, \quad (1.15)$$

where $\bar{\rho}$ is the LES filtered density, C_S the model constant chosen equal to 0.1 (Deardorff (1970); Meyers and Sagaut (2006)) and \widetilde{S} the symmetric part of the filtered velocity gradient tensor.

In CEDRE, the filter size $\widehat{\Delta}$ is modified with respect to the normal distance to the wall d as $\min(\Delta, 0.4d/C_S)$ to obtain a vanishing subgrid scale viscosity at the walls. The filter size Δ is evaluated as the ratio between the volume of the cell and the sum of its faces' area, in order to obtain the length of the edge for a cubic cell:

$$\Delta = \frac{6V}{\sum_k A_k}, \quad (1.16)$$

where V is the volume of the cell and A_k the surface of its k^{th} face.

1.3.3 ZDES approach

In meshes typically used in LES of reactive simulations, the boundary layer is not discretized down to the viscous sublayer. Despite the use of wall laws (described in Sec. 1.3.4.2), LES may not be adapted to all complex geometries, where the properties of the boundary layers are not well described by the wall law. To overcome this limitation, the advanced turbulence model called Zonal Detached Eddy Simulation (ZDES) is used.

In this thesis, when using ZDES, the turbulent viscosity μ_t (see Eq. 1.13) is modelled with the Spalart-Allmaras one-equation model (Spalart and Allmaras (1992)) as:

$$\mu_t = \bar{\rho} \widetilde{\nu} f_{v1} \text{ where } f_{v1} = \frac{\chi^3}{\chi^3 + C_{v1}^3} \text{ is a low-Reynolds correction function}$$

$$\text{with } \chi = \frac{\widetilde{\nu}}{\nu} \text{ and } C_{v1} = 7.1,$$

$$(1.17)$$

where the transported scalar is the pseudo-viscosity $\tilde{\nu}$ which obeys:

$$\frac{D\tilde{\nu}}{Dt} = c_{b1}\tilde{S}\tilde{\nu} + \frac{1}{\sigma} \left\{ \nabla \cdot [(\nu + \tilde{\nu}) \nabla \tilde{\nu}] + c_{b2} (\nabla \tilde{\nu})^2 \right\} - c_{w1} f_w \left(\frac{\tilde{\nu}}{d_w} \right)^2, \quad (1.18)$$

where c_{b1} , σ , c_{b2} and c_{w1} are model constants, f_w a low-Reynolds correction function and d_w the distance to the walls. Further details can be found in the original paper (Spalart and Allmaras (1992)).

Based on this simple one-equation model adapted for RANS, Spalart et al. (1997) proposed a new formulation, called Detached Eddy Simulation (DES), that would act as an hybrid RANS/LES formulation. The main idea of the DES methods is to modify the definition of the distance to the wall d_w in the $\tilde{\nu}$ destruction term with:

$$\hat{d} = \min(d_w, C_{DES}\Delta). \quad (1.19)$$

This modification means that close to the wall, the original Spalart-Allmaras equation is not modified. Away from the walls, assuming that production and destruction terms in the transport equation of $\tilde{\nu}$ are balanced, the pseudo-viscosity $\tilde{\nu}$ scales in DES with the mesh size Δ and the local vorticity modulus $|\tilde{S}|$:

$$\tilde{\nu} \propto (C_{DES}\Delta)^2 |\tilde{S}|, \quad (1.20)$$

which corresponds to a definition equivalent to the Smagorinsky model (Eq. 1.15). The constant C_{DES} is set to 0.65. This value was found by Shur et al. (1999) to retrieve the correct decay of turbulent kinetic energy in homogeneous isotropic turbulence.

The original definition of \hat{d} (Eq. 1.19) introduces issues such as Grid Induced Separation (GIS) (Menter et al. (2003); Menter and Kuntz (2004)) or Model Stress Depletion (MSD) (Gritskevich et al. (2012); Deck et al. (2011)). That is why Spalart (Spalart et al. (2006)) proposes a new definition:

$$\hat{d} = d_w - f_d \max(0, d_w - C_{DES}\Delta), \quad (1.21)$$

where f_d is defined as:

$$f_d = 1 - \tanh[(8r_d)^3] \quad \text{with} \quad r_d = \frac{\nu_t + \nu}{\kappa^2 d_w^2 \sqrt{\nabla \tilde{\mathbf{u}} : \nabla \tilde{\mathbf{u}}}} \quad (1.22)$$

where ν_t is the kinematic turbulent viscosity, ν the molecular kinematic viscosity, $\nabla \tilde{\mathbf{u}}$ the velocity gradient and κ the Kármán constant. This new approach was called Delayed Detached Eddy Simulation (DDES).

The Zonal Detached Eddy Simulation (ZDES) was first derived by [Deck \(2005\)](#) in parallel of the work of [Spalart et al. \(2006\)](#) on DDES. The complete formulation that proposes an efficient solution to prevent delay in the formation of instabilities was published in [Deck \(2012\)](#) and was implemented in the CEDRE platform.

This approach is fully zonal by nature and presents two advantages: the user can specify RANS and LES regions and also use different formulations within the same calculation. Thus, ZDES offers an attractive flexibility in the treatment of turbulent flows in technical applications and was applied often with good results over a range of Mach numbers and configurations (for examples, see [Deck et al. \(2014\)](#)).

Four formulations, also called "modes" and which differ by the definition of the hybrid length scale, are then optimized to be used on three typical flow field topologies (see [Fig. 1.1](#)):

- **Mode 0** corresponds to the classical RANS formulation.
- **Mode 1** deals with flows where the separation is triggered by a relatively abrupt variation in the geometry.
- **Mode 2** is retained when the location of separation is induced by a pressure gradient on a gently-curved surface or when separation location is not known a priori.
- **Mode 3** for flows where the separation is strongly influenced by the dynamics of the incoming boundary layer. This latter mode is often referred to as Wall-Modelled Large Eddy Simulation (WMLES) mode (see [Deck et al. \(2011\)](#); [Deck et al. \(2014\)](#)).

The ZDES method aims at treating all classes of flow problems indicated in [Fig. 1.1](#) in a single model, which of length scale reads as :

$$\tilde{d}_{ZDES} = \begin{cases} d_w & (mode = 0) \\ \tilde{d}_{DES}^I & (mode = 1) \\ \tilde{d}_{DES}^{II} & (mode = 2) \\ \tilde{d}_{DES}^{III} & (mode = 3) \end{cases} \quad (1.23)$$

The definition of the hybrid length scales (modes 1 to 3) are:

$$\tilde{d}_{DES}^I = \min(d_w, C_{DES} \tilde{\Delta}_{DES}^I) \text{ (original DES formulation),} \quad (1.24)$$

$$\tilde{d}_{DES}^{II} = d_w - f_d \max(0, d_w - C_{DES} \tilde{\Delta}_{DES}^{II}) \text{ (DDES formulation),} \quad (1.25)$$

$$\tilde{d}_{DES}^{III} = \begin{cases} d_w & \text{if } d_w < d_w^{interface} \\ \tilde{d}_{DES}^I & \text{if } d_w \geq d_w^{interface} \end{cases} \quad (\text{WMLES formulation}), \quad (1.26)$$

where $d_w^{interface}$ is prescribed by the user.

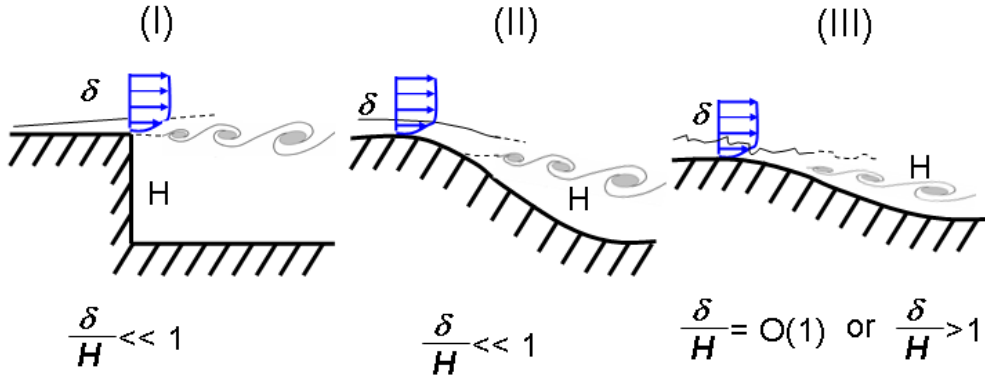


Figure 1.1: Classification of typical flow problems. I: separation fixed by the geometry, II: separation induced by a pressure gradient on a curved surface or when separation location is not known a priori, III: separation strongly influenced by the dynamics of the incoming boundary layer (adapted from [Deck \(2012\)](#)).

An example where the three modes of ZDES are used at the same time on a curvilinear geometry (three-element airfoil with deployed slat and flap) can be found in [Deck and Laraufe \(2013\)](#).

In Chapters 4 and 5, only mode 2 is used since the location of separation is not known in advance.

The ZDES approach introduces a new way to modify Δ_{DES}^I in Eq. 1.25 in order to further avoid MSD. It takes advantage of the function f_d defined earlier and changes the definition of Δ based on a limit value f_{d0} of this function. The new definition reads:

$$\Delta_{DES}^{II} = \begin{cases} \Delta_{max} & \text{if } f_d < f_{d0} \\ \Delta_{vol} & \text{if } f_d \geq f_{d0} \end{cases}, \quad (1.27)$$

where $\Delta_{max} = \max(\Delta x, \Delta y, \Delta z)$, $\Delta_{vol} = (\Delta x \Delta y \Delta z)^{1/3}$ and $f_{d0} = 0.8$ in the present work, following [Deck \(2012\)](#). This value of f_{d0} was found to be optimal in flat plate simulations. This last modification is the only difference between the DDES formulation and the ZDES mode 2.

1.3.4 Wall law

1.3.4.1 Boundary layer model

An attached turbulent boundary layer can be described, following Cousteix (2005), by two equations, describing the two internal regions of the boundary layer. The non-dimensional distance from the wall y^+ is defined as:

$$y^+ = y \frac{u_\tau}{\nu} \text{ with } u_\tau = \sqrt{\frac{\tau_p}{\rho}}, \quad (1.28)$$

where y is the distance from the wall, ν the kinematic viscosity, τ_p the wall friction and ρ the density. The non-dimensional velocity u^+ is defined as:

$$u^+ = \frac{u}{u_\tau}. \quad (1.29)$$

For a flat plate, in the logarithmic region, u^+ is linked to y^+ by the following equation:

$$u^+ = A_u \ln(y^+) + B_u, \quad (1.30)$$

where $A_u = 1/\kappa$ (κ is the Kármán constant) and $B_u = 5.3$. In the viscous sublayer, the relation becomes:

$$u^+ = y^+. \quad (1.31)$$

1.3.4.2 Wall law implementation

In the LES presented in this thesis, the boundary layer is not meshed down to the viscous sublayer region. Therefore a wall law is needed to retrieve the correct friction τ_p . It is assumed that the boundary layer model presented above is correct for all the boundary layers present in the simulations that use a wall law. The wall law is assumed to be valid if:

$$\frac{\nu}{u_\tau} \ll y_1 \ll \delta, \quad (1.32)$$

where y_1 is the distance to the wall of the center of the first cell and δ is the thickness of the boundary layer. The first limit corresponds to the limit between the viscous sublayer and the logarithmic region. The second limit corresponds to the limit of the boundary layer. Satisfying both conditions ensures that the first cell size is within the validity of the wall law.

The wall friction τ_p is computed in CEDRE as:

$$\tau_p = \left(\mu \frac{\partial u}{\partial y} \right)_p = (1 + \alpha) \mu \frac{u_1}{y_1}, \quad (1.33)$$

where μ is the dynamic viscosity, u_1 the velocity component parallel to the wall in the first cell and α a correction factor that must be modeled. In all the CEDRE simulations presented in this thesis, it is closed based on the mixing length model. In this model, it is assumed that the friction for the flat plate is constant in the internal region of the boundary layer. Therefore, the friction τ in the boundary layer is expressed as:

$$\tau = \mu \frac{\partial u}{\partial y} - \rho \langle u'v' \rangle = \tau_p \quad (1.34)$$

The term $\rho \langle u'v' \rangle$ is closed, following [Van Driest \(2003\)](#), in the mixing length model as:

$$\tau = \mu \frac{\partial u}{\partial y} + \rho F^2 l^2 \left(\mu \frac{\partial u}{\partial y} \right)^2 = \tau_p \quad (1.35)$$

where $F = 1 - \exp(-y^+/A^+)$ (with $A^+ = 26$) is the dampening function and $l = 0.085\delta \tanh\left(\frac{\kappa y}{0.085\delta}\right)$ the mixing length. This equation can be written with non-dimensional quantities:

$$\frac{\partial u^+}{\partial y^+} + \kappa^2 y^{+2} \left[1 - e^{-\frac{y^+}{A^+}} \right] \left(\frac{\partial u^+}{\partial y^+} \right)^2 = 1. \quad (1.36)$$

The solution to this equation is then computed (with $y^+ = 0$ for $u^+ = 0$). The values of τ , u_1 , y and α are then stored in a table as a function of the local Reynolds number based on the cell diameter $Re_\Delta = \frac{u_1 \Delta}{\nu}$. Finally, the value of α is computed in the simulations with the following function, resulting of an interpolation of the table previously stored:

$$\alpha = \frac{f_c}{1 + f_c} \left(\frac{Re_\Delta}{447} \right)^{0.825} \quad \text{with } f_c = \frac{Re_\Delta}{80} + \left(\frac{Re_\Delta}{120} \right)^2 \quad (1.37)$$

In YALES2, the wall law is based on the same principle. The major difference with the implementation in CEDRE is that the computation of the wall friction τ_p is not the result of a tabulation. Instead, a Newton's method is used to compute u_τ and then the wall friction is computed as ρu_τ^2 .

1.4 Combustion modeling

1.4.1 Existing approaches for chemistry reduction

In order to simulate combustion processes, a chemical scheme is necessary to describe the evolution of the system. However, for hydrocarbon fuels, a detailed

chemical scheme involves typically tens to thousands species and reactions. For industrial applications, it is impossible to use these schemes because they are too expensive in terms of computational cost. Numerous techniques exist that aim at decreasing the cost of the chemistry in simulations. It is possible to distinguish three main routes: scheme reduction, global step chemistry and tabulated chemistry.

Scheme reduction is based on identifying the species and reactions in a detailed scheme that are not necessary for achieving a certain goal (typically the laminar flame speed or the evolution of a specie mass fraction) and eliminate them from the scheme. Several methods exist in the literature (Tomlin et al. (1997); Valorani et al. (2006); Pepiot-Desjardins and Pitsch (2008)). It still produces large schemes that can be treated with additional methods (Jaravel et al. (2018)) to decrease the cost even more and make it affordable for complex configurations. Global step chemistry relies on the choice of key species (typically reactants and major products) and adapted reactions for reproducing the most important aspects of the flame propagation (Jones and Lindstedt (1988)).

Finally, tabulated chemistry revolves around the storage in a look-up table of 1-D premixed, partially premixed or non-premixed flames computed with a detailed scheme. It is described in Sec. 1.4.2. A review of this kind of approach is proposed in Fiorina et al. (2015).

1.4.2 Chemistry tabulation

The tabulated chemistry method based on premixed flamelets is retained in this thesis. The advantage of this method is its moderate cost compared to reduced schemes or even global schemes in most cases. It is compatible with complex geometry applications but also includes the most important features of complex chemistry.

It is based on the principle that the evolution of a system in combustion can be described by a reduced set of trajectories (or manifold) in the chemical space. In this thesis, the approach for tabulating premixed flamelets is FPI (Flame Prolongation of ILDM), proposed by Gicquel et al. (2000) and extended for non-adiabatic combustion by Fiorina et al. (2003). In a similar approach, Oijen and Goey (2000) proposed the Flamelet Generated Manifold (FGM) model. In FPI for partially-premixed combustion, the evolution of the system in the chemical space is described by two quantities: the progress variable Y_c and the mixture fraction z , that will compose the coordinates of the look-up tables used in the simulations.

The mixture fraction Y_z is defined as (following for instance Bilger (1976)):

$$Y_z = Y_e \tag{1.38}$$

where Y_e is the mass fraction of the chemical element e . It is typically chosen as C (carbon) in hydrocarbon combustion. Y_z evolves monotonically with the

equivalence ratio ϕ . It can be normalized as:

$$z = \frac{Y_z(\phi) - Y_z(\phi_{min})}{Y_z(\phi_{max}) - Y_z(\phi_{min})} \quad (1.39)$$

where ϕ_{min} and ϕ_{max} are the minimum and maximum equivalence ratios chosen for a given configuration. By construction, z is bounded between 0 and 1.

The progress variable Y_c is defined as a linear combination of the specie mass fractions Y_k :

$$Y_c = \sum_{k=1}^{N_{sp}} n_k Y_k \quad (1.40)$$

where n_k is a coefficient linked to the n th specie. The choice of the n_k coefficients is made in order to have a unique set of thermochemical quantities for a given progress variable, i.e. Y_c evolves in a monotonous way between fresh and burnt gases. Y_c can be normalized as c :

$$c = \frac{Y_c - Y_c^f(z)}{Y_c^{eq}(z) - Y_c^f(z)} \quad (1.41)$$

where the superscripts f and eq represent the fresh and burnt gases states, respectively. In this formulation, c is bounded between 0 and 1.

In Chapters 2 and 3, chemical look-up tables are computed with the RE-GATH thermochemistry package developed at the EM2C laboratory (Pons et al. (2009); Candel et al. (2011)).

In Chapter 5, premixed flamelets are computed using the CANTERA solver (Goodwin et al. (2017)) and the look-up table used contains 150 points in the z direction and 100 points in the c direction.

1.4.3 Coupling FPI tabulated chemistry with LES

The simulation of combustion in LES faces two majors issues, highlighted in Fig. 1.2:

- **Issue 1:** the flame thickness is typically smaller than the size of the LES grid.
- **Issue 2:** the flame wrinkling is not fully resolved at the scale of the LES grid.

Two strategies are followed in this thesis to overcome **Issue 1** based on flame filtering (Sec. 1.4.3.1) and thickening (Sec. 1.4.3.2), respectively. **Issue 2** is solved by modelling the subgrid scale flame wrinkling using different approaches. The one retained here is presented in Sec. 1.4.5.

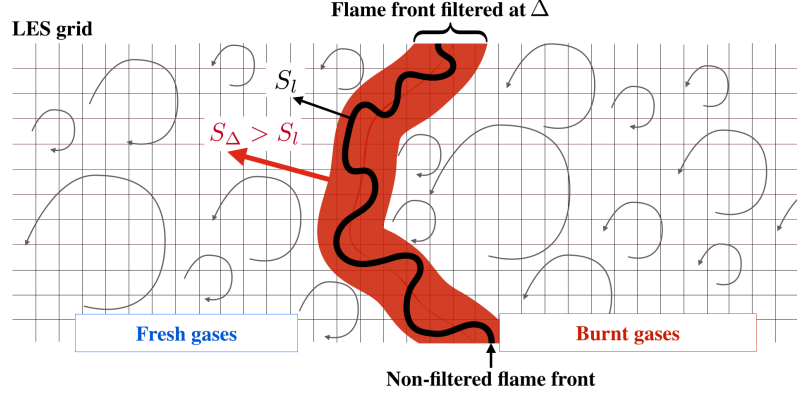


Figure 1.2: Scheme of a turbulent flame front with subgrid scale flame wrinkling. Extracted from [Mercier \(2015\)](#).

1.4.3.1 The F-TACLES formalism

In Chapters 2 and 3, reacting numerical simulations are performed with the turbulent combustion model F-TACLES (Filtered Tabulated Chemistry for LES) based on the tabulation of filtered 1-D premixed flames ([Fiorina et al. \(2010b\)](#)), extended to account for heat losses in [Mercier et al. \(2014b\)](#). The flame front is captured by the progress variable Y_c , equal to 0 and $Y_c^{eq}(z)$ in fresh and burnt gases, respectively.

The F-TACLES model consists in solving the filtered progress variable \tilde{Y}_c balance equation instead of the species equations (Eq. 1.2), closed under flamelet regimes as follows ([Mercier et al. \(2014b\)](#)):

$$\begin{aligned} \frac{\partial \tilde{\rho} \tilde{Y}_c}{\partial t} + \frac{\partial}{\partial x_i} (\tilde{\rho} \tilde{u}_i \tilde{Y}_c) &= \frac{\partial}{\partial x_i} \left(\Xi_{\Delta} \alpha_{Y_c} [\tilde{Y}_c, \tilde{z}] \rho_0 D_0 \frac{\partial \tilde{Y}_c}{\partial x_i} \right) \\ &+ \Xi_{\Delta} \Omega_{Y_c} [\tilde{Y}_c, \tilde{z}] + \Xi_{\Delta} \tilde{\rho} \tilde{\omega}_{Y_c} [\tilde{Y}_c, \tilde{z}] \end{aligned} \quad (1.42)$$

where Ξ_{Δ} is the subgrid scale flame wrinkling modelled with the Charlette model (detailed in Sec. 1.4.5), α_{Y_c} the progress variable diffusion factor, ρ_0 the density in fresh gases, D_0 the diffusion coefficient in fresh gases, Ω_{Y_c} the progress variable unresolved convective fluxes due to thermal expansion and $\tilde{\omega}_{Y_c}$ the progress variable reaction rate. The terms α_{Y_c} , Ω_{Y_c} and $\tilde{\omega}_{Y_c}$ are closed from the F-TACLES look-up table as a function of the mixture fraction \tilde{z} and the progress variable \tilde{Y}_c .

The functions $\alpha_{Y_c}^{ad}$, $\Omega_{Y_c}^{ad}$ and $\tilde{\omega}_{Y_c}^{ad}$ in Eq. (1.42) are designed to model the subgrid scale (SGS) laminar contributions to molecular diffusion, convection and chemical reaction, respectively. They are tabulated by filtering 1-D adiabatic premixed flame elements computed including detailed chemistry and complex transport and stored as a function of \tilde{Y}_c , and the filter scale Δ :

$$\alpha_{\tilde{Y}_c}^{ad} = - \frac{\overline{\sum_{k=1}^{N_{sp}} (n_k \rho^* Y_k^* V_k^*)}}{\rho_0 D_0 \frac{\partial \tilde{Y}_c^*}{\partial x^*}}, \quad (1.43)$$

$$\Omega_{\tilde{Y}_c}^{ad} = \overline{\rho_0^* S_l^* \frac{\partial Y_c^*}{\partial x^*}} - \overline{\rho_0^* S_l^* \frac{\partial \tilde{Y}_c^*}{\partial x^*}}, \quad (1.44)$$

$$\tilde{\omega}_{\tilde{Y}_c}^{ad} = \tilde{\omega}_{Y_c}^*, \quad (1.45)$$

where the superscript $*$ denotes quantities issued from the computations of 1-D unstrained laminar premixed flames. The parameters D_0 and ρ_0 are reference parameters that are constant in time and space. They are chosen as the diffusivity and density in the fresh gases as proposed in [Auzillon et al. \(2012b\)](#). This choice is conserved for all cases investigated. The Lewis number is not defined by the user in the present modeling strategy as the tabulation is performed from 1-D laminar premixed flames computed with detailed chemistry and the [Hirschfelder et al. \(1954\)](#) approximation for the diffusion fluxes. The impact of differential diffusion in the direction normal to the flame front, and in particular on the flame consumption speed, is therefore captured by the model ([Mercier et al. \(2014b\)](#)). The impact of preferential diffusion on the local mixture equilibrium properties, highlighted in [Vreman et al. \(2009\)](#), [Barlow et al. \(2012\)](#) and [Nambully et al. \(2014\)](#) and promoted by H_2 in the study of the EM2C burner (see Chapter 2), is not captured by the F-TACLES model.

By construction, this model propagates the resolved flame front at the sub-grid scale turbulent flame speed $S_{T,\Delta}$ ([Mercier et al. \(2014b\)](#); [Mercier et al. \(2015b\)](#)):

$$S_{T,\Delta} = \Xi_{\Delta} \gamma S_l^0, \quad (1.46)$$

where S_l^0 is the adiabatic consumption speed of a freely propagating laminar premixed flame. The model for Ξ_{Δ} is presented in Sec. 1.4.5.

The coefficient γ accounts for heat losses ([Mercier et al. \(2014b\)](#)) and is defined as follows:

$$\gamma = \frac{S_l(\Delta \tilde{h})}{S_l^0}, \quad (1.47)$$

The enthalpy defect relative to the fresh gases is defined as $\Delta h = h^{ad} - h$, where h is the chemical plus sensible enthalpy and the superscript *ad* refers to adiabatic conditions. The $S_l(\Delta \tilde{h})$ and the laminar consumption speed at a given Δh is calculated from burner-stabilized 1-D flames ([Fiorina et al. \(2003\)](#)). In adiabatic flows, γ equals 1 and decreases when heat losses slow down combustion chemistry, to the limit of a quenched flame for $\gamma = 0$. Modeling details are

given in [Mercier et al. \(2014b\)](#).

The detailed chemical scheme from [Lindstedt \(1997\)](#), which includes 29 species and 141 reactions, is used for the simulations of the EM2C burner (see Chapter 2).

1.4.3.2 The TFLES-FPI model

In Chapter 5, the Dynamic Thickened Flame (DTF) model, proposed by [Legier et al. \(2000\)](#), is used to thicken the under-resolved flame front solved with the FPI model in the LES.

The DTF model introduces a change in the transport equations, as shown for example for the species in Eq. 1.48:

$$\frac{\partial \bar{\rho} \tilde{Y}_i}{\partial t} + \nabla \cdot (\bar{\rho} \tilde{\mathbf{u}} \tilde{Y}_i) = \nabla \cdot \left\{ \bar{\rho} [\mathcal{F} \Xi_{\Delta} D_i + (1 - \alpha) D_i^t] \nabla \tilde{Y}_i \right\} + \frac{\Xi_{\Delta}}{\mathcal{F}} \tilde{\omega}_i, \quad (1.48)$$

where $\mathcal{F} = 1 + \alpha(\mathcal{F}^{max} - 1)$,

where α is the flame sensor, Ξ_{Δ} the subgrid scale flame wrinkling (see Sec. 1.4.5) and \mathcal{F}^{max} the maximal thickening factor. The flame sensor is defined as in Eq 1.49:

$$\alpha = \tanh \left(\beta \frac{\Omega}{\Omega_{max}} \right), \quad \text{where } \beta = 500 \text{ and } \Omega = Y_F^{\nu_F} Y_O^{\nu_O} \exp \left(-\Gamma \frac{T_a}{T} \right), \quad (1.49)$$

where Y_F and Y_O are the mass fractions of fuel and oxydizer, ν_F and ν_O the exponents representative of a pseudo single-step reaction, Γ a model constant, T_a the activation temperature of the pseudo single-step reaction and Ω_{max} the maximal value of Ω .

A similar approach, called Artificially Thickened Flame (ATF), is proposed by [Kuenne et al. \(2011\)](#) with the FGM model.

1.4.4 Tabulated chemistry for two-phase reacting flows

In two-phase flows, the use of tabulated chemistry is very recent. The validity of using a premixed flames archetype in two-phase was analyzed in [Franzelli et al. \(2013\)](#). It was shown that this choice was able to recover the proper flame properties if the combustion regime is "premixed-like" but failed in regions where the flame archetype diverges from a premixed one. In this thesis, we choose to keep a look-up table composed of premixed flames, even in two-phase combustion, to assess the ability of this approach to recover the correct flame structure in 3-D configurations.

Because of the evaporation of the liquid fuel, the transport equation used for the mixture fraction in partially premixed combustion has to be modified. The

balance equation for the mixture fraction \tilde{z} becomes in Chapters 3 and 5:

$$\frac{\partial \bar{\rho} \tilde{z}}{\partial t} + \frac{\partial}{\partial x_i} (\bar{\rho} \tilde{u}_i \tilde{z}) = \frac{\partial}{\partial x_i} \left(\left(\overline{\rho D_{th}} + \frac{\mu_t}{Sc_t} \right) \frac{\partial \tilde{z}}{\partial x_i} \right) + \tilde{\omega}_{evap} \quad (1.50)$$

where ρ is the density, D_{th} the thermal diffusivity, μ_t the turbulent viscosity, Sc_t the turbulent Schmidt number, $\tilde{\omega}_{evap}$ the source term of mixture fraction due to the evaporation of the spray.

In YALES2, the term $\tilde{\omega}_{evap}$ in the mixture fraction equation is obtained by adding the mass transfer contribution of all the droplets around each node of the mesh:

$$\tilde{\omega}_{evap} = -\frac{1}{V_{node}} \sum_{droplet \in node} \dot{m}_p \quad (1.51)$$

where V_{node} is the volume around the node. In CEDRE, the principle is the same, except that the contribution is computed at the center of each cell and V_{cell} replaces V_{node} in Eq. 1.51.

1.4.5 The subgrid scale flame wrinkling model

The Charlette model is considered to take into account the subgrid scale flame wrinkling due to both the mesh resolution and the flame thickening (or filtering) in the simulations presented in this thesis. The subgrid scale flame front wrinkling factor Ξ_{Δ} is modeled by the expression initially proposed by Charlette et al. (2002b):

$$\Xi_{\Delta} = \left(1 + \min \left[\max \left(0, \frac{\Delta}{\delta_l^0} - 1 \right), \Gamma_{\Delta} \left(\frac{\Delta}{\delta_l^0}, \frac{u'_{\Delta}}{S_l^0}, Re_{\Delta} \right) \frac{u'_{\Delta}}{S_l^0} \right] \right)^{\beta} \quad (1.52)$$

where $Re_{\Delta} = (u'_{\Delta} \Delta) / \nu$ and u'_{Δ} are the subgrid scale Reynolds number and turbulence intensity, respectively, while δ_l^0 is the laminar flame thickness. S_l^0 and δ_l^0 were in practice estimated from adiabatic flamelets, therefore the impact of heat losses on the subgrid scale flame wrinkling is neglected. The efficiency function Γ_{Δ} (Charlette et al. (2002b)) estimates the net straining effect of all turbulent scales smaller than Δ . The exponent β is set constant and equal to $\beta = 0.5$ as initially prescribed in Charlette et al. (2002a). Recent studies (Wang et al. (2011); Schmitt et al. (2013); Mercier et al. (2015b)) demonstrate that this value is not universal but can be accurately estimated through a dynamic procedure.

1.4.6 Coupling tabulated chemistry with a compressible code

The coupling of tabulated chemistry with a compressible code requires an additional treatment because the generation of the look-up table does not take into

account compressibility effects. Indeed, in a compressible flow, the temperature cannot be extracted directly from the table. Two approaches were derived to overcome this problem.

Galpin et al. (2008) proposed several methods to couple the information coming from the table and the quantities transported in the compressible code. In a similar way, Vicquelin et al. (2011) proposed the TTC (Tabulated Thermochemistry for Compressible flows) method.

In this thesis, the issues of compressibility are tackled with one of the methods proposed by Galpin et al. (2008). The source term of mass of each transported specie is computed from the terms found in the look-up table with the couple (c,z) , with a relaxation term:

$$\dot{\omega}_i = \dot{\omega}_i^{TAB} + \rho \frac{Y_i^{TAB} - Y_i}{\tau_c}, \quad (1.53)$$

where TAB indicates a term coming from the look-up table, $\dot{\omega}_i$ the mass source term of specie i , ρ the density, Y_i the mass fraction of specie i and τ_c a characteristic time chosen by the user. The validation of the implementation of this model in CEDRE is presented in Boucher (2015).

Chapter 2

Application of the F-TACLES model to the EM2C burner in steady and pulsed conditions

Contents

1.1	Governing equations	13
1.1.1	Flow governing equations	13
1.1.2	Dispersed phase governing equations	14
1.2	Flow solvers	15
1.2.1	YALES2	15
1.2.2	CEDRE	16
1.3	Turbulence modeling	16
1.3.1	The Boussinesq hypothesis	16
1.3.2	LES approach	16
1.3.3	ZDES approach	17
1.3.4	Wall law	21
1.4	Combustion modeling	22
1.4.1	Existing approaches for chemistry reduction	22
1.4.2	Chemistry tabulation	23
1.4.3	Coupling FPI tabulated chemistry with LES	24
1.4.4	Tabulated chemistry for two-phase reacting flows	27
1.4.5	The subgrid scale flame wrinkling model	28
1.4.6	Coupling tabulated chemistry with a compressible code	28

This chapter focuses on the experimental and numerical investigation of the shape taken by confined turbulent CH_4/H_2 /air premixed flames stabilized over a bluff-body swirling injector, in both steady and pulsed conditions.

2.1 Objectives of this chapter

The primary objective is to identify the issues in current turbulent combustion modeling for the simulation of the response of a swirl-stabilized flame to flow disturbances when heat losses need to be considered. The current knowledge is limited with respect to the impact of grid resolution, the choice of parameters of the subgrid scale flame wrinkling model and finally the importance of strain rate on the flame extinction for the reproduction of the flame dynamics (Tay Wo Chong et al. (2016); Tay Wo Chong et al. (2017)). The major question we want to address is: which physical phenomena must be captured to compute the dynamics of turbulent flames? Also, we aim to find which physical quantity is the most important to model: is it the laminar flame speed, the turbulent flame speed, the strain, the heat losses?

To achieve this, a configuration which challenges the ability of turbulent combustion model to capture swirled premixed flame stabilization mechanisms in a confined geometry is proposed. The combustion chamber recently studied experimentally at the EM2C laboratory is retained for that purpose (Guiberti et al. (2015a)). It was shown that the V to M flame shape transitions observed in this experiment are controlled by heat losses and fuel composition. As boundary conditions (inlet velocity profiles and wall temperatures) were characterized in this combustor (Guiberti et al. (2015a)), the resulting experimental database is a useful benchmark target for turbulent combustion model validation.

Simulations will involve the F-TACLES (Filtered Tabulated Chemistry for LES) model (Fiorina et al. (2010b)), recently developed to account for the impact of heat losses on detailed chemistry (Mercier et al. (2014b); Mercier et al. (2015b)), to capture such complex flame stabilization mechanisms.

The present chapter is divided into three parts. First, the experimental setup is presented. The diagnostics along with the investigated operated conditions are described. Two configurations, which correspond to two levels of H₂ enrichment in the fuel blend, are investigated. Experiments show that high H₂ concentrations promote M flame shapes, whereas V flame shapes are observed for lower values of H₂ enrichment.

Then the simulations in steady conditions are presented. An analysis is then carried out to examine the ability of F-TACLES to capture both V and M flame stabilization processes.

Finally, the simulations conducted in pulsed conditions are described, where a comparison between experimental and numerical FTF is shown and an analysis of the impact of grid resolution, subgrid scale flame wrinkling model and combined effects of strain rate and heat losses on the FTF is proposed.

2.2 Experimental setup

2.2.1 Geometry

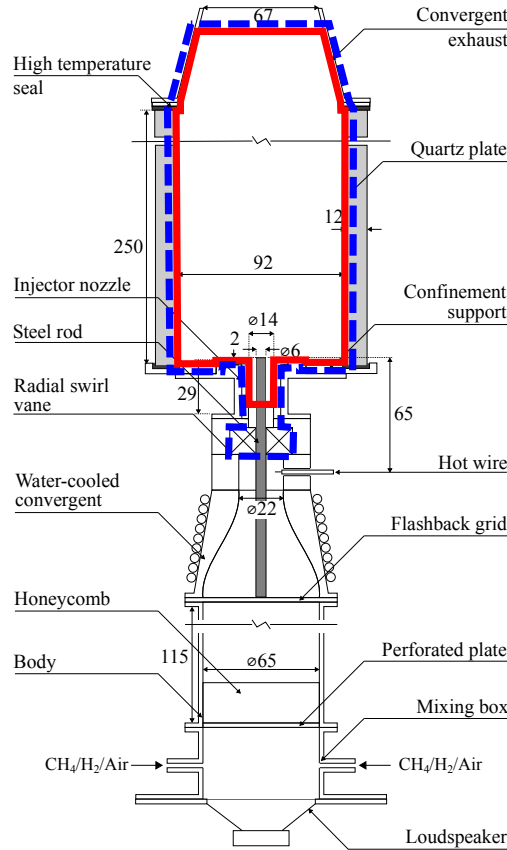


Figure 2.1: *Combustor geometry. The red solid line shows the computational domain CD1 for reactive flow simulations. The blue dashed lines show the computation domain CD2 for cold flow simulations. Dimensions are indicated in millimeters.*

The experimental setup presented in Fig. 2.1 was used in Guiberti et al. (2015a) for the study of the impact of heat losses on the shape of confined swirling flames. The burner, fed by mixtures of methane (CH_4), hydrogen (H_2) and air, includes a cylindrical injection tube with a 14 mm exit diameter. The flow is put in rotation by a radial swirling vane located upstream of the injection tube. The radial swirler features 12 blades with an angle $\theta = 35^\circ$ and a 4 mm span. The swirl number $S^{PIV} = 0.33$ has been measured at the burner outlet using Particle Image Velocimetry (PIV) in longitudinal and transversal planes under non-reacting conditions. A 6 mm diameter central rod installed on the burner axis helps anchoring the flame at the injection unit outlet 2 mm above the combustor dump plane. The mixture enters the burner through a plenum and subsequently passes through a set of grid/honeycomb/grid arrangement

before entering a water-cooled convergent nozzle to reach a nearly uniform top hat velocity profile at the entrance of the swirler. The flame is stabilized in the combustion chamber featuring four quartz windows. The windows are maintained using four vertical steel-bars not sketched in Fig. 2.1.

2.2.2 Operating conditions

Experiments in Guiberti et al. (2015a) show that flame stabilization is strongly influenced by heat losses at the combustor wall. In addition, transitions between V and M flame shapes are observed when increasing the H₂ concentration in CH₄/H₂ fuel blend. Two fuel compositions of $\{X_{\text{H}_2}^{\text{fuel}} = 0.6; X_{\text{CH}_4}^{\text{fuel}} = 0.4\}$ and $\{X_{\text{H}_2}^{\text{fuel}} = 0.9; X_{\text{CH}_4}^{\text{fuel}} = 0.1\}$ are retained for this study, where $X_{\text{H}_2}^{\text{fuel}}$ and $X_{\text{CH}_4}^{\text{fuel}}$ denote the volumetric concentration of H₂ and CH₄ in the fuel. For all cases, the flame power is $P = 4$ kW and the equivalence ratio is set to $\phi = 0.7$. The mass flows of the different dry gases injected are regulated by thermal mass flow controllers. The mixture composition and bulk flow velocity at the injection tube outlet are known with a relative accuracy better than 5%. Experiments were conducted at bulk flow velocities close to $U_{\text{bulk}} = 14$ m.s⁻¹ at the injector outlet for gases injected at room temperature ($T = 293$ K). Non-reacting experiments are also conducted by substituting the fuel by air and conserving the same bulk flow velocity. The investigated cases are listed in Tab. 2.1. Experiments show that a V flame shape is observed for $X_{\text{H}_2}^{\text{fuel}} = 0.6$ whereas a M flame shape is detected for $X_{\text{H}_2}^{\text{fuel}} = 0.9$.

Table 2.1: Simulated cases.

Fuel composition	Flame shape	LES assumption	Mesh (Nb. nodes)	Simu. #
-	-	Non-reacting	8.6M	S0
$X_{\text{H}_2}^{\text{fuel}} = 0.6$	V	Adiabatic	8.6M	S1
		Non-adiabatic	8.6M	S2
		Non-adiabatic	67.2M	S2R
$X_{\text{H}_2}^{\text{fuel}} = 0.9$	M	Non-adiabatic	8.6M	S3

2.2.3 Velocity measurements

Particle Imaging Velocimetry (PIV) was used to characterize the flow under reacting and non-reacting conditions.

For the non-reacting case, the direct integration of the measured velocity profiles at the exit of the injection tube using PIV data at $z = 2$ mm gives a bulk jet velocity of $U_{\text{bulk}}^{\text{PIV}} = 14.1$ m.s⁻¹, corresponding to less than 1% difference with the prescribed bulk jet velocity $U_{\text{bulk}} = 14$ m.s⁻¹.

2.2.4 Flame position measurements

Laser Induced Fluorescence of the hydroxyl radical (OH-PLIF) measurements were carried out to delineate the location of the flame front and hot burnt gases and infer the shape taken by the flame in a vertical plane.

The shape taken by the flame can also be deduced from chemiluminescence measurements.

An Abel deconvolution was then applied on the mean images to infer the OH* emission from the axial longitudinal plane. This signal is a good indicator of the heat release rate for perfectly premixed flames (Palies et al. (2010b)).

2.2.5 Wall temperature measurements

By altering the temperature field in the recirculating burnt gases, heat losses alter flame stabilization as shown in Guiberti et al. (2015a). LES are then extremely sensitive to the prescription of thermal boundary conditions, which are here carefully measured for the two reacting configurations listed in Tab. 2.1. Figure 2.2 shows the position of the temperature measurement points at the different combustor wall surfaces. Under reacting conditions, all the measurements were performed after thermal steady-state was reached.

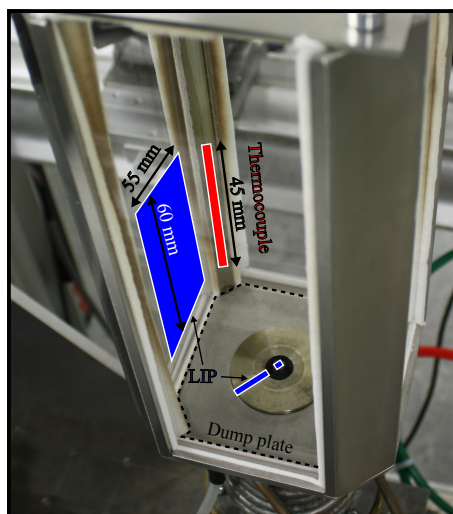


Figure 2.2: Photograph of the combustion chamber showing the location of temperature measurements for the characterization of the thermal boundary conditions in the combustor.

Results are presented here for the V flame case (Tab. 2.1). The vertical temperature profile along the surface of one of the four vertical steel bars of the combustion chamber is plotted in Fig. 2.3. The temperature increases slightly and almost linearly with the distance to the dump plate, from $T = 593$ K at $z = 16$ mm to $T = 637$ K at $z = 56$ mm.

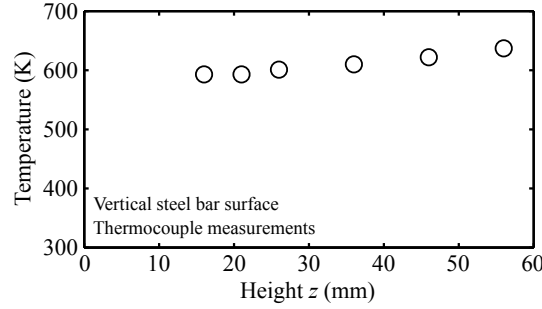


Figure 2.3: Temperature profiles along the vertical steel bar as a function of the height z above the rod tip. $\text{CH}_4/\text{H}_2/\text{air}$ flame at $P = 4$ kW, $X_{\text{H}_2}^{\text{fuel}} = 0.60$, and $\phi = 0.7$.

Figure 2.4 shows the measured radial profile of the temperature at the surface of the injector and along the dump plane. These data were obtained by Laser Induced Phosphorescence (LIP) measurements (Brübach et al. (2013)). More details about the LIP setup are given in Guiberti et al. (2015a).

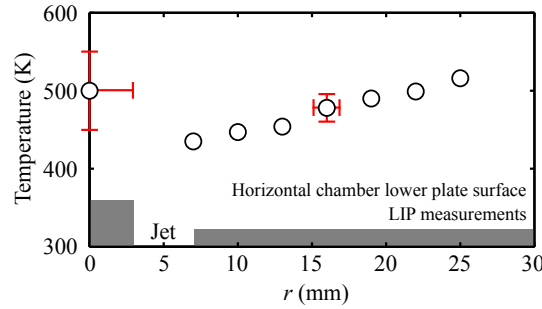


Figure 2.4: Temperatures measured by LIP on the combustor dump plane as a function of the radial distance r . $\text{CH}_4/\text{H}_2/\text{air}$ flame at $P = 4$ kW, $X_{\text{H}_2}^{\text{fuel}} = 0.60$, and $\phi = 0.7$. The grey regions indicate the location of solid surfaces. Error bars are shown in red.

The temperature near the injector linearly increases with the radial distance for $r > 7$ mm and ranges from $T = 435$ K at $r = 7$ mm to $T = 516$ K at $z = 25$ mm. The temperature on the rod tip surface is $T = 500 \pm 50$ K and is averaged both spatially and temporally.

LIP was also used to measure the temperature at different positions over the surface of a quartz window as shown in Fig. 2.2. Figure 2.5 shows the temperature for 30 measurement points regularly distributed over this surface. The wall temperature increases with the distance above the injector and is minimum close to the vertical steel bars featuring lower temperatures. Temperature differences along the x axis can reach $\Delta T = 27$ K. Temperature differences along the z axis can reach $\Delta T = 140$ K. This figure also shows that the quartz window temperature is not uniform along the x and z directions. A linear interpolation

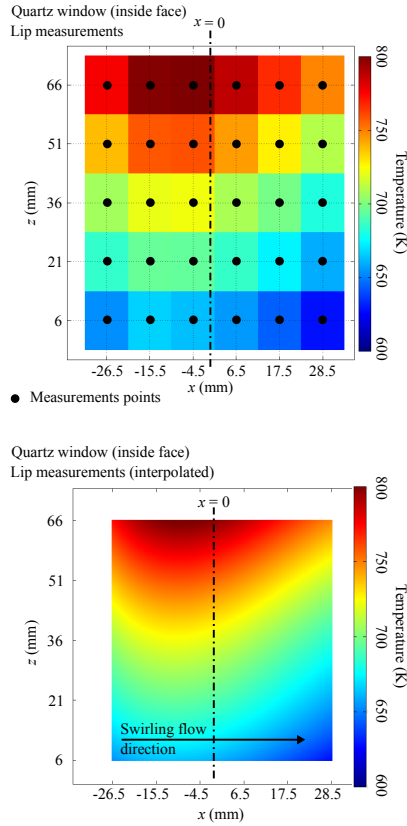


Figure 2.5: *Top: Temperatures, measured by LIP at the inner surface of a quartz window of the combustion chamber, of a $\text{CH}_4/\text{H}_2/\text{air}$ flame at $P = 4 \text{ kW}$, $X_{\text{H}_2}^{\text{fuel}} = 0.60$, and $\phi = 0.7$. Bottom: Linear interpolation of the data presented above. The dashed-dotted lines indicate the vertical symmetry axis of the windows.*

of these data shows that the temperature field is not perfectly symmetric with respect to the vertical symmetry axis of the window. This is attributed to the swirling motion of the flow. The swirling flow has an azimuthal velocity altering heat transfers to the walls. This analysis demonstrates the impact of swirl on the thermal state of the combustor walls.

The wall temperatures presented in Figs. 2.3, 2.4, and 2.5 are lower than the adiabatic flame temperature $T_{ad} = 1881 \text{ K}$ for $X_{\text{H}_2}^{\text{fuel}} = 0.60$, and $\phi = 0.7$. This confirms that significant heat losses take place in this combustor.

Additional temperature measurements were conducted in the ORZ filled with non-adiabatic burnt gases that were presented in [Guiberti et al. \(2015a\)](#).

2.2.6 Diagnostics in pulsed conditions

In pulsed conditions, a loudspeaker is placed at the bottom of the injection system to modulate the flow at a given frequency. The Flame Transfer Function (FTF) is measured with a hot wire and a photomultiplier. The hot wire is introduced in the stream of fresh reactants 65 mm upstream of the injector outlet as indicated in Fig. 2.1.

The photomultiplier is used to detect the OH* global emission from the flame. The OH* signal is not linearly related to the heat release rate as there are also dependencies on equivalence ratio, strain and the combustion regime. It is however an acceptable indicator for lean premixed conditions as the OH* species profiles is not affected by local fuel stratification. For this reason, this quantity has been used in the past in many analysis of the dynamics of lean premixed flames as for example in Palies et al. (2010a). A discussion about the validity of this assumption can be made in configurations with stratified equivalence ratio, strain or combustion regime effects, but it is assumed here that these effects do not affect the conclusion on the fluctuations of OH* global emission.

The flame response to flow modulations is also analyzed by imaging the spatial distribution of OH* emission. The distribution of hot burnt gases is inferred from Laser Induced Fluorescence of the OH radical (OH-PLIF) in a light sheet through the axial plane of the burner as described previously. For a given forcing frequency, OH* and OH-PLIF images are phase averaged over more than 100 snapshots to get a statistically converged information at five regularly distributed phases within a modulation period. These data are used to analyze the flame motion.

Particle Image Velocimetry (PIV) is also used to characterize the modulated flowfield in reacting conditions and analyze the dynamics of large coherent structures in the shear layers of the swirled jet during a modulation period, with the same PIV setup as in steady conditions.

2.3 Simulations in steady conditions

2.3.1 Motivations

This section focuses on the experimental and numerical investigation of the shape taken by confined turbulent CH₄/H₂/air premixed flames stabilized over a bluff-body swirling injector in steady conditions. Two configurations, which correspond to two levels of H₂ enrichment in the CH₄/H₂ fuel blend, are investigated. Experiments show that high H₂ concentrations promote M flame shapes, whereas V flame shapes are observed for lower values of H₂ enrichment. All temperatures of solid walls of the experimental setup including the combus-

tor dump plane, the nozzle exhausting the burnt gases, the combustor sidewalls and the quartz windows were also characterized. This detailed experimental database represents an excellent validation case for turbulent combustion modeling.

In both cases, non-reacting and reacting flow Large Eddy Simulation (LES) calculations are performed. Numerical results are compared with detailed velocimetry measurements under non-reacting and reacting conditions, OH-laser induced fluorescence and OH* chemiluminescence measurements.

2.3.2 Numerical setup

Large Eddy Simulations are performed using the node-centered YALES2 low-Mach number code (Moureau et al. (2011b)). Closure of Reynolds stresses is performed using the SIGMA model (Nicoud et al. (2011b)), presented in Chapter 1.

The computational domain for all the non-reacting and reacting LES starts at $z = -20$ mm as shown by the red domain delimited in Fig. 2.1. The origin of the domain is located at the bluff-body tip indicated by the yellow dot in Fig. 2.1. The associated tetrahedral element mesh is composed of 8.6 million of nodes. The mean cell size in the flame front region evolves from $\Delta_x = 0.25$ mm to $\Delta_x = 0.5$ mm. A filter width $\Delta = 3.5$ mm $\approx 8\delta_l^0$, where $\delta_l^0 = 0.44$ mm is the laminar flame thickness, is chosen to generate the filtered chemical database. It ensures a numerical resolution ($\Delta \geq 5\Delta_x$) of the filtered reactive layer sufficient to track the flame front propagation without introducing numerical artifacts. A refined mesh has also been generated to perform a mesh sensitivity analysis. For that purpose, the cell size have been divided by two everywhere in the computational domain. The resulting tetrahedral mesh is composed of 67.2 million nodes and its associated flame filter size is $\Delta = 1.75$ mm $\approx 4\delta_l^0$.

Mean velocity profiles prescribed in the inlet plane $z = -20$ mm have been extracted from a non-reacting simulation including the swirl injection device (see the blue domain in Fig. 1). An effective bulk flow velocity within the LES of $U_{\text{bulk}}^{\text{LES}} = 14.1$ m.s⁻¹ in both non-reactive and reactive cases is then ensured. An homogeneous and isotropic turbulent field (HIT) is superimposed to the mean velocity profiles. This HIT is generated from a spectrum (Passot and Pouquet (1987)) with an integral length scale $L_t = 2.5$ mm and a turbulence intensity equal to 10% of the bulk velocity. This turbulence intensity reproduces the RMS levels observed at $z = -20$ mm in the full domain non-reacting computation.

Isothermal wall boundary conditions are imposed in the non-adiabatic simulations. As the wall temperature measurements only partially cover the com-

bustor surface (see Fig. 2.2), linear interpolations and extrapolations are performed to provide complete temperature boundary conditions. Although the temperature of the bluff-body wall surface (rod tip) is imposed to 500 K (measured value), the wall surfaces within the injection tube are assumed adiabatic. Therefore, the preheating of the fresh gases within the injection tube is not considered in the present work. This assumption is reasonable since a simple convective heat transfer analysis estimates the elevation of the fresh gas temperature flowing near the heated tube to $\Delta T = +4$ K. It means that a solid-gas temperature gap of 200 K is not sufficient to preheat significantly the injected fresh gases in the present flow conditions.

2.3.3 Initialization of the non-adiabatic LES

The combustor geometry promotes large ORZ of the flow characterized by a long residence time in these regions. The typical turn-around time of the ORZ is $\tau_{\text{ORZ}} \approx 40$ ms (Guiberti et al. (2015a)). The transient state required to reach steady-state thermal regime is therefore very long and remains out of reach for the LES. To overcome this issue, a RANS simulation is first performed with the Fluent commercial solver (ANSYS® Fluent (2009)) using the same computational domain as for the LES but without considering chemical reactions. Burnt gases, which composition and temperature correspond to the adiabatic combustion of the fresh fuel/air mixture studied in the experiment, are directly injected through the feeding inlet to approximate the thermochemical state of the flow. As for the LES computations, the measured wall temperatures are imposed at the wall surfaces. Using this methodology, the time period needed to obtain converged statistics is optimized.

Figure 2.6 compares thermocouple measurements in the ORZ filled with burnt gases with RANS calculations. The good agreement between the RANS simulation and the experiments validates the prescription of the thermal boundary conditions used in the simulations. The mean temperature field obtained by the steady RANS simulation is used to initialize the reacting non-adiabatic LES computation.

2.3.4 Simulations performed

A non-reacting simulation (S0) is first conducted to validate the ability of the computational setup to capture the flow dynamics. To analyze the impact of heat losses on the flame shape, two different LES of the reacting case $X_{\text{H}_2}^{\text{fuel}} = 0.60$ are then performed using the F-TACLES model. The first one (S1) assumes an adiabatic burner while the second one (S2) accounts for heat losses at the walls. A mesh sensitivity analysis (S2R) is conducted on this last case using the refined mesh introduced in Sec. 2.3.2. To understand the impact of a variation

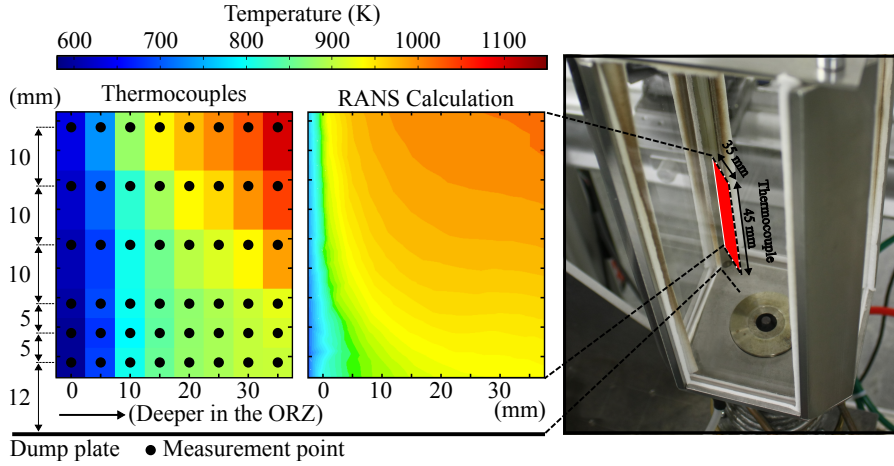


Figure 2.6: Comparison of the mean temperature in the ORZ filled with burnt gases obtained by thermocouple measurements (left) and RANS simulation (middle). A photograph (right) of the combustion chamber delineates the positions of thermocouple measurements in the flow.

in fuel composition on the flame shape and stabilization process, a sensitivity analysis (S3) is also carried out to determine the impact of hydrogen enrichment on the flame shape. For that purpose, the fuel composition is increased from $X_{\text{H}_2}^{\text{fuel}} = 0.60$ to $X_{\text{H}_2}^{\text{fuel}} = 0.90$ while other operating conditions are kept constant. In this latter case, the flame takes an M shape. The list of LES performed is also indicated in Tab. 2.1.

2.3.5 Analysis of the results

2.3.5.1 Non-reacting flow configuration

Figures 2.7 (a) and (c) show the measured mean axial velocity field in two parallel longitudinal planes (x, z) at two different positions along the y direction, respectively ($y = 0$ and 4 mm). The positions of the Inner Recirculation Zone (IRZ), Outer Recirculation Zone (ORZ), Inner Shear Layer (ISL) and Outer Shear Layer (OSL) are indicated in Fig. 2.7 (a). The radial expansion of the jet due to the swirl imparted to the flow is also evidenced. As shown in Figs. 2.7 (b) and (d), LES computation S0 capture well the mean flow topology. In particular the correct location and angle of the IRZ is well predicted at $y = 0$ mm around $z = 6$ mm. The flow field structure at $z = 40$ mm is also well predicted except that the swirling jet arms feature a slightly wider angle in the experiments. The good agreement between the experimental and numerical results remains valid for off-axis longitudinal planes, as shown in Fig. 2.7 (c) and (d). However, simulations over-predict the axial velocity magnitude for $z > 25$ mm. The quality of the PIV measurements at these locations is questionable because of the very low displacement of the particles between two laser pulses (low flow

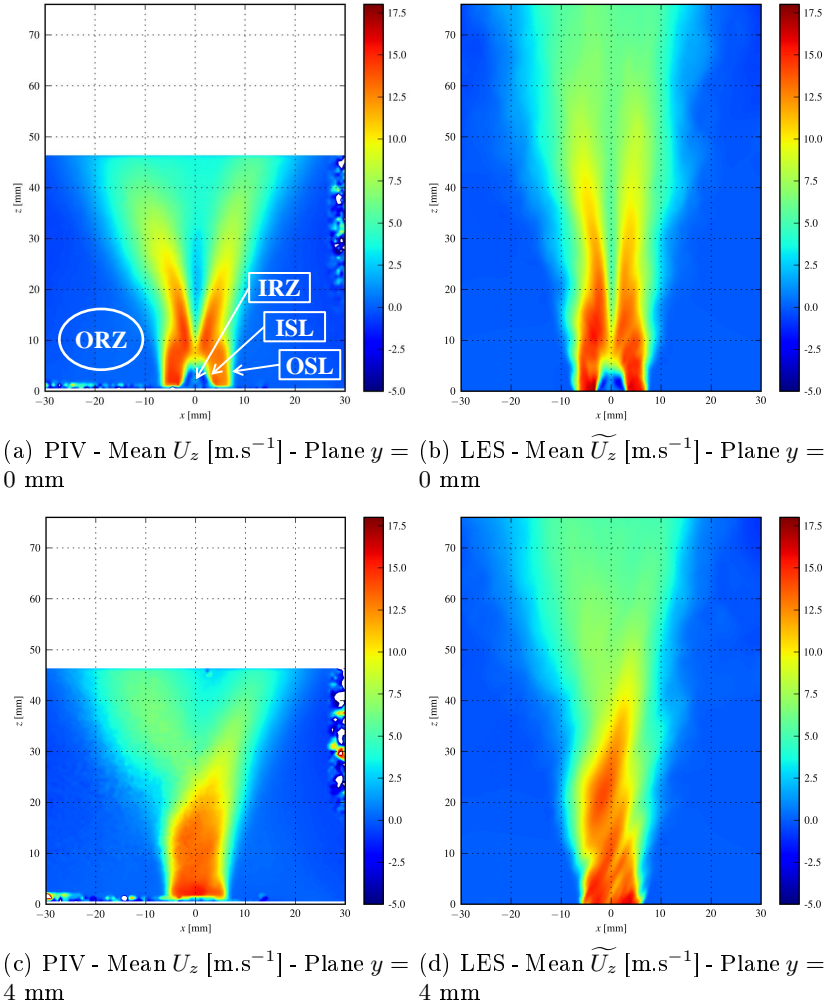


Figure 2.7: 2-D cut of the mean axial velocity U_z in two different longitudinal planes. The Inner Recirculation Zone (IRZ), Outer Recirculation Zone (ORZ), Inner Shear Layer (ISL) and Outer Shear Layer (OSL) are indicated in figure (a).

velocity). It is worth noting that, in the reacting cases discussed later, the flame is located far under the area where the velocity discrepancies appear. Wave patterns are observed in the outer shear layer in the mean numerical field of U_z . This is due to low frequencies shear flow instabilities within the outer shear layer that are not statistically converged.

Figure 2.8 shows the mean axial (left column) and orthoradial (right column) velocities in the axial longitudinal plane $y = 0$ mm at different axial positions z above the burner. Both axial U_z and orthoradial U_y velocities are well predicted by the LES from $z = 0$ mm to $z = 20$ mm. The maximum axial velocity

is reached by the jet at a radial position $|x| = 5 \text{ mm}$ and is $U_z \simeq 15 \text{ m} \cdot \text{s}^{-1}$. Mean values of U_z and U_y at $z = 2 \text{ mm}$ are used to compute the simulated swirl number S^{LES} with the method given by Palies et al. (2010b) (Eq. (1)). The simulated and experimental swirl numbers are $S^{\text{LES}} = 0.31$ and $S^{\text{PIV}} = 0.33$, respectively. The swirling motion is therefore correctly reproduced by the LES and the slight gap can be attributed to geometrical differences between the injector CAD and its real geometry (Bourgouin et al. (2013)).

Figure 2.9 plots a comparison between measured and computed Root Mean Square (RMS) axial (left column) and radial (right column) velocities. Large RMS values can be observed at $z = 2 \text{ mm}$ for $x < -15 \text{ mm}$. This behavior, not seen in the LES results, should not be accounted for since it is a measurement artifact due to laser sheet reflections near the dump plate. The measured RMS components feature high values for $|z| \simeq 3 \text{ mm}$ and $|z| \simeq 7 \text{ mm}$ that correspond to the positions of the ISL and OSL. The maximum value of the axial rms velocity fluctuations is $U_z^{\text{rms}} \simeq 5 \text{ m} \cdot \text{s}^{-1}$, which corresponds to 36% of the bulk flow velocity $U_{\text{bulk}} = 14 \text{ m} \cdot \text{s}^{-1}$. LES predicts the position of these shear layers and the amplitude of the fluctuations. Differences between measurements and simulations increase for $z > 20 \text{ mm}$ where the rms fluctuations are underestimated in the simulations for $|z| > 10 \text{ mm}$.

The good agreement between measured and computed flow fields under non-reacting conditions validates the methodology retained to prescribe the velocity boundary conditions at the injection tube outlet $z = 0 \text{ mm}$.

2.3.5.2 Impact of heat losses on the flame topology

The influence of heat losses on the turbulent flame structure is investigated through adiabatic (S1) and non-adiabatic (S2) simulations for the configuration with $X_{\text{H}_2}^{\text{fuel}} = 0.6$. Figure 2.10 compares the normalized mean heat release rates predicted by both simulations with the OH^* chemiluminescence measurements. The measured and computed hot burnt gases probabilities (right plots) are also presented. Experiments exhibit a V flame shape, which is mainly due to local flame extinctions induced by wall heat losses. Burnt gases flowing inside the outer recirculation zone (ORZ) are cooled by the combustor walls. This leads to local flame extinction and promotes the transition from an M to V flame shape (Guiberti et al. (2015a)). The adiabatic computation plotted in Fig. 2.10(b) cannot capture this phenomenon and consequently predicts an M flame shape where two reaction fronts are observed. The inner flame front is located in the ISL between the fresh stream of the reactant jet and the IRZ filled with burnt products above the bluff-body wall surface. An outer flame front is hosted in the OSL between the fresh gas stream of reactants and the burnt gases in the ORZ. This prediction is not in agreement with the measurements shown in Fig. 2.10(a), where no reactive layer is observed in the OSL,

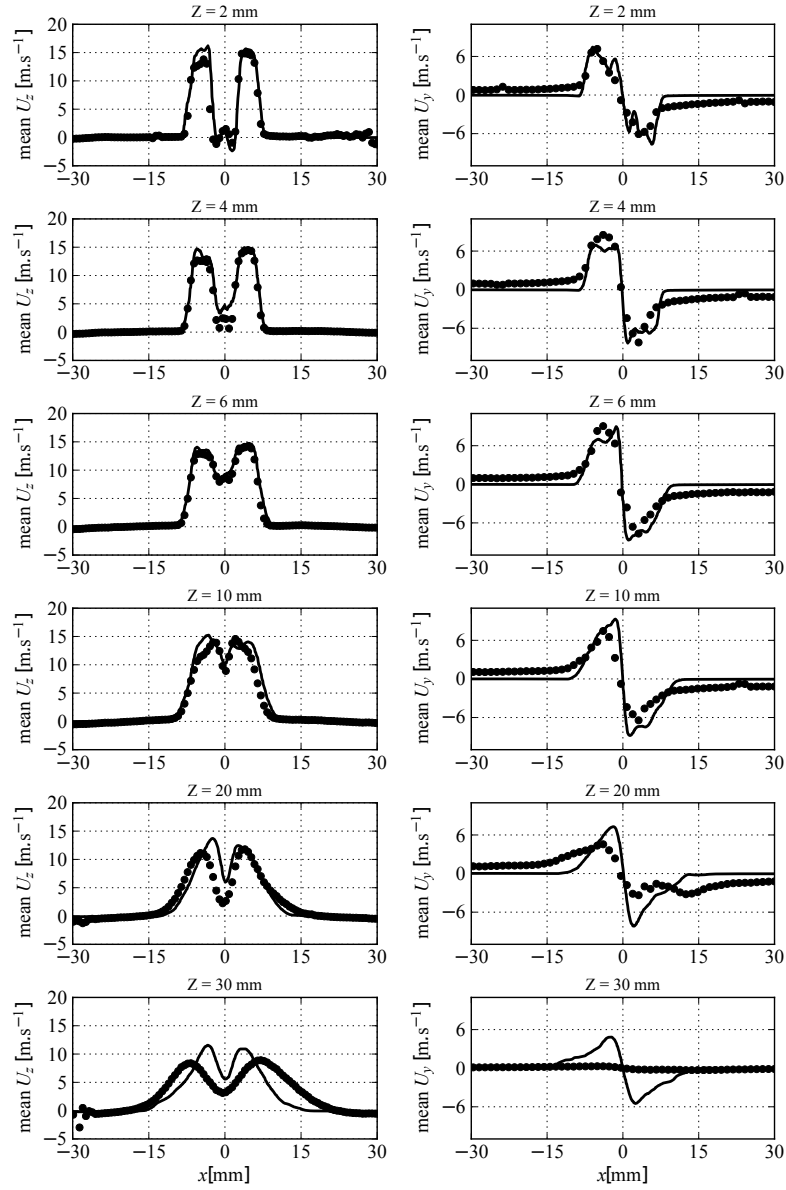


Figure 2.8: 1-D radial mean profiles of U_z axial velocity (left) and U_y orthoradial velocity (right) components at different heights z above the rod tip for the $y = 0$ mm plane. Black lines and black symbols correspond to simulation S0 and PIV measurements respectively.

leading to a V flame shape structure.

The normalized mean volumetric heat release rate predicted by the non-adiabatic simulation (S2) is shown in Fig. 2.10(c). As the model accounts for the impact of heat losses on the chemical activity, the reactive layer intensity differs be-

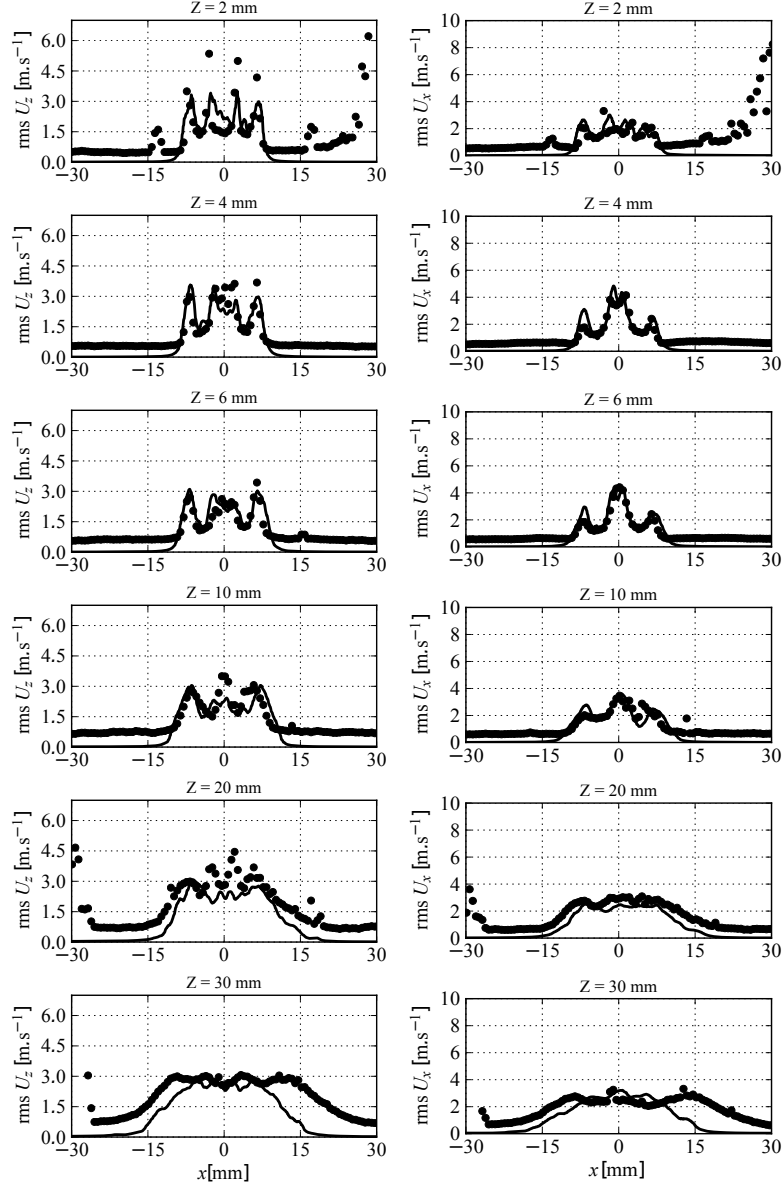


Figure 2.9: 1-D radial rms profiles of U_z axial velocity (left) and U_x radial velocity (right) components at different heights z above the rod tip for the $y = 0$ mm plane. Black lines and black symbols correspond to simulation S0 and PIV measurements respectively.

tween the ISL and OSL. Indeed, heat losses induced by the sidewalls of the combustion chamber cool the burnt gases in the ORZ, which are convected to the OSL, decreasing the mixture reactivity (Guiberti et al. (2015a)). Unlike S1 results, the outer flame front is not attached to the burner lips anymore. However, in contrast with experiments, a weak reactive layer still exists in the

downstream OSL, near the flame tip. As discussed later in this section, additional quenching phenomena not captured by the F-TACLES model remain to be identified.

Figure 2.11 plots computed mean and rms temperature profiles at different distances above the bluff-body tip. Important differences are observed between mean temperature profiles predicted by both adiabatic and non-adiabatic LES. In particular, a difference of approximately 1000 K is observed in the very slow ORZ of the flow, for which an estimation of the characteristic time is $\tau_{\text{ORZ}} \approx 40$ ms (Guiberti et al. (2015a)). During this recirculation time, hot gases exchange heat with the cooler combustion chamber side walls at $T_{\text{wall}} \approx 800$ K. It can also be noted that for the non-adiabatic computation S2, turbulent structures are mixing cold and hot burnt gases in the ORZ. This leads to important fluctuations of the temperature unlike the adiabatic computation S1. In both S1 and S2 computations, no temperature fluctuations are found in the IRZ. This may be explained by the stability of this recirculation zone and by the smaller gap between the temperature of burnt gases for both computations within the IRZ because of the limited surface area of the central rod.

The mean and RMS values of the radial and axial velocity components are shown in Figs. 2.12 and 2.13, respectively. In the present configuration, the radial velocity is an indicator of thermal expansion due to combustion. The presence of the outer flame front in the adiabatic simulation S1 causes an over prediction of the heat expansion from $z = 5$ mm to $z = 20$ mm. A better agreement with the experiments is obtained in the non-adiabatic simulation S2. The difference is also visible on the RMS velocity profiles. It means that the presence of the outer flame front in the OSL damps the fluctuations of the flow in the burnt gases unlike to the non-adiabatic simulation, where heat expansion is reduced. These fluctuations are due to shear layer instabilities developing in the OSL between the injected stream of reactants and the slow ORZ. Differences are less visible on the mean and RMS axial velocity profiles shown in Fig. 2.13 which are both in good agreement with the experiments. The very low and negative mean axial velocities at large radial distances confirms the presence of the ORZ for all heights z where the measurements have been performed.

Flame fronts stabilized in the OSL are more subject to extinction due to heat losses in comparison to those lying in the ISL as shown in Guiberti et al. (2015a). This recirculation of cooler burnt gases corresponds to a low enthalpy region leading to a drop in the flame consumption speed and causes the flame extinction. The reaction process is then inhibited in the OSL leading to the extinction of the outer flame front and the stabilization of a V flame shape. This conclusion is corroborated by the results obtained in Tay Wo Chong et al. (2009) on a similar configuration using RANS simulations. Heat losses were also identified in Nogenmyr et al. (2013) as altering the flame shape of a swirl

burner studied with and without confinement using a MILES approach.

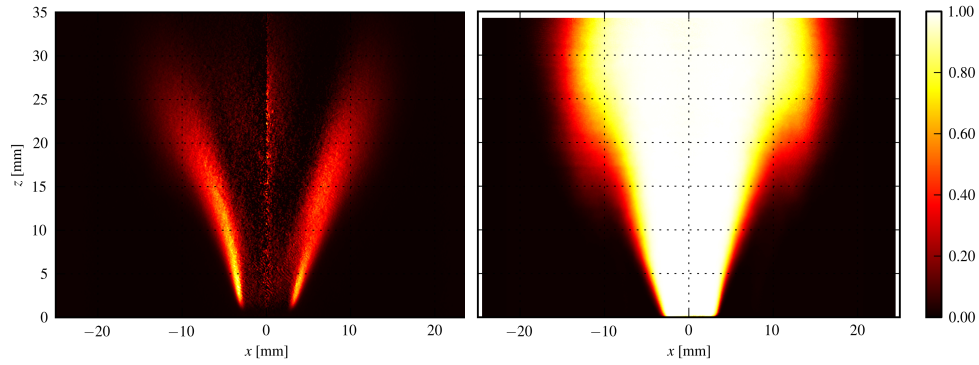
A very small reaction zone is identified in the OSL regions of the non-adiabatic simulation S2, both in Fig. 2.10(c) and in the mean temperature profiles (Fig. 2.11, $z > 15$ mm and $x = 10$ mm), where a slight temperature increase is observed. This reaction layer is an artifact, not observed in experiment, where the flame is quenched because of combined effect of strain and heat losses (Coriton et al. (2013); Tay-Wo-Chong et al. (2015)). To capture this phenomenon, the present model should account for the impact of local strain rate on the flame consumption speed, which is very challenging because it occurs at the sub-grid scale.

2.3.5.3 Mesh sensitivity analysis

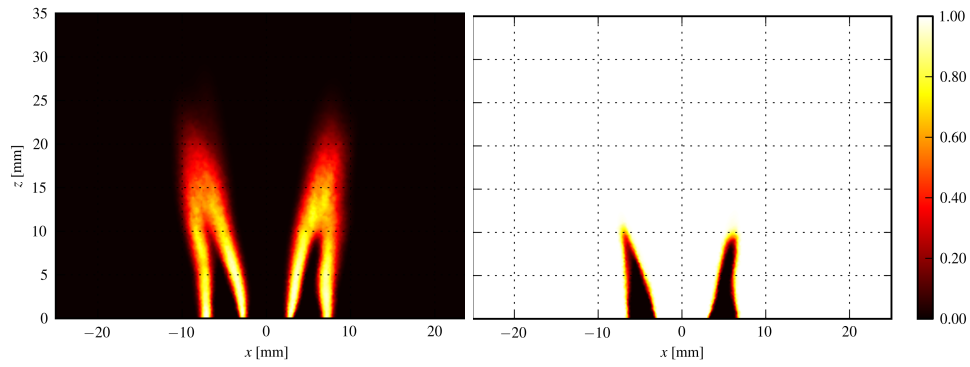
A homogeneous mesh refinement has been performed on the simulation S2 so that the refined cell size is twice finer than in the original mesh. The mean volumetric heat release rates are plotted in Fig. 2.14. For the simulation S2R, as the F-TACLES filter size has also been divided by a factor 2, the impact of the sub-filter scale flame wrinkling is less important. The mesh refinement does not modify the prediction of the mean flame brush position. Indeed, the predicted flame angle is not impacted. However, it is worth noting that the distribution of the volumetric heat release rate is in better agreement with the experimental data shown in Fig. 2.10(a). For $z < 15$ mm, the mean heat release is more intense than for $z > 15$ mm both in the experiment and refined mesh simulation S2R. This shift in heat release intensity is less perceptible in the reference mesh simulation S2 and only takes place for $z > 20$ mm. As the mean heat release rate is lower for $z > 15$ mm in the S2R simulation, the mean flame length is slightly higher in this case. We also observe that the mesh refinement does not improve the prediction of flame quenching in the OSL.

2.3.5.4 Impact of fuel composition on the flame topology

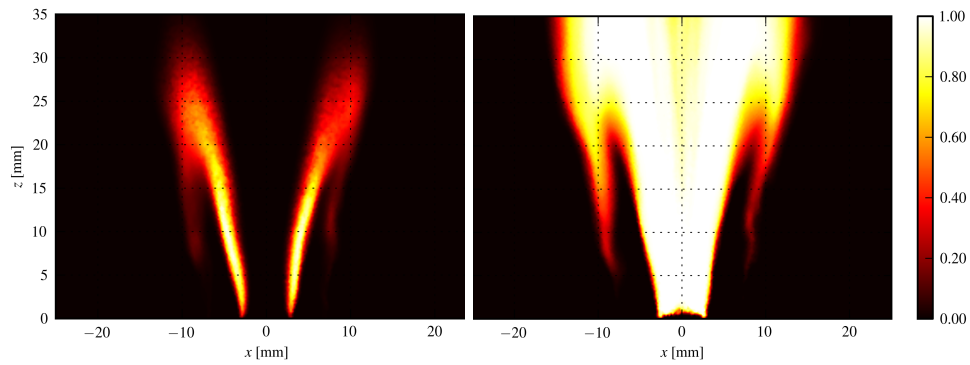
The case $X_{\text{H}_2}^{\text{fuel}} = 0.60$ considered in the experiments and simulations S1, S2 and S2R exhibits a V flame shape, only anchored on the central rod tip. The flame front lies in the inner shear layer (ISL) formed by the fresh combustible mixture jet and the IRZ filled with burnt gases. It was shown in Guiberti et al. (2015a) that increasing the molar fraction of H_2 in the fuel $X_{\text{H}_2}^{\text{fuel}}$ continuously increases the probability p to find a flame front in the OSL. In the present study, the H_2 concentration is set to $X_{\text{H}_2}^{\text{fuel}} = 0.90$ leading to a very high probability to find an M flame shape. Figure 2.15(a) shows the mean flame structure for $X_{\text{H}_2}^{\text{fuel}} = 0.90$ using two different diagnostics. The left plot shows a mean Abel inverted OH^* chemiluminescence image while the right plot shows a mean binarized OH-PLIF result. The outer flame front in the OSL can clearly be identified in both images leading to an M flame shape. As suggested in Kim



(a) Experiments. (left) Normalized Abel deconvoluted OH* chemiluminescence. (right) Mean binarized OH-PLIF signal.



(b) Simulation S1. (left) Normalized mean volumetric heat release. (right) Mean binarized OH molar fraction.



(c) Simulation S2. (left) Normalized mean volumetric heat release. (right) Mean binarized OH molar fraction.

Figure 2.10: Comparisons of the mean flame position for the case $X_{H_2}^{fuel} = 0.60$. Experiments, adiabatic (S1) and non-adiabatic (S2) simulations results are shown.

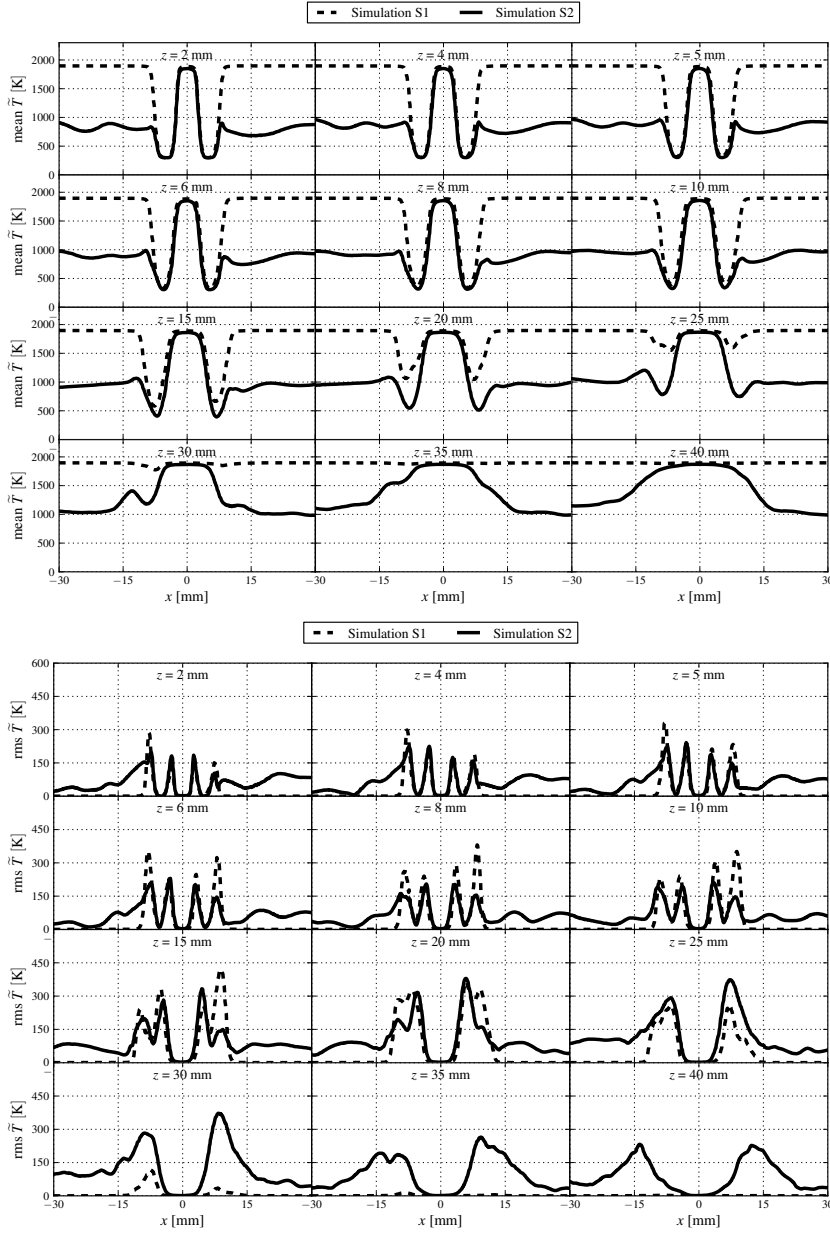


Figure 2.11: 1-D radial profiles of temperature at different distances z from the bluff-body wall surface for the case $X_{H_2}^{fuel} = 0.60$. (top) Mean profiles. (bottom) rms profiles.

et al. (2010), the increase in laminar burning velocity S_l^0 due to the increase of $X_{H_2}^{fuel}$ helps the reaction zone to propagate upstream through the OSL. The presence of the outer flame front in the OSL also depends on the stretch limit which is strongly extended when the Lewis number of the combustible mixture

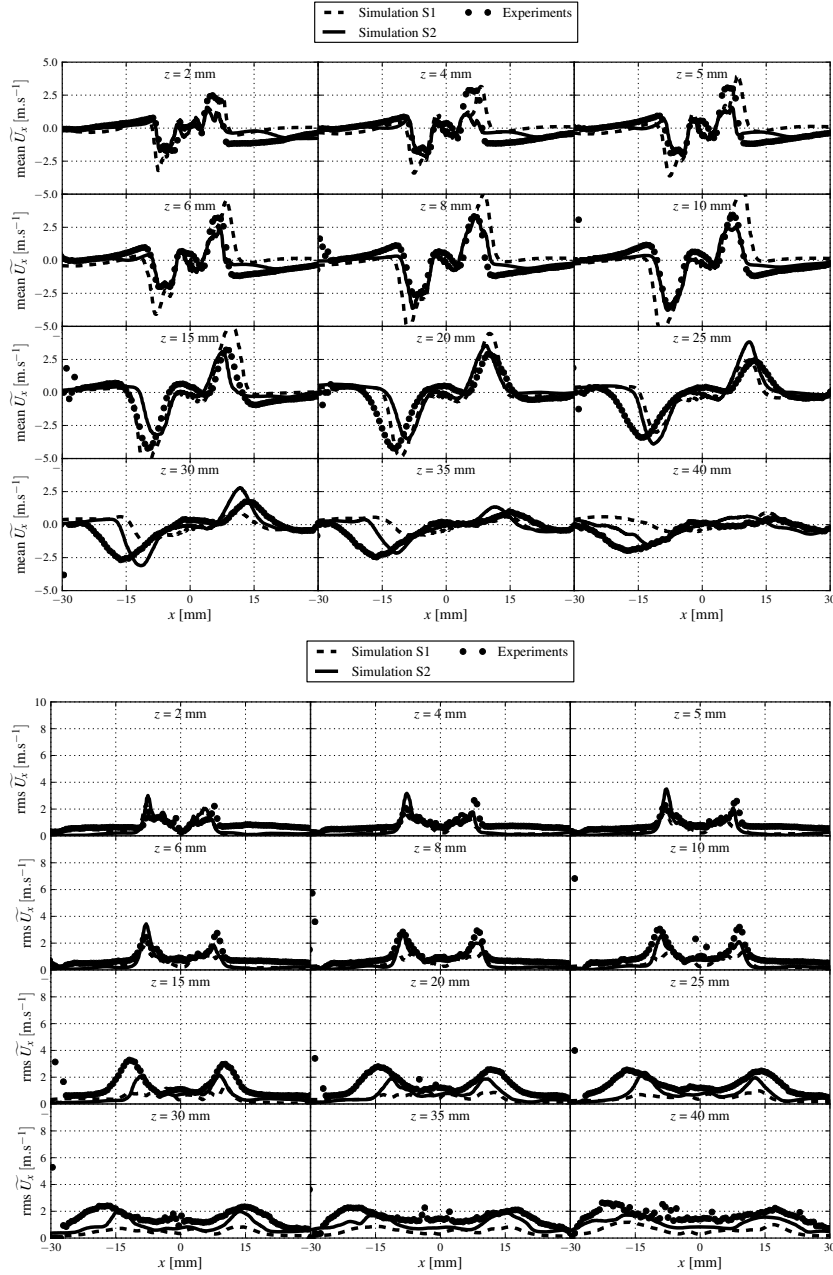


Figure 2.12: 1-D radial profiles of the radial velocity U_x at different distances z from the bluff-body wall surface for the case $X_{H_2}^{fuel} = 0.60$. (top) Mean profiles. (bottom) rms profiles.

decreases (Guberti et al. (2015a)) as it is the case when the fuel is enriched with hydrogen (Hawkes and Chen (2004); Lipatnikov and Chomiak (2005)).

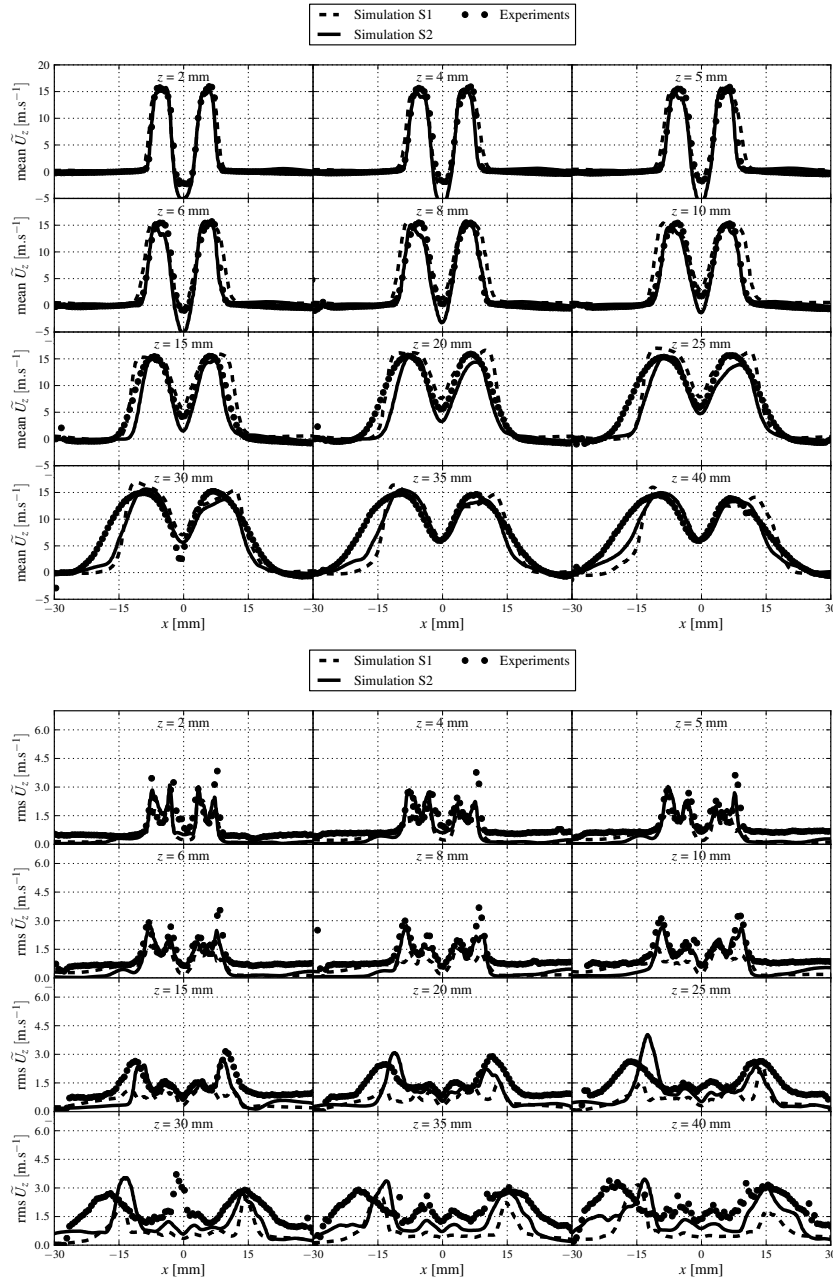


Figure 2.13: 1-D radial profiles of the axial velocity U_z at different distances z from the bluff-body wall surface for the case $X_{H_2}^{fuel} = 0.60$. (top) Mean profiles. (bottom) rms profiles.

Figure 2.15(b) shows the mean flame position predicted by the simulation S3. By accounting for both the effect of heat losses and hydrogen enrichments, the LES recovers the correct M flame shape observed in the experiment. There

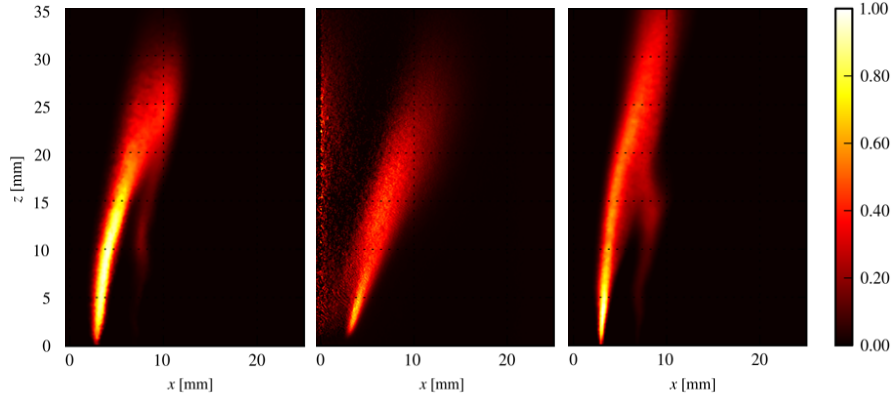
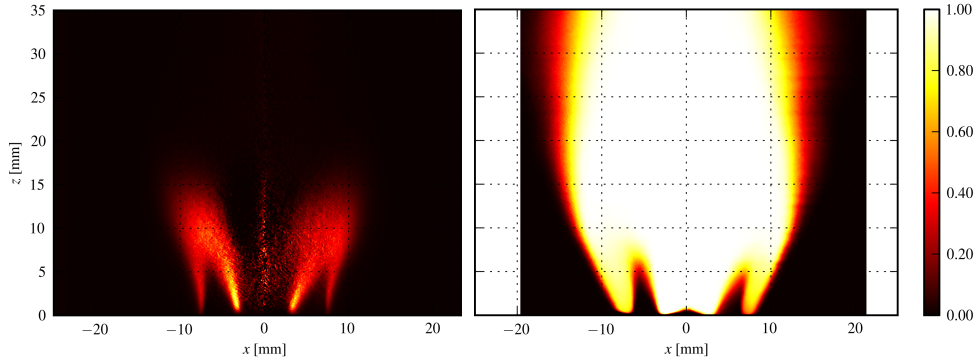


Figure 2.14: Mesh sensitivity analysis for the case $X_{H_2}^{fuel} = 0.60$. Comparison of the normalized mean volumetric heat release predicted by simulation S2 (left), experiments (middle) and the refined mesh simulation S2R (right).

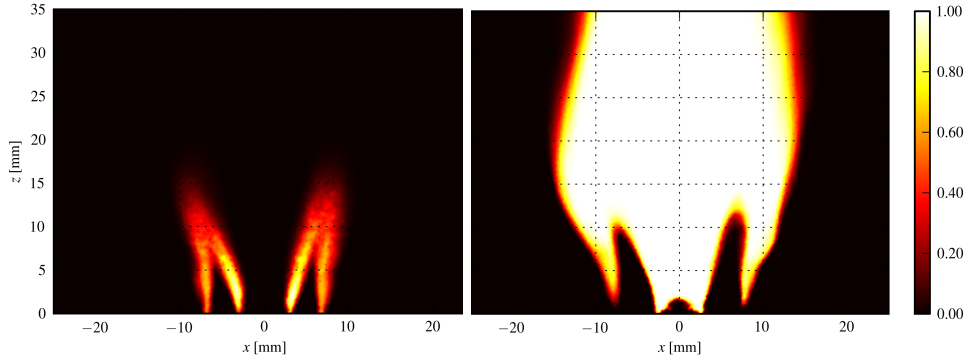
are however still differences between the experiment and the simulation. The flame length is slightly overpredicted in the simulation. In the experiment, the reactivity is elevated in the ISL and much lower in the OSL. The reactivity then progressively decreases towards the flame tip. In the simulation, the reactivity keeps high values in the ISL, but also in the OSL, except close to the flame tip where it drops rapidly. The turbulent flame brush in the experiment also spreads over a wider region than in the simulation. These differences might be attributed to the sub-grid scale wrinkling model that does not fully capture the flame wrinkling near the flame tip. As both flame fronts are located at the ISL and OSL, flame strain effects, which are not accounted for by the F-TACLES model, may also explain the differences in reactivity. It is however worth recalling that the shape of the flame is well captured by the proposed methodology.

2.3.6 Conclusions on the simulations in steady conditions

An experimental configuration has been developed to challenge numerical simulations for capturing premixed swirling flame stabilization mechanisms in confined geometry. Large Eddy Simulations of this combustor have been performed using the turbulent combustion model F-TACLES, based on filtered premixed flamelet tabulation. Two configurations, with two levels of H_2 enrichment in a CH_4/H_2 fuel blend, have been investigated. Experiments show that higher H_2 concentration promotes flames with an M flame shape, whereas V flame shapes are observed for lower values of hydrogen enrichment. Assuming a fully adiabatic combustion chamber, LES always predicts an M flame shape. Another set of LES was performed accounting for measured thermal boundary conditions. These non-adiabatic LES predict the correct flame stabilization and show good agreement with experiments.



(a) Experiments. (left) Normalized Abel deconvoluted OH* chemiluminescence. (right) Mean binarized OH-PLIF.



(b) Simulation S3. (left) Normalized mean volumetric heat release. (right) Mean binarized OH molar fraction.

Figure 2.15: Comparisons of the mean flame position for the case $X_{H_2}^{fuel} = 0.90$. Experiments and non-adiabatic simulation results are shown.

It was also found that the non-adiabatic simulation of the case $X_{H_2}^{fuel} = 0.60$ still predicts a low probability of having a flame front in the OSL, unlike in the experiments where this probability is zero. This slight difference suggests the importance of other physical phenomena in the V or M flame shape stabilization process. It might be due to the fact that the F-TACLES model does not explicitly account for the impact of local strain rate on turbulent consumption speed. In particular, the combined effects of strain rate and heat losses may influence the flame extinction within the OSL. In addition, as explained previously the influence of heat losses on the subgrid scale flame wrinkling has not been considered. This assumption should not impact the inner flame, which is almost adiabatic. However, at the outer flame location, where the flame is quenched due to heat losses, it may also explain the misprediction of local flame extinctions. Accounting for heat losses in the flame wrinkling modeling

is a remaining issue which requires further investigations.

Experiments (Guiberti et al. (2015)) indicate that in general the OSL only hosts a flame intermittently and its probability of presence p decreases when the H_2 concentration is progressively reduced in the fuel blend. For instance, the probability to find a flame front in the OSL is $p = 0.01$ for the case $X_{H_2}^{fuel} = 0.55$ and increases to $p = 0.41$ for $X_{H_2}^{fuel} = 0.78$. In the two limit cases that were studied herein $p=0.90$ for $X_{H_2}^{fuel} = 0.90$ with a well defined M flame shape and $p=0.01$ for $X_{H_2}^{fuel} = 0.60$ with a well defined V flame shape. In between these two limits, the physical processes leading to intermittent M to V and V to M flame shape bifurcations are not well understood and need to be further investigated.

2.4 Simulations in pulsed conditions

2.4.1 Motivations

Turbulent combustion models for Large Eddy Simulation (LES) aims at predicting the flame dynamics. So far, they have been proven to predict correctly the mean flow and flame properties in a wide range of configurations. A way to challenge these models in unsteady situations is to test their ability to recover turbulent flames submitted to harmonic flow modulations. In this section, the Flame Transfer Function (FTF) of a CH_4/H_2 /air premixed swirled-stabilized flame submitted to harmonic flowrate modulations in a non-adiabatic combustor is compared to the response computed using the Filtered TABulated Chemistry for LES (F-TACLES) formalism.

2.4.2 Numerical setup

Simulations are still conducted with the incompressible, unstructured finite volume YALES2 flow solver (Moureau et al. (2011a)). The numerical setup is almost identical to the one used in the simulations in steady conditions, except for the flow forcing, detailed in the next section.

2.4.3 Flow forcing

A pulsed cold flow simulation is performed on CD2 to determine the inlet boundary conditions for the reactive simulations on CD1. The inlet flow velocity is submitted to an harmonic oscillation at a frequency $f = 350$ Hz and a modulation level $u'_z/\bar{u}_z = 0.17$, where \bar{u}_z is the local axial velocity in the 22-mm diameter injection channel (with the central insert) and u'_z denotes the fluctuation amplitude. The signals for the axial and azimuthal velocity compo-

nents are extracted from planes at $z = -35$ mm corresponding to the exit of the swirler and $z = -20$ mm corresponding to the reactive simulations inlet as shown in Fig. 2.16.

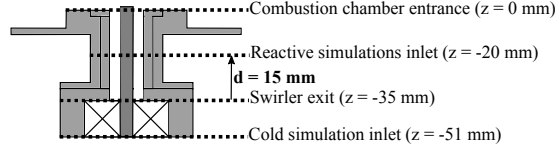


Figure 2.16: Geometry of the injection unit and locations of the planes of interest.

Phase averaged results to eliminate effects of turbulence are shown in Fig. 2.17. The axial velocity at the exit of the swirler (solid blue line in Fig. 2.17) and at the inlet of the numerical domain CD1 (red dashed lines in Fig. 2.17) separated by a distance $d = 15$ mm are in phase. This is not the case for the azimuthal component of velocity that features a phase shift $\Delta\varphi = 2.19$ rad due to the presence of the swirler, which generates a vorticity wave as a response to the axial pulsation (Komarek and Polifke (2010); Palies et al. (2010a)). Under the low Mach number flow assumption, the axial velocity perturbation is convected instantaneously along the axial direction. In reality, an acoustic perturbation propagating at the sound speed $c = 340$ m.s⁻¹ leads to a phase shift $\Delta\varphi = 2\pi fd/c \simeq 97 \cdot 10^{-3}$ rad, which is negligible at $f = 350$ Hz. The azimuthal velocity perturbation is convected at the bulk flow velocity $u_b = 14$ m.s⁻¹ in the annular injection channel. This leads to a phase shift $\Delta\varphi$ that linearly increases with the distance from the exit of the swirler (Palies et al. (2011)):

$$\Delta\varphi \simeq 2\pi \frac{fd}{u_b} \quad (2.1)$$

For the present case, Eq. (2.1) yields a phase shift $\Delta\varphi$ of 2.32 rad at $f = 350$ Hz, a value which is only 5% larger than the value found in the cold flow simulation. For all the reactive flow simulations presented in this work, Eq. (2.1) is used to set the phase shift between the azimuthal and axial velocity perturbations at the numerical domain inlet of CD1.

2.4.4 Flame Describing Function

The FDF is a nonlinear transfer function linking heat release rate fluctuations \dot{Q}' to velocity disturbances u' at some location before the flame zone. This frequency response is both a function of the forcing frequency and the disturbance level (Noiray et al. (2008)):

$$F(\omega, |u'|) = \frac{\dot{Q}'/\bar{Q}}{u'/\bar{u}} = G(\omega, |u'|) e^{i\varphi(\omega, |u'|)} \quad (2.2)$$

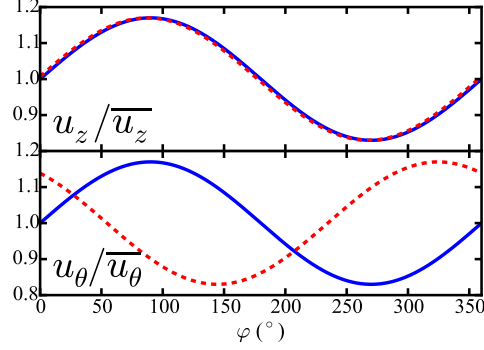


Figure 2.17: Normalized phase averaged velocity signal at $z = -35$ mm (solid blue line) and $z = -20$ mm (dashed red lines) for a forcing frequency of $f = 350$ Hz and $u'_z/\bar{u}_z = 0.17$. Top: axial velocity u_z/\bar{u}_z . Bottom: azimuthal velocity u_θ/\bar{u}_θ .

where G is the gain of the FDF and φ its phase. This formulation makes an hypothesis of weak nonlinearity of the flame response to the harmonic velocity disturbance u' and only considers the first harmonic \dot{Q}' of the flame response. The higher harmonics are not considered. The quantities \bar{u} and \bar{Q} denote the time averaged values. In the experiments, the velocity disturbances u' are measured with a hot wire located upstream of the inlet of the swirler at $z = -65$ mm (see Fig. 2.1) in a region where the flow is axial, laminar with a top hat velocity profile. The mean \bar{Q} and fluctuating \dot{Q}' heat release rate components are deduced from OH* light intensity I measurements collected over the whole flame volume (Palies et al. (2010a)): $I'/\bar{I} = \dot{Q}'/\bar{Q}$. In LES, the local filtered heat release rate $\bar{\dot{\omega}}_T$ is computed as:

$$\bar{\dot{\omega}}_T = \gamma(\Delta h) \Xi \bar{\dot{\omega}}_T^*(\tilde{c}) \quad (2.3)$$

where $\gamma(\Delta h)$ is a parameter introduced to take into account heat losses (Mercier et al. (2014a)), Ξ is the subgrid scale wrinkling modeled as in Charlette et al. (2002c) and $\bar{\dot{\omega}}_T^*(\tilde{c})$ is the heat release rate tabulated in the filtered F-TACLES look-up table. The progress variable \tilde{c} is the solution of a filtered balance equation, as discussed in Fiorina et al. (2010a). The filtered heat release rate $\bar{\dot{\omega}}_T$ is integrated over the whole computational domain to obtain the heat release rate \dot{Q} :

$$\dot{Q} = \int_V \bar{\dot{\omega}}_T dV \quad (2.4)$$

The time averaged value is noted \bar{Q} and \dot{Q}' corresponds to the Fourier component at the harmonic forcing frequency f . The velocity disturbance u' is computed in the simulation from the fluctuating mass flow rate. In both experiments and simulations, the FDF is calculated as the ratio between the cross

spectral density $P_{y,x}$ of \dot{Q} and u and the power spectral density $P_{x,x}$ of u taken at the forcing frequency, which is then normalized by \bar{u}/\bar{Q} :

$$F(\omega, |u'|) = \frac{P_{\dot{Q},u} \bar{u}}{P_{u,u} \bar{Q}} \quad (2.5)$$

The gain G and the phase φ of each point of the FDF are respectively determined as the modulus and phase lag of F with respect to the velocity signal at the hot wire location:

$$G(\omega, |u'|) = |F(\omega, |u'|)| \quad (2.6)$$

$$\varphi(\omega, |u'|) = \arg(F(\omega, |u'|)) \quad (2.7)$$

Experiments are conducted for harmonic flowrate excitations from $f = 10$ Hz to 370 Hz with 10 Hz steps and two forcing levels $u'/\bar{u} = 0.09$ and $u'/\bar{u} = 0.17$. Numerically, twelve simulations are performed on CD1 with a mesh including 49 million elements to investigate the flame response at six forcing frequencies for both levels of velocity disturbance. All cases are synthesized in Tab. 2.2.

Simulations are carried out on an IBM Blue Gene/Q cluster on 1024 processors. Simulating one period of modulation for the case FT-350-09 takes 2800 CPUh, while for case FT-100-17 it reaches 10 000 CPUh.

Table 2.2: *Investigated cases in simulations.*

Simulation	Frequency (Hz)	u'/\bar{u}	Number of elements ($\times 10^6$)
FT-100-09	100	0.09	49
FT-100-17	100	0.17	49
FT-160-09	160	0.09	49
FT-160-17	160	0.17	49
FT-160-09-F	160	0.09	395
FT-200-09	200	0.09	49
FT-200-17	200	0.17	49
FT-250-09	250	0.09	49
FT-250-17	250	0.17	49
FT-300-09	300	0.09	49
FT-300-17	300	0.17	49
FT-350-09	350	0.09	49
FT-350-17	350	0.17	49
FT-350-09-F	350	0.09	395

2.4.5 Results

2.4.5.1 Flame Describing Function

Results of the simulations described in Tab. 2.2 are compared to experimental data for the FDF gain and phase lag in Fig. 2.18. The simulated phase lag is in fairly good agreement with experiments for the range of frequencies investigated. Results better match for the largest perturbation level $u'/\bar{u} = 0.17$. The inflection point of the phase lag curve in the experiments at $f = 160$ Hz is however not reproduced by the simulations at $u'/\bar{u} = 0.09$.

The quality of the FDF gain prediction by the LES is much more sensitive to the excitation frequency. Slight differences are observed at $f = 100, 200, 250, 300$ and 350 Hz, with a significant over-prediction of the FDF gain for an excitation at $f = 160$ Hz. Figure 2.18 shows that the measured FDF gain curves feature a low response at $f = 160$ Hz and a high value at $f = 350$ Hz. Differences between simulations and measurements are interpreted in the following by analyzing the flow and flame responses at these two forcing frequencies.

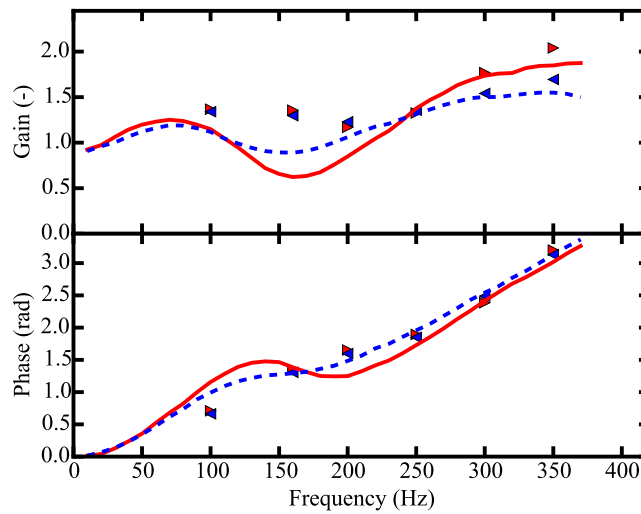


Figure 2.18: *FDF gain (top) and phase lag (bottom). Experiments : $u'/\bar{u} = 0.09$ (red solid line), $u'/\bar{u} = 0.17$ (blue dashed lines). Simulations obtained with the 49 million element mesh: $u'/\bar{u} = 0.09$ (red items), Red items: $u'/\bar{u} = 0.17$ (blue items).*

2.4.5.2 Flow and flame dynamics

Figures 2.19 and 2.20 (left side of each panel) show the experimental data gathered for five phase angles regularly distributed in a modulation period at $f = 350$ Hz and $f = 160$ Hz, respectively. These images show on the left,

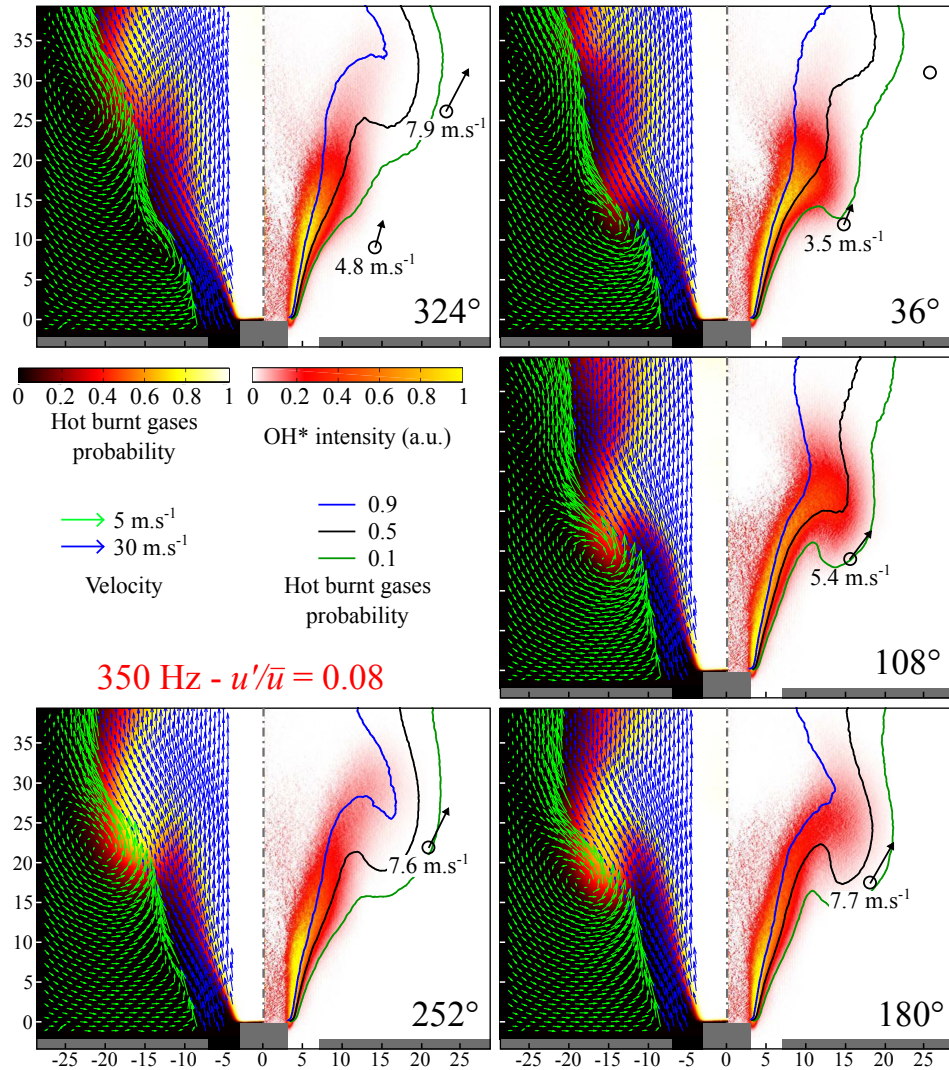


Figure 2.19: Modulation at $f = 350$ Hz and $u'/\bar{u} = 0.08$. Experimental results for the phase-averaged velocity field, probability of presence of hot burnt gases (left) and OH* intensity with iso-contours of hot burnt gas probability (right) at five regularly distributed phase angles in the oscillation cycle. The position of the center of a large vortical structure and its convection velocity are indicated as a circle and an arrow. Dimensions are indicated in millimeters.

phase conditional averages of the velocity field superimposed on the probability of presence of hot burnt gases in the axial plane of the burner. Two types of arrows are used to emphasize differences between the large velocities reached by the flow in the swirling jet (blue arrows) and the smaller velocities in the outer recirculation zones of the flow (green arrows). The trace of the OH* chemiluminescence signal in the same axial plane (after Abel deconvolution) is plotted on the right together with iso-levels of probability of presence of burnt

gases. The convection velocities of large coherent structures detected by post-processing and the velocity field are also indicated together with the position of the center of these vortices.

For the case at $f = 350$ Hz shown in Fig. 2.19, $\varphi = 324^\circ$ corresponds to the first phase, out of the five examined, where a large coherent vortical structure is detected in the outer shear (mixing) layer of the swirling jet with a center at about 9 mm above the top of the central insert and which is convected at a velocity 4.8 m.s^{-1} . Note that two consecutive vortices corresponding to two consecutive modulation periods are visible in the field of view for this phase. The second one with a center at about 25 mm moves faster at a speed of 7.9 m.s^{-1} . The loop sequence $324^\circ \leq \varphi \leq 324^\circ + 360^\circ$ allows following the growth and downstream convection of each coherent structure in the mixing layer along the flame brush until it reaches the flame tip at a phase lag around $\varphi = 252^\circ$. The right sides in Fig. 2.19 show the measured OH* emission intensity (red/orange colormap) after an inverse Abel transform is applied on the phase averaged images. These images ease analyzing interactions between the flame and the large vortical structures during a modulation period.

At a forcing frequency $f = 350$ Hz and a forcing level $u'/\bar{u} = 0.08$, the flame brush in Fig. 2.19 progressively rolls up around the large vortical structure at $\varphi = 36^\circ$ and 108° and the flame length increases, before the flame is disrupted between phases $\varphi = 108^\circ$ and 180° when the vortical structure reaches the flame tip. The flame then rapidly shrinks at phases $\varphi = 180^\circ$ and 252° . This mechanism is similar to the one observed for laminar V flames submitted to harmonic flow modulations (Durox et al. (2005)). This process leads to large flame surface area fluctuations during a modulation period and is responsible for the large FDF gain observed at this forcing frequency in Fig. 2.18. The probability to find hot burnt gases ($T \geq 1800$ K (Guiberti et al. (2015b))) deduced from OH-LIF measurements is also shown in Fig. 2.19. The circular pocket of hot burnt gases entrained around each vortical structure during a modulation period confirms the flame/vortex roll-up process taking place in the external shear layer of the swirling flow. One may also note an interesting feature. The convection velocity of these structures depends on the height above the burner and features a complex behavior (Oberleithner et al. (2015)). With the data available, the vortical structure seems to first decelerate before reaccelerating. This observation is in contrast with simplified assumptions made in many low order models (Schuller et al. (2003); Preetham et al. (2008)).

Figure 2.20 shows the experimental results found at a lower forcing frequency $f = 160$ Hz, but a slightly higher forcing level $u'/\bar{u} = 0.12$. The sequence of phase conditioned data again allows following the growth and downstream convection of a large vortical structure shed from the injector lip during a modulation period. In comparison to results at $f = 350$ Hz at $u'/\bar{u} = 0.08$, the

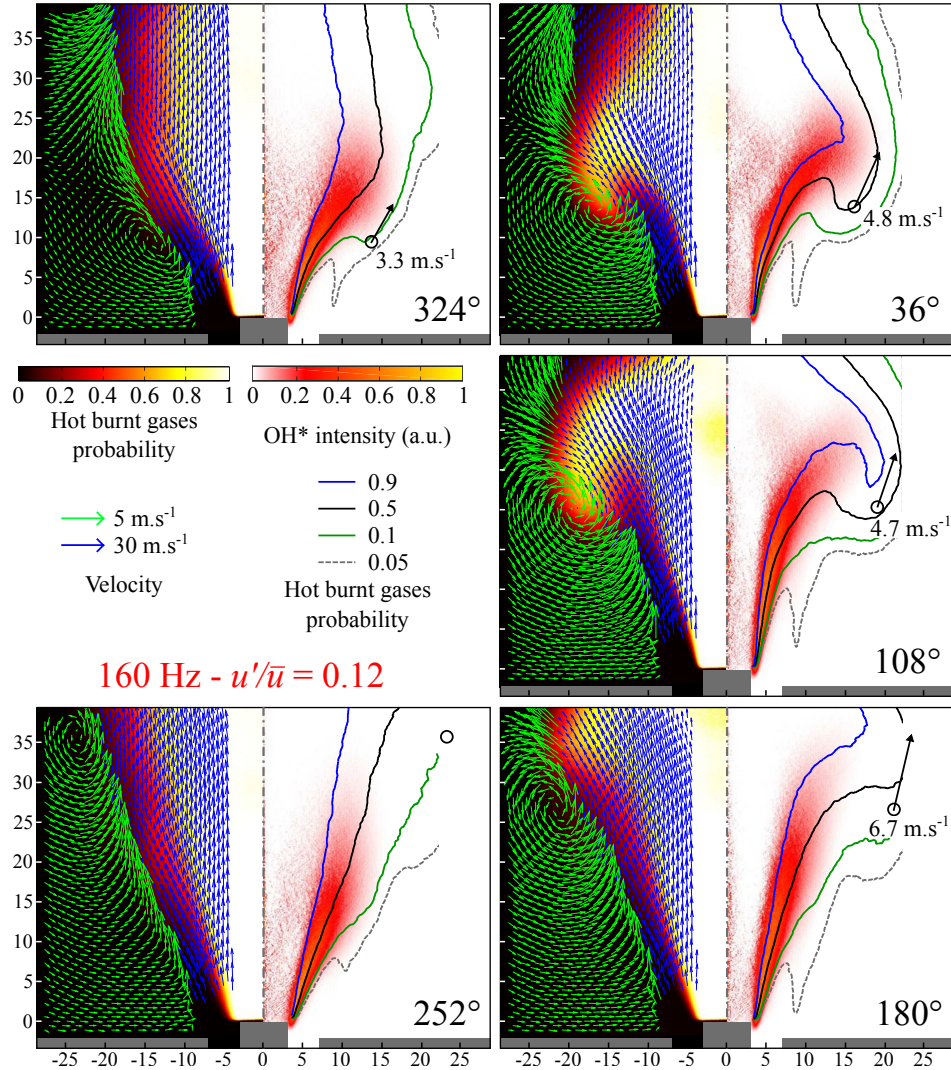


Figure 2.20: Measured phase-averaged velocity field and hot burnt gases probability (left) and OH^* intensity with iso-contours of hot burnt gases probability (right) for five phase angles during a modulation period for $f = 160$ Hz and $u'/\bar{u} = 0.12$. The vortex center position and its convection velocity are indicated as a circle and an arrow. Dimensions are indicated in millimeters.

vortex consistently features a larger diameter due to the lower forcing frequency and the higher modulation level (Oberleithner et al. (2015)). A large circular pocket of hot burnt gases entrained by the vortical structure is again visible for this forcing frequency in each image. However, the OH^* emission data also reveal that the flame tip is less bent by these large structures during a modulation period at $f = 160$ Hz than at $f = 350$ Hz. Therefore, it can be concluded that the flame/vortex roll-up process is less efficient for $f = 160$ Hz and $u'/\bar{u} = 0.12$ than for an excitation at $f = 350$ Hz $u'/\bar{u} = 0.08$. This observation highlights

the determinant role of the complex flame/vortex roll-up process taking place in the flame response. A larger and more energetic structure does not necessarily leads to a stronger flame response.

One may already suggest that the vortical structure produced for the forcing conditions explored in Fig. 2.20 is too large in comparison to the flame length to maximize the flame/vortex roll-up process, even though this structure is energetic enough to recirculate the hot burnt gases. The role of these coherent structures in the peak value of the FTF gain has already been highlighted for the response of laminar V flames (Durox et al. (2005)) and for the response of swirling flames (Palies et al. (2011); Oberleithner et al. (2015)). Oberleithner et al. (2015) showed that the receptivity of the shear layer is an essential feature to understand the streamwise growth of these coherent structures. They found that the FDF gain of their swirling flame is correlated to the receptivity of the shear layer when the forcing frequency and amplitude are varied. It is found here that the flame/vortex interaction needs also to be considered and the process is not purely hydrodynamic. Interaction of a large coherent structure with the flame may also lead to a low heat release rate response.

A close examination of Figs. 2.19 and 2.20 also reveals that the flame angle fluctuates at the base of the central rod during a modulation period. These fluctuations are difficult to see in these images and are better highlighted in Fig. 2.28, which is later discussed. They are larger at $f = 160$ Hz than at $f = 350$ Hz and are attributed to temporal fluctuations of the swirl number (Palies et al. (2010a); Bunce et al. (2013)). For an excitation at $f = 160$ Hz, the flame motion is controlled by two distinct mechanisms : flame/vortex roll-up and swirl number fluctuations. It has been shown in Palies et al. (2010a) that interferences between these two mechanisms are responsible for a drop of the FDF gain. It is suggested here that the efficiency of the flame/vortex interaction needs also to be considered to understand the observed drop of the flame response at $f = 160$ Hz.

2.4.5.3 Comparison with simulations

The FDF only yields an integrated information on the global flame response to the flow perturbations. A deeper analysis is made in this section by comparing the measured and computed velocity fields, the OH* emission and heat release distributions and the hot burnt gas distributions in the experiments and simulations when the flow is modulated. The OH* intensity distribution is here again directly compared to numerical fields of volumetric heat release rate, as was done for instance in Armitage et al. (2006). This hypothesis could be avoided by using a mechanism which includes OH* species for chemistry tabulation Hall and Petersen (2006). However as the burner operates in the fully

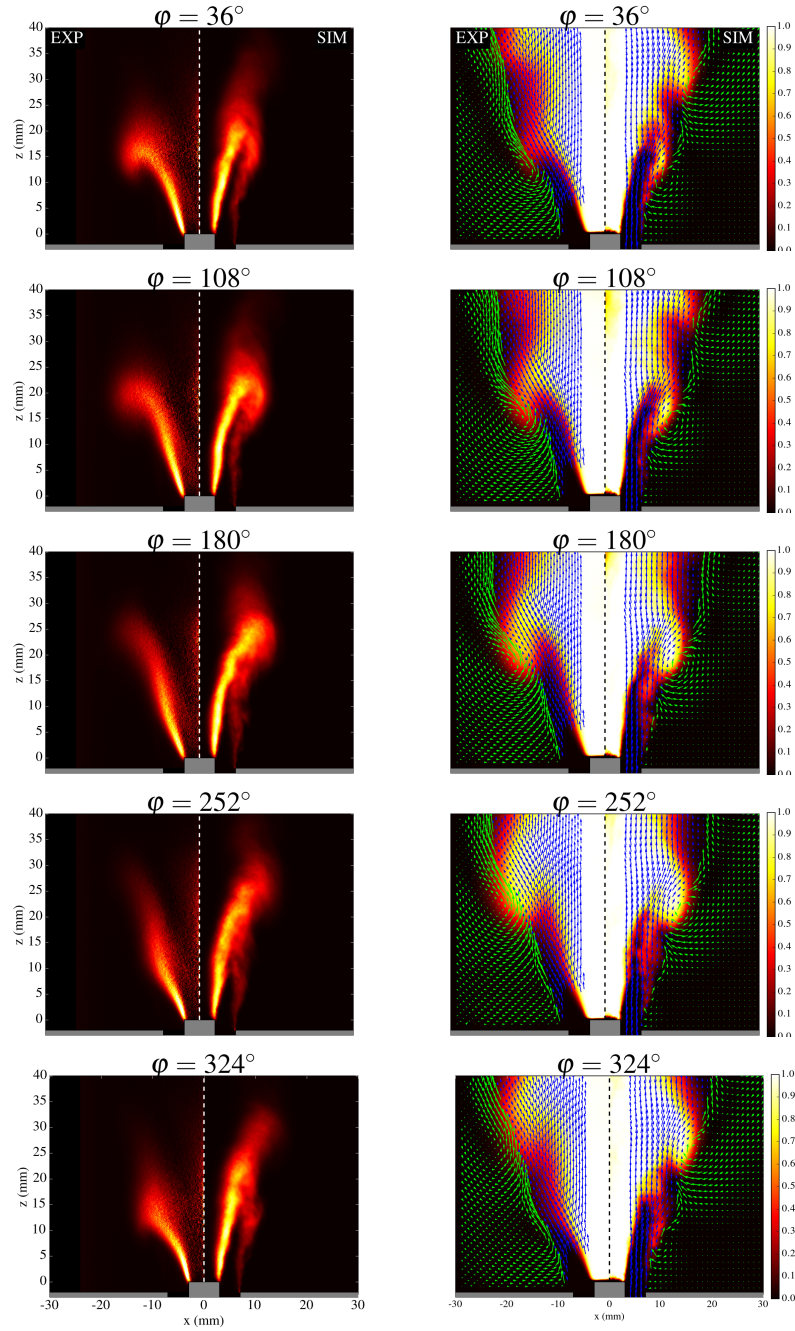


Figure 2.21: First column: phase-averaged measured OH^* emission (left) and computed heat release rate (right). Values are normalized by the maximum. Second column: measured (left) and computed (right) phase-averaged velocity field and hot burnt gas probability of presence. Results are presented for five phase angles of the modulation period. Case FT-350-09 at $f = 350$ Hz and $u'/\bar{u} = 0.09$ in Tab. 2.2.

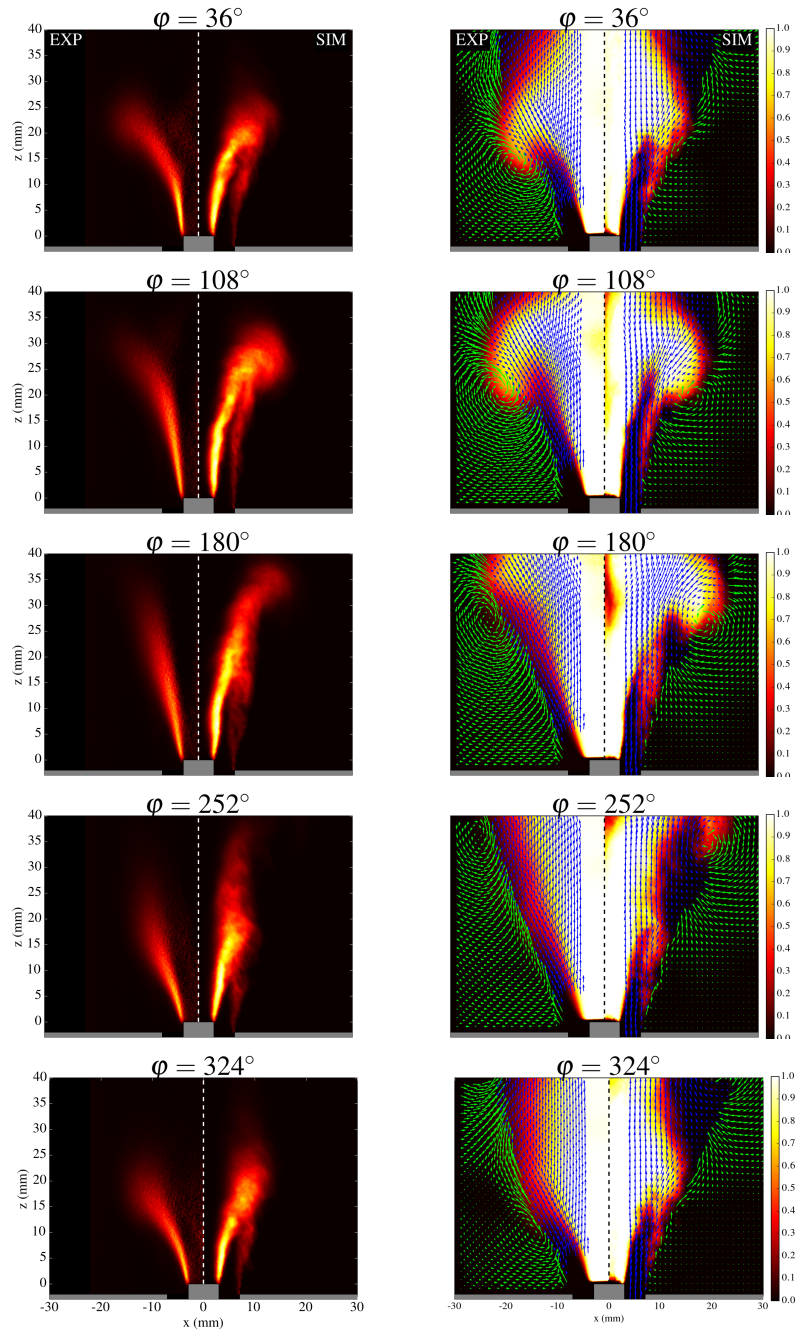


Figure 2.22: *First column: phase-averaged measured OH^* emission (left) and computed heat release rate (right). Values are normalized by the maximum. Second column: measured (left) and computed (right) phase-averaged velocity field and hot burnt gas probability of presence. Results are presented for five phase angles of the modulation period. Case FT-160-17 at $f = 160$ Hz and $u'/\bar{u} = 0.17$ in Tab. 2.2.*

premixed mode and all signals are normalized by their maximum values, the errors induced by this approximation are expected to be limited and will not alter the following analysis. Also, a kinetic scheme with OH^* would need to be validated with the 1D flame solver used here and a new look-up table would be generated with this new species.

The left columns in Figs. 2.21 and 2.22 show images with the measured phase averaged OH^* emission distribution plotted on the left and the phase averaged heat release rate calculated in the simulation on the right for excitations at $f = 350$ Hz and $f = 160$ Hz, respectively. The right columns in these figures compare the measured (on the left side) and computed (on the right side) phase averaged hot burnt gas probability of presence superimposed to the corresponding velocity fields. These comparisons are conducted for five phases in the modulation cycle. One recalls that the phase lag φ in these figures is indicated with respect to the velocity signal measured at the hot wire location.

Regardless of the forcing frequency and the phase in the forcing cycle, the experimental and numerical data are close in Figs. 2.21 and 2.22. The position and size of the large vortical structures convected in the outer shear layer of the swirling jet are well reproduced at each phase in the cycle. The shape and size of the recirculating hot burnt gases pockets entrained by these vortical structures are also well captured by the LES. Overall, the shape of the flame brush at the different phases in the forcing cycle is also fairly well predicted by the simulations in Figs. 2.21 and 2.22. For $f = 350$ Hz, the large flame/vortex roll-up process is reproduced by the simulations for the phases $36^\circ \leq \varphi \leq 180^\circ$ where the vortex interacts with the flame tip. For $f = 160$ Hz, the calculated flame/vortex roll-up process also appears less intense in Fig. 2.22, which is consistent with the experimental observations.

The velocity fields calculated in the simulations through the axial plane of the burner and the PIV data are extracted at heights $z = 5, 15, 25$ and 35 mm above the combustion chamber dump plane and are plotted in Figs. 2.23 and 2.24. The experimental values are masked for $x < 5$ mm because flow seeding is not high enough to provide statistical meaningful information in the central region of the flow. The numerical values are kept in this region to highlight the evolution of the flow in the inner recirculation zone. These additional figures confirm that the shape of the velocity profiles for both components are the same between experiments and simulations at all heights z and phases φ . There are however differences in the peak values reached by the perturbed flow in experiments and simulations. The largest differences are observed at $x \sim 10$ mm in the outer shear layer of the swirling flow.

One may identify other differences between experiments and simulations in Figs. 2.21 and 2.22. The first one is the presence of residual heat release in

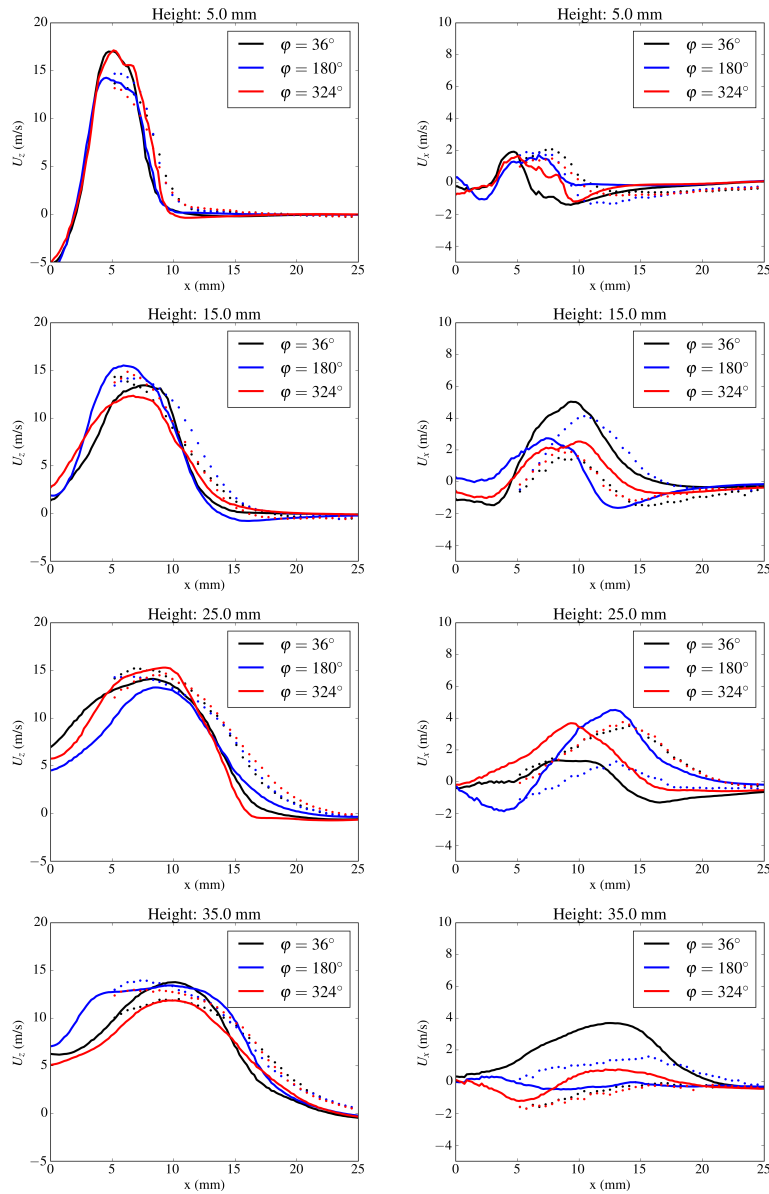


Figure 2.23: First column: measured (symbols) and computed (solid lines) phase-averaged axial velocity u_z . Second column: measured (symbols) and computed (solid lines) phase-averaged radial velocity u_x . Results are presented for three phase angles of the modulation period and different heights z . Case FT-350-09 at $f = 350$ Hz and $u'/\bar{u} = 0.09$ in Tab. 2.2.

the outer shear layer of the swirling jet in the simulations. This difference in volumetric heat release distribution can also be observed for the unperturbed flame shown in Fig. 2.10. The second one is the difference between the axial expansion of the zones with large heat release rate values. Overall, the flame

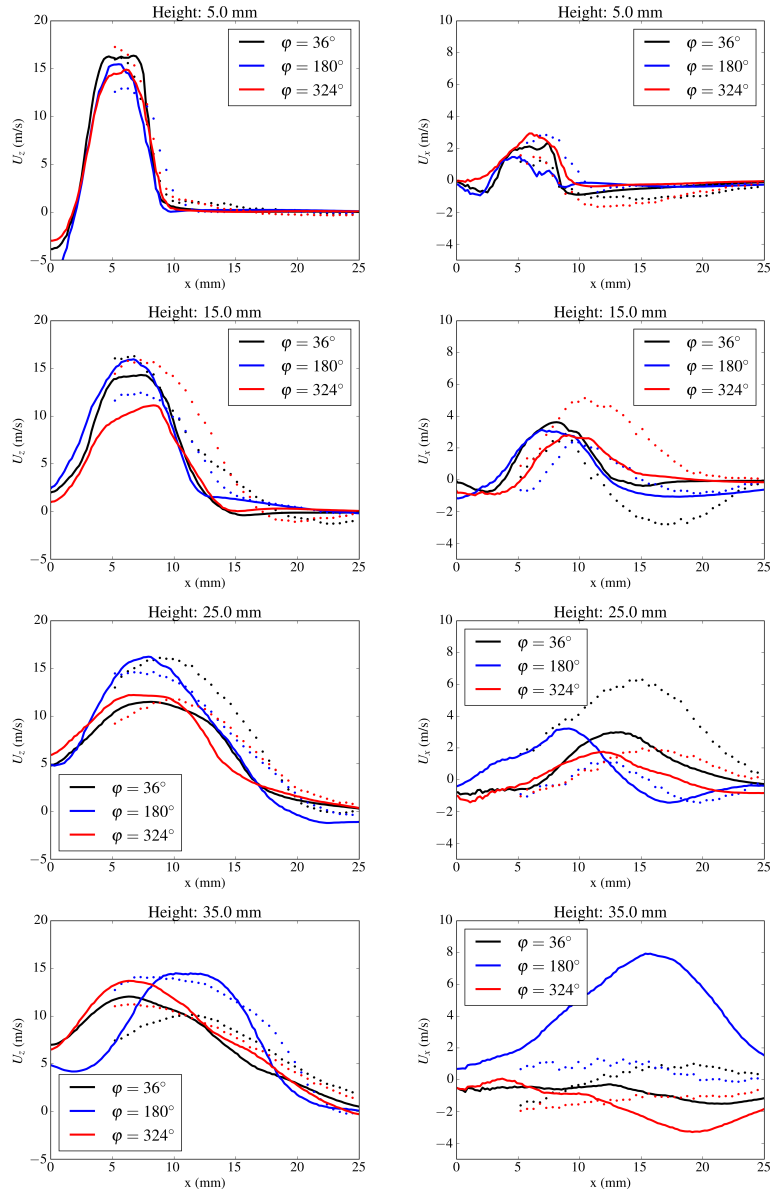


Figure 2.24: First column: measured (symbols) and computed (solid lines) phase-averaged axial velocity u_z . Second column: measured (symbols) and computed (solid lines) phase-averaged radial velocity u_x . Results are presented for three phase angles of the modulation period and different heights z . Case FT-160-17 at $f = 160$ Hz and $u'/\bar{u} = 0.17$ in Tab. 2.2.

appears taller in the simulations compared to experimental observations. The largest differences are observed for the case at $f = 350$ Hz and $\varphi = 252^\circ$ and $\varphi = 324^\circ$ in Fig. 2.21. It is known that the flame angle and flame height are important features that affect the flame frequency response to flow perturba-

tions (Schuller et al. (2003)). Therefore, it is worth examining if differences between the measured and computed FDF gain can be attributed to differences of the observed and simulated flame shapes.

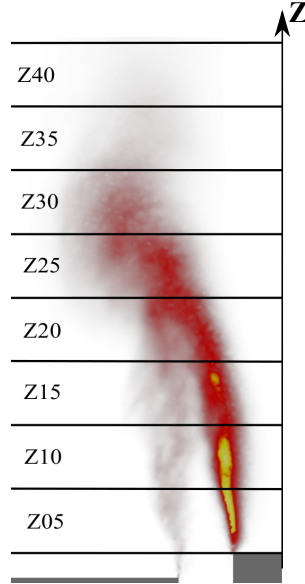


Figure 2.25: Definition of interrogation regions.

To this end, data are further analyzed by splitting the images in eight interrogation regions of 5 mm each, as shown in Fig. 2.25. Layer Z05 denotes the region between the rod tip and 5 mm above. Layer Z10 comprises the region between $5 \text{ mm} \leq z \leq 10 \text{ mm}$ and so on. Figures 2.26 ($f_{Scena} = 350 \text{ Hz}$) and 2.27 ($f = 160 \text{ Hz}$) compare, for each of these layers, the measured (top) and computed (bottom) evolutions of the phase averaged integral of OH* intensity (measurements) and heat release rate (simulations) calculated over the region covered by the layer as a function of the phase in the forcing cycle. Values are normalized by the average value obtained in each layer during a modulation period.

Results in Fig. 2.26 are analyzed first for an excitation at $f = 350 \text{ Hz}$. For layers Z05, Z10, Z15, Z20, Z25 and Z30, which correspond to small and intermediate distances from the injector nozzle, agreement between the measured OH* intensity I/\bar{I} and heat release rate \dot{Q}/\bar{Q} deduced from the simulation is good. The simulation reproduces well the shape of the measured signal both in phase and amplitude in the different interrogation windows. Agreement however worsens when results are compared for the upper layers Z35 and Z40. Both the amplitude and the phase lag of the measured I/\bar{I} and computed \dot{Q}/\bar{Q} signals differ in these regions. These differences have however a limited impact on the global flame response and its FDF as shown in Fig. 2.18 at $f = 350 \text{ Hz}$

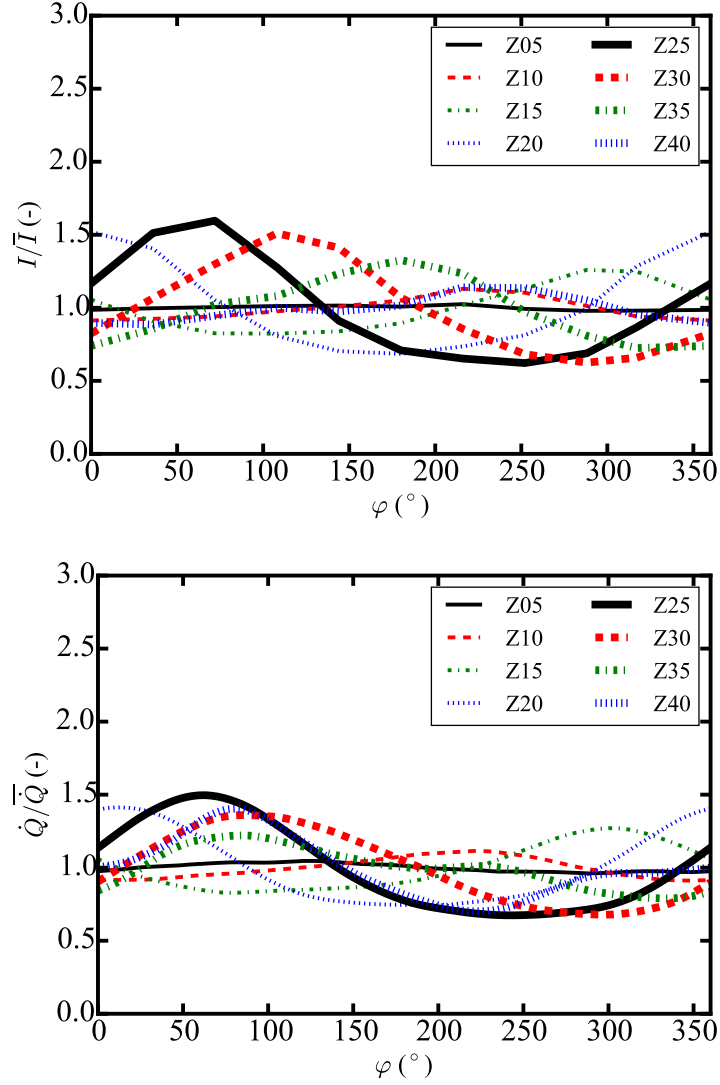


Figure 2.26: Evolution of the normalized phase-averaged integral of heat release rate for each layer defined in Fig. 2.25 during a modulation period. Top: experiments. Bottom: simulations. Case FT-350-09 at $f = 350$ Hz and $u'/\bar{u} = 0.09$ in Tab. 2.2.

because the relative fluctuations \dot{Q}/\bar{Q} remain relatively weak in the regions Z35 and Z40 in Fig. 2.26 compared to the ones found at Z25 and Z20 which are better reproduced by the simulations.

Results in Fig. 2.27 for an excitation at $f = 160$ Hz are now analyzed. Except for layer Z20, the shape of the relative fluctuation I/\bar{I} observed for the OH^* signal in the experiment is well reproduced by the relative heat release rate fluctuation \dot{Q}/\bar{Q} found in the LES. The amplitude of these signals is also well

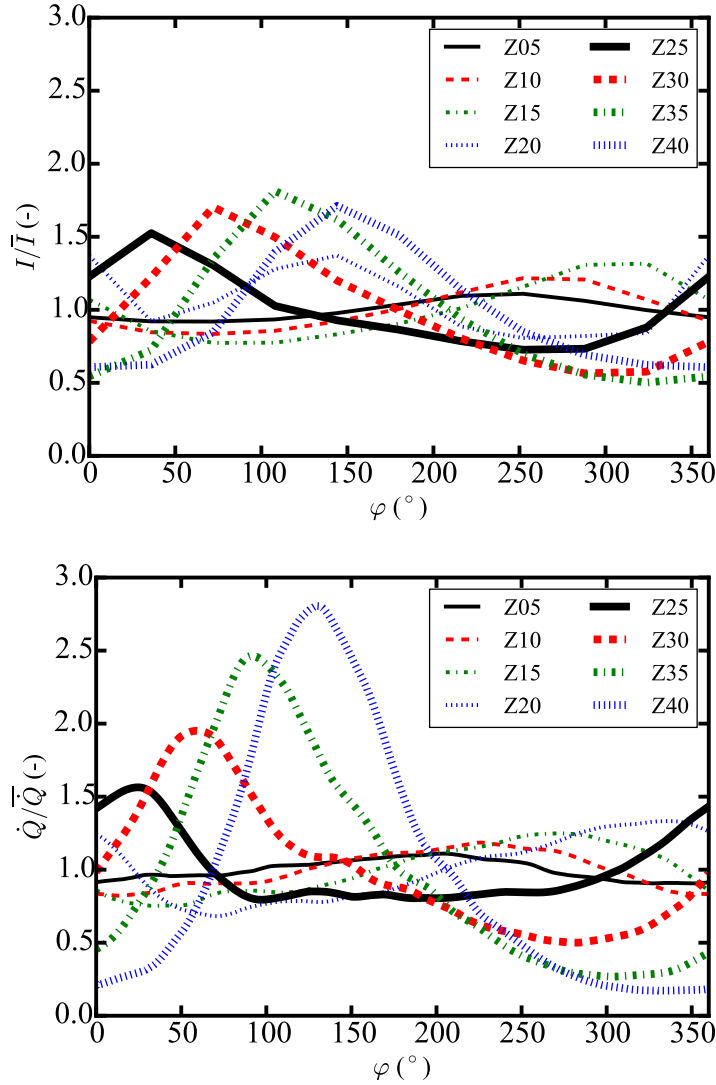


Figure 2.27: Evolution of the normalized phase-averaged integral of heat release rate for each layer defined in Fig. 2.25 during a modulation period. Top: experiments. Bottom: simulations. Case FT-160-17, $f = 160$ Hz and $u'/\bar{u} = 0.17$ in Tab. 2.2.

reproduced by the LES for layers Z05, Z10, Z15, Z20 and Z25. However, simulations largely over-predict the amplitude of heat release rate fluctuations in layers Z30, Z35 and Z40, corresponding to the upper part of the flame. Because the flame stabilizes with a V-shape, the upper parts of the flame comprise a large fraction of the total flame surface area and contribute significantly to the total heat release rate oscillation. Therefore, over-predicting the amplitude of heat release rate fluctuations in these regions is likely to have a significant impact on the predicted FDF. This could explain why the FDF gain is largely over-

predicted by the simulation at the forcing frequency $f = 160$ Hz in Fig. 2.18.

The previous figures reveal that heat release rate fluctuations are poorly predicted by the simulation in the upper region of the flame at both forcing frequencies $f = 350$ Hz due to phase mismatch between the experimental and numerical signals and at $f = 160$ Hz due to an amplitude mismatch, but LES predicts the correct FDF gain for an excitation at $f = 350$ Hz and overpredicts it for $f = 160$ Hz in Fig. 2.18. To better understand this behavior, Fig. 2.28 plots the minimum and maximum values of the heat release rate \dot{Q} and OH* light intensity I signals found in each interrogation region over a forcing cycle. This comparison gives an indication on how well the envelope of the flame motion is reproduced by the simulation as a function of the distance to the injector outlet.

Results for $f = 350$ Hz and $u'/\bar{u} = 0.09$ are shown at the left in Fig. 2.28. One first sees that the envelope of the perturbed flame brush does not move close to the flame anchoring region, meaning that the flame root angle does not vary in this region at this forcing condition. The flame brush envelope then starts to grow further downstream and this motion grows in amplitude with the downstream distance to the rod tip up to the region Z20. At this distance, the amplitude of this motion starts to shrink in the experiments further downstream. These features are well reproduced by the LES, except very close to the flame tip where the LES overestimates the amplitude of the flame brush motion at Z40. As already stated, this has a limited impact on the FDF at $f = 350$ Hz, because the contribution to the total heat release fluctuation of the signal originating from the flame tip remains relatively weak in this case.

The situation differs in the right graph in Fig. 2.28 obtained for a forcing frequency $f = 160$ Hz and $u'/\bar{u} = 0.17$. One may already note a sizable motion of the flame brush envelope very close to the flame anchoring region associated to large fluctuations of the flame root angle for this modulation. The envelope of the flame brush motion then also grows with the downstream distance to the rod tip and this is again well reproduced by the simulation up to region Z20. The maximum fluctuation amplitude is reached for Z30 in the experiments. The measured signal then slightly drops at Z=40 while the envelope of the simulated signal continuously grows with the distance to the rod tip and reaches the largest oscillations at the flame tip. Therefore, LES does not accurately predict the FDF gain at $f = 160$ Hz in Fig. 2.18 due to a difficulty at reproducing the correct flame tip motion at this forcing condition.

2.4.6 Analysis

The objective of the following analysis is to identify the reasons which explain the limitation of the LES and to provide routes for improvement. Differences

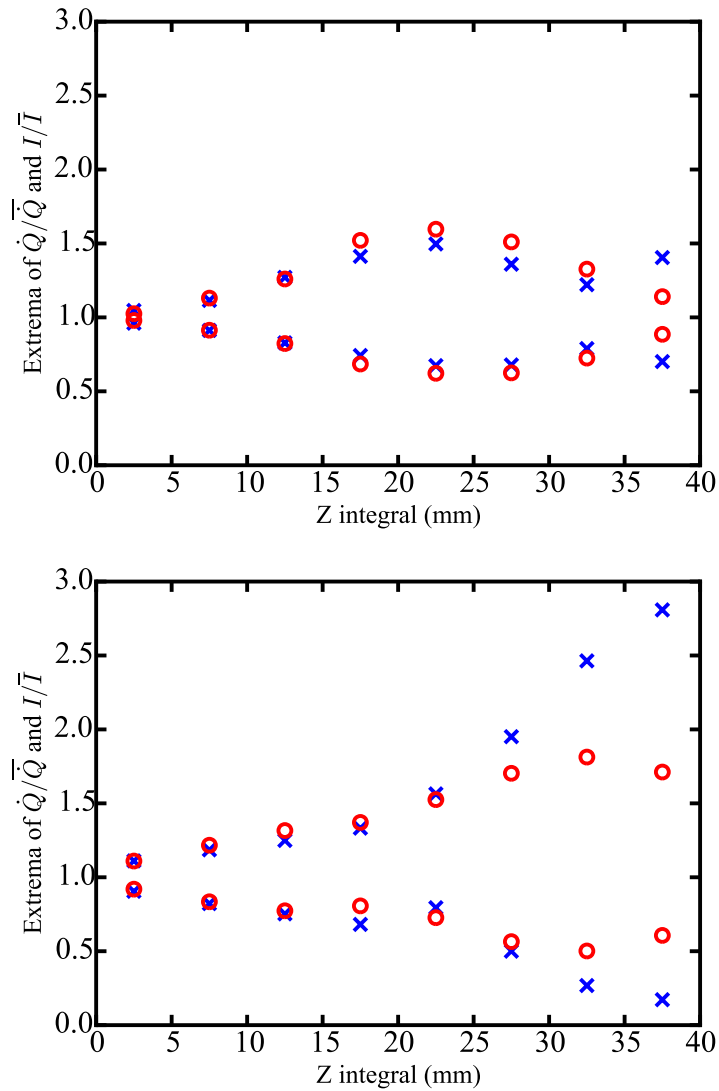


Figure 2.28: Extrema of the normalized phase-averaged integral heat release rate in each layer defined in Fig. 2.25 as a function of the downstream position. Blue crosses: simulations. Red circles: experiments. Top: case FT-350-09. Bottom: case FT-160-17.

between LES predictions and experiments for the FDF gain and flame motion suggest that turbulent heat release fluctuation prediction should be improved. The data presented in the previous sections also indicate that these differences may be specifically attributed to difficulties in computing the spatial distribution of the heat release rate, particularly near the tip of the flame. This issue potentially derives for errors in determining the correct flame consumption speed, which controls the flame shape and flame height. Different scenarii

are now envisaged to explore these issues.

2.4.6.1 Scenario A: impact of the grid resolution

Original simulations carried out on a mesh with 49 million elements have been reconducted on a homogeneously refined grid made of 395 million elements for both forcing frequencies $f = 160$ Hz and $f = 350$ Hz. Results for the flame dynamics are not shown here, but one barely sees any difference with the phase averaged fields plotted in Figs. 2.21 and 2.22 that were obtained with the original grid. Values for the FDF gain and phase lag obtained on the fine grid are added to the FDF plotted in Fig. 2.29. The results are a bit improved at $f = 350$ Hz, but there is no significant difference, meaning that the grid resolution does not improve the quality of the prediction of flame response to flow perturbations and in particular does not help to reduce the difference observed at $f = 160$ Hz.

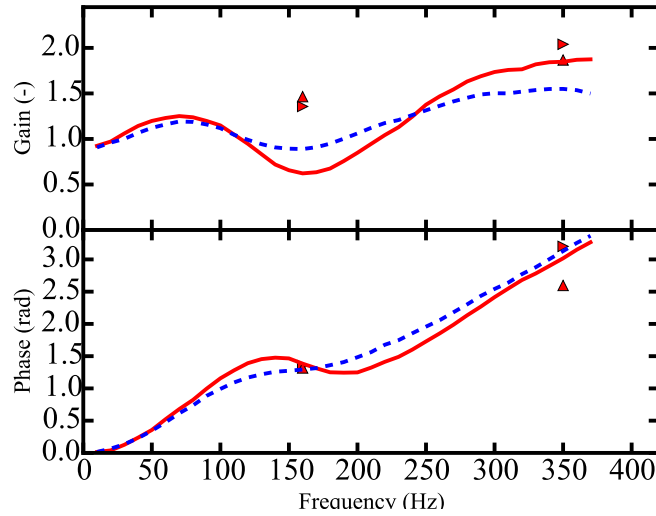


Figure 2.29: FDF gain (top) and phase lag (bottom). Experiments : $u'/\bar{u} = 0.09$ (red solid line), $u'/\bar{u} = 0.17$ (blue dashed lines). Simulations : $u'/\bar{u} = 0.09$ (red items). Upward oriented triangles: refined mesh with 395 million elements. Rightward oriented triangles: original mesh with 49 million elements.

2.4.6.2 Scenario B: impact of the subgrid scale flame wrinkling model

Subgrid scale flame wrinkling directly alters the effective propagation speed of the turbulent flame and may therefore influence the quality of the FDF prediction. In the present formulation, uncertainties in flame wrinkling modeling

are mainly concentrated in the estimation of the ad-hoc β parameter of the Charlette model (Charlette et al. (2002c)) given by:

$$\Xi_{\Delta} = \left(\frac{\Delta}{\delta_l^0} \right)^{\beta} \quad (2.8)$$

where Δ is the spatial filter width and δ_l^0 the laminar flame thickness. In the present simulations, the efficiency function Ξ_{Δ} reaches 2.83. Assuming the saturated form of the Charlette model, changing the β value leads to changes of the turbulent flame speed S_T as follows:

$$\frac{S_T^{\beta+\Delta\beta}}{S_T^{\beta}} = \left(\frac{\Delta}{\delta_l^0} \right)^{\Delta\beta} \quad (2.9)$$

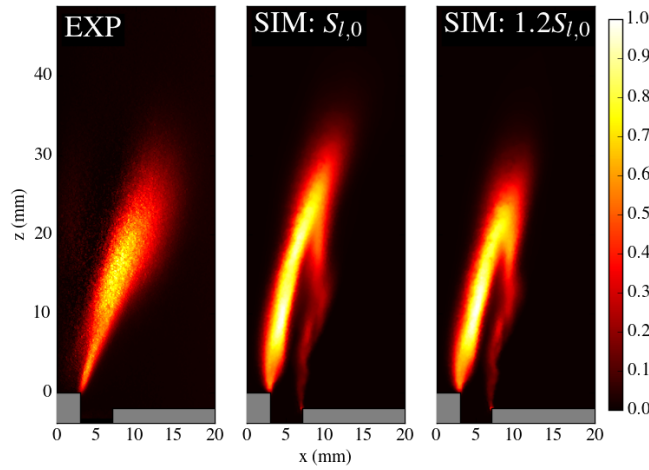


Figure 2.30: Comparison of the measured OH^* signal and simulated heat release rate distributions without acoustic forcing. Left: experiments. Middle: simulations with $\beta = 0.5$. Right: simulations with $\beta = 0.6$.

Figure 2.30 compares the flame shapes calculated for $\beta = 0.5$ and $\beta = 0.6$ with the experimental data in the absence of external forcing. Increasing β to 0.6 corresponds to an increase of 20% of $S_{l,0}$. According to Eq. (2.9), with $\Delta = 3.5$ mm and $\delta_l^0 = 0.44$ mm, this corresponds to an increase of S_T approximately equal to 23%. As expected, the flame brush is shorter in Fig. 2.30 with an increased turbulent flame speed for $\beta = 0.6$. The distribution of volumetric heat release rate now also better matches the OH^* distribution in the experiments. The main difference between experiments and these new simulations is now related to the thin residual reaction layer in the outer shear layer of the swirling jet, which is absent in the OH^* experiment, but is still present in the simulated heat release distribution.

This new numerical solution is retained to assess the influence of the β parameter on the flame response to a flow modulation at $f = 160$ Hz and $u'/\bar{u} = 0.17$ (case FT-160-17 in Tab. 2.2). This case is chosen because the largest differences with experiments are observed for the FDF gain at $f = 160$ Hz. The same procedure is applied for the flow modulation, the only change being the increase of β from 0.5 to 0.6. As shown in Fig. 2.31, the calculated FDF gain with $\beta = 0.6$ is not improved in any way with respect to the experimental data and to the previous simulations made with $\beta = 0.5$.

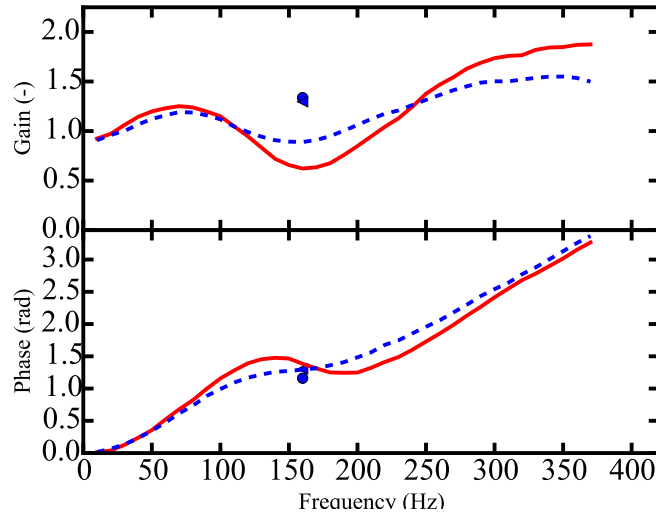


Figure 2.31: FDF gain (top) and phase bottom. Experiments : $u'/\bar{u} = 0.09$ (red solid line), $u'/\bar{u} = 0.17$ (blue dashed lines). Simulations : $u'/\bar{u} = 0.17$ (blue items). Triangles: $\beta = 0.5$. Circles: $\beta = 0.6$.

This test shows that the β parameter cannot explain the discrepancy of the FDF gain observed at $f = 160$ Hz between experiments and simulations. The flame dynamics is, for this configuration, not very sensitive to the subgrid scale flame modeling. As Ξ decreases with mesh refinement, this conclusion is somehow consistent with scenario A, where it has been shown that results are not very sensitive to the grid size. This result also reveals that despite the flame length is better reproduced by LES for the unforced case, the flame response observed in the experiments is still not recovered. This means that the role of the residual reaction rate observed in the simulations for $\beta = 0.5$ or $\beta = 0.6$ in the outer shear layer of the swirling flow may have a major effect on the flame response to acoustic modulations and its FDF at $f = 160$ Hz.

2.4.6.3 Scenario C: influence of the strain rate on the flame response

In F-TACLES, the chemistry is tabulated from unstrained premixed laminar flames. It is assumed that the flame structure is not altered by the strain rate leading to a constant flame thickness. However, in the investigated configuration, the flame is subjected to large velocity fluctuations that stretch the flame up and down during a forcing cycle. To investigate this issue, the LES velocity fields are post-processed to estimate the resolved strain rate as follows:

$$\tilde{S} = \sqrt{2(\tilde{S}_{ij}\tilde{S}_{ij})} \text{ where } \tilde{S}_{ij} = \frac{1}{2} \left(\frac{\partial \tilde{u}_i}{\partial x_j} + \frac{\partial \tilde{u}_j}{\partial x_i} \right) \quad (2.10)$$

Note that subgrid scale strain effects are not included in this expression and Eq. (2.10) only provides an estimate of the effective strain rate acting on the flame front elements. An instantaneous view of \tilde{S} is shown at the left in Fig. 2.32 for an excitation at $f = 350$ Hz and $u'/\bar{u} = 0.09$. The corresponding temperature field is plotted at the right in Fig. 2.32. As expected, the strain rate is high in the inner and outer shear layers of the swirling jet. As discussed in [Mercier et al. \(2016b\)](#) and the previous analysis of the simulations in steady conditions, simulations predict a thin residual reaction zone in the outer shear layer of the swirling jet, which is not observed in the OH* light signal measured in the experiments. This region is also characterized by large heat losses ([Guiberti et al. \(2015b\)](#)). This is highlighted by the temperature field in Fig. 2.32, where the burnt gases are cooled down to 800 K and the fresh gases from the swirling reactant stream meet the cooled burnt gases that are recirculating in the corner of the combustor.

The combined effects of heat losses and strain rates are not included in the LES model used in this work and may explain the differences observed between simulations and experiments ([Klarmann et al. \(2016\)](#); [Tay Wo Chong et al. \(2016\)](#); [Tay Wo Chong et al. \(2017\)](#)). One possibility would be to include these effects in the tabulated chemistry. One can mention the work presented in [Chong et al. \(2009\)](#) or [Breda et al. \(2018\)](#), where the effect of heat losses and strain rate is taken into account in the tabulation process. This raised however critical modeling issues out of the scope of the present study such as the estimation of unresolved strain rate in the LES. The following simplified approach is therefore preferred to analyze the results.

The following 1D numerical analysis is undertaken. A collection of 1D strained premixed flames is computed with the REGATH solver ([Franzelli et al. \(2013\)](#)). The simulated configuration consists in a 1D steady isobaric laminar premixed flame stabilized between two counter-flows. A CH₄/H₂/air mixture is injected from one side at the equivalence ratio $\phi = 0.70$ and temperature $T_f = 298$ K. The opposite injector is fed with burnt gases of the same mixture for which a given enthalpy defect Δh is applied. For that purpose, the equilibrium composition of the burnt gases at an imposed temperature is computed first for

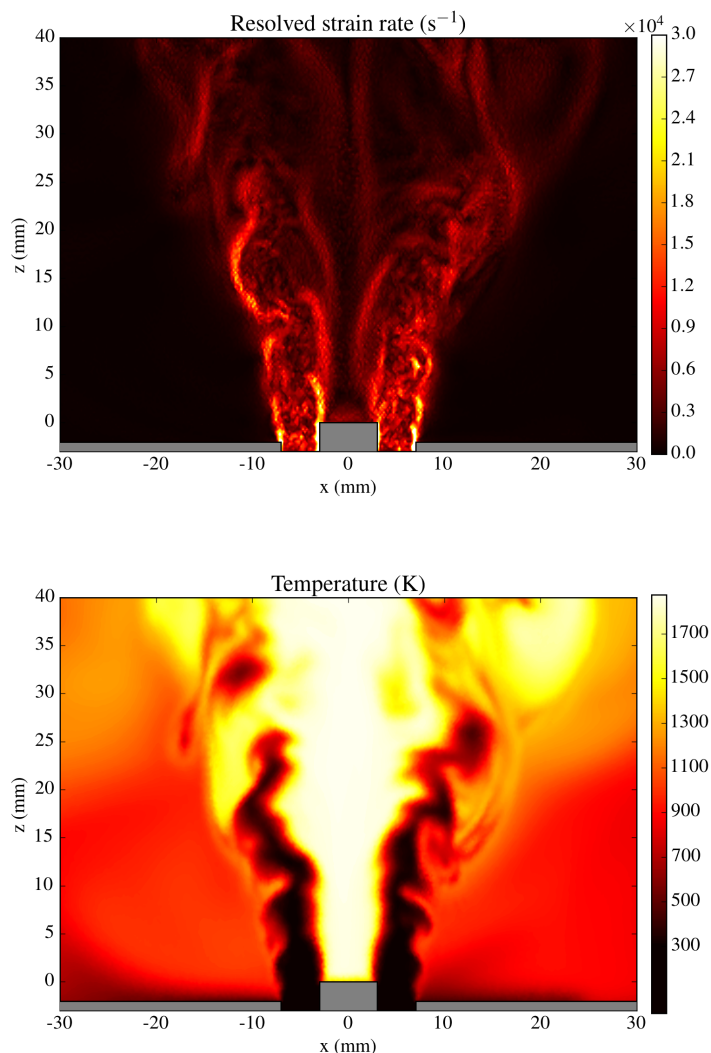


Figure 2.32: Instantaneous LES resolved strain rate (left) and temperature (right) for the case FT-350-09.

the CH₄/H₂/air mixture composition injected in the system. The imposed burnt gas temperature is then varied between the adiabatic flame temperature reached in the absence of heat losses and the minimum temperature set here to 800 K approximately. This latter temperature roughly corresponds to the temperature of the burnt gases in the coldest zones of the combustor found in Fig. 2.32. The critical strain rate leading to flame quenching is then extracted from the 1D simulations as the strain rate for which the laminar flame speed of the non-adiabatic strained flame drops below 5 cm.s⁻¹. The results are plotted in Fig. 2.33 as a black line, delimiting two zones. For a given enthalpy loss,

combustion persists below a specific strain rate threshold level. Increasing the strain rate beyond this value results in flame extinction.

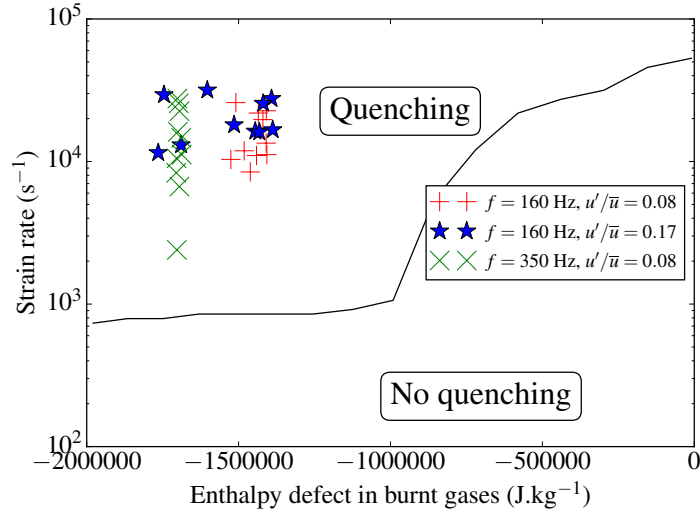


Figure 2.33: Black line: critical strain rate as a function of the enthalpy defect delimiting the quenching and no quenching zones. Symbols: resolved strain rate at $z = 0$ mm and at the point of maximum heat release in the outer shear layer of the swirling jet as a function of the enthalpy defect in the burnt gases at $x = 10$ mm and $z = 0$ mm.

It is worth examining the LES calculations and see where the results are located in this diagram. The cases FT-160-09, FT-160-17, FT-350-09 are selected. Resolved (or filtered) value of the strain rate is picked in the LES calculations at $z = 0$ mm corresponding to the top of the central bluff-body and at the point of maximum heat release in the outer shear layer of the swirling jet. This particular location is selected because this is where the highest strain rates are observed in the outer shear layer of the jet in Fig. 2.33. The value of the enthalpy defect δh needs also to be estimated and is taken here in the burnt gases at $x = 10$ mm and $z = 0$ mm. This region is again selected in the outer shear layer of the swirling jet at the same altitude z as for the estimation of the strain rate, but in the cold burnt gases as shown in Fig. 2.33. The values for the strain rate and enthalpy defect are extracted from LES for twenty regularly distributed instants, each separated by $T/10$, where $T = 1/f$ is the oscillation period of the forcing signal. This duration covers two full cycles of excitation. These data are then added to Fig. 2.33 for each case explored.

Figure 2.33 clearly shows that, even by neglecting unresolved (or subfilter) strain rate contribution, the flame should be quenched in the outer shear layer of the swirling jet at $z = 0$ mm for the three cases explored and all instants

considered in the forcing cycle. The flame cannot sustain such levels of strain rate for these levels of enthalpy defect. One may also note that the values found lie quite far from the boundary of the quenched zone, which has been calculated with a laminar counter-flow configuration. Slight variations of the enthalpy defect or strain rate estimates due to the region of interest in the outer reaction layer where these values are probed and effects of turbulence will thus not affect the conclusion. Therefore, the limitations of the combustion modeling may explain the remaining reaction zone in the outer shear layer of the swirling jet.

This is confirmed by a supplementary post-processing of the numerical results which demonstrates the combined effects of strain and enthalpy defect on the turbulent flame topology. By using laminar flame data from Fig. 2.33, isolines of the critical strain rate associated to a given enthalpy defect are indicated in Fig. 2.34, at one selected time instant of case FT-350-09. This post-processing avoids the need to model unresolved strain rate contributions. Being superimposed to the field of heat released, these isolines evidence regions where the strain rate would lead to flame quenching. Even at moderate levels of strain rate (as low as 600 s^{-1}), flame quenching by strain would occur primarily in the outer flame region. At the opposite, the effect of strain rate on the inner flame region is not significant, as the enthalpy defect in this region is small compared to the one in the outer recirculation zone.

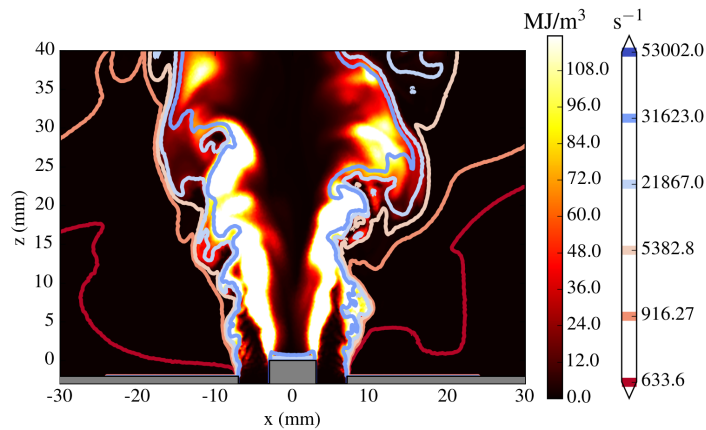


Figure 2.34: Instantaneous heat release rate field for case FT-350-09 with superimposed isolines corresponding to the critical strain rate for a given enthalpy defect (extracted from Fig. 2.33).

The response of this additional reaction layer is considered in the computation of the FDF gain in the numerical results. The differences in flame response between $f = 160$ and 350 Hz result in a variable additional gain due to the response of the outer reaction zone to acoustic forcing. At the forcing frequency $f = 160$ Hz and $u'/\bar{u} = 0.16$, the flame envelope varies greatly in height over an excitation cycle (Fig. 2.22), the outer reaction zone changing accordingly. At $f = 350$ Hz and $u'/\bar{u} = 0.16$, the flame envelope is less altered by the forcing with a weakly evolving outer reaction zone. Therefore, the additional FDF gain is more noticeable at $f = 160$ Hz than at $f = 350$ Hz. The FDF data in Fig. 2.18 corroborate this scenario.

2.4.7 Conclusion on the simulations in pulsed conditions

Comparisons between experiments and numerical simulations for the FDF of a swirl-stabilized premixed flame have been carried out. The FDF phase shift between velocity and heat release rate fluctuations integrated over the flame volume is fairly well reproduced by the simulations for the two modulation levels $u'/\bar{u} = 0.09$ and 0.17 examined. However, differences appear for the FDF gain at both forcing levels. Detailed examinations of the flame response at two forcing frequencies $f = 160$ Hz and $f = 350$ Hz indicate differences in the way the volumetric heat release is distributed over the flame raising questions regarding the modeling choices. An analysis of the dynamics of the turbulent flame brush envelope to the acoustic excitation reveals a complex response that depends on the forcing conditions. The current turbulent combustion formalism (F-TACLES) makes the assumption that the flame stays in the regime of unstretched flamelets with constant subgrid flame wrinkling parameters. These two hypotheses need to be reconsidered for the pulsed flows analyzed in this study. Several scenarios are explored and show that the main issue that should be taken into account in the numerical modeling approach is the combined effects of strain rate and enthalpy defect on flame structure. This conclusion is not specifically limited to the F-TACLES formalism. A similar approach with TFLES would have probably given the same results.

Chapter 3

Application of the F-TACLES model to the CORIA spray burner

Contents

2.1	Objectives of this chapter	32
2.2	Experimental setup	33
2.2.1	Geometry	33
2.2.2	Operating conditions	34
2.2.3	Velocity measurements	34
2.2.4	Flame position measurements	35
2.2.5	Wall temperature measurements	35
2.2.6	Diagnostics in pulsed conditions	38
2.3	Simulations in steady conditions	38
2.3.1	Motivations	38
2.3.2	Numerical setup	39
2.3.3	Initialization of the non-adiabatic LES	40
2.3.4	Simulations performed	40
2.3.5	Analysis of the results	41
2.3.6	Conclusions on the simulations in steady conditions	52
2.4	Simulations in pulsed conditions	54
2.4.1	Motivations	54
2.4.2	Numerical setup	54
2.4.3	Flow forcing	54
2.4.4	Flame Describing Function	55
2.4.5	Results	58
2.4.6	Analysis	71
2.4.7	Conclusion on the simulations in pulsed conditions	80

This chapter aims to address the ability of the F-TACLES model to retrieve the correct turbulent spray flame structure of a liquid n-heptane/air laboratory jet burner. LES results are compared against experimental measurements in terms of heat release, spray properties and flow characteristics.

3.1 Context of the study and objectives

3.1.1 General context

Aeronautical engines are operated with liquid fuel directly injected in the combustor. Two-phase combustion is extremely difficult to understand as it requires a simultaneous access to a large number of highly-correlated thermo-physical properties (Jenny et al. (2012)). The Large Eddy Simulation (LES) approach represents nowadays the best compromise between cost and accuracy to simulate complex reactive flows. Despite recent impressive progress, many efforts are still performed by the combustion modeling community to develop and validate LES for turbulent spray flame computational strategies (Jones et al. (2017); Jones et al. (2014); Shum-Kivan et al. (2016); Franzelli et al. (2016); Heye et al. (2015)). Model comparison against accurate experimental data is crucial to properly assess the ability of numerical strategies to recover the turbulent spray flame properties. It includes the flow velocity, the droplets characteristics and the flame structure.

3.1.2 State of the art on the simulations of the present experiment

The experiment presented in Sec. 3.2 has been previously studied numerically by Shum-Kivan et al. (2016) by using a global two-step chemistry (Paulhiac (2015)) combined with the TFLES approach (Legier et al. (2000); Colin et al. (2000)). The flow velocity, as well as the droplet size distribution and velocity have been well predicted. However, an underestimation of the flame lift-off has been observed, which is probably due to the limitation of the reduced two-step chemistry model. Other approaches were tested on this configuration, for example with the stochastic fields method (Gallot Lavalée et al. (2017)).

3.1.3 Objectives

This chapter presents the first application of the filtered tabulated chemistry model F-TACLES in a turbulent spray combustion configuration. The retained configuration is a new well-instrumented experimental turbulent spray flame that has been designed and operated at CORIA laboratory (Verdier et al. (2016)). Simulations are conducted on two different grids: a coarse one, representative of meshing constraints encountered in industrial applications, and a fine one for which the size of the cells within the reaction zones has been cho-

sen so that both flame thickness and subgrid flame wrinkling are fully resolved. The fine grid simulation will challenge the ability of the chemistry tabulation to retrieve the spray flame structure (Franzelli et al. (2013)), whereas the coarse LES will also test the suitability of F-TACLES to capture unresolved interactions between the spray flame and turbulence. Experimental and numerical data are compared and analyzed in terms of flame structure, gas velocity, spray diameter distribution and velocity and spray temperature.

3.2 Experimental configuration

The experimental configuration is an n-heptane spray/air jet burner experimented at CORIA by Verdier et al. (2016). It is operated at atmospheric pressure and 298 K. The air injection is performed from a plenum to a non-swirling injector in order to generate the co-flow where the liquid fuel is atomized. The air mass flow rate is $6 \text{ g}\cdot\text{s}^{-1}$. The injection of liquid n-heptane comes from a simplex injector that generates a hollow cone with a mass flow rate of $0.28 \text{ g}\cdot\text{s}^{-1}$. A general view of the configuration geometry is shown in Fig. 3.1.

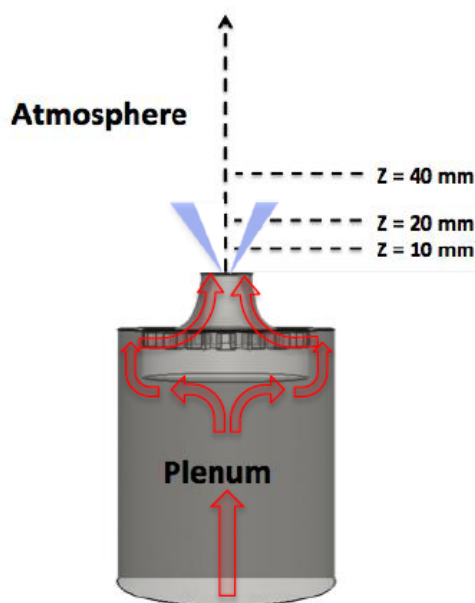


Figure 3.1: *Experimental setup. Air path in red, spray injection in blue. From Shum-Kwan et al. (2016).*

Several experimental measurements have been performed. The Phase Doppler Anemometry (PDA) gives access to the gas and spray velocity and the spray diameter distribution. The flame structure is determined thanks to OH Planar Laser Induced Fluorescence (PLIF). Finally, the Global Rainbow Technique (GRT) (Saengkaew et al. (2013)) provides the spray temperature, which is

rarely available in experimental diagnostics. Further details about these measurements can be found in [Verdier et al. \(2016\)](#).

The flame structure shown in Fig. 3.2 by the OH-PLIF measurement exhibits a double branch. The inner flame front corresponds to a premixed flame where the small droplets are vaporized rapidly and the high levels of turbulence favor the air/fuel mixing, forming a highly wrinkled flame front. The outer flame front is closer to a diffusion flame, where air located outside reacts with rich hot gases still containing a large amount of unburnt gaseous n-heptane. OH-PLIF also shows that the flame is lifted from the injection plane.

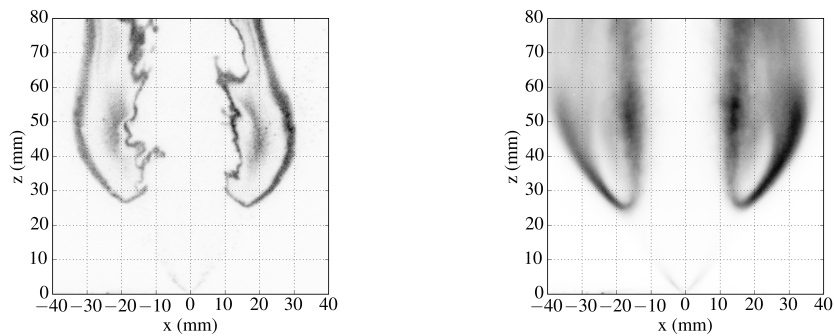


Figure 3.2: *Instantaneous (left) and mean (right) OH-PLIF shots, from [Verdier et al. \(2016\)](#).*

3.3 Numerical Setup

3.3.1 General parameters

The YALES2 flow solver, presented in Chapter 1, is used for this configuration. The full modeling details are also presented in Chapter 1. The subgrid scale Reynolds stresses are closed with the SIGMA model ([Nicoud et al. \(2011a\)](#)), as in Chapter 2.

The computational domain defined in [Shum-Kivan et al. \(2016\)](#) is also used in this thesis.

The injected spray is polydispersed in size, following a two-parameter Rosin-Rammler distribution ([González-Tello et al. \(2008\)](#)) with a Sauter Mean Diameter (SMD) d_{32} of 31 microns and a spread parameter q of 2.3. The form of the injected spray is obtained with the Liquid Injection for Swirl Atomizers (LISA) formalism ([Guedot \(2015\)](#)) to obtain the desired swirled hollow cone spray. Parameters of droplet distribution in size are empirically adjusted to fit measurements at 10 mm above the burner exit as shown in Figure 3.3.

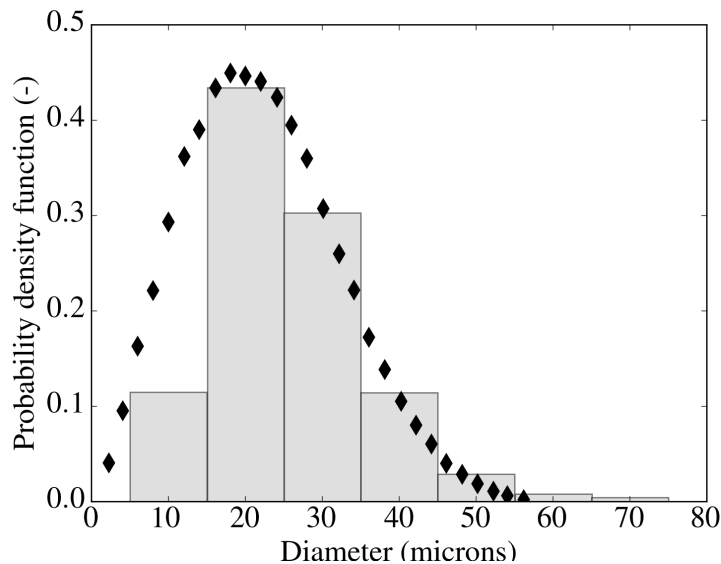


Figure 3.3: Particle size distribution. Experiments: grey bars, Rosin-Rammler distribution: black diamonds.

3.3.2 Application of the F-TACLES table generation process to n-heptane

In order to simulate the KIAI burner, the generation of a F-TACLES table is necessary. The KIAI burner is operated with n-heptane, a fuel that has never been considered for the generation of a F-TACLES table.

3.3.2.1 Chemical table generation

The chemical table is built from a library of laminar freely propagating n-heptane/air premixed flamelet computed with the REGATH code (Darabiha (1992)) and by using the POLIMI 106 detailed mechanism made of 106 species and 1738 reactions (Ranzi et al. (2014)).

A comparison for the laminar flame speed between this mechanism, experiments and two other is shown in Fig. 3.4.

3.3.2.2 Filtered look-up table generation

In order to generate a look-up table for the simulations, the CAFE code is used to generate a table containing the filtered flamelets.

The flamelets are filtered using a filter width equal to 0 or 3.5 mm, depending on the case, and stored in a table that contains 200 points in the progress variable direction and 151 points in the mixture fraction direction.

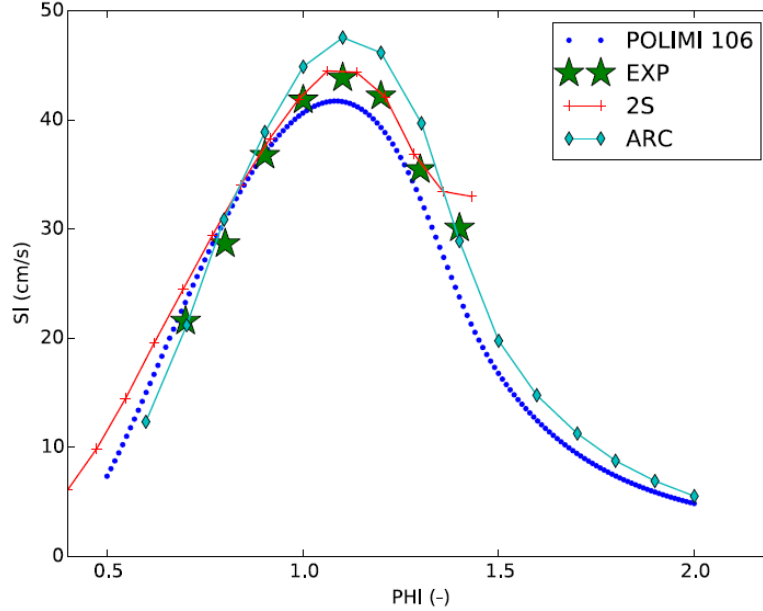


Figure 3.4: Comparison of laminar flame speed between experimental data from *Kumar et al. (2007)* (green stars), a two-step reduced mechanism (red line), an analytically reduced mechanism (cyan line), both used in *Shum-Kivan et al. (2016)* and the POLIMI 106 detailed mechanism from *Ranzi et al. (2014)* used in this work.

3.3.3 Simulations presented

Two cases (A and B) are presented in this chapter. Case A features an unstructured mesh composed of 53 million elements and 10.5 million nodes, identical to *Shum-Kivan et al. (2016)*. Case B is performed on a coarser mesh of 17 million elements and 3.5 million nodes. Case A is sufficiently resolved so that artificial broadening of the flame front is not required. Indeed, the mesh size in the reaction zone is less than 0.1 mm, whereas the minimum possible flame thickness, given by a laminar stoichiometric premixed freely propagating flames, is about 0.5 mm. With 5 nodes across the flame front, the resolution of the chemical layer is therefore sufficient to ensure the proper propagation of the flame without introducing numerical artifact (*Fiorina et al. (2010a)*). The flame front resolution in Case B is more representative of LES conditions encountered in industrial configurations. The mesh size in the reaction zone, around 0.5 mm, is not sufficient to resolve the flame front.

For case A simulation, as the flame is fully resolved on the LES mesh, this look-up table is directly used to close Eq. 1.42 without being filtered ($\Delta = 0$). Consequently, by assuming flamelet regime, the flame wrinkling is also fully resolved on the LES grid and $\Xi_{\Delta} = 1$. At the opposite, the flamelets library is filtered in Case B by using a filter width $\Delta = 3.5$ mm so that the resolved

Table 3.1: *Studied cases.*

Case	A	B
Elements (million)	53	17
F-TACLES Filter size Δ (mm)	0.0	3.5
Subgrid flame wrinkling Ξ_{Δ}	1.0	Charlette et al. (2002c)

filtered flame thickness is sufficient to capture the flame consumption speed on the coarse mesh. Subgrid scale flame wrinkling is modelled as in Charlette et al. (2002c). Combustion model properties used for case A and B are summarized in Table 3.1.

3.4 Results and analysis

The two cases A and B are computed in both non-reactive and reactive configurations. Therefore, four simulations are presented in the following sections. The non-reacting cases are appended with the suffix *-NR* and the reacting ones with *-R*.

Figure 3.5 shows the positions of the profiles that are used for comparing experimental and numerical results. The temperature field of case A-R is shown in transparency to indicate the position of the flame in reacting cases.

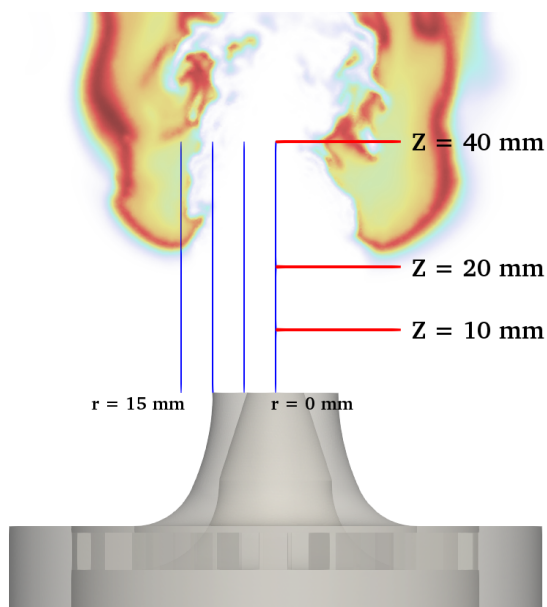


Figure 3.5: *Positions of the profiles of the experimental database. Red lines: radial profiles at $Z = 10, 20$ and 40 mm. Blue lines: axial profiles at $r = 0, 5, 10$ and 15 mm.*

3.4.1 Flow topology and gas velocity

Figures 3.6 and 3.7 show for cases A-NR and B-NR the instantaneous and mean axial velocity fields in the central vertical plane. The flow topology is very similar on average for both meshes. Several zones are identified. The injector effect is to accelerate the flow up to 30 m/s before exiting into the atmosphere. A recirculation zone appears at the exit of the injector, where the liquid injection is made. The effect of the injection of the droplets is visible in this zone, with a local increase of the axial velocity. Finally, a mixing layer appears between the fast air that exits the injector and the air at rest in the atmosphere.

The effect of the mesh is visible in the instantaneous field, where smaller vortices appear for the fine mesh.

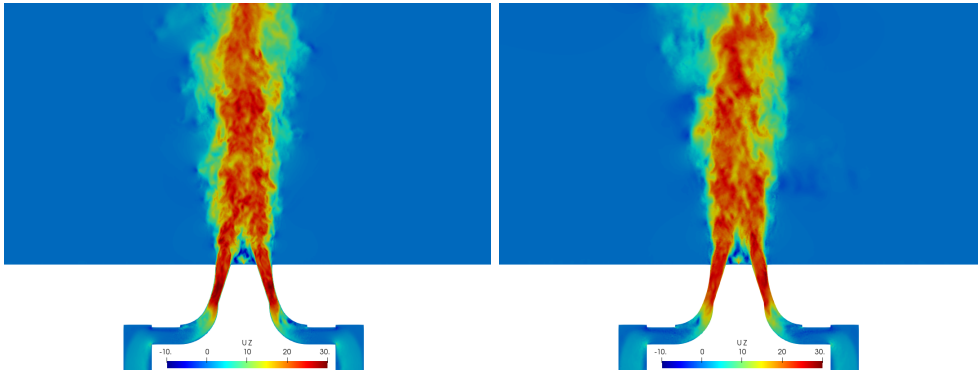


Figure 3.6: Instantaneous axial velocity fields for cases A-NR (left) and B-NR (right) in the central vertical plane.



Figure 3.7: Mean axial velocity fields for cases A-NR (left) and B-NR (right) in the central vertical plane.

Figures 3.8 and 3.9 show for cases A-R and B-R the instantaneous and mean axial velocity fields in the central vertical plane. The general flow topology is similar to non-reacting cases. The main difference is linked to the presence of

the flame, which broadens the width of the jet through thermal expansion.

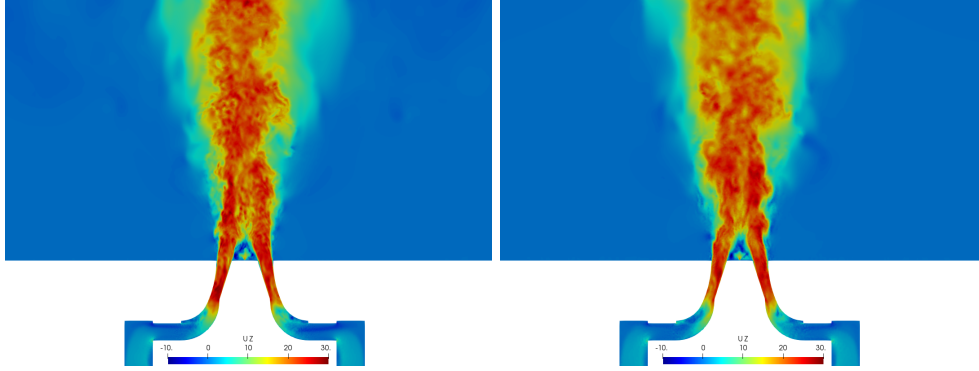


Figure 3.8: Instantaneous axial velocity fields for cases A-R (left) and B-R (right) in the central vertical plane.

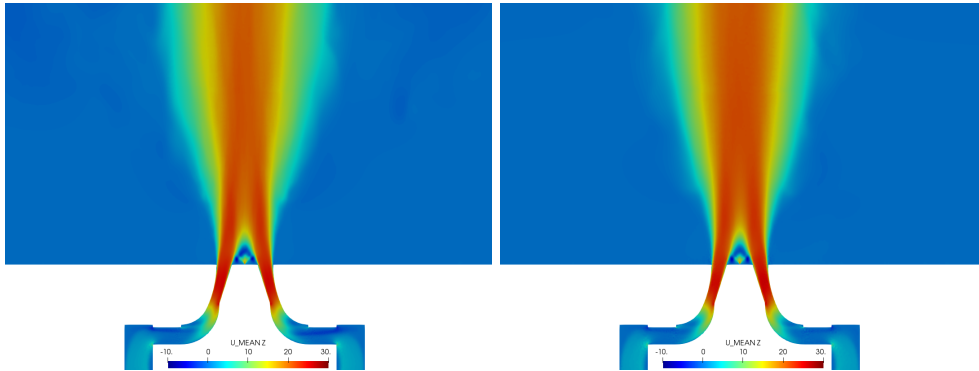


Figure 3.9: Mean axial velocity fields for cases A-R (left) and B-R (right) in the central vertical plane.

For the axial velocity component, non-reacting (left) and reacting (right) LES results are compared against the measurements at 10, 20 and 40 mm high above the burner exit in Figs. 3.10 for the mean and 3.11 for the RMS.

Both cases A and B solutions match well the experimental data, meaning that the flow statistics are well captured, even on the coarse grid.

The main difference is the underestimation of the maximal axial velocity around 10 mm above the injection plane. The origin of this discrepancy can be attributed to the resolution of the boundary layer in the injector. Indeed, a wall-law approach is chosen for this configuration and the boundary layer velocity profile is not fully resolved. A finer mesh close to the injector walls would probably improve the prediction of the peak velocity.

The effect of the thermal expansion from the flame is visible on the profiles at $Z = 40$ mm. The axial velocity in non-reacting conditions drops rapidly to 0 m/s between $r = 5$ mm and $r = 20$ mm while in reacting conditions, the axial

velocity decreases slowly between $r = 5$ mm and $r = 20$ mm.

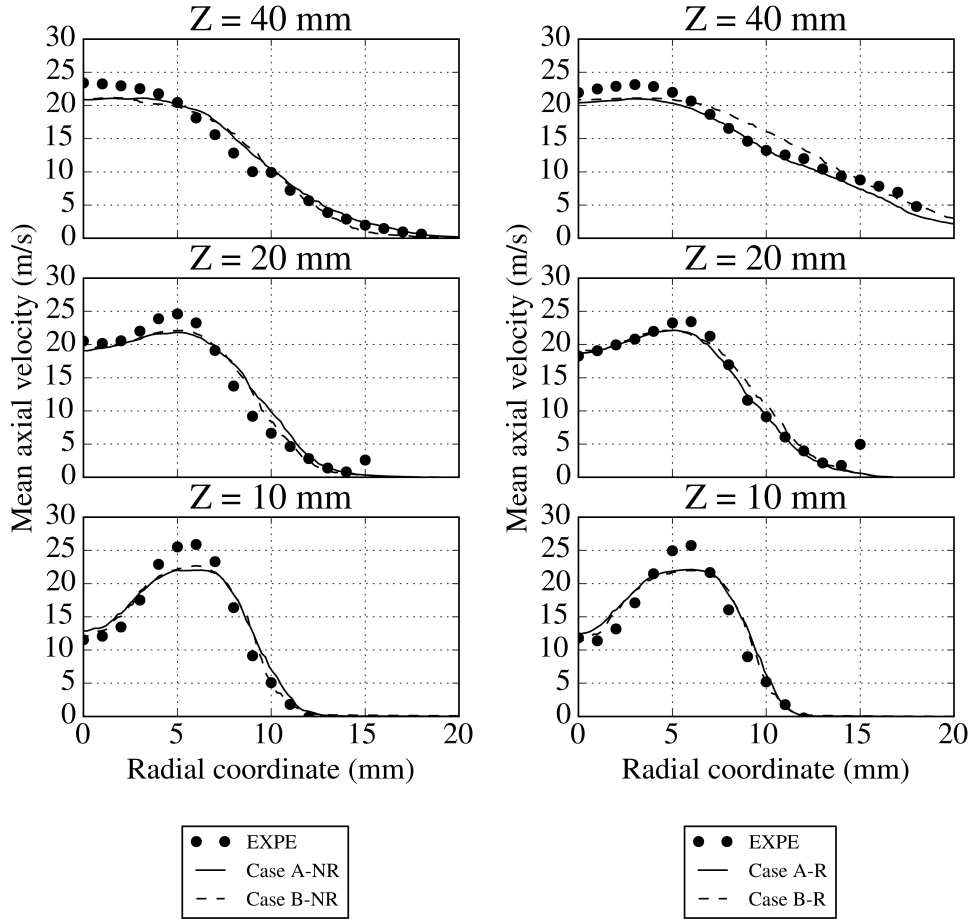


Figure 3.10: Radial profiles of mean axial velocity for non-reacting (left) and reacting case (right). Symbols: experiments, solid line: Case A, dashed line: Case B.

The RMS are correctly captured for both meshes. The effect of the mixing layers (between the recirculation zone and the main flow and between the main flow and the air at rest) is visible as the two peaks of axial velocity RMS at $Z = 10$ mm.

The results for the radial velocity component are plotted in Figs. 3.12 (mean) and 3.13 (RMS). The simulations capture the general features of the mean radial velocity profiles. However, the radial velocity is not as well predicted as the axial velocity. The absolute value of radial velocity (≈ 3 m/s) is much smaller than the axial velocity one (≈ 30 m/s). This difference between the two velocity components can explain the discrepancy for the radial velocity. Indeed, the precision of both simulations and experiments may not be enough for such small velocity value.

The RMS are on the contrary rather well predicted by the simulations. At

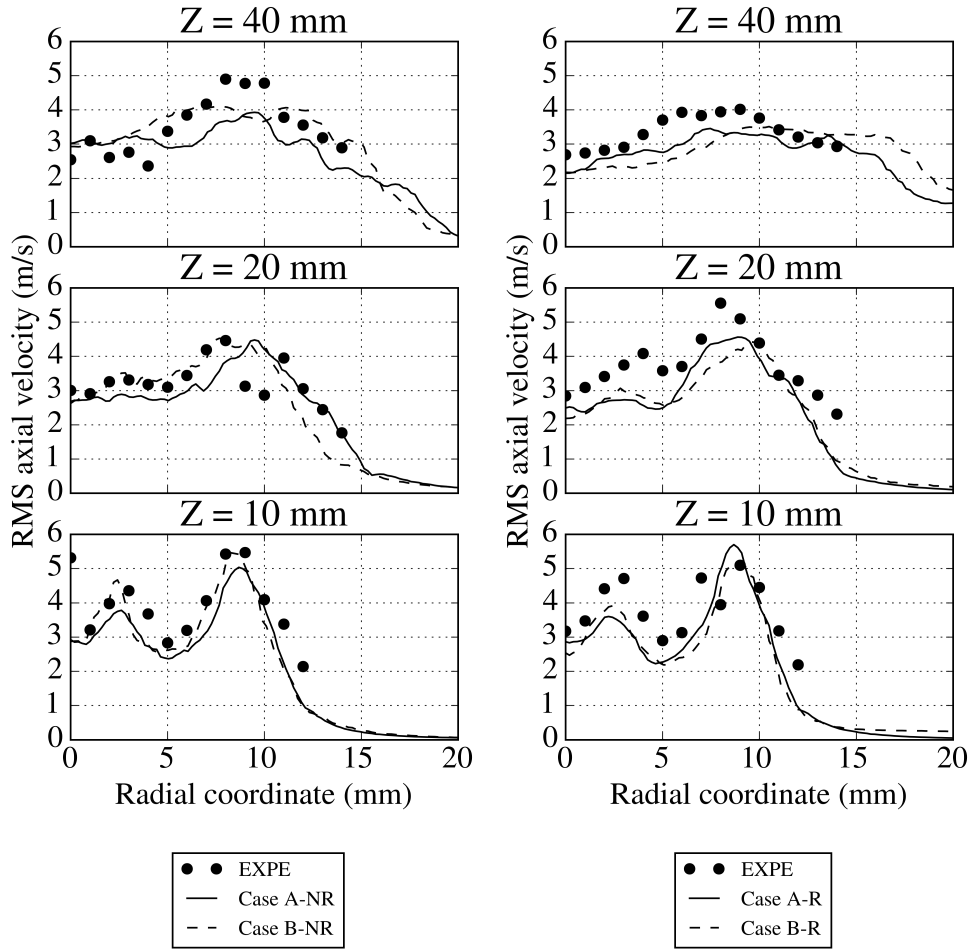


Figure 3.11: Radial profiles of axial velocity RMS for non-reacting (left) and reacting case (right). Symbols: experiments, solid line: Case A, dashed line: Case B.

$Z = 10$ mm, the peaks at $r = 0$ and 10 are correctly located in the simulations. The general flow topology prediction by the simulations is satisfactory, for both meshes and for non-reacting and reacting conditions. The minor discrepancies can be explained by under-resolved meshes in certain regions.

3.4.2 Flame topology

Figure 3.14 (left column) shows an instantaneous normalized OH mass fraction field for each simulated case and an instantaneous snapshot of OH-PLIF measurements to compare qualitatively the instantaneous flame structure. The flame structure is challenging to compute because the flame structure as well as the stabilization process are very sensitive to finite-rate chemistry effects. The inner flame front, characterized by a high resolved wrinkling, is correctly

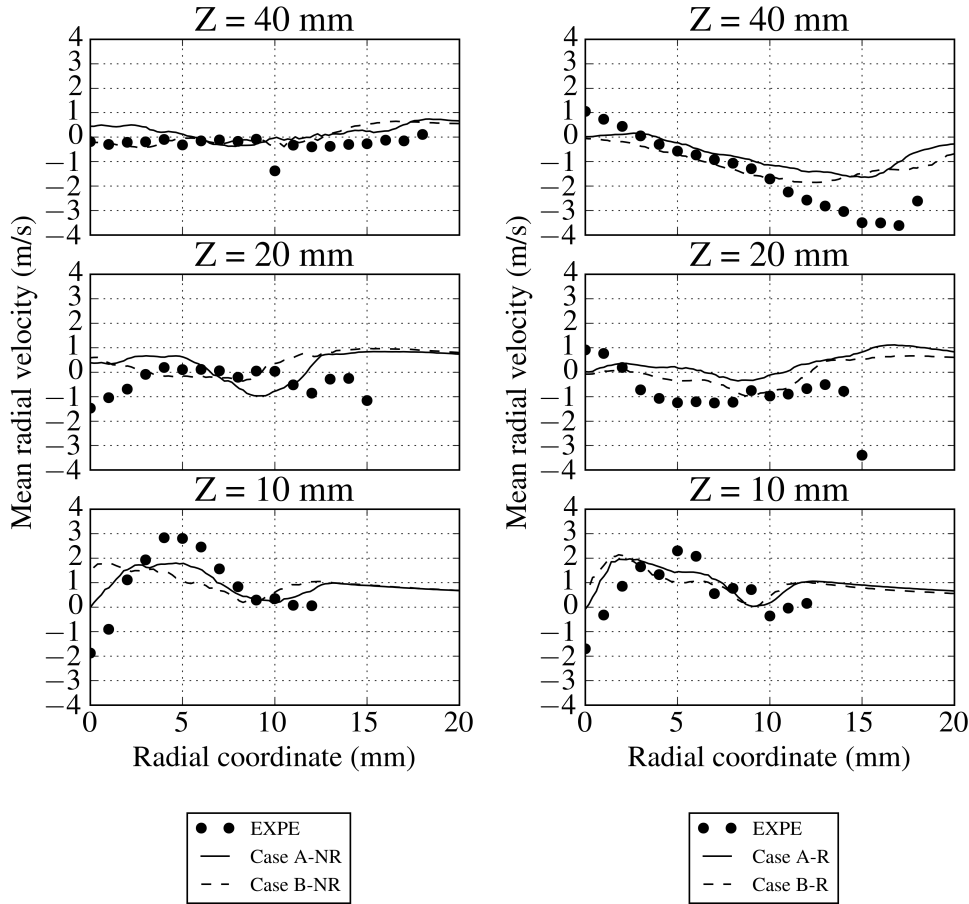


Figure 3.12: Radial profiles of mean radial velocity for non-reacting (left) and reacting case (right). Symbols: experiments, solid line: Case A, dashed line: Case B.

reproduced. The outer diffusion flame observed in the experiments, featuring a large and unwrinkled reaction zone, is also present.

Figure 3.14 (right column) shows the mean normalized OH mass fraction field for each simulated case and the mean shot of OH-PLIF measurements to compare qualitatively the mean flame structure.

The mean inner flame front position is well captured by the simulations and is located at $|x| \approx 15\text{mm}$ up to $z = 80\text{mm}$.

In the mean OH-PLIF shot, the outer flame front extends up to $|x| = 40\text{mm}$. This comparison shows that even if the instantaneous flame structure seems qualitatively well retrieved by the simulations, the mean outer flame front position is not perfectly captured by the simulations. Indeed, both simulations on coarse and fine grids predict that the outer flame front extends up to $|x| \approx 30\text{mm}$ and quickly merges with the inner flame front for $z > 50\text{mm}$.

The inner flame front is located in a region of high velocity while the outer

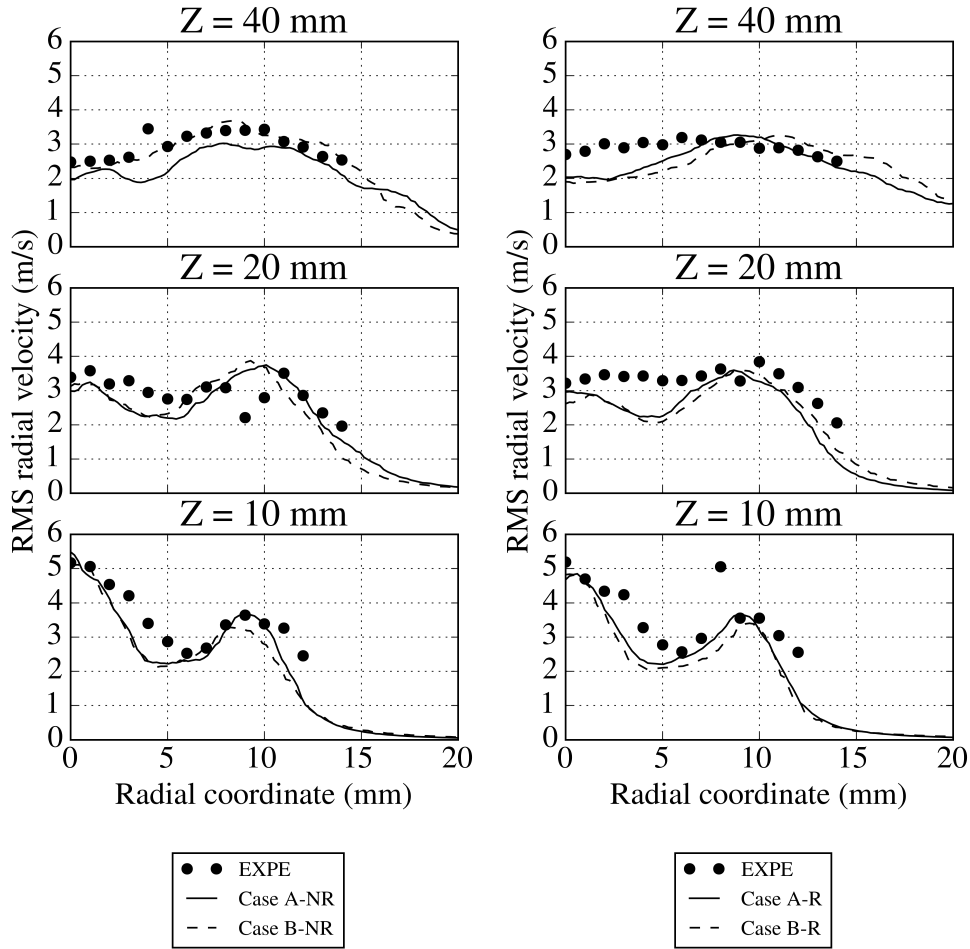


Figure 3.13: Radial profiles of radial velocity RMS for non-reacting (left) and reacting case (right). Symbols: experiments, solid line: Case A, dashed line: Case B.

one is located in a low velocity region, as shown in Fig. 3.10. Therefore, the amount of flow-through times simulated differs between the two flame fronts. The statistics are well converged for the inner flame front, because the velocity is much higher. On the contrary, as the velocity in the outer flame front is low, the simulated physical time (tens of milliseconds) may not be sufficient to capture the dynamics of the outer flame front that was found in the experiments, where the OH-PLIF shots are averaged over a much longer period of time (several seconds).

The lift-off of the flame is a critical aspect of this flame. In order to assess the lift-off height in the simulations, Figs. 3.15 and 3.16 show a contour of temperature in transparency for both meshes. These views demonstrate that the lift-off height is fairly constant for both meshes.

Figures 3.17 and 3.18 show a clip in the central vertical plane of the contour of

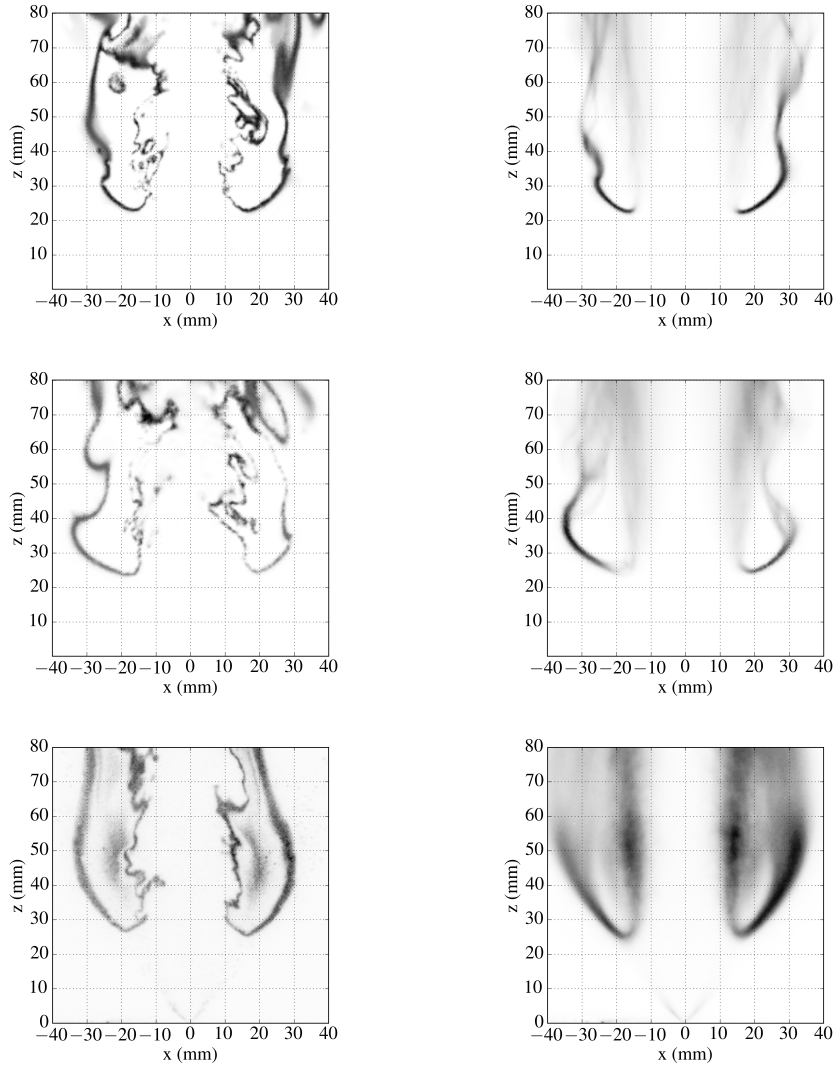


Figure 3.14: Normalized OH mass fraction (Case A: top, case B: middle). Experiments (bottom): OH-PLIF shot, from Verdier et al. (2016). Left column: instantaneous signal, right column: mean signal.

temperature presented above. The influence of the mesh is visible in Fig. 3.17 where the flame wrinkling is more resolved in case A (fine mesh) than in case B (coarse mesh).

The lift-off of the flame is estimated in the simulations as the lowest height where the mean temperature is equal to 1300 K. This height depends on the angular position since the flame is not perfectly axisymmetric and therefore the final height given below is the average one with an indication of the variation. In the experiment, the lift-off is estimated visually on the mean OH-PLIF shot

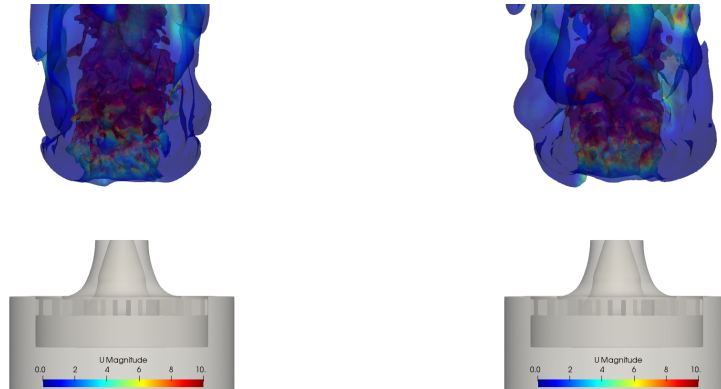


Figure 3.15: Contour of instantaneous temperature $T_{inst} = 1300\text{ K}$ colored by the instantaneous velocity magnitude for cases A-R (left) and B-R (right).

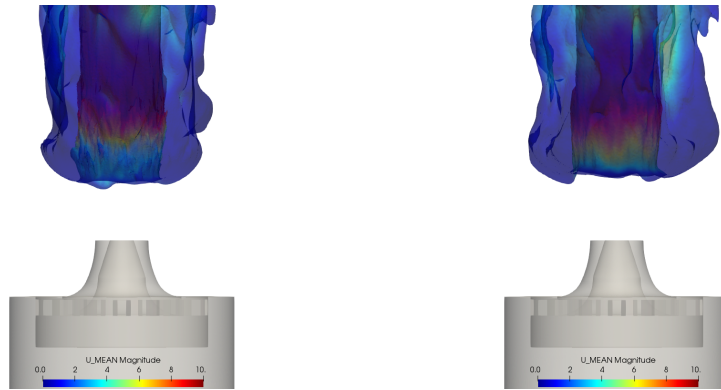


Figure 3.16: Contour of mean temperature $T_{mean} = 1300\text{ K}$ colored by the mean velocity magnitude for cases A-R (left) and B-R (right).

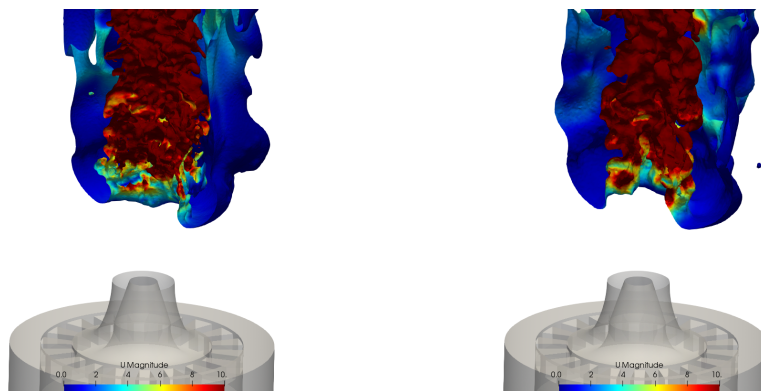


Figure 3.17: Contour of instantaneous temperature $T_{inst} = 1300\text{ K}$ colored by the instantaneous velocity magnitude for cases A-R (left) and B-R (right).

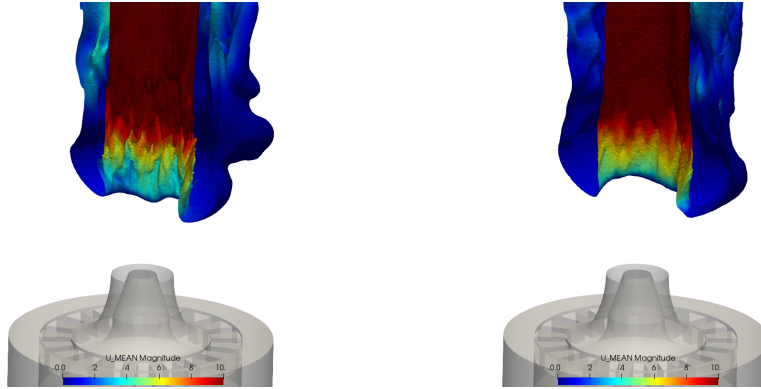


Figure 3.18: Contour of mean temperature $T_{mean} = 1300$ K colored by the mean velocity magnitude for cases A-R (left) and B-R (right).

in Fig. 3.2.

The experimental value is 25 ± 3 mm while case A recovers a lift-off of 22 ± 1 mm and case B a lift-off of 24 ± 1 mm. Comparison between case A and B shows that the F-TACLES approach is able to model fairly well unresolved flame turbulence interaction on mesh representative of practical industrial conditions. Previously published computations with a global two-step mechanism (Shum-Kivan et al. (2016)) underpredict the flame lift-off h_{lo} by approximately 20%. Figure 3.14 shows that the flame position and structure is here well retrieved in both LES by qualitative comparison with OH-PLIF snapshot. Moreover, simulations conducted with a reduced analytical scheme involving 24 transported species, 32 quasi-steady state species and 217 reactions did not succeed to retrieve the flame lift-off, with a CPU cost 10 times higher (Shum-Kivan (2017)).

With the F-TACLES tabulated chemistry method, the flame lift-off height is recovered for both meshes and for a CPU cost even lower than the global mechanism since there are only two transport equations for the chemistry (the progress variable and the mixture fraction) compared to six transported species. The good performances of F-TACLES are attributed to its ability to retrieve the flame propagation speed in turbulent stratified mixture (Auzillon et al. (2012a)), even on coarse grid where the flame front is not fully resolved.

The edge flame propagation is not influenced by the diffusion branch. Even if error are observed in the diffusion flame regions by the F-TACLES model (Auzillon et al. (2012a)), this will not influence the lift-off height in this configuration. Table 3.2 compares against experiments the flame lift-off height predicted by global, analytical and tabulated chemistry on the investigated spray flame configuration. The CPU cost required to obtain reactive flow statistics, normalized by the global scheme computation, is also indicated.

Table 3.2: Comparison between chemistry modeling strategies.

	Experiment	Two-steps scheme [3]	Analytical scheme [3]	F-TACLES (case A)	F-TACLES (case B)
Grid	-	fine	fine	fine	coarse
Lift-off (mm)	25±3	20±1	20±1	22±1	24±1
Estimated relative CPU cost	-	1	10	0.5	0.1

3.4.3 Spray diameter

Figures 3.19 and 3.20 show the particles in the central vertical plane colored by their diameter for the cold and reacting cases respectively. For both conditions, the distribution of diameter is similar. The smaller droplets are located in the central part of the flow while the larger droplets are located on the outer part of the spray. The influence of the flame in Fig. 3.20 is the low density of particles above $z = 20$ mm, especially on the outer region.

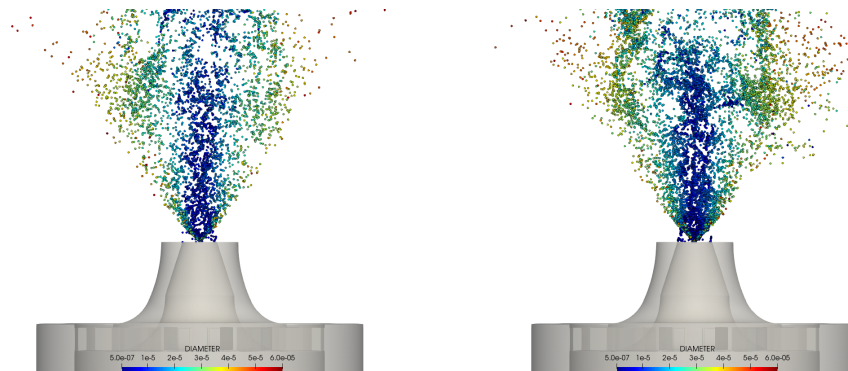


Figure 3.19: Droplet diameter for cases A-NR (left) and B-NR (right).

Figure 3.21 compares at 10, 20 and 40 mm high above the burner exit, the mean spray diameter as a function of the radial coordinates for the cold and reacting cases, respectively. The LES results show a correct evolution of the radial stratification in droplet diameter for both cases A and B. The small droplets follow the streamlines because of their small Stokes number (see Eq. 1.11) and are therefore located at the center of the flow. The larger droplets, characterized by a higher Stokes number, follow a ballistic trajectory and are located on the outer rim of the spray, as a result of the hollow cone injection. The profiles are similar in both reacting and non-reacting cases between 0 and 20 mm, as flame is located further downstream. The smaller diameters encountered at 40 mm in the reacting case are the result of the stronger evaporation process due to the presence of the flame. This phenomenon is well captured by the F-TACLES model, even in case B where subgrid scale contributions are significant.

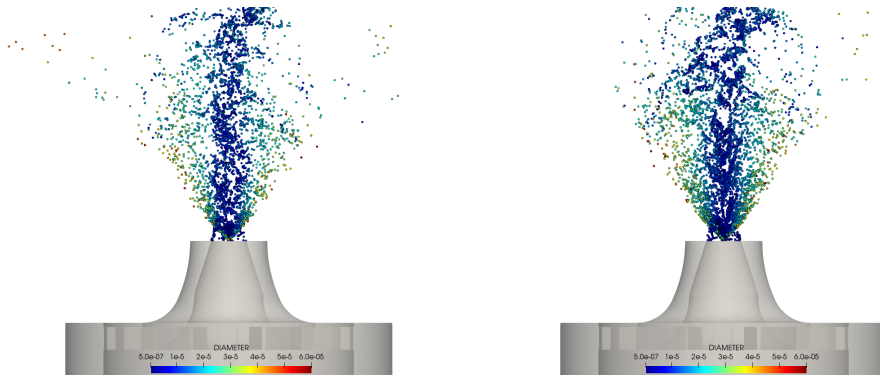


Figure 3.20: Droplet diameter for cases A-R (left) and B-R (right).

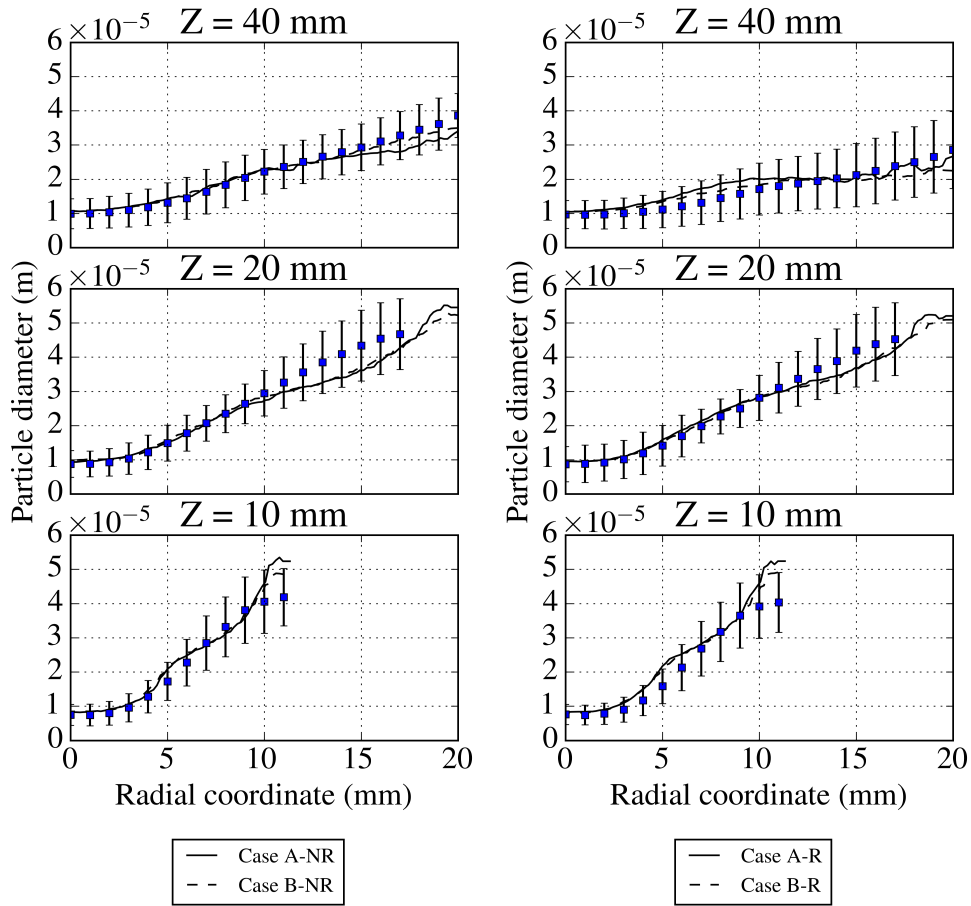


Figure 3.21: Radial profiles of droplet diameter for non-reacting (left) and reacting case (right). Symbols: experiments, solid line: Case A, dashed line: Case B.

3.4.4 Spray velocity

Figures 3.22 and 3.23 show the particles in the central vertical plane colored by their axial velocity for the cold and reacting cases respectively. In Fig. 3.22, the small droplets reach high axial velocity (up to 30 m/s), carried by the surrounding gas while the large droplets velocity decreases because of drag. In Fig. 3.23, the droplets have the same behavior. Some large droplets are not entering the flame and are not consumed at the extremity of the spray.

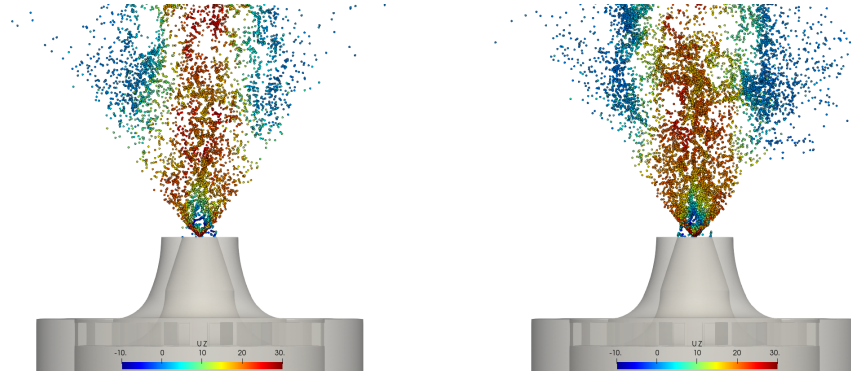


Figure 3.22: Droplet axial velocity for cases A-NR (left) and B-NR (right).

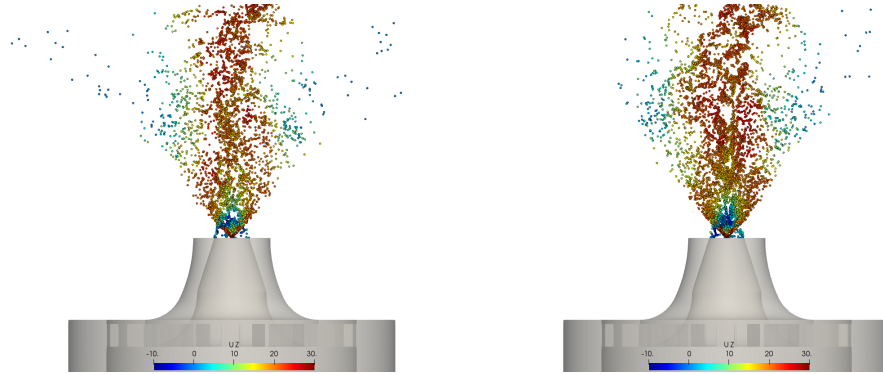


Figure 3.23: Droplet axial velocity for cases A-R (left) and B-R (right).

Droplet axial velocity is reported in Fig. 3.24 for the cold and reacting cases, respectively. The experimental measurements are colored by the diameter of the spray at the considered radial position. Green squares correspond to particle diameters lower than 15 microns, blue squares to diameters between 15 and 35 microns and red squares to diameters larger than 35 microns. The agreement is good for small to medium droplets (below 35 microns), but both LES cases predicts a higher velocity than the experiments for the large droplets. This discrepancy is attributed to the method of injection (from Guedot (2015)) that may overestimate the large droplets velocity.

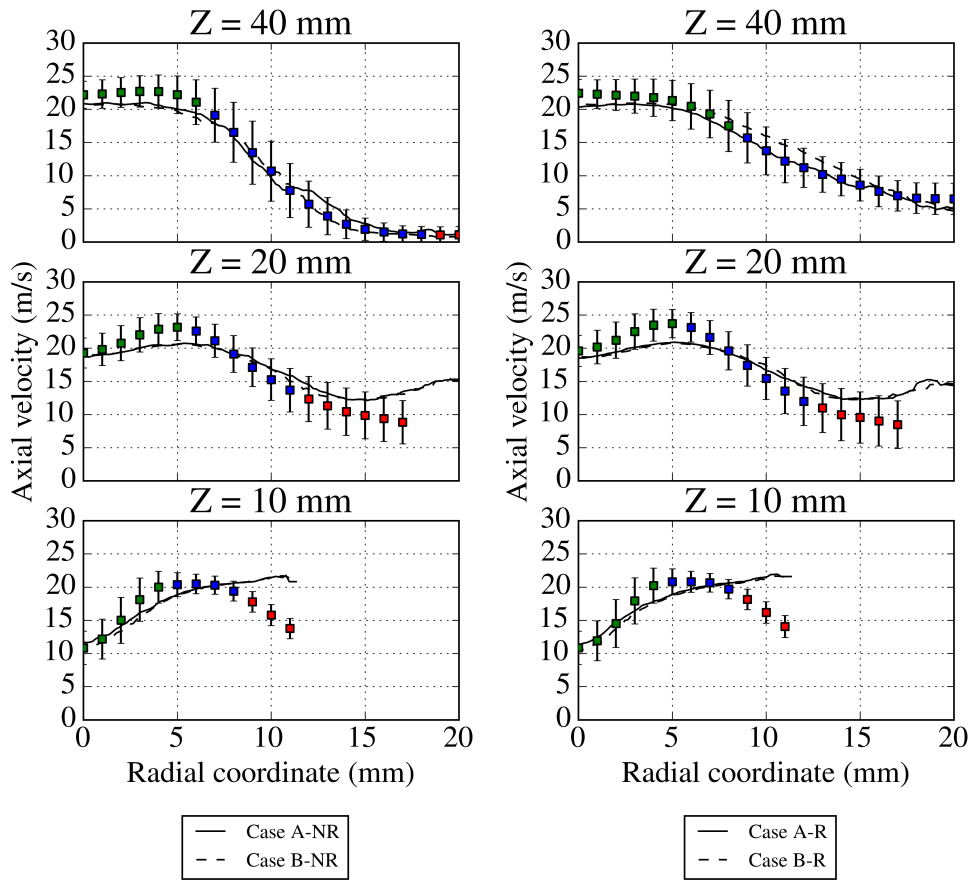


Figure 3.24: Radial profiles of droplet axial velocity for non-reacting (left) and reacting case (right). Symbols: experiments, solid line: Case A, dashed line: Case B.

Droplet radial velocity is reported in Fig. 3.25 for the cold and reacting cases, respectively. As for the axial velocity, the velocity of the small droplets is well predicted by all the simulations and the velocity of the large droplets is overestimated.

3.4.5 Spray temperature

Figures 3.26 and 3.27 show the particles in the central vertical plane colored by their temperature for the cold and reacting cases respectively. The scale is $280K < T_p < 300K$ for the cold case and $280K < T_p < 370K$. In Fig. 3.26, the small droplets temperature decreases rapidly to ≈ 280 K as they are convected downstream. This evolution is due to the evaporation. The same process exists for the larger droplets, but much slower. In the reacting case, below the flame, the behavior is the same as in the cold case. When the droplets enter the flame, the ones that are not entirely evaporated are heated rapidly to ≈ 370 K because

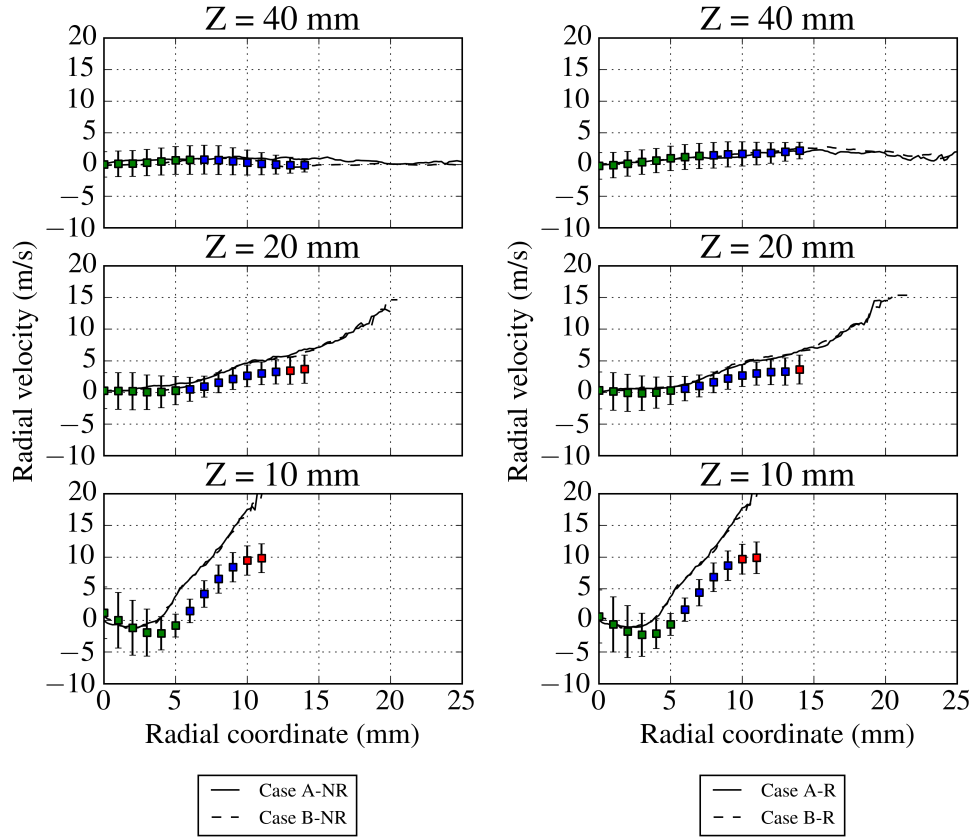


Figure 3.25: Radial profiles of droplet radial velocity for non-reacting (left) and reacting case (right). Symbols: experiments, solid line: Case A, dashed line: Case B.

of the heating of the flame. The small droplets located in the center of the flow are progressively heated by the hot gases until they are fully evaporated.

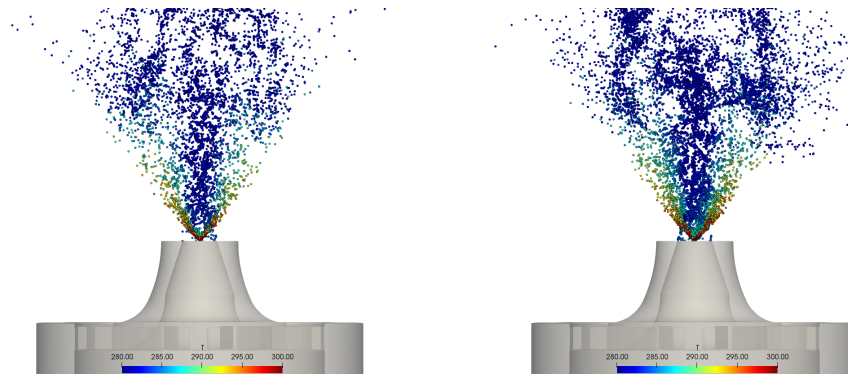


Figure 3.26: Droplet temperature for cases A-NR (left) and B-NR (right).

The droplet temperature predicted by the LES is now compared with the Global

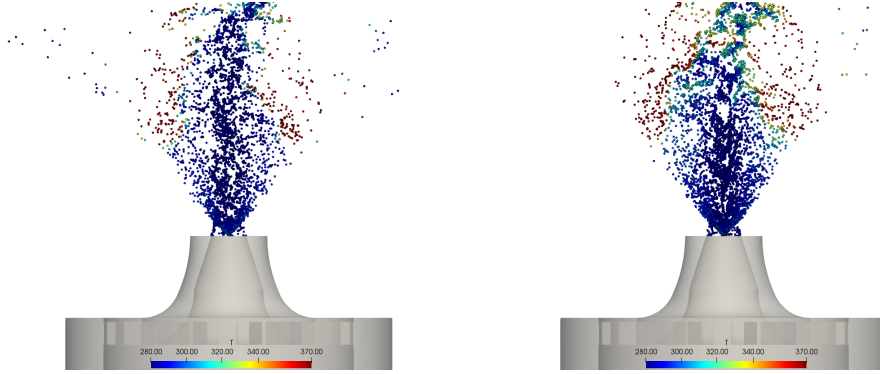


Figure 3.27: Droplet temperature for cases A-R (left) and B-R (right).

Rainbow Technique (GRT) measurements. Figure 3.28 presents radial profiles of temperature for the cold (left) and reacting (right) configurations. The experimental data highlight two zones. For $r > 5$ mm, the droplets reach quickly the wet bulb temperature, from the first measured radial profiles, i.e. 20 mm above the burner exit, whereas the liquid spray remains at the injection temperature around the centerline. This trend is not captured by the simulation, which predicts the wet bulb temperature for all droplet positions. The wet bulb temperature is defined as the equilibrium temperature reached by evaporating a liquid to saturation in a gas. This difference between simulations and experiments could be explained by limitations of the evaporation model (Shashank et al. (2011)).

The thermal characteristic time of the Spalding model, noted τ_{th} , is expressed as:

$$\tau_{th} = \frac{\rho_p d_p^2}{6} \frac{Sc}{Sh \mu_{1/3}} \frac{C_{p,k}}{C_{p,1/3}} \frac{B_T}{\log(1 + B_M)}, \quad (3.1)$$

where ρ_p is the droplet density, d_p^2 its diameter, Sc the Schmidt number, Sh the Sherwood number, $C_{p,k}$ the heat capacity at constant pressure of the n-heptane, $C_{p,1/3}$ and $\mu_{1/3}$ the heat capacity at constant pressure and the dynamic viscosity of the mixture according to the 1/3-2/3 rule (see Chapter 1), B_T the thermal Spalding number and B_M the mass Spalding number.

τ_{th} is therefore proportional to the square of the droplet diameter, which means that the larger droplet temperature will evolve slower than the one of the small droplets in the same conditions.

Figure 3.29 presents axial profiles of temperature for the cold (left) and reacting (right) configurations. For $r = 0$ mm, the droplets (which are small at this radial position) temperature drops quickly to ≈ 282 K. As r increases (and therefore as their diameter increases as shown in Sec. 3.4.3), the droplets temperature decreases slower. This tendency is consistent with the implementation of the Spalding model.

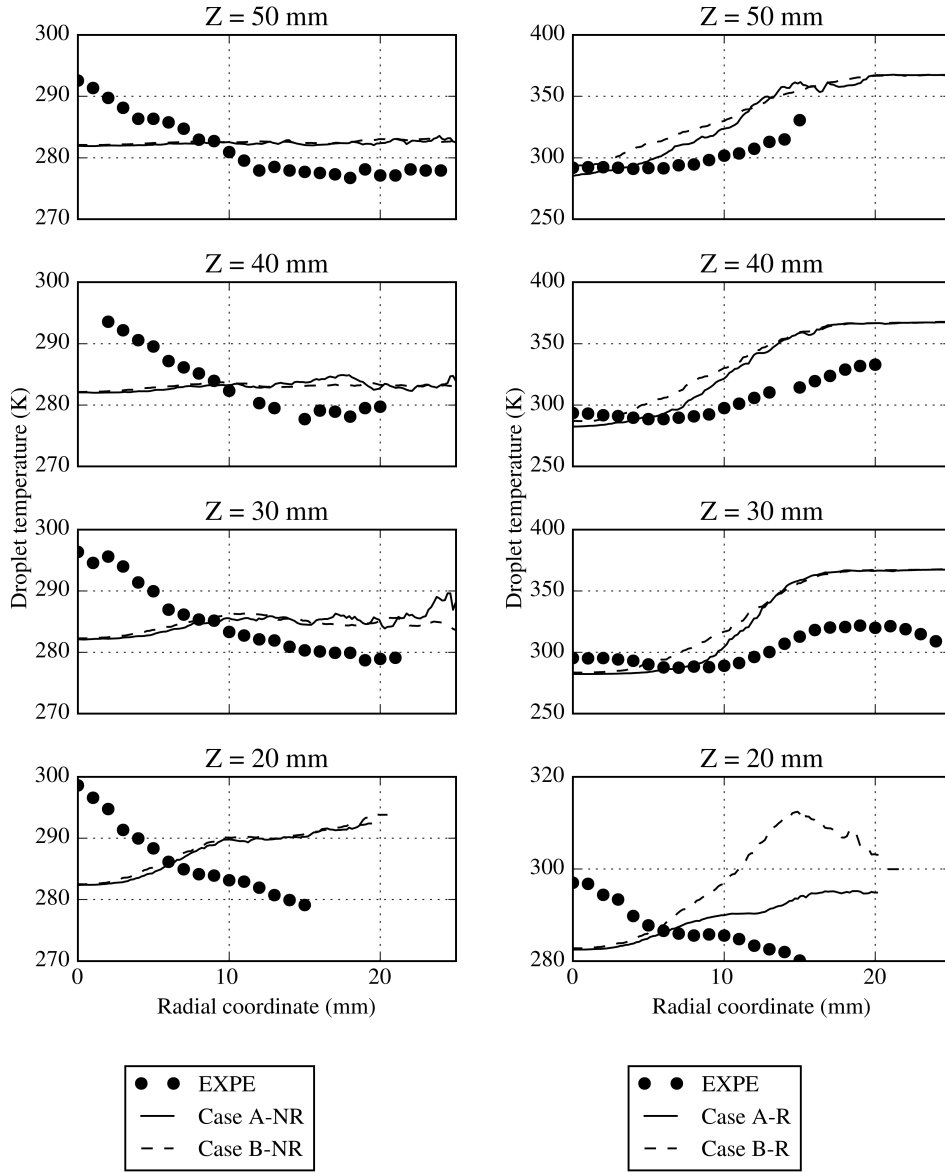


Figure 3.28: Radial profiles of droplet temperature for non-reacting (left) and reacting case (right). Symbols: experiments, solid line: Case A, dashed line: Case B.

Another possible explanation would be the choice of the injection model, which, by injecting all droplets from the same point, does not reproduce the spatial distribution of droplets induced by the liquid sheet break-up. Despite a correct prediction of the overall particle size, a local misprediction of the droplet distribution would also impact the mean liquid temperature. A way to overcome this difficulty would be to inject the droplets further downstream, and not at the real position of injection.

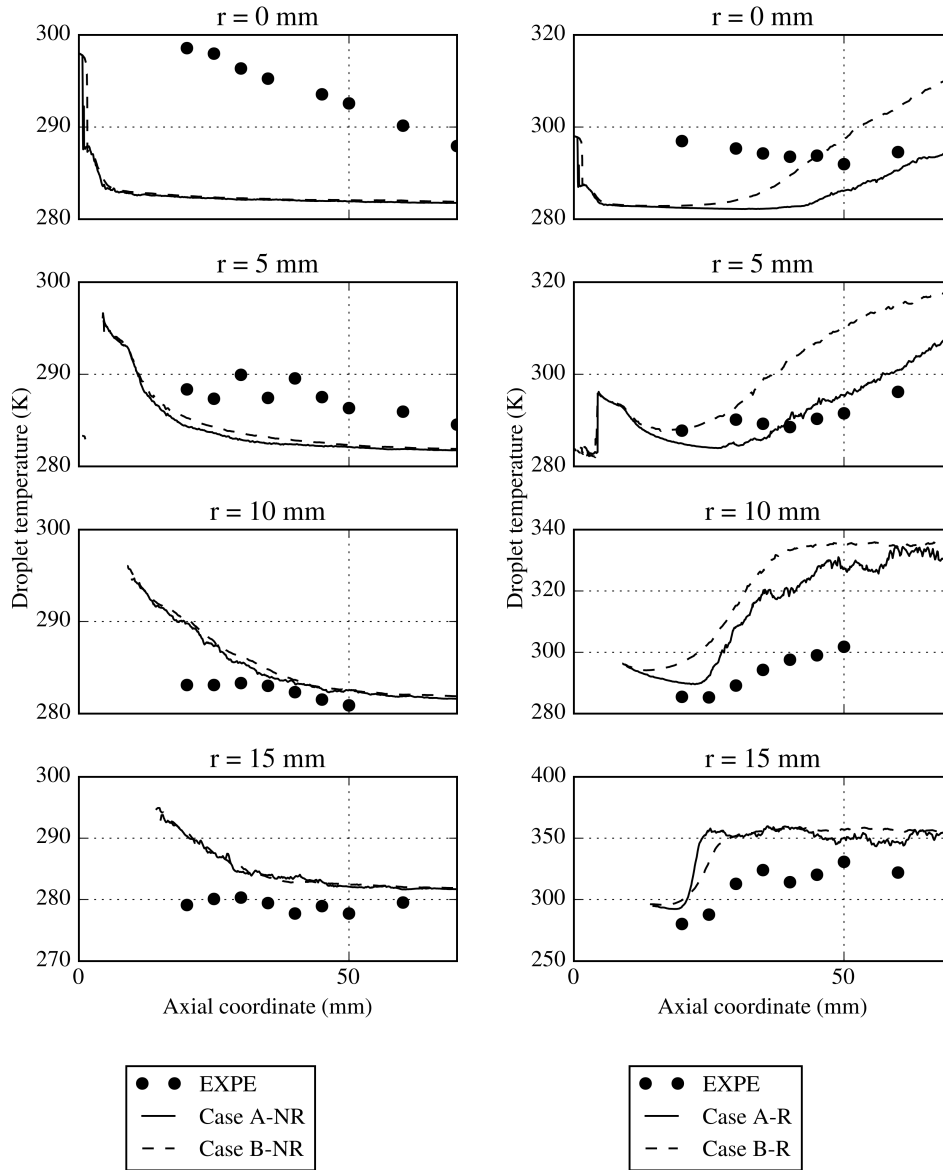


Figure 3.29: Axial profiles of droplet temperature for non-reacting (left) and reacting case (right). Symbols: experiments, solid line: Case A, dashed line: Case B.

In reacting conditions, in the burnt gases region, located at $r > 10$ mm and $z > 20$ mm, the droplet temperature rises quickly due to the high gas temperature in this zone. This phenomenon observed in the experiments is fairly tackled by the simulations. However, the droplet temperature measured downstream, between the inner and the outer branch of the flame, reaches a thermal equilibrium around 331 K whereas the numerical simulation predicts 367 K, which is close to the boiling temperature of n-heptane. As discussed in [Miller et al.](#)

(1998), this discrepancy may be attributed to the Spalding evaporation model, where the limiting value is the boiling temperature. A comparison between the Spalding and Abramzon-Sirignano models is proposed in Sierra Sánchez (2012) that highlights the differences that are found on the droplet temperature between the two models.

3.5 Conclusion

The first simulation with the F-TACLES formalism in a spray combustion configuration has been performed. The results show good agreement on the spray diameter and velocity, gas velocity, flame structure and lift-off with respect to experimental data. The complex flame structure, which presents a inner premixed flame front and an outer diffusion branch, is well reproduced by the simulation, even on the coarse grid representative of meshing conditions encountered in industrial applications. Case A simulations showed that tabulated chemistry based on premixed flamelets is adequate to capture the spray flame chemistry. The good prediction obtained on the coarse grid also demonstrates the ability of F-TACLES to model the unresolved interactions between the spray flame and turbulence. As the supplementary CPU cost induced by the combustion model is very low, this method is of interest for the gas turbine engineering community. However, another issue remains to be addressed. Significant discrepancies are indeed found for the droplet temperature. The influence of the droplet evaporation model and of the liquid sheet atomization on the spray temperature should be investigated in the future.

Part II

Prediction of turbulent reactive
flows in complex geometries:
application of the ZDES
approach to a realistic
aeronautical geometry

Chapter 4

Validation of the ZDES approach to the TLC configuration in non-reacting conditions

Contents

3.1	Context of the study and objectives	82
3.1.1	General context	82
3.1.2	State of the art on the simulations of the present experiment	82
3.1.3	Objectives	82
3.2	Experimental configuration	83
3.3	Numerical Setup	84
3.3.1	General parameters	84
3.3.2	Application of the F-TACLES table generation pro- cess to n-heptane	85
3.3.3	Simulations presented	86
3.4	Results and analysis	87
3.4.1	Flow topology and gas velocity	88
3.4.2	Flame topology	91
3.4.3	Spray diameter	97
3.4.4	Spray velocity	99
3.4.5	Spray temperature	100
3.5	Conclusion	105

This chapter focuses on the validation of the ZDES turbulence approach for a complex configuration of a realistic aeronautical injector in non-reacting conditions, along with a comparison with a LES approach.

4.1 Context of the study

4.1.1 Issue of realistic aeronautical injector experiments

Detailed comparisons between experiments and simulations are often limited to very simplified cases (gaseous flows, chambers functioning at atmospheric pressure, bare-boned geometry...). More complex configurations provide most of the time only scarce experimental data, for example a single profile at the output of the chamber, due to the fact that realistic conditions introduce major difficulties for reliable measurements.

4.1.2 Choice of the injector

The present chapter and the next one present unsteady non-reacting and reacting simulations (with LES or ZDES - Zonal Detached Eddy Simulation -) of a TAPS-like (Twin Annular Premixing Swirler) realistic aeronautical injector mounted in a square-section chamber, equipped with optical access. The operating conditions in mass flow rate, inlet air temperature and chamber pressure are representative of a cruise flight regime.

Detailed experimental measurements were acquired in the TLC chamber on the so-called M1 test bench at ONERA : Coherent Anti-Stokes Raman Spectroscopy (CARS) temperature profiles, Planar Laser Induced Fluorescence (PLIF) on OH and gaseous kerosene, Laser Induced Incandescence (LII) for soot volume fraction and gas analysis for NO_x, CO and soot at the exit of the chamber. These data were acquired for four operating points (taxi, climb, cruise and approach) but this work focuses only on the cruise regime (for which there is four temperature profiles available, versus only one for the climb regime).

To our knowledge, it is rare to have this amount of data on a such complex configuration, which permits to validate the results of the simulations with a high degree of confidence.

Owing to the complexity of the injector, the simulation of this configuration is a real challenge for CFD codes because it involves highly complex aerodynamics (with several types of regime-dependent flow separation in the swirlers), two-phase flow. Moreover, combustion regimes in this configuration can be significantly different from the conditions for which the usual models are valid. Indeed the majority of turbulent combustion models are based on the flamelet assumption, and were initially designed for gaseous combustion.

4.2 Objectives of the chapter

The present chapter challenges the ZDES method in a representative aeronautical injector configuration. A detailed comparison in terms of flow structures between ZDES and LES simulations is proposed. It aims at determining if the ZDES approach predicts the correct flow structure of the chosen aeronautical

injector in non-reacting conditions, and at discussing if the ZDES improves the prediction of flow features compared to the LES. The same injector will be studied in reacting conditions in the next chapter.

This chapter is divided in four parts. Firstly, the injector is presented. Secondly, the numerical methodology and the performed simulations are detailed. Then, a comparison between experimental data and simulations is presented, in which the interest of the ZDES approach on this complex configuration is demonstrated. Finally, an analysis on key parameters of the simulations is made to highlight the advantages and flaws of each method.

4.3 The TLC configuration

The injector studied in this chapter is the TLC (for "Towards Lean Combustion", studied in the TLC European Project) configuration, which is a prototype based on the Twin Annular Premixing Swirler (TAPS) principle. It was designed by engine manufacturers to study advanced combustion systems by operating in lean conditions and reducing NO_x emissions (Mongia (2003); Shaw and Peddie (2004); Foust et al. (2012)). A general view of the injector is presented in Fig. 4.1.

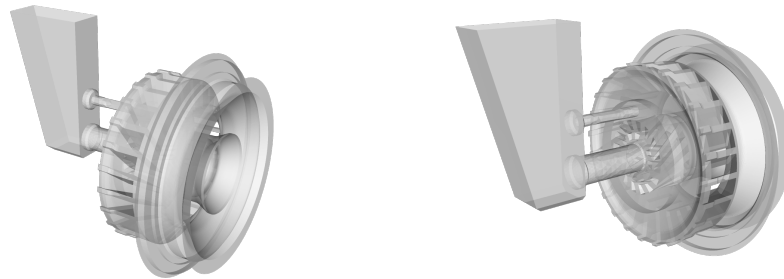


Figure 4.1: *TLC TAPS injector general view. Left: front view, right: back view.*

In this injector, the liquid kerosene injection is divided in two separated zones, identified in Fig. 4.2. The pilot injection creates a hollow cone and the so-called "multipoint" injection is performed with 24 holes, generating jets of fuel. The fuel mass flow rate can be split between the pilot and the multipoint injections in order to optimize the use of the injector for a broad range of operating points. The splitting ratio for the cruise operating point is 50% of the mass flow rate on the pilot injection and 50% on the multipoint one.

The injector includes three swirlers. Two counter-rotating swirlers with axial inlets and outlets are located in the pilot stage to enhance atomization and mixing near the pilot fuel injection. A third swirler, with radial inlets, ensures the atomization and the mixing of the fuel from the multipoint injection with the incoming air from the plenum, before the flow enters the combustion cham-

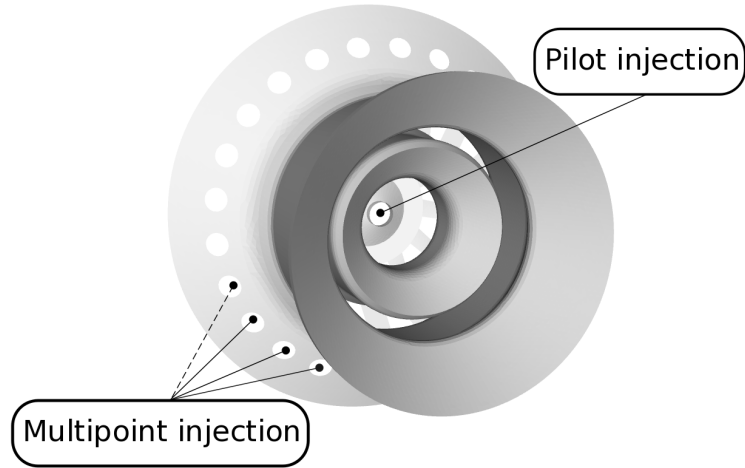


Figure 4.2: *View of the two zones of injection. The injection inlets are artificially enlarged.*

ber. Figure 4.3 presents the different air paths in the TLC configuration and highlights the positions of the swirlers.

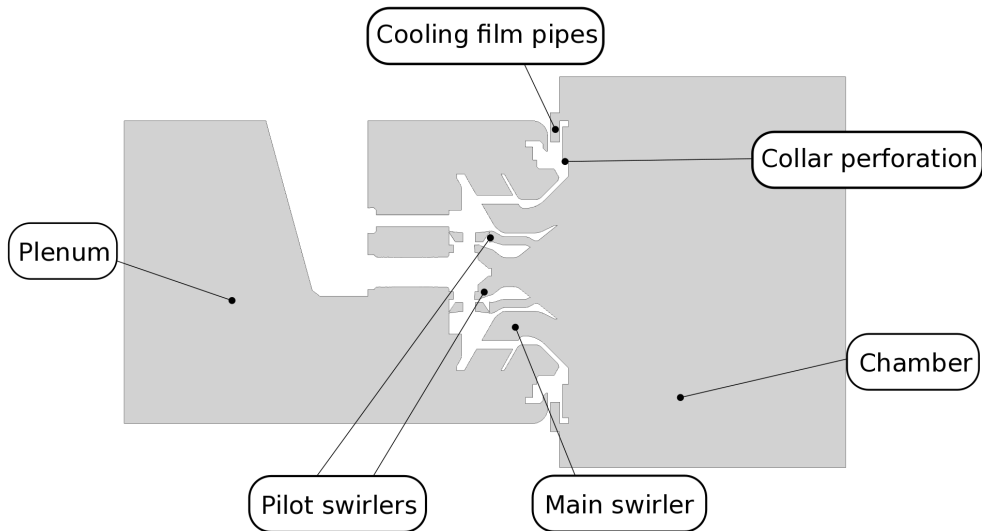


Figure 4.3: *Air paths in the TLC configuration.*

The TLC injector is mounted on an experimental rig as the connection between a plenum, where the air is injected, and a chamber where the flame is stabilized (only in reactive conditions). The chamber is pressurized, with a choked nozzle at the outlet to reach the expected pressure. Even if the studied configuration is not reactive, cooling films are included in the geometry, being part of the

experimental setup. The tubes that connect the plenum and the chamber are included in the computational domain. Finally, a collar perforation is present on the back wall of the chamber and is simplified in the simulations as an equivalent inlet condition. A global view of the whole computational domain is presented in Fig. 4.4.

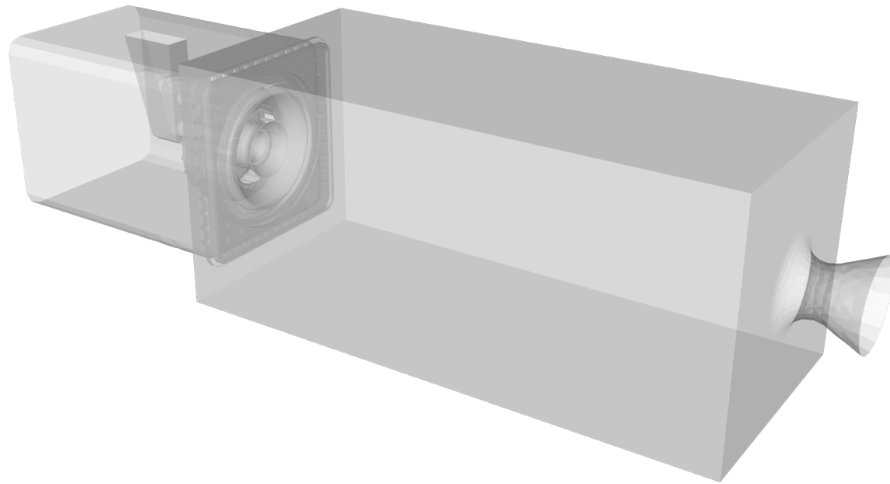


Figure 4.4: *Entire TLC computational domain view.*

Several experimental measurement techniques were used to characterize the behavior of this injector for various injection conditions, which is rare for such a complex configuration. The LDA (Laser Doppler Anemometry) technique was chosen to retrieve the gaseous phase velocity (other methods were used in two-phase conditions, but are not mentioned here because this work focuses solely on the gaseous flow).

The available experimental data were acquired by ONERA in a campaign carried out in the TLC framework. The injector was studied in both reactive (Hannebique et al. (2012); Dorey (2012); Boucher (2015)), and non-reactive (Lavedrine (2008); Jaegle (2009); Jaegle et al. (2011)) conditions on two different geometries for the plenum and the chamber.

4.4 Simulations

4.4.1 General parameters

Two simulations are performed in this chapter, which only differ by the turbulence approach and the related mesh. The mesh is adapted near the wall for each approach, as it will be shown later. The timestep for the temporal integration is $\Delta t = 5.10^{-7}$ s for both simulations.

The impact of the CFL number on the results' consistency is discussed in Section 4.5.4.

The statistics are averaged over 50 ms, which represents five estimated flow-through times and it was verified that this period of time was sufficient for a good convergence of the mean and RMS quantities. The boundary conditions are summarized in Table 4.1. The initial conditions are an uniform field of air with a temperature of 473 K and a pressure of 4.5 bar.

Table 4.1: *Boundary conditions of the TLC simulations.*

Boundary	Type
Walls	No-slip adiabatic wall (ZDES and LES), logarithmic wall law (LES only)
Plenum inlet	Subsonic inlet, air mass flow rate: 465 g/s, temperature: 473 K
Collar perforation inlet	Subsonic inlet, air mass flow rate: 12 g/s, temperature: 473 K
Nozzle outlet	Supersonic outlet

4.4.2 LES mesh

The mesh used for the LES simulation is the same as in Jaegle (2009). It is a hybrid mesh with a single layer of triangular prisms on the wall with a thickness of 120 μm and tetraedra elsewhere. The mesh is refined in the injector, the chamber at the exit of the injector and in the cooling films. The general features of the LES mesh are shown in Fig. 4.5 (top). The single prism layer of the LES mesh is highlighted in Fig. 4.6 (top).

4.4.3 ZDES mesh

The mesh used for the ZDES simulation shares the same characteristic cell size in the volume as the LES mesh but contains more prism layers near the walls. In order to resolve the boundary layer with the RANS model, the size of the first prism layer must satisfy the condition $y^+ < 1$. A RANS simulation was performed to calibrate the thickness of the first prism layer. The size of the first prism layer in the ZDES mesh is then set to 1 μm . The thickness of the

prism layers in the injector follows a geometric sequence with a common ratio of 1.25 to obtain a smooth transition to the tetrahedral region.

Convex areas (e.g. corners) present in the geometry require a special treatment to avoid meshing issues. In these regions, the default setting of the meshing software used in this study (Centaur) is the connection of prism layers from both sides of the convex area. However, the resulting prisms are extremely thin in the normal direction to the wall and become too skewed. To overcome this problem, the cells that have a single node on the selected curves are forced to be tetrahedral. The general features of the ZDES mesh are shown in Fig. 4.5 (bottom). The differences between the two meshes on this global view of the computational domain are not visible. The prism layers are highlighted for the ZDES mesh in Fig. 4.6 (bottom). The treatment of convex areas in the ZDES mesh is visible in Fig. 4.7 (bottom) in comparison with a ZDES-type mesh without this treatment in Fig. 4.7 (top), where the thickness of the first prism layers does not comply with the imposed thickness.

The properties of the meshes are summarized in Tab. 4.2.

	LES mesh	ZDES mesh
Number of cells (total)	8 540 311	14 681 887
Number of tetraedra	8 325 113	12 396 333
Number of prism layers	1	22
Number of prisms	214 002	2 226 876
Thickness of the first prism layer	120 μm	1 μm
Target y^+ at the wall	≈ 100	< 1

Table 4.2: Meshes characteristics.

4.5 Results and analysis

4.5.1 Positions of the planes of interest

Figure 4.8 shows the location of the reference plane in the direction normal to the axis of the configuration ($x = 0$ mm) and the three planes where the experimental data are available at $x = 10, 15$ and 30 mm. The reference plane is aligned with the back wall of the chamber. An additional plane of interest is the one located at the change of curvature of the outer wall of the main swirler. It is identified in Fig. 4.8 by a red line and will be used in Sec. 4.5.5 in the analysis of the simulations.

4.5.2 Comparison of the velocity between simulations and experiments

The statistics are converged in the simulations to obtain the mean and the Root Mean Square (RMS) values of the quantities of interest. The RMS of velocity

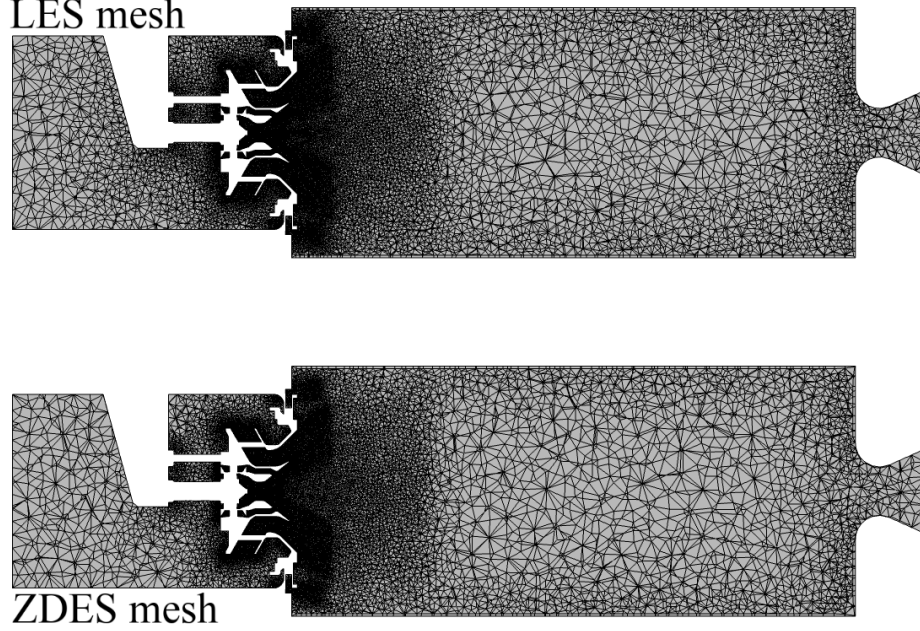


Figure 4.5: General view of the meshes. Top: LES mesh, bottom: ZDES mesh.

reads:

$$u_{i,rms}^2 = \langle \widetilde{u_i u_i} \rangle - \langle \widetilde{u_i} \rangle \langle \widetilde{u_i} \rangle, \quad (4.1)$$

where the $\langle \cdot \rangle$ operator denotes a temporal averaging. Both quantities are compared with experimental data obtained with LDA. Two planes are considered: the horizontal plane ($z = 0$ mm) and the vertical one ($y = 0$ mm). The comparison is presented for both planes in Fig. 4.9 for the mean axial velocity and Fig. 4.10 for the RMS of axial velocity. The same procedure is done for the tangential velocity in Fig. 4.11 (mean) and 4.12 (RMS).

The comparison with experimental data raises several remarks. The first one is that both simulations, LES and ZDES, predict very well the general features of the velocity profiles.

In Fig. 4.9, for $x = 10$ mm, i.e. at the profile closest to the injector exit, two pairs of peaks are observed in both experiments and simulations. The outer pair (for $|y|$ and $|z|$ between 45 and 55 mm) is observed because of the cooling films.

The peak position is correctly reproduced by the LES, while the ZDES underestimates it. Also, the ZDES overestimates slightly the peak velocity value. Overall, the thickness of the peak is well recovered.

The inner pair (for $|y|$ and $|z|$ between 20 and 45 mm) corresponds to the flow from the injector. The profile in the vertical plane is not symmetric according

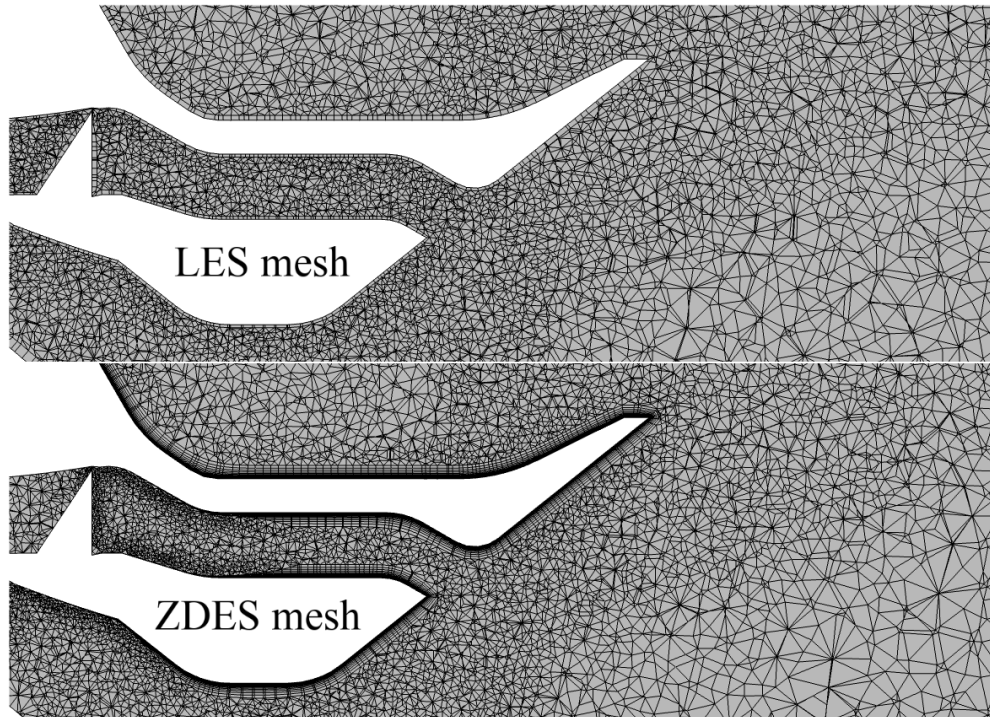


Figure 4.6: *Close-up view on the prism layers of the meshes. Top: LES mesh, bottom: ZDES mesh.*

to experimental data.

The profiles in the simulations are almost symmetric in the vertical plane, and larger differences between the two half of the profile are found in the horizontal plane. The origin of the absence of symmetry is the presence of an obstacle in the plenum, which is the fuel injection arm used in reactive conditions. This equipment introduces an imbalance in the flow that enters the injector and explains this absence of symmetry. This effect however is not well captured by the simulations because the plenum region is not well discretized in the present meshes.

The ZDES predicts higher values of peak axial velocity, which corresponds to the value for positive y and the LES predicts lower values for the peak, which is close to the value for negative y . Moreover, the position of the peak is not the same for the simulations and the experiments. In the ZDES, it is located closer to the center of the injector. The LES peak is closer to the experimental one. Finally, the thickness of the peak is smaller in the ZDES than in the LES, and both simulations underestimate it with respect to the experiments.

The recirculation zone (for $|y|$ and $|z|$ between 0 and 20 mm) extent is slightly underestimated by the simulations.

For the second profile, at $x = 15$ mm, the same conclusions are drawn. The only noticeable differences with respect to the flow topology are that the two

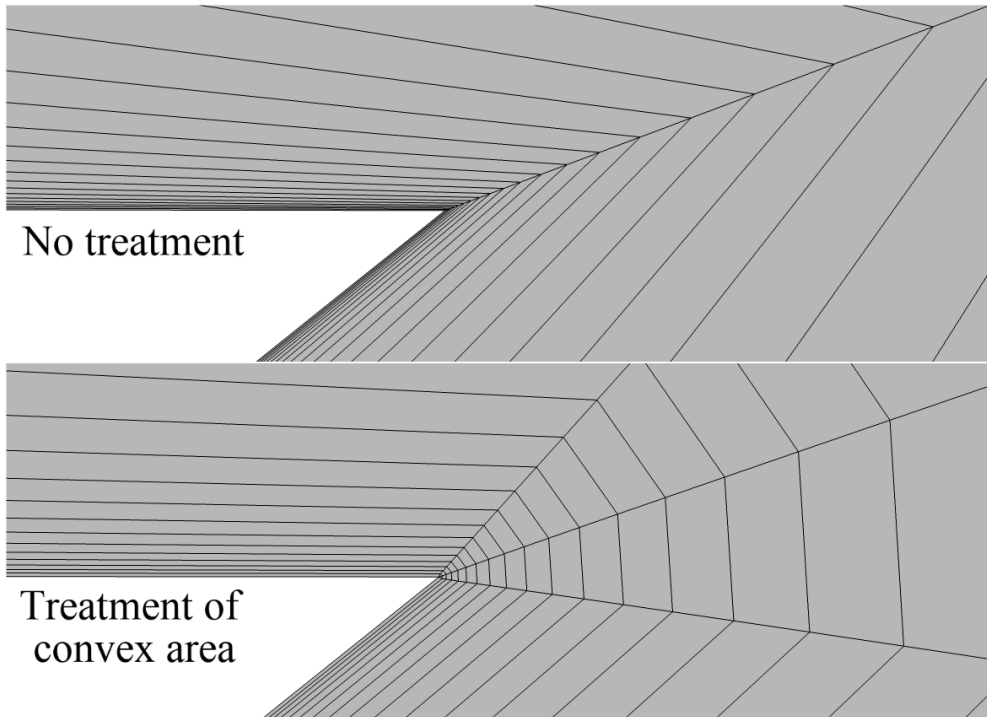


Figure 4.7: *Close-up view of the treatment of convex areas. Top: ZDES mesh without treatment, bottom: ZDES mesh with treatment.*

pairs of peaks are closer to one another and that the recirculation zone is larger than at $x = 10$ mm.

The last profile, at $x = 30$ mm, i.e. twice as far from the injector exit as the previous one, features a different shape. Only one region of high axial velocity is observed (for $|y|$ and $|z|$ between 30 and 60 mm). The recirculation zone is again larger than at $x = 15$ mm.

In Fig. 4.10, the RMS of axial velocity are plotted for $x = 10, 15$ and 30 mm in both vertical and horizontal planes. As in the mean velocity profiles, the general features of the RMS profiles are well reproduced by the simulations. The major difference lies in the value of the RMS. The simulations consistently underestimate the RMS, except in the inner recirculation zone.

In Fig. 4.11, the mean tangential velocity profiles are plotted for $x = 10, 15$ and 30 mm in both vertical and horizontal planes. The component of the velocity highlights the effect of the swirlers on the flow, by introducing a rotating motion. In both planes, the simulations recover well the general features of the velocity profiles. As in the axial velocity profiles, the differences with the experiments are the position of the mean peak and its value. The position of the peak is slightly better reproduced by the LES. The peak value is underestimated for both simulations in the vertical plane and overestimated in the horizontal plane with respect to the experimental database.

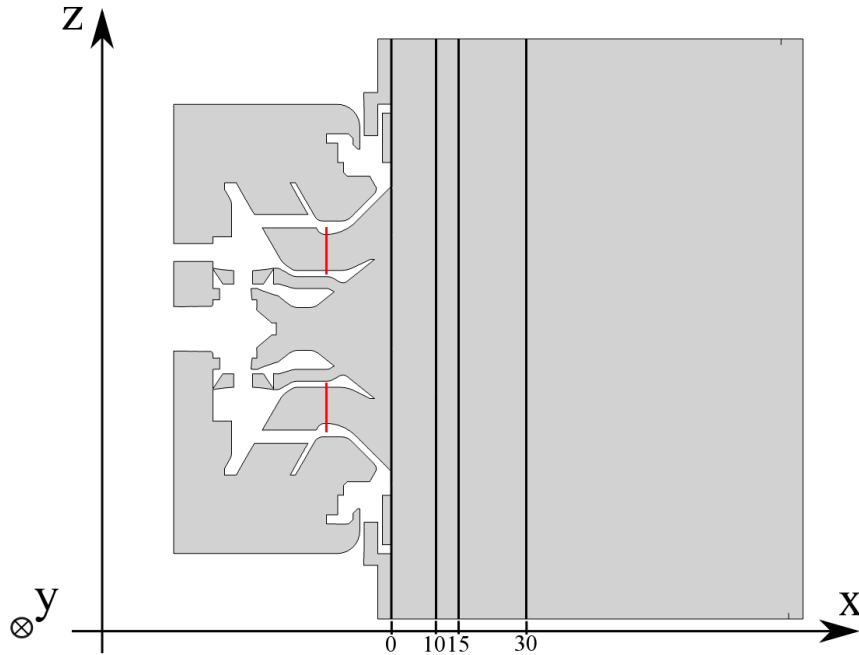


Figure 4.8: Location of the reference plane ($x = 0$ mm), the three profiles for comparison with experiments ($x = 10, 15$ and 30 mm) and the reference plane for section 4.5.5 in red.

Finally, in Fig. 4.12, the RMS of tangential velocity are plotted for $x = 10, 15$ and 30 mm in both vertical and horizontal planes. As in the profiles for the RMS of axial velocity, the simulations underestimate the value of RMS. However, the main features are correctly reproduced.

It appears with respect to the experimental profiles that the flow detaches in the two vertical and horizontal planes where the measurements are performed. One can notice that the experimental profiles of axial velocity are not symmetrical in the vertical plane. The presence of the fuel injection arm in the plenum (see Fig. 4.3) might explain this behavior. The numerical profiles however are almost symmetrical in the two planes.

In order to get a general view of the flow topology for both simulations, the fields of mean axial velocity are compared between simulations for the vertical plane in Fig. 4.13 and the horizontal plane in Fig. 4.14. In both planes, several zones are identified.

The first one corresponds to the flow before the injector, in the plenum. Flow velocity is relatively slow compared to the injector. The fuel injection arm in the plenum introduces a break of symmetry in the vertical plane, as is explained above.

The second zone is inside the injector. The change of section in the injector induces an acceleration of the flow. Also, the orientation of the swirling vanes creates a swirling motion in the flow, mainly due to the main swirler.

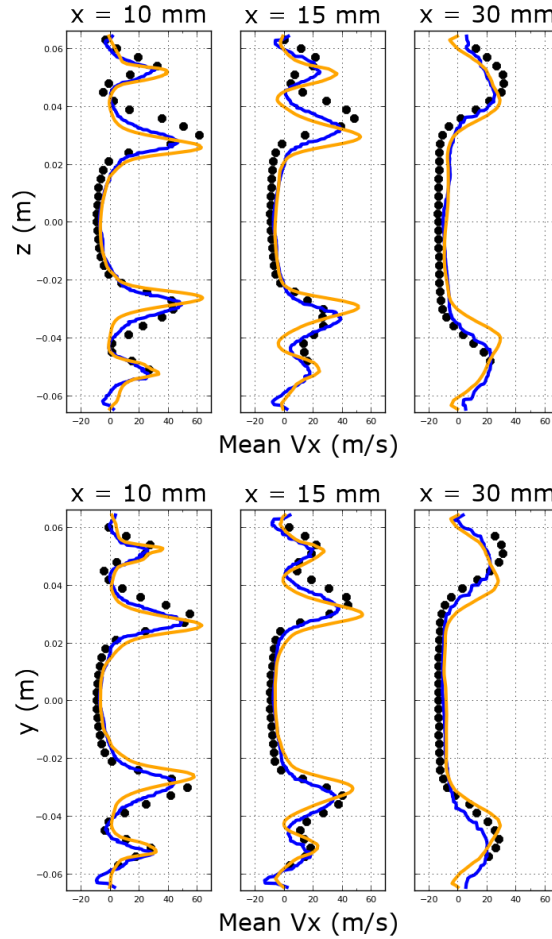


Figure 4.9: Mean axial velocity for the three planes ($x = 10, 15$ and 30 mm). Top: vertical plane ($y = 0$ mm), bottom: horizontal plane ($z = 0$ mm). Dots: experiments, orange: ZDES, blue: LES.

The last zone is the combustion chamber itself. A large central recirculation zone is visible at the center of the chamber. It is the consequence of the swirling motion induced by the swirler. Close to the chamber walls, two smaller recirculation zones are present. The flow created by the cooling films is observed close to these zones.

An interesting feature of this flow is the detachment that appears on the outer wall of the main swirler. This swirler is radial and features steep curvature changes. This geometry favors the apparition of recirculation zones, due to a stronger adverse pressure gradient on the outer wall. This zone is larger in the ZDES than in the LES, it leads to a different flow topology. Indeed, the large central recirculation zone grows larger downstream in the ZDES than in the LES. Also, the peak flow velocity at the exit of the main swirler is higher in

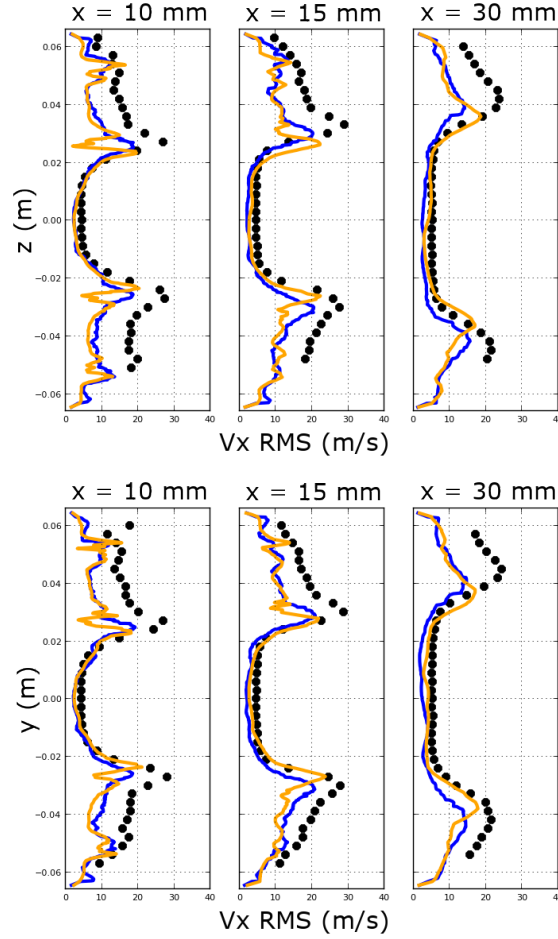


Figure 4.10: *RMS of axial velocity for the three planes ($x = 10$, 15 and 30 mm). Top: vertical plane ($y = 0$ mm), bottom: horizontal plane ($z = 0$ mm). Dots: experiments, orange: ZDES, blue: LES.*

the ZDES than in the LES.

In order to confirm the observations made in the horizontal and vertical planes, Figs. 4.15, 4.16, 4.17 show the mean axial velocity in the three planes ($x = 10$ mm, $x = 15$ mm and $x = 30$ mm) where the LDA measurements are available. In the first plane (Fig. 4.15), the influence of the cooling films on the flow is highlighted by the four regions of positive axial velocity close to the chamber walls. The flow from the main swirler is visible as the region of high axial velocity with a circular shape. The difference of peak velocity between the ZDES and LES is also observed. In the second plane (Fig. 4.16), the flow has a very similar topology with respect to the first plane. The only major difference is the increased size of the central recirculation zone. In the third plane (Fig. 4.17), which is located farther downstream, the flows from the cooling films and the

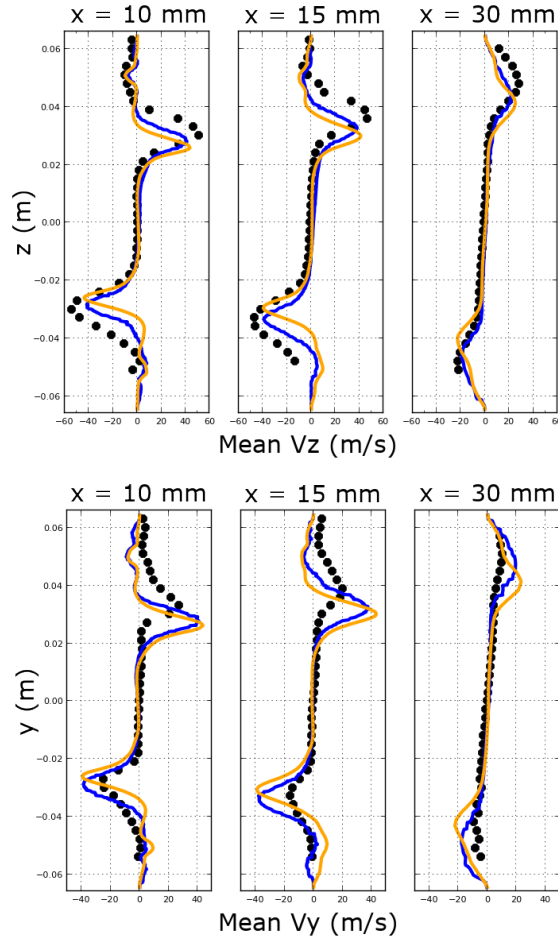


Figure 4.11: Mean tangential velocity for the three planes ($x = 10, 15$ and 30 mm). Top: vertical plane ($y = 0$ mm), bottom: horizontal plane ($z = 0$ mm). Dots: experiments, orange: ZDES, blue: LES.

main swirler are merged, as it is observed in the experimental profiles (Fig. 4.9). Pseudo-streamlines of mean axial velocity are visible in Fig. 4.18, in the vertical plane. It is possible to identify the general features of the recirculation zones, especially the one between the cooling films and the main flow. The two parts of the central recirculation zone are not symmetrical in this plane. The top half is both longer and larger for both simulations.

In order to visualize the 3D aspect of the flow, Figure 4.19 shows a contour of velocity magnitude, colored by the axial velocity for both simulations. This view is designed to show the areas of high velocity. The cooling films are observed close to the chamber walls, while the flow from the main swirler is visible at the center. The swirling motion is highlighted by the shape of the contour. Each "bump" on the outer face of the flow from the main swirler is

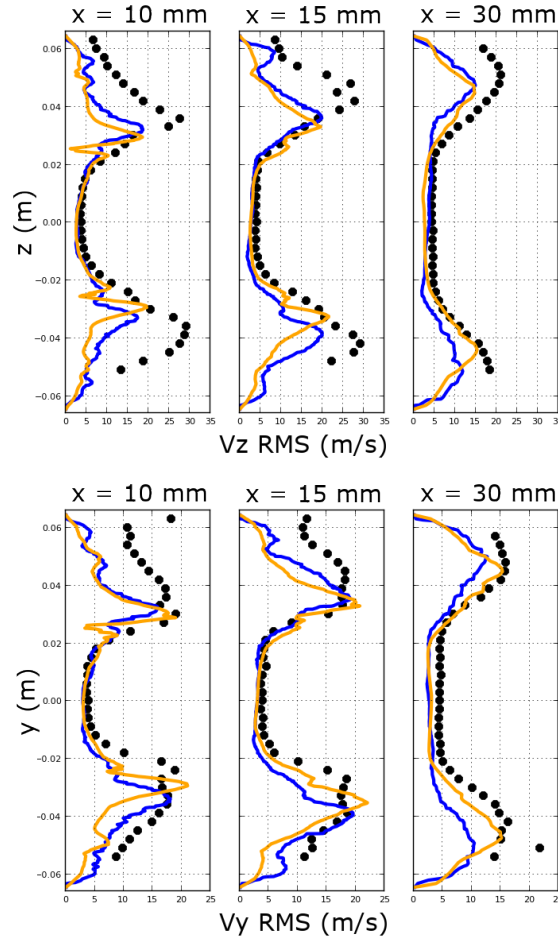


Figure 4.12: *RMS of tangential velocity for the three planes ($x = 10, 15$ and 30 mm). Top: vertical plane ($y = 0$ mm), bottom: horizontal plane ($z = 0$ mm). Dots: experiments, red: ZDES, blue: LES.*

created by one of the 24 swirling vanes.

Figure 4.20 compares the mean resolved turbulent kinetic energy k (computed as $\frac{1}{2}(\langle \tilde{\mathbf{u}}^2 \rangle - \langle \tilde{\mathbf{u}} \rangle^2)$) between ZDES and LES. This quantity indicates the intensity of the velocity fluctuations. For both simulations, two regions feature high values of k . The first one is located at the exit of the inner axial swirler and the second one at the limits of the main swirler flow. These two regions are the frontiers between the positive and negative axial velocity zones, as is observed in Fig. 4.18. The LES predicts lower levels of k , especially in the inner axial swirler. This is also the case for the RMS of velocity as is shown in the profiles (Figs. 4.10 and 4.12).

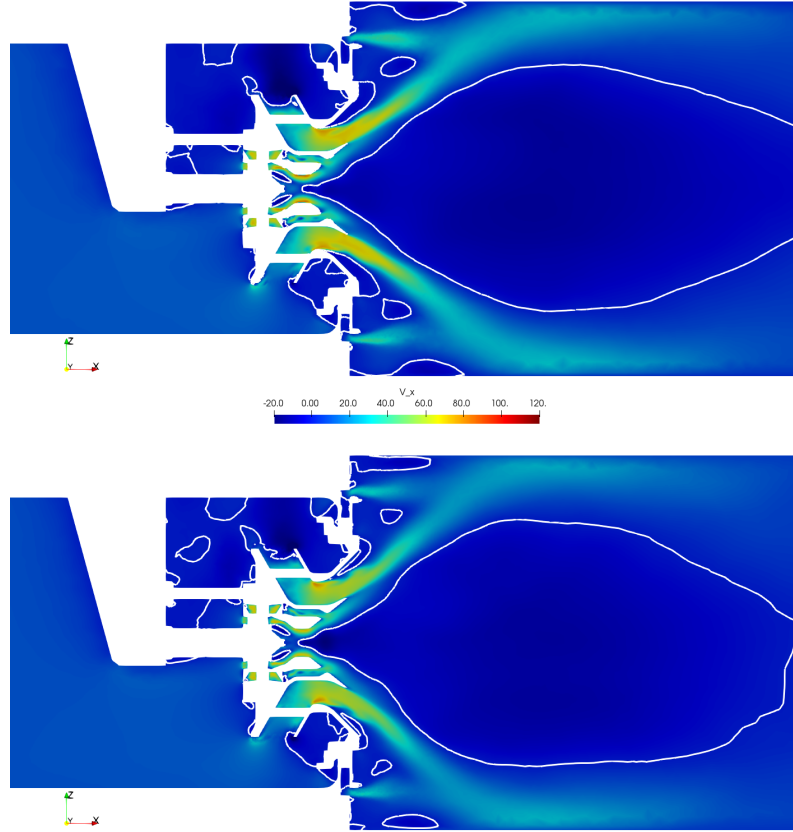


Figure 4.13: Comparison of mean axial velocity in the vertical plane ($y = 0$ mm) between ZDES (top) and LES (bottom). White line corresponds to $V_x = 0$ m/s.

4.5.3 Validation of the ZDES switch behavior

To verify the consistency of the ZDES, an instantaneous field of f_d in the vertical plane is presented in Fig. 4.21. As can be derived from Eq. 1.21, f_d tends to 0 in the RANS region, leading to $\hat{d} = d$, and to 1 in the LES region, in order to have $\hat{d} = C_{DES}\Delta$.

The general view shows that the region where the model adopts an LES formulation for the turbulent viscosity covers the major part of the computational domain, which is the desired behavior. The focus on the swirler walls demonstrates the transition of the function (and thus the switch to the RANS formulation) in the vicinity of the walls. Therefore the boundary layers are qualitatively correctly protected in the ZDES simulation. While these observations are satisfying for the treatment of the swirler, some parts of the domain would require a specific treatment. Indeed, the f_d function behaves poorly outside of the swirler walls due to a lack of spatial discretization. This is visible for

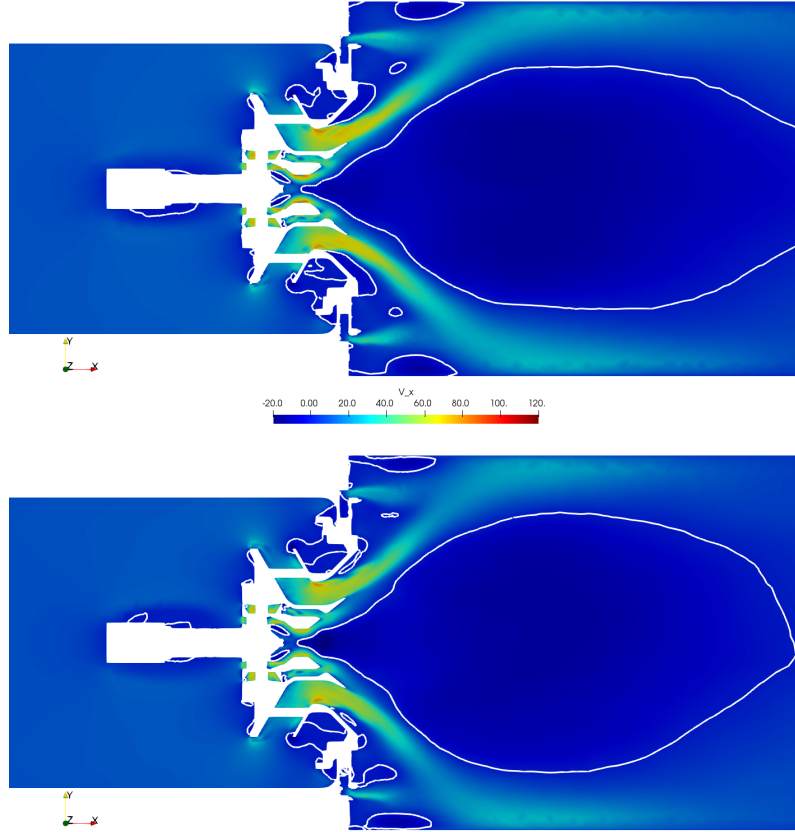


Figure 4.14: Comparison of mean axial velocity in the horizontal plane ($z = 0$ mm) between ZDES (top) and LES (bottom). White line corresponds to $V_x = 0$ m/s.

the walls of the plenum, the fuel injection arm and the chamber. This behavior is linked to the absence of prism layers on these walls. However, the flow in this injector is piloted by the swirlers, so this limitation on the other walls is expected to have a very low influence on the results.

4.5.4 Analysis of the CFL number distribution

The CFL number is defined as:

$$\text{CFL} = \frac{(\|\tilde{\mathbf{u}}\| + c)\Delta t}{\Delta x}, \quad (4.2)$$

where c is the speed of sound, Δt the time step and Δx the characteristic mesh

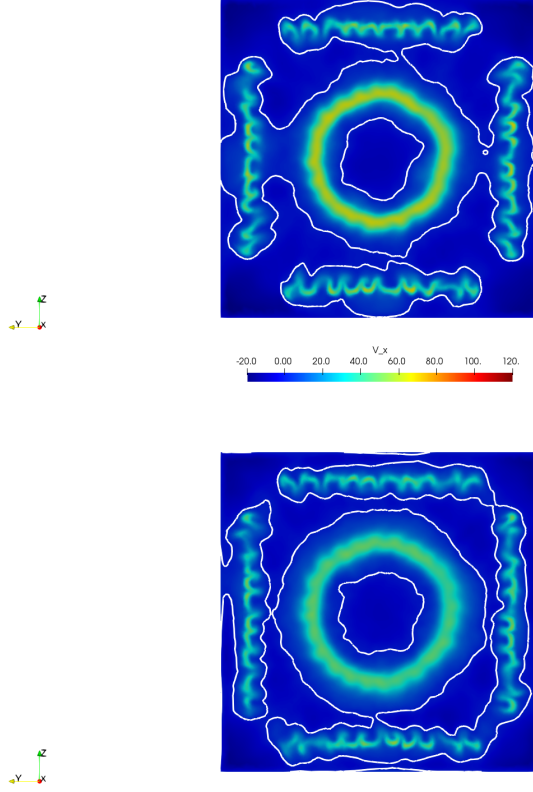


Figure 4.15: Comparison of mean axial velocity in the plane $x = 10$ mm between ZDES (top) and LES (bottom). White line corresponds to $V_x = 0$ m/s.

size. A convective CFL number may also be defined:

$$\text{CFL}_c = \frac{\|\tilde{\mathbf{u}}\| \Delta t}{\Delta x}. \quad (4.3)$$

The use of explicit schemes for temporal integration is common when performing LES of reacting flows. The choice of ZDES implies meshing the boundary layers properly to satisfy the condition $y^+ < 1$ in the first cell. The respect of the CFL condition of explicit schemes requires time steps of 10^{-9} s with the meshes used here. The use of implicit schemes allows the user to overcome this limitation and thus reduces considerably the cost of the simulation. Moreover, the time step is chosen in order to respect the characteristic times of the convective phenomena (the criterion being a convective CFL number below 1), which is essential to guarantee the good quality of the results. With this approach, the acoustics in the boundary layers is not correctly resolved but it is assumed

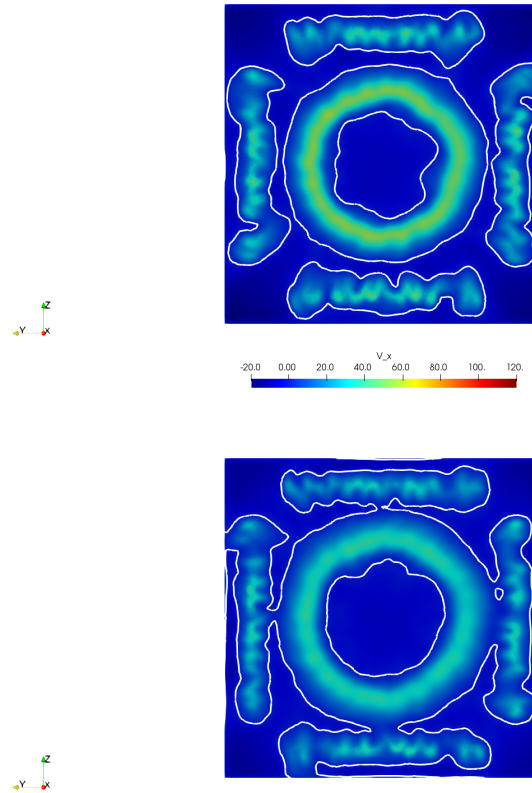


Figure 4.16: Comparison of mean axial velocity in the plane $x = 15$ mm between ZDES (top) and LES (bottom). White line corresponds to $V_x = 0$ m/s.

that this does not have an impact on the global flow. A similar choice for the time integration was made in Deck (2012) for example.

Figures 4.22 and 4.23 compare the CFL and convective CFL numbers distribution between the two simulations. The CFL number reaches high values in the boundary layers in the ZDES (up to 200). This results from the presence of the very thin prism layers in the boundary layers. The maximum CFL number in the LES is 3.5 and is found close to the walls. Elsewhere in the volume, the CFL number is low even if it can be locally over 1 in both simulations. The convective CFL number is permanently below 1 in both simulations.

4.5.5 Analysis of the treatment of the boundary layers in the simulations

The massive flow separation in this injector occurs on the outer radial swirler wall. Its position and the size of the detached flow region determines the global

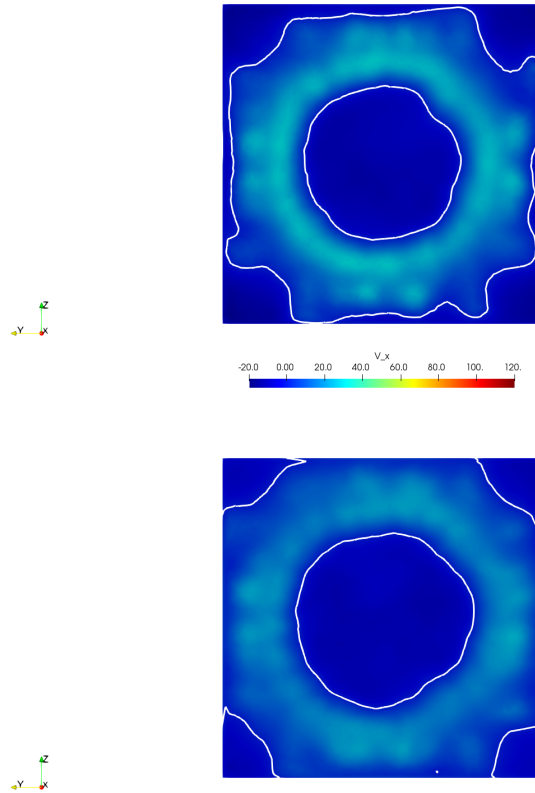


Figure 4.17: Comparison of mean axial velocity in the plane $x = 30$ mm between ZDES (top) and LES (bottom). White line corresponds to $V_x = 0$ m/s.

flow topology. This is why this section focuses on studying how the boundary layers are treated close to this region.

Figures 4.24, 4.25, 4.26 and 4.27 present two views of the outer radial swirler wall, from its origin in the plenum to the exit in the chamber. The first 3D view shows the curvature of the surface. The second one is a developed surface of the 3D view around the central axis of the computational domain for comparison purposes.

The surface distribution of y^+ is an important criterion to validate or not the wall treatment of the simulations. An instantaneous field is presented in Fig. 4.24 for the ZDES and in Fig. 4.25 for the LES. y^+ is always below 1 in the ZDES, which means that the thickness of the first prism layer is correctly set. The values of y^+ are below 70 in the LES. The values of y^+ are generally in the range of the wall-law validity, except near the exit of the swirler, where the values of y^+ tend to be lower. This behavior is linked to the drop in friction, shown below.

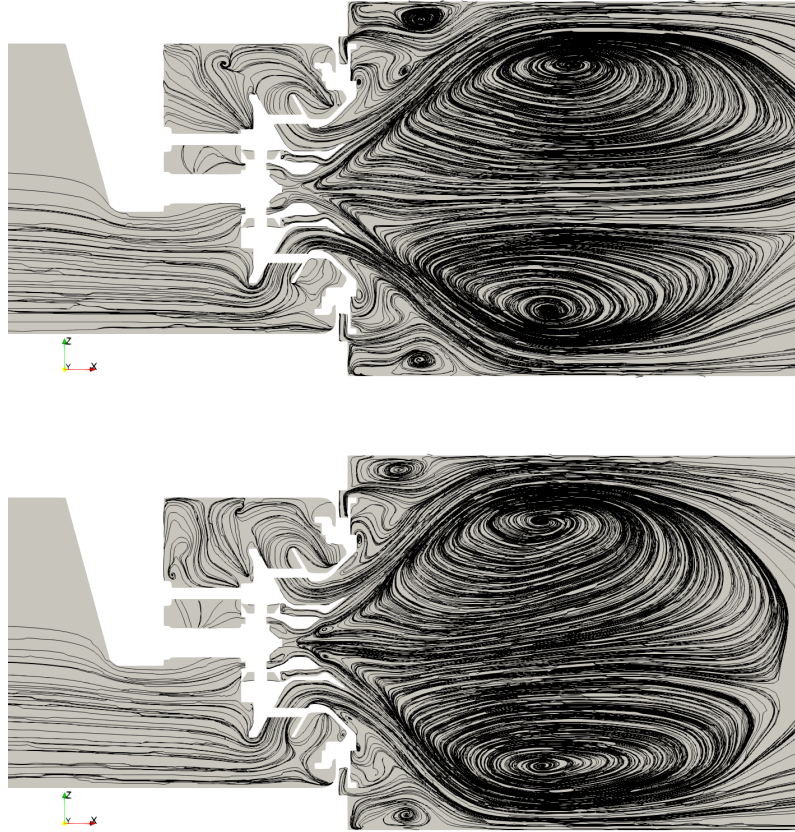


Figure 4.18: Comparison of pseudo-streamlines of mean velocity in the vertical plane ($y = 0$ mm) between ZDES (top) and LES (bottom).

The mean friction is compared in Figs. 4.26 (ZDES) and 4.27 (LES). The maximum level of friction, located in the change of curvature of the outer radial swirler wall, is higher in the ZDES (around 200 N.m^{-2}) than in the LES (around 100 N.m^{-2}). Also, the friction distribution is different between the two simulations. In the ZDES, the friction is low (below 40 N.m^{-2}) in the swirling vanes and on the swirler wall downstream. The area of high friction is narrow and located at the exit of each swirling vane. In the LES, the friction reaches 50 N.m^{-2} in the swirling vanes and it features higher relative levels with respect to the maximum value downstream in comparison with the ZDES. Again, the peak values of friction are retrieved at the exit of the swirling vanes.

To understand more precisely how the boundary layers are treated by both simulations, two analysis are proposed.

The first analysis is the comparison of velocity profiles in wall units in the simulations with theoretical results for an attached boundary layer.

Figure 4.28 shows a post-processing of the velocity profiles in wall units in the

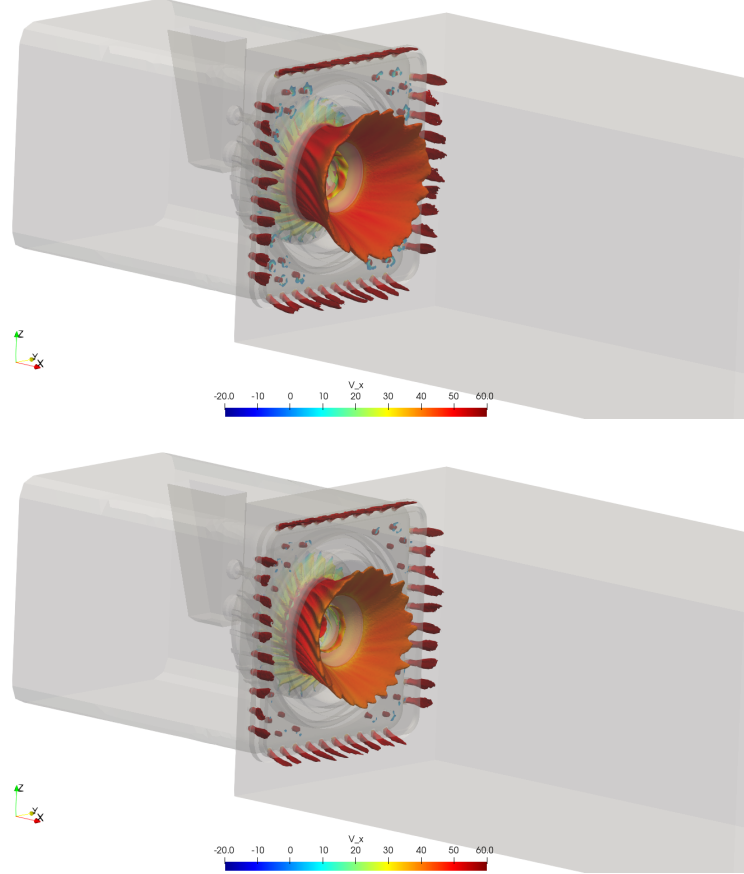


Figure 4.19: Comparison of a contour of velocity magnitude between ZDES (top) and LES (bottom), colored by the axial velocity.

boundary layers for the inner and outer walls of the main swirler at the change of curvature. In this figure, the first part of the black curve corresponds to the linear region of an attached boundary layer ($u^+ = y^+$) while the second one denotes the log region, defined by the equation $u^+ = 1/\kappa \log(y^+) + 5.1$ (where κ is the Kármán constant). This theoretical profile acts as a reference for the simulations for an attached boundary layer.

For the inner wall, by analyzing the velocity field for both simulations, the profile of an attached boundary layer should be found. For the outer wall, a different behavior is expected because the flow detaches in this region (see Fig. 4.13).

In order to assess the variability of the boundary layer velocity profiles, they are extracted at 24 angular positions in the injector, i.e. every 15° .

The first remark is that, as expected, the first values of y^+ are correct with respect to the turbulent modeling approach. For the LES, y^+ is around 70 for the outer wall and 100 for inner wall in the first cell, for all 24 profiles. For the

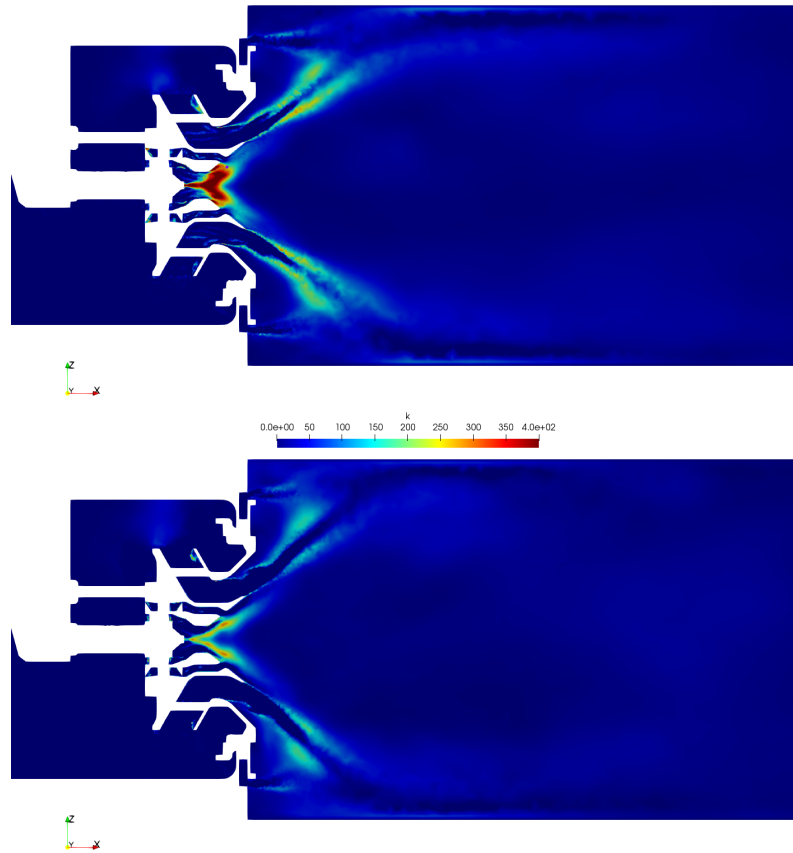


Figure 4.20: Comparison of mean resolved turbulent kinetic energy between ZDES (top) and LES (bottom).

ZDES, y^+ is below 1 for the first cells and the profiles are well discretized up to the end of the boundary layer.

For the inner wall, the linear region is well retrieved by the ZDES. The profile for high y^+ (above 100) is similar for both simulations and does not have the same slope as the theoretical one. This discrepancy with the analytic solution for an attached boundary layer can be attributed to the effect of curvature and swirl.

For the outer wall, the simulations predict two different types of profiles. In the LES, the values of u^+ are close to the analytic solution for an attached boundary layer in the log region. In the ZDES, the analytic profile is not recovered. Indeed, negative values of u^+ are found in the linear region, which means that at this position, the flow is already detached in the ZDES. In the log region, the values of u^+ are much higher (up to 35) than the analytic solution. This behavior shows the complex form of the boundary layer in this region. This also highlights a major difference between LES and ZDES: even if the two

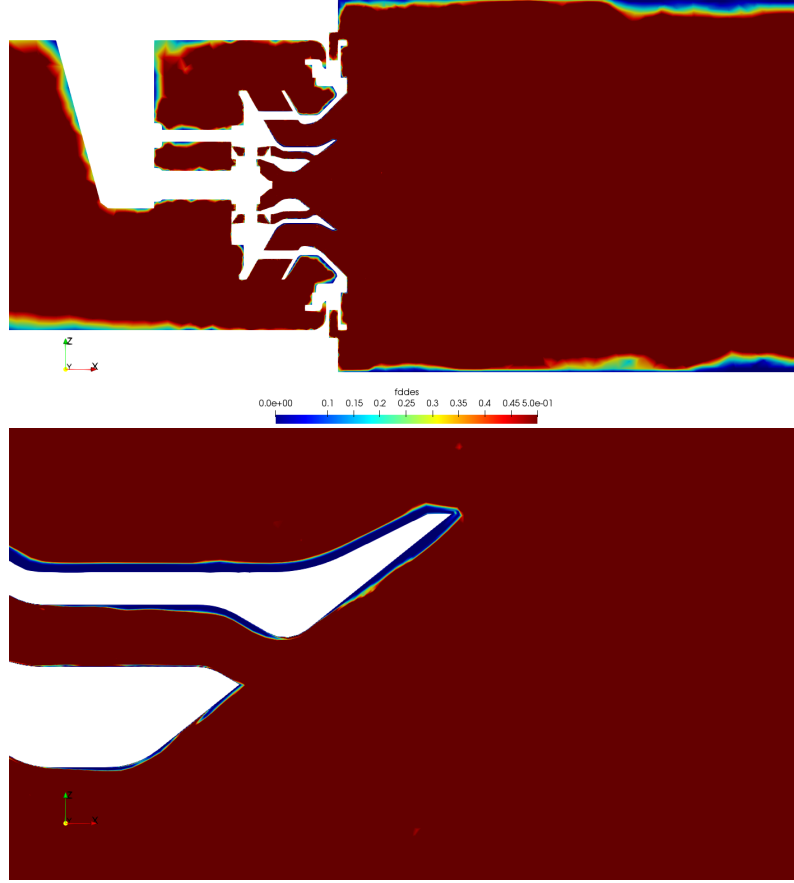


Figure 4.21: Instantaneous field of f_d in the vertical plane ($y = 0$ mm). Top: general view, bottom: focus on the swirler walls.

simulations predict similar flow topologies in the chamber, the boundary layers are treated very differently.

In the second analysis, global parameters of the boundary layers are computed with the mean quantities: the displacement thickness δ^* (Eq. 4.4), the momentum thickness θ (Eq. 4.5) and the shape factor H (Eq. 4.6):

$$\delta^* = \int_0^\zeta \left(1 - \frac{u_{//}}{u_{//,\infty}} \right) dy, \quad (4.4)$$

where $u_{//}$ is the velocity component parallel to the wall, $u_{//,\infty}$ the value of this quantity outside of the boundary layer, ζ the distance from the wall where $u_{//} = u_{//,\infty}$ and y is the direction normal to the wall,

$$\theta = \int_0^\zeta \left(1 - \frac{u_{//}}{u_{//,\infty}} \right) \frac{u_{//}}{u_{//,\infty}} dy, \quad (4.5)$$

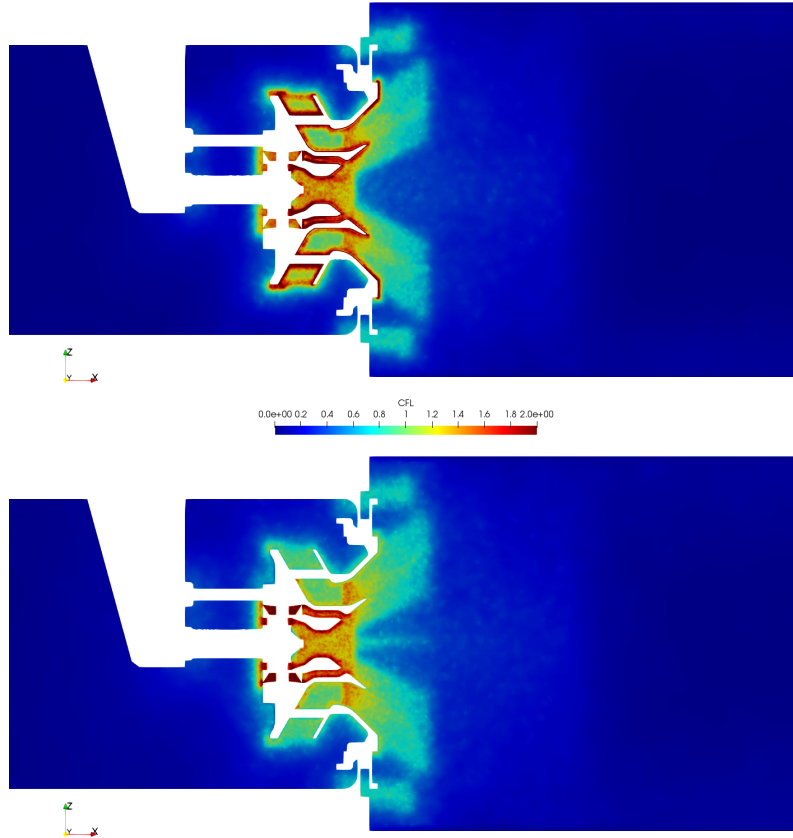


Figure 4.22: Instantaneous CFL number in the vertical plane ($y = 0$ mm). Top: ZDES, bottom: LES.

$$H = \frac{\delta^*}{\theta}. \quad (4.6)$$

These quantities are computed where the curvature changes in the outer radial swirler wall, for both sides of the swirler and with an angular resolution of 1° . The results for H are presented in Fig. 4.29 as a function of the angle in the injector, the corresponding line being the average H for each set of data.

The high values of H on the outer wall for the ZDES is characteristic of a detached boundary layer (Simpson (1996)). The boundary layer of the inner wall is attached and its shape factor in the ZDES is 1.2, a value close to 1.4, a typical value for zero pressure gradient turbulent boundary layers (Schlichting and Gersten (2016)).

The LES gives a shape factor of 1.15 for the inner boundary layer and of 1.25 for the outer one. These values show that the modeling approach (LES combined

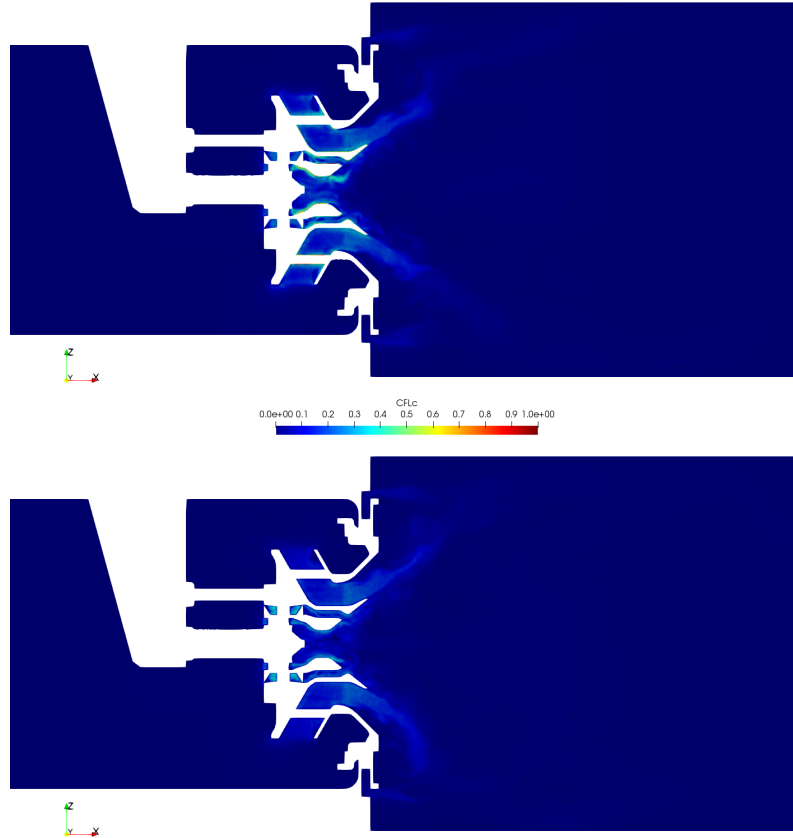


Figure 4.23: Instantaneous convective CFL number in the vertical plane ($y = 0$ mm). Top: ZDES, bottom: LES.

with wall law or ZDES) has a strong effect on the properties of the boundary layer.

Also, the values of H as a function of θ indicate the variability of the boundary layer properties. For both simulations, the value of H for the inner wall remains fairly constant over all values of θ . In contrast, for the outer wall, the dispersion of values is much higher for both simulations.

4.6 Conclusion

The TLC injector studied in this chapter is an interesting configuration for validating the ability of numerical simulations to predict the aerodynamics of representative aeronautical injectors. The LES approach is compared with a hybrid method, the ZDES. This is the first time that the ZDES is applied to this kind of geometry.

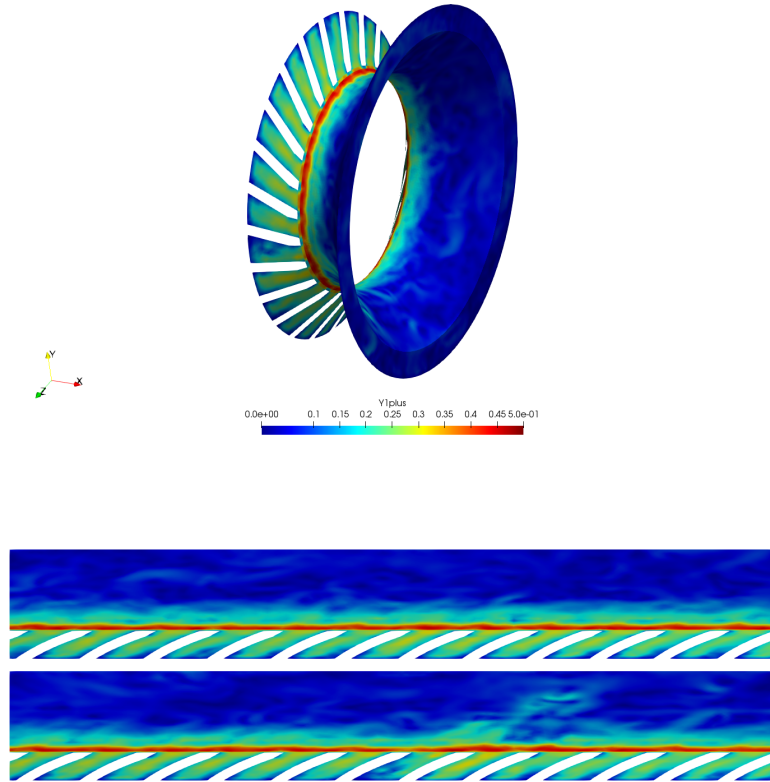


Figure 4.24: *Instantaneous surface distribution of y^+ on the outer radial swirler wall for the ZDES simulation. Top: 3D view, bottom: developed surface view.*

This comparison showed that both approaches are able to recover the flow topology observed in the experiments. Indeed, the two simulations show slight differences in the overall shape of the flow and on the velocity profiles that are available in the experimental database. The only differences are located on the wall, which is expected because the major difference between the two approaches is the treatment of the turbulence close to the wall. The effect on the results is the distribution of friction on the wall and its absolute value, and also the spatial resolution of the boundary layer profiles.

The results presented in this chapter validates the ability of the ZDES to predict the flow topology in a representative aeronautical injector in non-reacting conditions. This study is necessary before extending the use of ZDES in reacting conditions, where the LES results on the temperature profiles were not satisfactory.

The present injector is studied in reactive conditions and a comparison between LES and ZDES is performed to study the impact of the turbulence model on

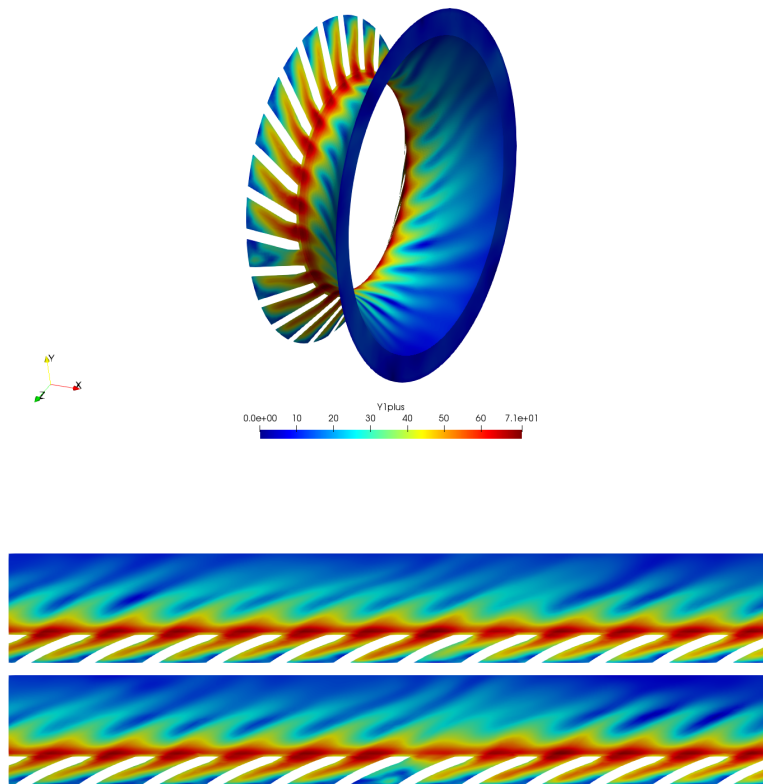


Figure 4.25: *Instantaneous surface distribution of y^+ on the outer radial swirler wall for the LES simulation. Top: 3D view, bottom: developed surface view.*

the prediction of the flame stabilization inside the combustion chamber in the next chapter.

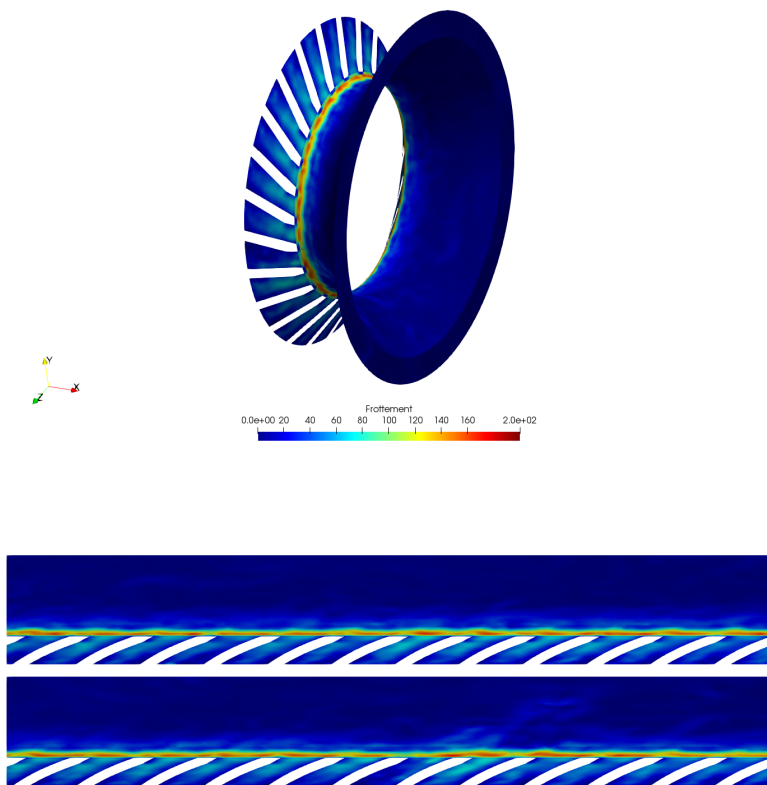


Figure 4.26: *Instantaneous surface distribution of friction τ_p on the outer radial swirler wall for the ZDES simulation. Top: 3D view, bottom: developed surface view.*

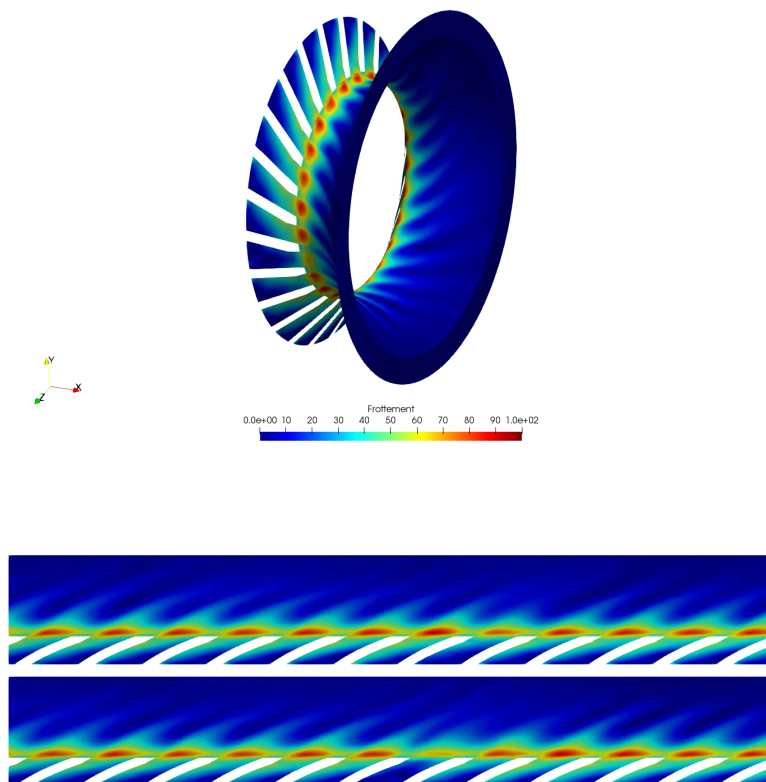


Figure 4.27: *Instantaneous surface distribution of friction τ_p on the outer radial swirler wall for the LES simulation. Top: 3D view, bottom: developed surface view.*

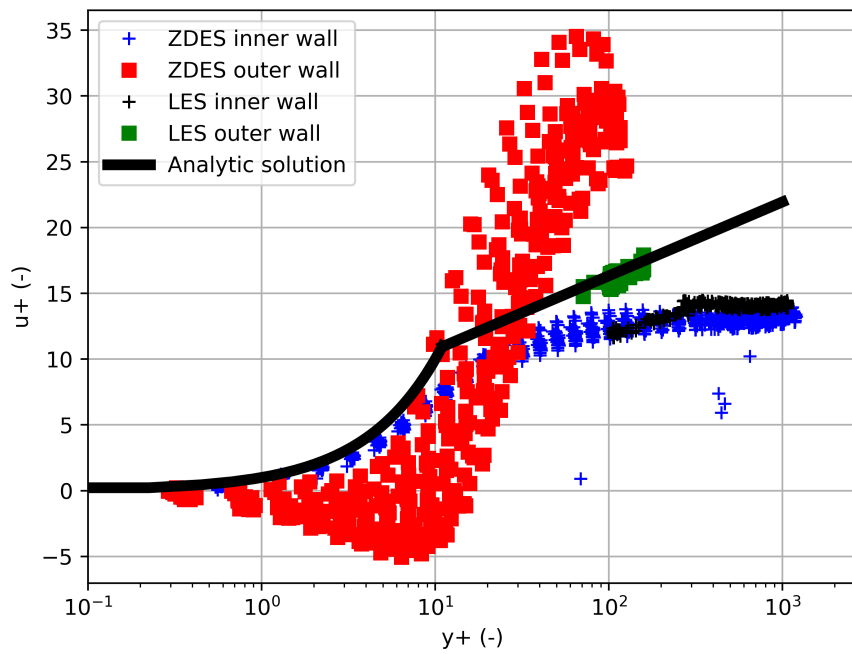


Figure 4.28: Velocity profiles in the boundary layers in wall units ($u^+ = f(y^+)$) for LES and ZDES for inner ('+' symbols) and outer (squares) radial swirler walls. Black line: analytic solution for an attached boundary layer

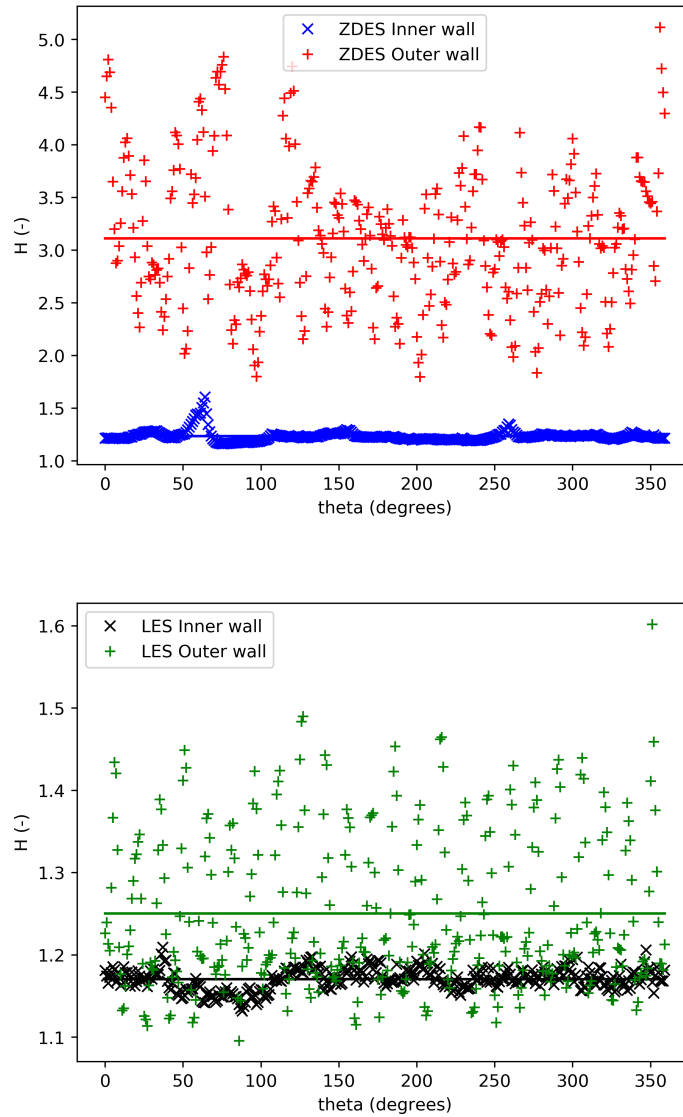


Figure 4.29: Shape factor of the boundary layer H based on the mean fields for simulations at the change of curvature of the radial swirler. Lines: average value over the angle θ , symbols: values for each angle θ . Top: ZDES, bottom: LES

Chapter 5

Comparison of the LES and ZDES approaches to the TLC configuration in reacting conditions

Contents

4.1	Context of the study	110
4.1.1	Issue of realistic aeronautical injector experiments	110
4.1.2	Choice of the injector	110
4.2	Objectives of the chapter	110
4.3	The TLC configuration	111
4.4	Simulations	114
4.4.1	General parameters	114
4.4.2	LES mesh	114
4.4.3	ZDES mesh	114
4.5	Results and analysis	115
4.5.1	Positions of the planes of interest	115
4.5.2	Comparison of the velocity between simulations and experiments	115
4.5.3	Validation of the ZDES switch behavior	124
4.5.4	Analysis of the CFL number distribution	125
4.5.5	Analysis of the treatment of the boundary layers in the simulations	127
4.6	Conclusion	134

This chapter focuses on the study of the TLC injector presented in the previous chapter, in reacting conditions. After the validation of the ZDES approach in non-reacting conditions, a comparison of LES and ZDES is performed with respect to experimental data.

5.1 Goal of this chapter

After the validation of ZDES in the previous chapter, the main goal of this chapter is to identify a computational strategy to simulate realistic aeronautical injectors, which can be extended to a complete chamber in the future. For this purpose, the focus is made here on the turbulence modeling, to evaluate the ability of a classical approach (LES) and an alternative approach (ZDES) to predict various quantities, such as temperature or species.

The chapter is divided in four parts. First, the TLC configuration is presented in its reacting setup. Then the numerical and modeling approach is explained. In a third part, the differences between the three simulations are highlighted. Finally, the results of the simulations are presented and analyzed.

5.2 The TLC configuration

The injector studied in this chapter is the TLC configuration, as in Chapter 4. The experimental reacting setup is slightly different from the non-reacting one. The fuel injection arm and the injector are identical in the two setups, but the surrounding elements are modified. The plenum has no longer a square section, but a circular one. The size of the chamber is decreased in reacting conditions to align the cooling films with the chamber walls. Its length is reduced and an additional module is added before the nozzle for new experimental diagnostics. In reactive conditions, the position of the flame is estimated by PLIF (Planar Laser Induced Fluorescence) of the OH radical and the distribution of gaseous kerosene by PLIF of a representative aromatic specie of kerosene in the medium plane of the injector and in several transverse planes. Temperature levels are measured with CARS (Coherent Anti-Stokes Raman Scattering) at several positions in the chamber. The soot volume fraction is measured by LII (Laser Induced Incandescence) in the medium plane. Finally, a measurement arm is added in the reactive setup after the chamber and before the nozzle to measure species mass fractions and the temperature of the burnt gases.

For computational purposes, the experimental geometry in reactive conditions is modified. The cooling film pipes and the collar perforation are simplified as an equivalent inlet. A global view of the computational domain, without the atmosphere, is presented in Fig. 5.1. The differences with the non-reacting computational domain (Fig. 4.4), described above, are visible.

Figure 5.2 presents the different air paths in the TLC configuration in reacting

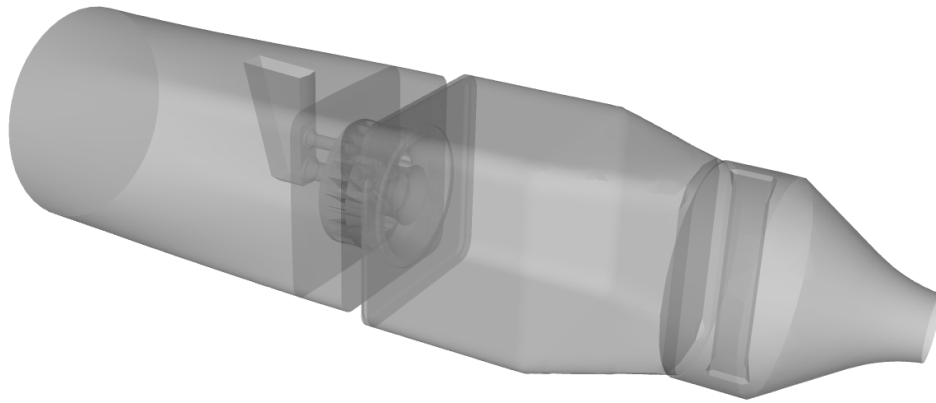


Figure 5.1: Global TLC computational domain view. The atmosphere is omitted.

conditions and highlights the positions of the swirlers and the reduction of section of the chamber.

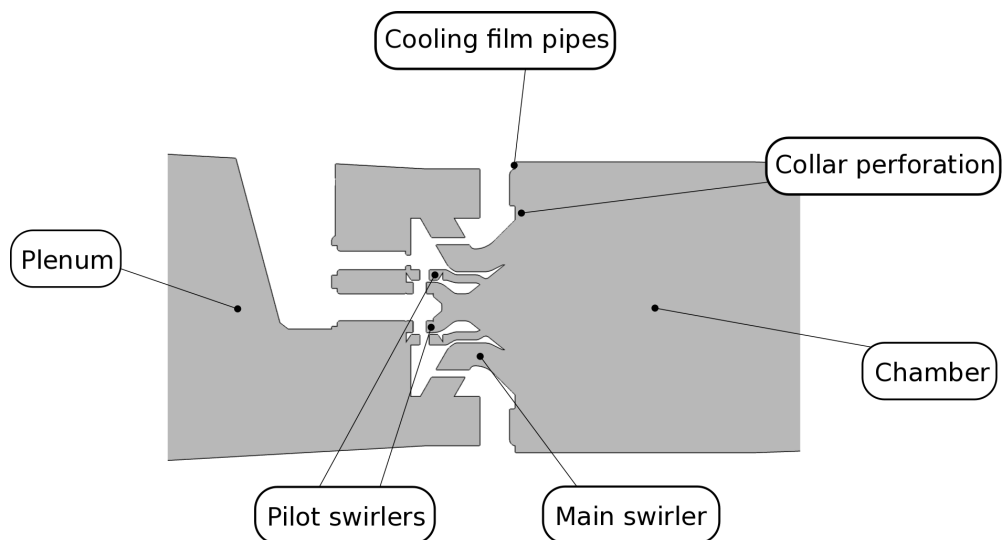


Figure 5.2: Air paths in the TLC configuration in the reacting setup.

5.3 Simulations

5.3.1 General parameters

Two simulations are compared in this work. They share the same numerical setup and only differ by the turbulence approach and the related mesh. Indeed, the mesh is adapted near the wall for each approach, as it will be shown later. The timestep for the temporal integration is $\Delta t = 2.10^{-7}$ s.

The model for turbulent combustion is TFLES-FPI, presented in Sec. 1.4.3.2. The progress variable Y_c is defined in Eq. 5.1 with the mass fractions of the transported species:

$$Y_c = \frac{Y_{CO_2}}{\mathcal{M}_{CO_2}} + \frac{Y_{CO}}{\mathcal{M}_{CO}} + \kappa \frac{Y_{NO}}{\mathcal{M}_{NO}}, \quad (5.1)$$

where κ is chosen equal to 100 and is designed to represent the slow chemistry of the NO in the post-flame region (Boucher (2015)).

The statistics are averaged over 50 ms for the LES and 30 ms for the ZDES, which was verified to be enough for a good convergence of the mean and RMS quantities. The boundary conditions are summarized in Table 5.1 for the gas and in Table 5.2 for the spray.

Boundary	Type
Walls	No-slip wall with logarithmic wall law with imposed temperature of 700 K
Plenum inlet	Subsonic inlet, mass flow rate: 485 g/s, temperature: 592 K
Cooling films equivalent inlet	Subsonic inlet, mass flow rate: 205 g/s, temperature: 592 K
Collar perforation inlet	Subsonic inlet, mass flow rate: 27 g/s, temperature: 592 K
Atmosphere	Subsonic outlet

Table 5.1: Gas boundary conditions of the TLC simulations.

5.3.2 LES mesh

The mesh used for the LES is a hybrid mesh with a single layer of triangular prisms on the wall with a thickness of 200 μm and tetraedra elsewhere. The general features of the LES mesh are shown in Fig. 5.3 (top). The single prism layer of the LES mesh is highlighted in Fig. 5.4 (top).

Boundary	Type
Pilot injection	100 point injectors (forming a hollow cone), total mass flow rate: 6.434 g/s, temperature: 338 K, diameter: 15 μm , axial velocity: 37.67 m/s, radial velocity: 21.75 m/s
Multipoint injection	1 injection patch per hole (24 total), total mass flow rate: 6.434 g/s, temperature: 343 K, diameter: 25 μm , normal velocity: 1.82 m/s
Walls	wall with rebound, minimum angle: 1°, maximum angle: 2°, energy restitution coefficient: 0.1
Atmosphere	Free boundary

Table 5.2: *Spray boundary conditions of the TLC simulations.*

5.3.3 ZDES mesh

The mesh used for the ZDES shares the same characteristic cell size in the volume as the LES mesh but contains more prism layers near the walls, as it is explained in Chapter 4 (Sec. 4.4.3). The same properties are chosen for both geometries.

The properties of the meshes are summed up in Tab. 5.3.

	LES mesh	ZDES mesh
Number of cells (total)	15 495 858	21 704 765
Number of tetraedra	15 245 340	18 532 571
Number of prism layers	1	22
Number of prisms	214 002	3 075 949
Thickness of the first prism layer	200 μm	1 μm
Target y^+ at the wall	≈ 100	< 1

Table 5.3: *Meshes characteristics.*

5.4 Results and analysis

5.4.1 Analysis of the behavior of the ZDES approach

As the ZDES is a zonal approach, the quantity that controls the zones, f_{DDES} , is fundamental and must be verified, as it was in Chapter 4. Figure 5.6 shows a field of f_{DDES} in the central vertical plane.

If it is equal to 0, it means that the ZDES behaves in RANS and if it is equal to 1, the ZDES behaves as a LES. This figure validates the switch between RANS and LES modes: the major part of the combustion chamber is in LES mode, because in this region the most important phenomenon is the mixing. The RANS mode is only present in the boundary layers of the injector, where

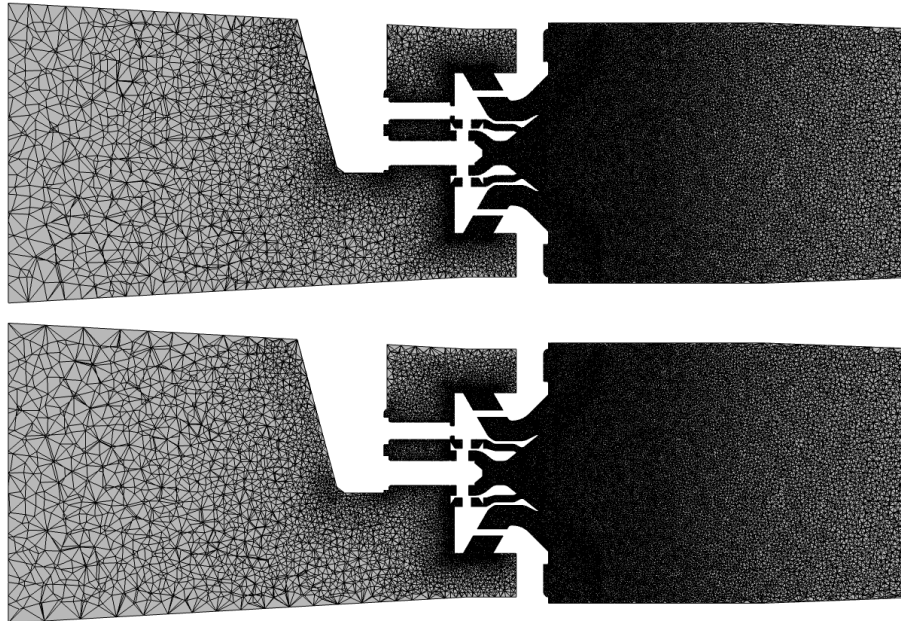


Figure 5.3: General view of the meshes. Top: LES mesh, bottom: ZDES mesh.

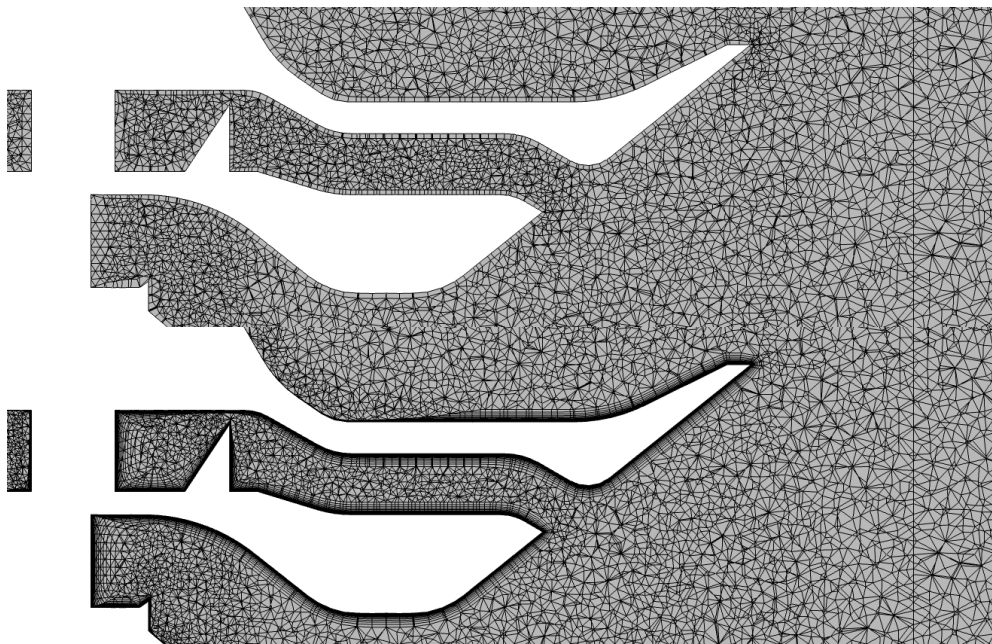


Figure 5.4: Close-up view on the prism layers of the meshes. Top: LES mesh, bottom: ZDES mesh.

it is designed to be activated. As for the cold simulations, the under-resolution of the boundary layers outside of the injector explains the aspect of the f_{DDES}

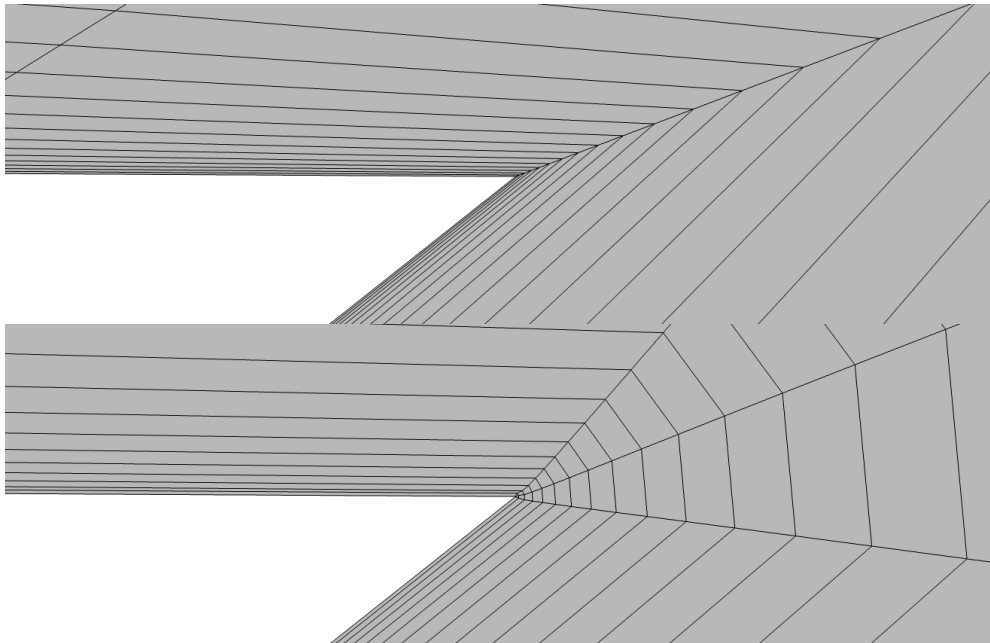


Figure 5.5: Close-up view of the treatment of convex areas. Top: ZDES mesh without treatment, bottom: ZDES mesh with treatment.

field close to the chamber walls.

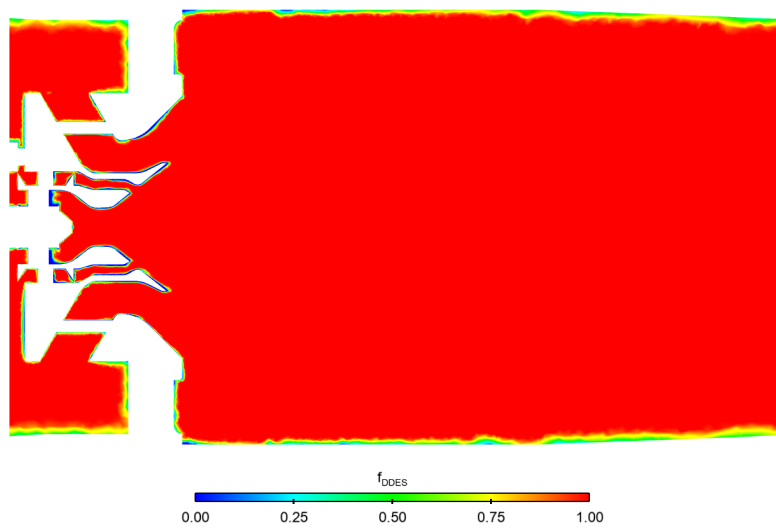


Figure 5.6: Field of f_{DDES} in the ZDES. 0 is the ZDES in RANS mode and 1 in LES-like mode.

5.4.2 Comparison of flow topology between LES and ZDES

The flame stabilization in swirled injectors is mostly driven by aerodynamics. Velocity profiles are compared for the simulations in Fig. 5.7. The effect of the cooling films is observed on the edges of the chambers in the LES and ZDES profiles. The two main peaks of velocity correspond to the flow exiting the main swirler. The profiles of LES and ZDES are very similar.

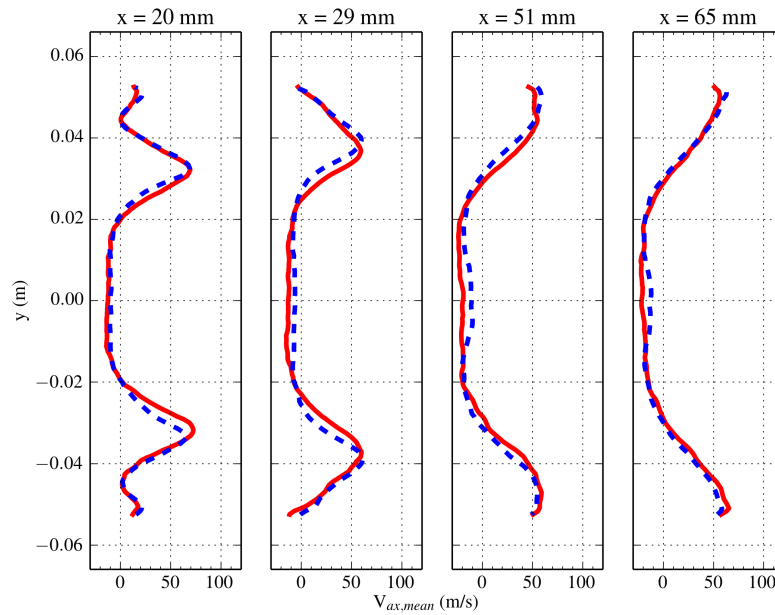


Figure 5.7: Comparison of the mean axial velocity profiles for four positions in the chamber. Dashed blue line: LES, solid red line: ZDES.

Figure 5.8 compares the mean axial velocity in the middle plane of the injector between LES and ZDES. The contour $V_x = 0$ m/s is represented as a black line. The recirculation zones in these two simulations have the same spatial position. The difference lies in the velocity at the exit of the injector. The LES reaches the peak velocity close to the outer wall of the main swirler while the ZDES features a more distributed velocity field.

5.4.3 Analysis of the wall treatment

The major difference close to the walls between ZDES and LES approaches is the treatment of the boundary layers. The analysis of the flow topology revealed a massive flow detachment on the outer wall of the main swirler. Figure 5.9 shows an instantaneous distribution of y^+ on this wall for the LES and the ZDES. The massive flow detached can be linked to a drop of y^+ , since y^+ scales as the square root of the friction (see Eq. 1.28). It appears that the detachment appears further downstream in the LES.

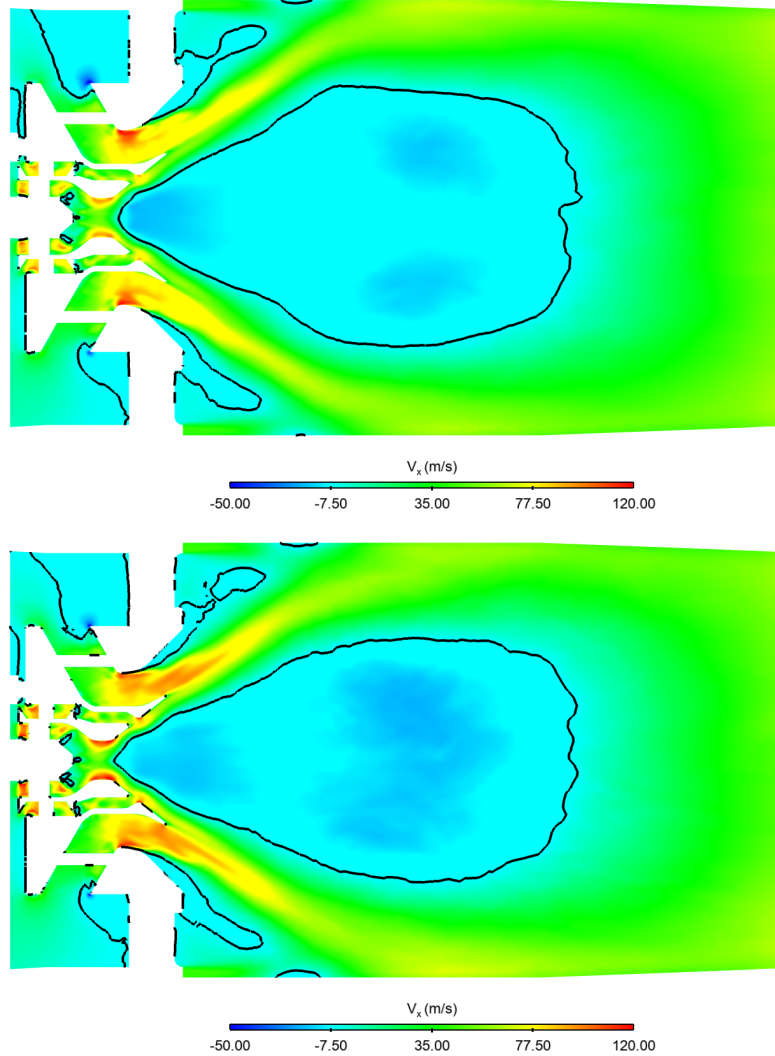


Figure 5.8: Comparison of mean axial velocity in the middle plane of the injector. Top: LES, bottom: ZDES. The black line represents $V_x = 0$ m/s.

The velocity profiles in the boundary layers of the outer and inner wall of the main swirler are analyzed at the axial position of inflexion of the main swirler outer bowl (the red line in Fig. 4.8). Figure 5.10 presents the boundary layers velocity profiles for the outer wall (in red) and the inner wall (in blue) of the main swirler for the LES and the ZDES in wall units. The black line corresponds to the analytic solution for an attached boundary layer presented in Chapter 4. The mesh for LES was designed to obtain $y^+ \approx 100$ in the first cell, while the ZDES requires $y^+ \approx 1$ in the first cell. The profiles of the outer wall are very different between the ZDES and the LES. The LES follows the log region while the ZDES reaches much higher values of u^+ . For the inner wall, the ZDES

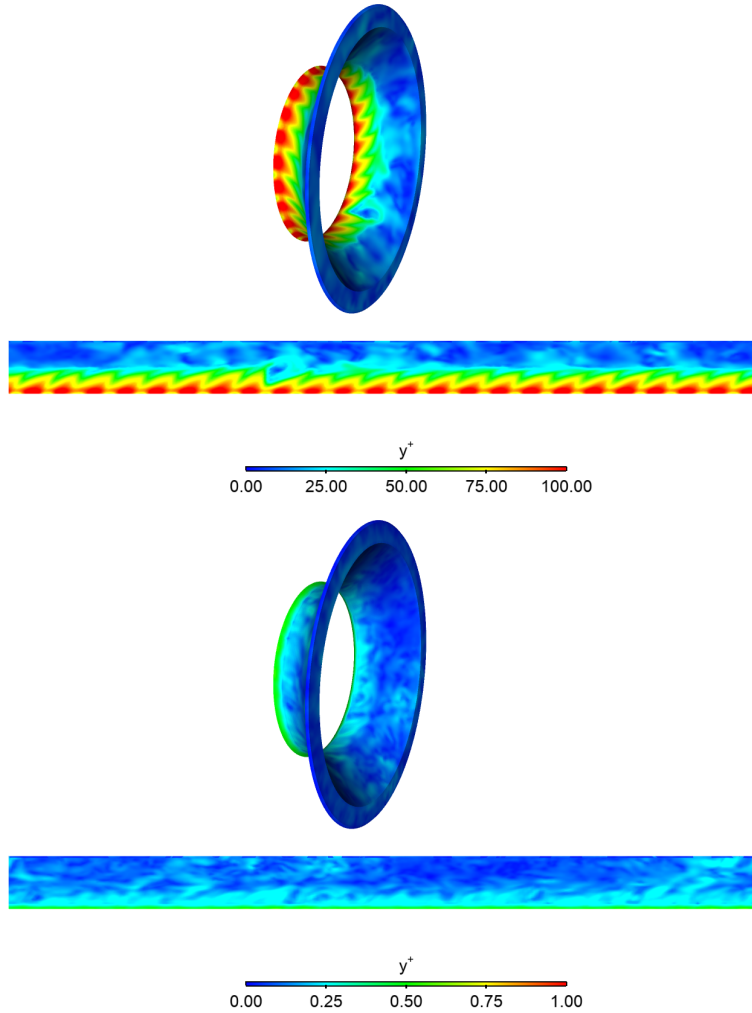


Figure 5.9: Instantaneous field of y^+ on the wall of the exterior main bowl. The first view is 3D, while the second one is the developed view of the first one around the axis of the injector. Top: LES, bottom: ZDES.

follows closely the theoretical profile up to $y^+ = 100$. The LES and ZDES predict the same value of u^+ above $y^+ = 100$.

In order to classify the boundary layers in both simulations, the shape factor H , introduced in Chapter 4 (Eq. 4.6) is computed. Figure 5.11 shows H as a function of the angular position in the injector for both walls. In the LES, the mean H values are close to 1.5 for both walls. This value is close to the value for an attached boundary layers. The ZDES predicts a shape factor H of 3.0 for the outer wall and 2.4 for the inner wall on average. These values are closer to the ones found in detached boundary layers. The analysis of the shape factor value highlights the difference between the two approaches. Indeed, the use of

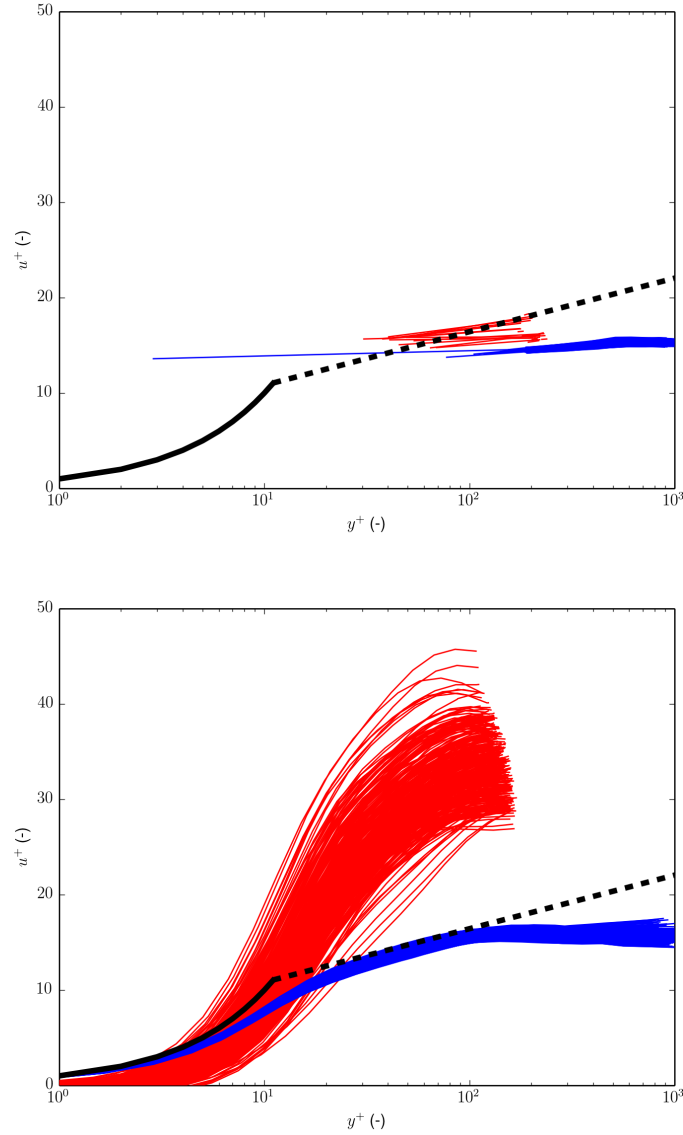


Figure 5.10: Velocity profile in wall units. Top: LES, bottom: ZDES.

a wall law in LES explains that the shape factor of the boundary layers is close to the one of an attached boundary layer. Since the boundary layer is meshed down to the viscous sublayer in ZDES, a wide range of shapes can be found.

5.4.4 Structure of the spray

Figure 5.12 isolates the droplets and compares their spatial distribution between LES and ZDES. They are colored with respect to their origin: blue for the

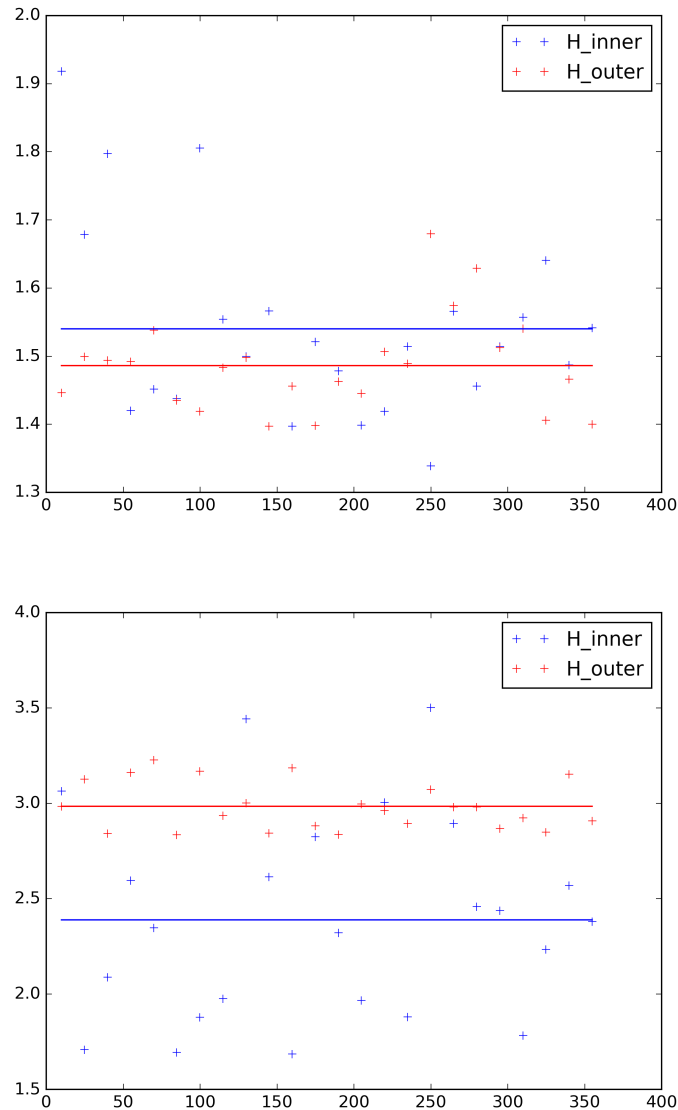


Figure 5.11: Shape factor H of the boundary layer as a function of the angular position in the injector. Top: LES, bottom: ZDES.

multipoint injection and red for the pilot one. The first observation is that there is no mixing between the droplets of the two injections. The major difference between the two simulations lies in the dispersion of the droplets coming from the multipoint injection. The droplets in the ZDES tend to quickly follow various paths, increasing the dispersion while in the LES, the droplets remain on the same path for a long time.

In the previous sections, the comparison of the velocity fields between LES and

ZDES did not highlight major differences in the core of the flow. The only difference is the treatment of the boundary layer, and especially the discretisation of the velocity profile in the vicinity of the wall.

For the multipoint injection, the injection is modelled by patches of injection that generate particles (see Tab. 5.2). The particles are injected with a fixed velocity, in the normal direction to the wall.

By using Eq. 1.11, with $\rho_p \approx 800 \text{ kg.m}^{-3}$, $d_p = 25.10^{-6} \text{ m}$ for the multipoint injection, $\mu_g \approx 3.10^{-5} \text{ kg.m}^{-1}.s^{-1}$ (for air at 592 K), $u_0 \approx 50 \text{ m.s}^{-1}$ and $l_0 = 1 \text{ cm}$ (approximately the swirling vanes height), the Stokes number of these particles is around 5. Since $Stk \approx 1$, the flow around particles has an effect on their trajectory.

Therefore, the difference of boundary layer resolution between LES and ZDES explains the variety of trajectories for the particles of the multipoint injection observed in the ZDES and the fairly identical paths followed by the particles injected through the same hole in the LES.

Figure 5.12 raises other questions. The first one is the amount of resolved turbulence in the main swirler. It appears that large structures interact with particles as they grow smaller by evaporation in the chamber. However, in the main swirler, especially for the LES, the particles appear to stay exactly on the same path, with no visible effect from the gas. Three hypotheses can explain this:

- the mesh may not be sufficiently refined in the main swirler to capture resolved vortices,
- there is not enough large structures generated in the plenum, which do not introduce enough velocity fluctuations at the inlet of the main swirler,
- the particles stay close to the inner wall, where the velocity profile is not well discretised in the LES.

Both the ZDES and LES can suffer from the first two hypotheses.

5.4.5 Prediction of the pressure drop in the injector

The pressure drop in the injector was measured in the experiments with pressure sensors placed in the plenum and the chamber. The pressure drop was estimated in the simulations with probes placed in the plenum and at several positions in the chamber.

Table 5.4 presents the pressure drop in the injector for the experiments and the three simulations. The pressure drop is well reproduced by the ZDES. The LES predicts a lower pressure drop, but remains close to the experimental value.

The discrepancy between experiments and simulations originates probably from the absence of the cooling films and the collar perforation internal geometry in the computational domain.

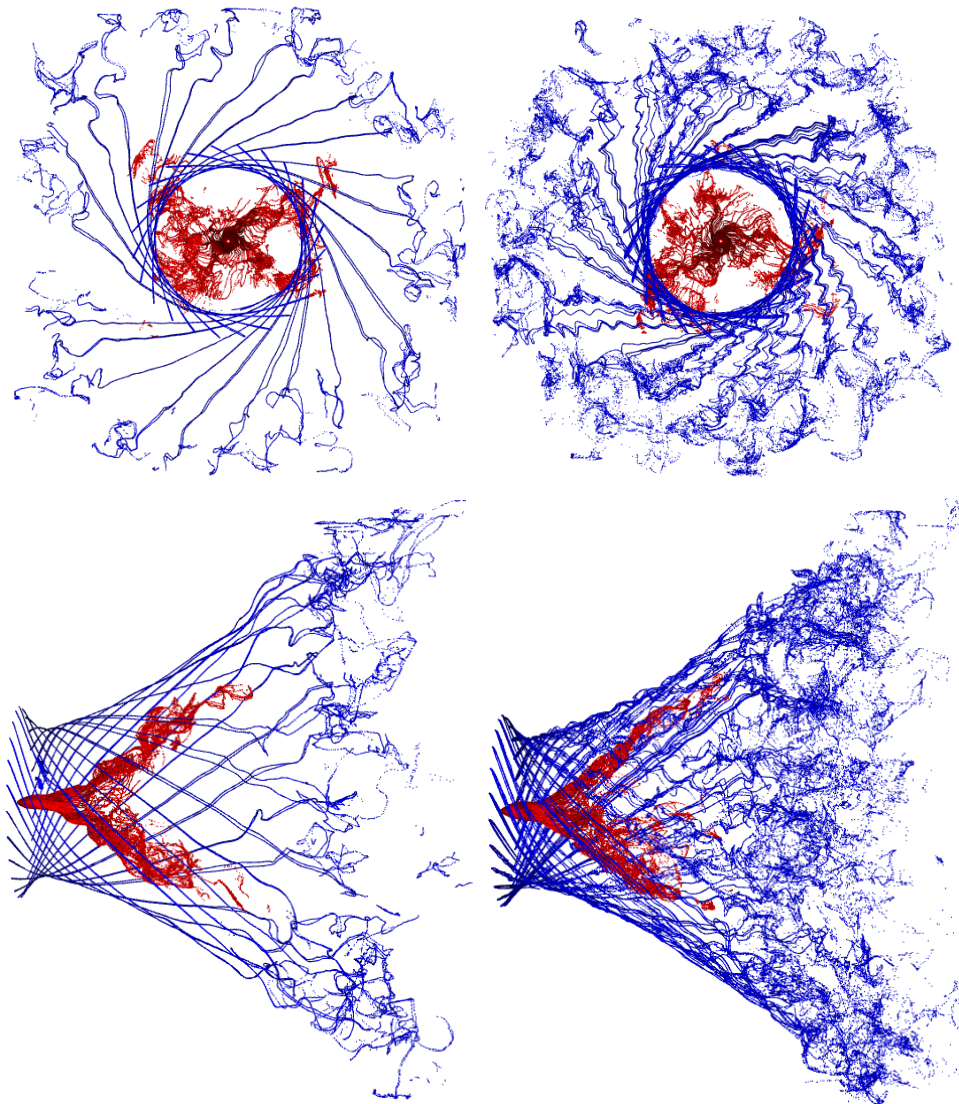


Figure 5.12: *Instantaneous comparison of LES and ZDES spray structure, as seen from the plenum (top), and as seen from the side of the chamber (bottom). The droplets are colored by their origin: red for the pilot injection and blue for the multipoint injection. Left: LES, right: ZDES.*

	Experiments	LES	ZDES
Pressure drop (Pa)	43 000	39 500	40 500

Table 5.4: *Pressure drop in the injector.*

5.4.6 Prediction of the distribution of fuel and OH

The distribution of fuel and OH was measured in the experiments with PLIF. Figure 5.13 compares qualitatively the normalized mean heat release rate in the simulations with the normalized mean PLIF-OH signal for the experiments. The PLIF-OH reveals the structure of the flame as a single broad branch. The simulations also predict a single branch, but much narrower.

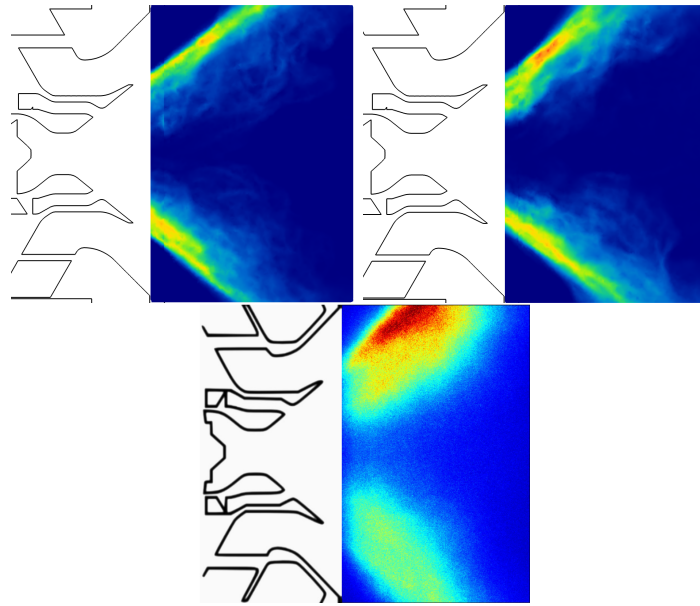


Figure 5.13: Mean comparison of normalized heat release rate (for the simulations) and OH PLIF signal (for the experiments). Top left: LES, top right: ZDES, bottom: experiments.

Figure 5.14 combines the instantaneous data of OH and kerosene. The kerosene presence is shown as a red isoline representing $Y_{kero} = 0.01$. In the experiments, two locations can be found: one in the inner part of the flow, coming from the pilot injection, and another one in the outer part of the flow, as a result of the evaporation of the droplets of the multipoint injection. A similar conclusion is drawn from the isoline of kerosene mass fraction in the simulations. The PLIF OH signal covers the same area as in the mean field. In the simulations, the flame front is thin and wrinkled and some flame structures can be observed at the center.

PLIF measurements were also made in radial planes. Figure 5.15 presents the comparison of instantaneous kerosene for the first plane, at 4 mm after the chamber back wall in a parallel plane to it. The central circular structure are similar between the experiments and the simulations. In the LES, the multipoint injection pattern can be noticed in the outer region. This effect is highlighted in Fig. 5.16, which shows mean kerosene mass fractions.

The radial planes for OH are reported in Figs. 5.17 and 5.18. As for the

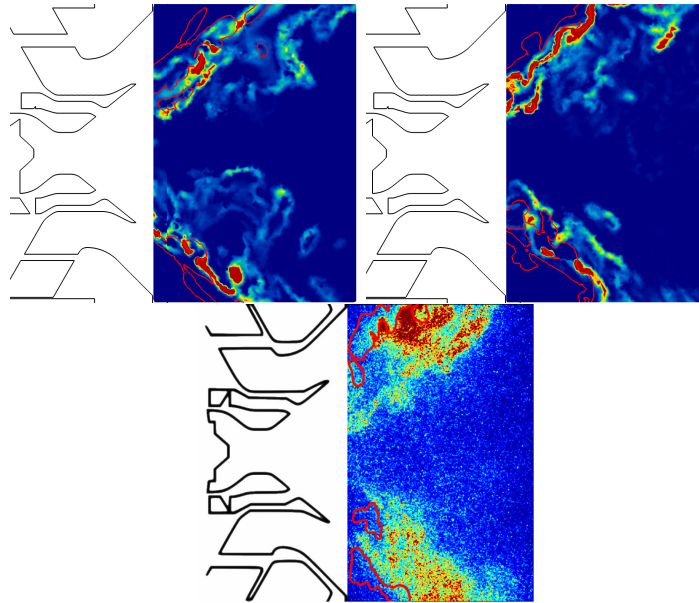


Figure 5.14: *Instantaneous comparison of normalized heat release rate (for the simulations) and OH PLIF signal (for the experiments) with a red iso-contour of $Y_{kero} = 0.01$. Top left: LES, top right: ZDES, bottom: experiments.*

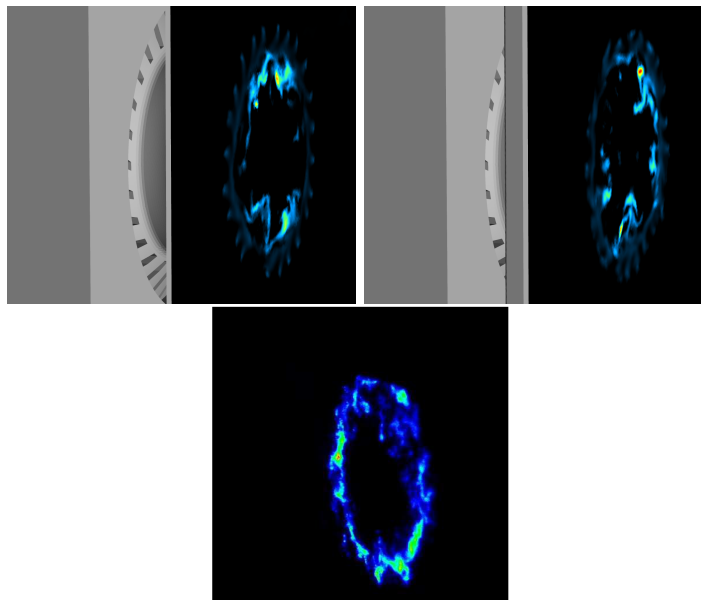


Figure 5.15: *Instantaneous comparison of normalized kerosene mass fraction (for the simulations) and PLIF signal (for the experiments) at 4 mm from the chamber back wall. Top left: LES, top right: ZDES, bottom: experiments.*

middle plane, the simulations predict a thinner flame brush with respect to the

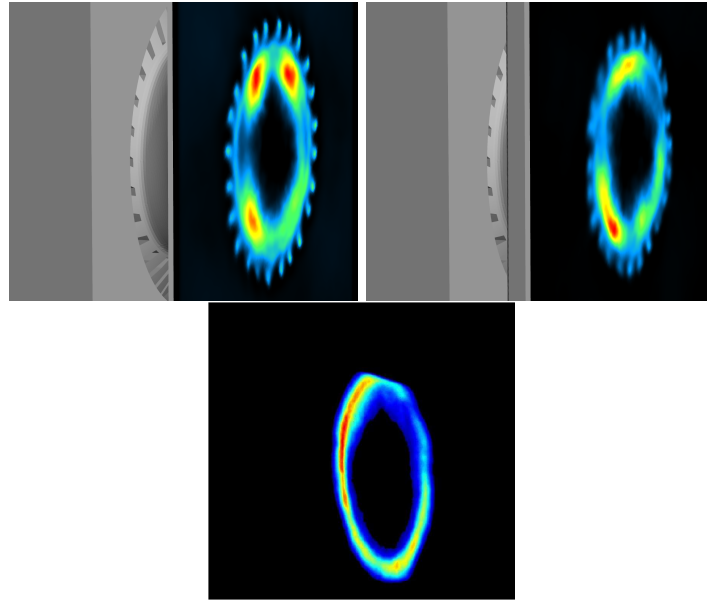


Figure 5.16: Mean comparison of normalized kerosene mass fraction (for the simulations) and PLIF signal (for the experiments) at 4 mm from the chamber back wall. Top left: LES, top right: ZDES, bottom: experiments.

experimental data.

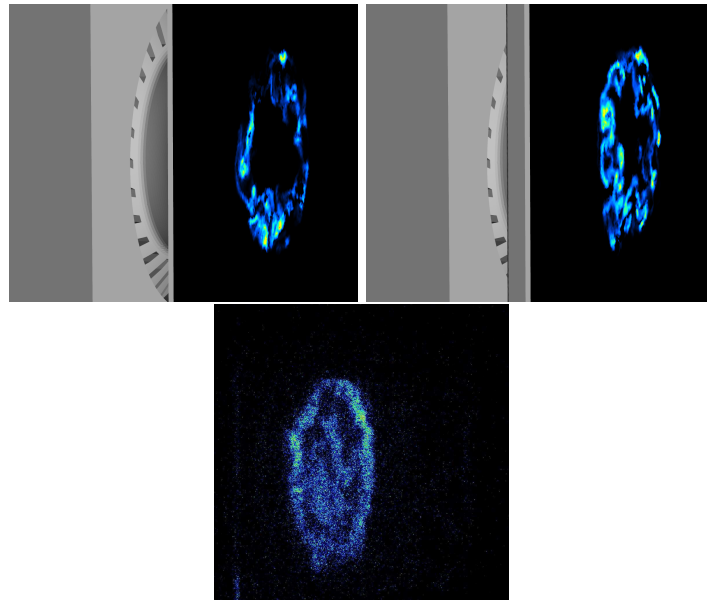


Figure 5.17: Instantaneous comparison of normalized heat release rate (for the simulations) and OH PLIF signal (for the experiments) at 4 mm from the chamber back wall. Top left: LES, top right: ZDES, bottom: experiments.

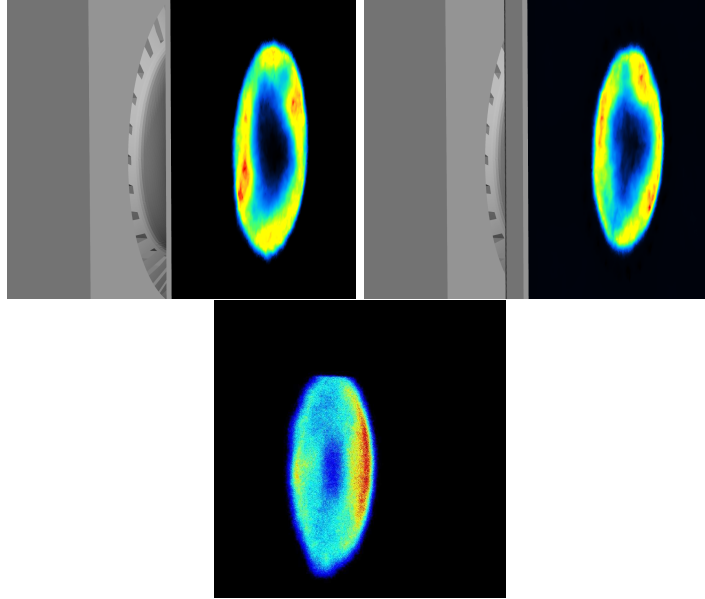


Figure 5.18: Mean comparison of normalized heat release rate (for the simulations) and OH PLIF signal (for the experiments) at 4 mm from the chamber back wall. Top left: LES, top right: ZDES, bottom: experiments.

5.4.7 Prediction of the pollutant emissions

The emission index is a quantity used by manufactures and regulation agencies to estimate the pollutant emissions. The emission index of specie N is defined as:

$$ie_N = \frac{1000 \int_S \overline{\rho \mathbf{v} Y_N} d\mathbf{S}}{\overline{\dot{m}_{fuel}}} \quad (5.2)$$

where ie_N is the emission index of specie N, S the exit section, $\rho \mathbf{v}$ the momentum, Y_N the mass fraction of specie N and $\overline{\dot{m}_{fuel}}$ the injected mass flow rate.

Table 5.5 presents the emission indexes for CO and fuel for the experiments and the simulations.

Emission index ($\text{g} \cdot \text{kg}_{KERO}^{-1}$)	Experiments	LES	ZDES
ieCO	173.1	100.3	116.74
ieKERO	83.3	34.42	34.23

Table 5.5: Emission indexes for CO and fuel.

Both emission indexes are underestimated by the simulations. This discrepancy can have multiple causes. For instance, the tabulation is a source of error for

the modeling of the CO chemistry (Fiorina *et al.* (2005)). Also, the low value for the fuel in the simulations means that more fuel is burned compared to the experimental one. Finally, there is a major difference between the way these indexes are estimated in experiments and simulations. In the experimental setup, the gas is analyzed close to the exit of the chamber through a series of holes. In the simulations, the mean field in the plane of the series of holes is directly postprocessed using Eq. 5.2.

5.4.8 Comparison of average temperature

Figure 5.19 presents a general view of the LES and ZDES, composed of an instantaneous field of temperature in the middle plane of the injector, the walls of the swirlers colored by y^+ and the fuel droplets colored by their temperature. The instantaneous field of temperature highlights a major difference between the ZDES and the LES. In the ZDES, the central part of the flow shows a temperature below 1500 K after the flame whereas the LES features higher temperatures, between 1500 and 1900 K.

A major interest of the TLC configuration is the measurement of temperature with CARS technique inside the combustion chamber. Four profiles are available at 20, 29, 51 and 65 mm from the end plane of the injector. Figure 5.20 presents the comparison of temperature profiles in the chamber between the experimental data, the LES and ZDES simulations. The first profile at 20 mm, the closest to the injector, shows a fairly constant temperature of 1850 K with the CARS measurements. The simulation profiles feature an inhomogeneous evolution. The fresh gases are on the outer position of the chamber. Both simulations underpredict the temperature at the center of the flow by 200 K for the LES and 400 K for the ZDES.

The measured temperature profile at 29 mm displays a large drop compared to the previous profile, at 1350 K. LES and ZDES exhibit a quick broadening of the flame brush. The ZDES is the closest to experimental data for all points. The profile at 51 mm in the experimental database is very similar to the previous one. At this position, the flame brushes of the three simulations become closer. Both LES overpredict the temperature by 200 K. The ZDES features a temperature very close to the experiments. The same observations hold at 65 mm.

Another experimental device is installed at the end of the combustion chamber to measure the properties of the flow. It is composed of a gas analyzer that details the composition and the temperature of the burnt gases. The comparisons between simulations and experiments are presented in Fig. 5.21. The LES and the ZDES follow the same trend as the experimental measurements.

The best results on temperature are obtained with the ZDES approach, except for the first profile in the chamber. The first profile is located the closest to the fuel injection and therefore is highly sensitive to what is imposed at these boundary conditions.

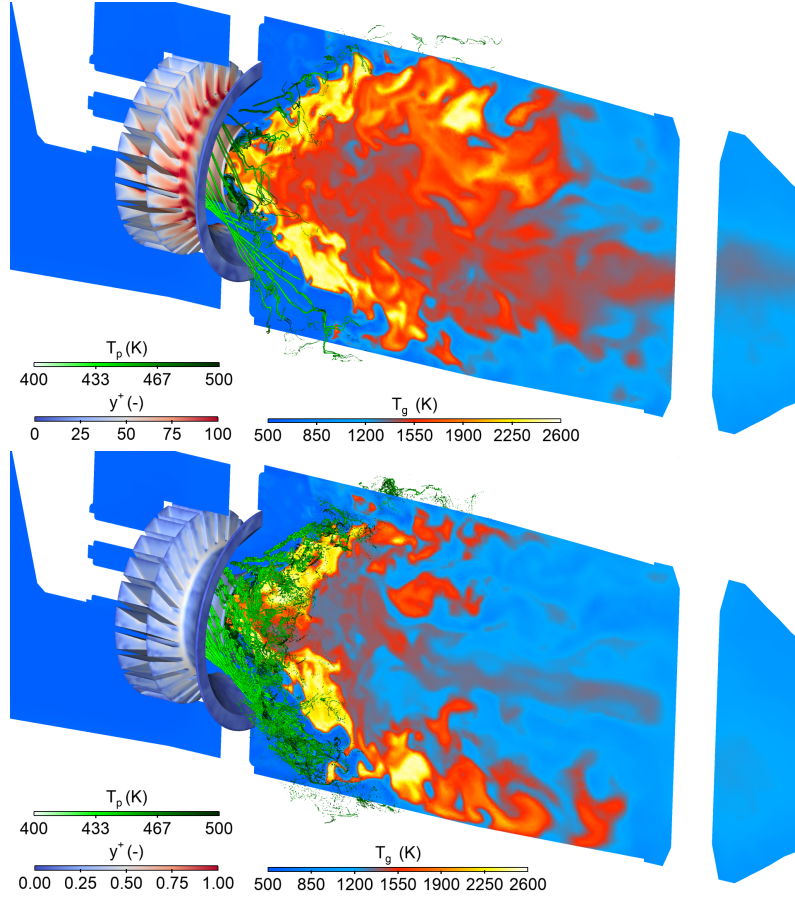


Figure 5.19: Instantaneous comparison of LES and ZDES on temperature field, spray structure and distribution of y^+ on the injector walls. Top: LES, bottom: ZDES.

5.4.9 Combustion regime analysis

The combination of complex aerodynamics and multiple injections of fuel introduces a wide range of possible combustion regimes. A way to determine the combustion regime is the Takeno criterion. It compares the orientation of the gradient of fuel and oxygen mass fractions. A Takeno index of 1 describes a premixed combustion regime, whereas -1 indicates a non-premixed flame structure.

Following the work of [Boucher \(2015\)](#), three indicators based on the Takeno index are introduced:

$$\xi_p = \max \left(0, \frac{\nabla Y_{O_2} \cdot \nabla Y_{C_{10}H_{22}}}{|\nabla Y_{O_2}| \cdot |\nabla Y_{C_{10}H_{22}}|} \right) \quad (5.3)$$

$$\xi_d = \max \left(0, -\frac{\nabla Y_{O_2} \cdot \nabla Y_{C_{10}H_{22}}}{|\nabla Y_{O_2}| \cdot |\nabla Y_{C_{10}H_{22}}|} \right) \quad (5.4)$$

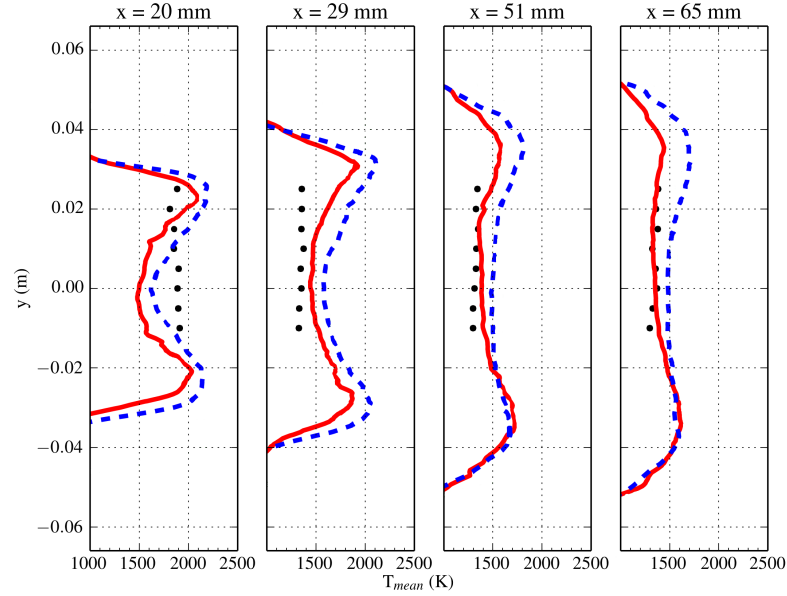


Figure 5.20: Comparison of temperature profiles for four positions in the chamber. Blue: LES, red: ZDES, black dots: experiments.

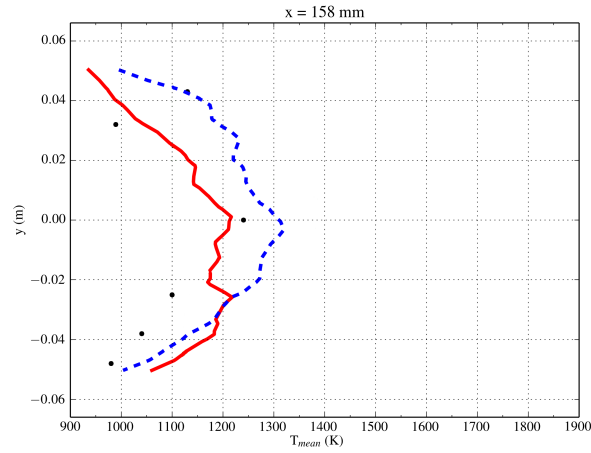


Figure 5.21: Comparison of temperature profiles at the exit of the chamber. Blue: LES, red: ZDES, black dots: experiments.

$$\xi_{pp} = 1 - \frac{\nabla Y_{O_2} \cdot \nabla Y_{C_{10}H_{22}}}{|\nabla Y_{O_2}| \cdot |\nabla Y_{C_{10}H_{22}}|} \quad (5.5)$$

By construction, $\xi_p + \xi_d + \xi_{pp} = 1$. For each cell of the computational domain, the indicators are computed based on the mean quantities. Figure 5.22 plots the distribution of heat release with respect to the equivalence ratio. The bars

are shaded with the combustion regime, based on the indicators introduced previously. The blue line corresponds to the global equivalence ratio ($\phi_g = 0.264$). A wide range of equivalence ratio is found, with a peak close to the stoichiometry. The major combustion regime, in terms of heat release, is the partially premixed one. ZDES and LES predict a similar distribution.

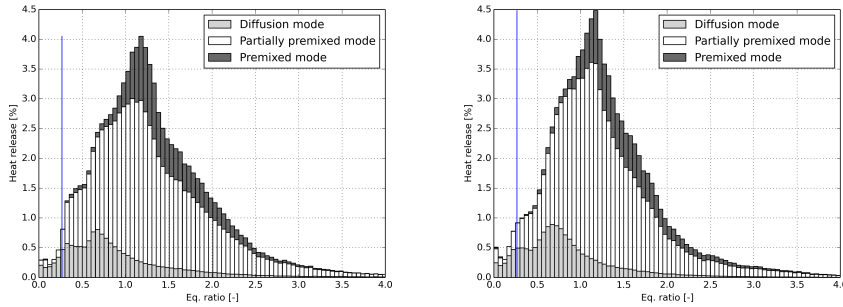


Figure 5.22: Comparison of the distribution of heat release with respect to the equivalence ratio, colored by the combustion regime. Left: LES, right: ZDES.

5.5 Conclusion

This chapter presents the second step in the study of the TLC injector in reacting conditions, after the study of the same injector in non-reacting conditions in the previous chapter. The focus is again made on the turbulence modeling. The LES and ZDES gave good results on the non-reacting configuration. The addition of two-phase flow and combustion represents a huge increase in the complexity of the physical phenomena that must be modeled. Previous works showed that LES was not able to recover the temperature profiles observed experimentally. A new LES is performed, which predicts a similar flow topology to the ZDES. However, the temperature profiles are now very well reproduced with the ZDES, but the new LES still fails to recover it. The effect of the turbulence approach on the dispersed phase is highlighted. The resolution of the boundary layers has a significant impact on the droplet trajectories and explains the difference between LES and ZDES, despite the similarities in the prediction of the flow topology.

Conclusion

The general objective of this thesis was to provide insight about modeling questions encountered in the simulations of aeronautical combustors. The main framework for the numerical choices was the use of tabulated chemistry with unsteady turbulent models.

Two axes were chosen to study the modeling choices: the ability to retrieve flame properties in non-adiabatic or two-phase conditions and the influence of the turbulent model on the flow topology in a complex geometry. For each axis, the simulations were compared with existing experimental databases. These comparisons led to the following achievements.

Major achievements

Study of the performances of the F-TACLES model in complex flow configurations

The thesis of [Mercier \(2015\)](#) led to the extension of the F-TACLES model to non-adiabatic flows. The challenges for this thesis were to determine if the F-TACLES model was able to:

- predict the correct shape of a non-adiabatic flame,
- recover the flame dynamics through the Flame Describing Function (FDF),
- predict the shape of a two-phase flame.

In the EM2C burner, fed with a $\text{CH}_4/\text{H}_2/\text{air}$ mixture, it was shown in [Mercier et al. \(2016a\)](#) that F-TACLES was able to predict the correct flame shape for two levels of H_2 enrichment, leading to an M flame shape for the higher level and a V flame shape for the lower one. This difference is explained by the heat losses in the outer recirculation zone that led to flame extinction in this region. In high levels of enrichment, the outer flame front is still present because of the H_2 content whereas this flame front was disappearing as the amount of H_2 decreased in the mixture. The new F-TACLES formalism, taking into account heat losses, was necessary to recover the correct flame shape. Despite these results, it was shown in this thesis that a residual outer flame front existed in the outer recirculation zone. This was attributed to the absence of strain effect on the flame front in the F-TACLES model.

For the same burner, in pulsed conditions, the comparison of the FDF showed

promising results with respect to experiments, as presented in [Chatelier et al. \(2019\)](#). The gain and the phase of the FDF were compared between simulations and experiments for several frequencies and two levels of velocity fluctuations. The correct gain and phase magnitudes were found in the LES for both levels. A detailed comparison between phase-averaged

- experimental OH* emission and LES heat release,
- experimental PIV and LES velocity field and
- hot burnt gas probability of presence

was proposed for two levels of velocity fluctuations and frequencies. The simulations demonstrated the accurate prediction of the flame dynamics, which depends on the frequency.

However, some discrepancies were identified on the gain prediction, especially for one frequency, where a drop of gain found in the experiments was not retrieved by the simulations. Further analysis showed that the mesh resolution or the subgrid scale flame wrinkling model were not the origin of the misprediction of the gain. Strain effects that are not included in the F-TACLES model were found to be the most probable cause for this discrepancy.

The analysis of the performances of the F-TACLES in a two-phase flow led to the simulation of KIAI burner. Excellent results were found in the flame shape prediction in two-phase conditions, as presented in [Chatelier et al. \(2019\)](#). Both the flame structure and its lift-off height were recovered by the LES. Two different flame structures appeared as in the experiments: a highly wrinkled premixed inner flame front and a diffusion outer flame front. The comparison with experimental diagnostics highlighted the ability of the YALES2 flow solver to predict the correct spray velocity and stratification and the correct flow topology for the gas.

However, issues appeared for the liquid phase temperature, that were not linked to the F-TACLES model. The evaporation model assumptions were responsible of the discrepancy between experiments and simulations.

Analysis of the interest of ZDES in complex geometries

The thesis of [Boucher \(2015\)](#) studied a complex configuration representative of a real aeronautical injector, called TLC. It was found that in reactive conditions, the simulations led to an incorrect prediction of the temperature field in the chamber. In this thesis, the goal was to:

- determine the ability of the LES model to recover the proper flow topology in cold conditions,
- examine the interest of the ZDES on this complex geometry in cold and reacting conditions.

The choice of the TLC configuration for the final application of this thesis was motivated by the complexity of its geometry and the implications of all the phenomena studied previous in this thesis. The presence of three swirlers

and a cooling system represents a real challenge for CFD codes, even in non-reacting conditions. Also, the liquid fuel is injected with two different methods, leading to many modeling questions regarding the spray in the simulations. The combination of all these parameters with diagnostics in the core of the flow makes the TLC configuration a really interesting case for validating modeling approaches in complex configurations.

The results presented in this thesis showed that both the LES and the ZDES were able to predict the correct flow topology in cold conditions. The discretisation of the boundary layers in the ZDES did not lead to major differences but enabled a fine analysis of the properties of the flow close to the walls. The ability of the ZDES model to capture complex boundary layer structures was demonstrated on this configuration.

In reacting conditions, despite the same flow topology and turbulent combustion modeling, it was demonstrated that the difference of treatment of the boundary layers led to two different spray distributions. The spray from the multipoint injection traveling through the boundary layer in the ZDES was sensitive to velocity fluctuations occurring close to the swirler walls, while the particles in LES were much less dispersed because of the single cell in the boundary layer. The increased dispersion of the spray in the ZDES led to a completely different distribution of the fuel vapor in the combustion chamber compared to LES. As a result, the resulting temperature field in the chamber was found to be very different between the two simulations. In the ZDES, the hot gases were not found in the central recirculation zone while in the LES, they remained in a large portion of the central region of the chamber. The comparison with experimental data showed that the ZDES gave the best prediction of temperature in the chamber.

Perspectives

The conclusions aforementioned raise the following perspectives:

- In order to recover the correct flame shape and dynamics, the inclusion of strain effect on the flame structure seems necessary. The current formulation of the F-TACLES model is not able to include this effect and further extension could be interesting.
- Even if the application of the F-TACLES model on two-phase flames is promising, the study of other two-phase configurations is necessary to identify the limits of the current formulation. For instance, the KIAI burner exists in a swirled, confined version that features a completely different flame structure ([Santiago et al. \(2016\)](#)). It was studied numerically by [Shum-Kivan \(2017\)](#) and would be an excellent candidate for the assessment of the F-TACLES model in two-phase flows.
- The modeling of the liquid phase in this thesis was not the primary focus,

but the new experimental data on the KIAI configuration showed that the droplet temperature was mispredicted by the simulations. The study of other evaporation models is necessary in order to correct these results.

- The use of ZDES in reactive conditions led to unexpected results. It would be interesting to study the impact of the dispersed phase modeling on the temperature field, for instance by adding secondary fragmentation.
- Because of the complexity of the TLC configuration, numerous aspects of the modeling issues were not explored in this thesis:
 - A mesh convergence would be necessary to fully validate the ZDES and LES approaches in both cold and reacting conditions to assess if the results are sensitive to the mesh resolution.
 - The influence of the flow in the plenum on the global flow topology was not studied. A focus could be made on the flow around the fuel injection arm. Also, a study of the inlet influence on the results (for instance through the properties of the injected velocity field) is an interesting matter.
 - The modeling of the spray injection was rather simple with only several numerical injectors for the multipoint injection. Additional simulations are necessary to study the influence of the spray injection method on the results.

References

- AVBP website. www.cerfacs.fr/avbp7x/. (p. 8)
- Code_Saturne website. code-saturne.org/cms/. (p.)
- ANSYS® Fluent (2009). *Theory Guide*. Release 12.0. (p. 40)
- Armitage, C., R. Balachandran, E. Mastorakos, and R. Cant (2006). Investigation of the nonlinear response of turbulent premixed flames to imposed inlet velocity oscillations. *Combustion and Flame* 146(3), 419–436. (p. 62)
- Auzillon, P., O. Gicquel, N. Darabiha, D. Veynante, and B. Fiorina (2012a). A filtered tabulated chemistry model for les of stratified flames. *Combustion and flame* 159(8), 2704–2717. (p. 6, 96)
- Auzillon, P., O. Gicquel, N. Darabiha, D. Veynante, and B. Fiorina (2012b). A filtered tabulated chemistry model for les of stratified flames. *Combust. Flame* 159(8), 2704 – 2717. (p. 26)
- Auzillon, P., E. Riber, L. Y. Gicquel, O. Gicquel, N. Darabiha, D. Veynante, and B. Fiorina (2013). Numerical investigation of a helicopter combustion chamber using les and tabulated chemistry. *Comptes Rendus Mécanique* 341(1-2), 257–265. (p. 5)
- Balachandran, R., B. Ayoola, C. Kaminski, A. Dowling, and E. Mastorakos (2005). Experimental investigation of the nonlinear response of turbulent premixed flames to imposed inlet velocity oscillations. *Combustion and Flame* 143(1), 37–55. (p. 9)
- Barlow, R. S., M. J. Dunn, M. S. Sweeney, and S. Hochgreb (2012). Effects of preferential transport in turbulent bluff-body-stabilized lean premixed ch4/air flames. *Combust. Flame* 159(8), 2563 – 2575. (p. 26)
- Barré, D., L. Esclapez, M. Cordier, E. Riber, B. Cuenot, G. Staffelbach, B. Renou, A. Vandel, L. Y. Gicquel, and G. Cabot (2014). Flame propagation in aeronautical swirled multi-burners: Experimental and numerical investigation. *Combustion and Flame* 161(9), 2387–2405. (p. 5)
- Bauerheim, M., G. Staffelbach, N. Worth, J. Dawson, L. Gicquel, and T. Poinot (2015). Sensitivity of les-based harmonic flame response model for turbulent swirled flames and impact on the stability of azimuthal modes. *Proceedings of the Combustion Institute* 35, 3355–3363. (p. 7)
- Berger, S., S. Richard, G. Staffelbach, F. Duchaine, and L. Gicquel (2015). Aerothermal prediction of an aeronautical combustion chamber based on

- the coupling of large eddy simulation, solid conduction and radiation solvers. In *ASME Turbo Expo 2015: Turbine Technical Conference and Exposition*, pp. V05AT10A007–V05AT10A007. American Society of Mechanical Engineers. (p. 5)
- Bilger, R. (1976). The structure of diffusion flames. *Combustion Science and Technology* 13(1-6), 155–170. (p. 23)
- Boger, M., D. Veynante, H. Boughanem, and A. Trounev (1998). Twenty-seventh symposium (international) on combustion volume one direct numerical simulation analysis of flame surface density concept for large eddy simulation of turbulent premixed combustion. *Symposium (International) on Combustion* 27(1), 917 – 925. (p. 8)
- Boileau, M., G. Staffelbach, B. Cuenot, T. Poinsot, and C. Bérat (2008). Les of an ignition sequence in a gas turbine engine. *Combustion and Flame* 154(1), 2–22. (p. 5)
- Boucher, A. (2015). *Modélisation de la formation des polluants au sein des foyers aéronautiques par une méthode de chimie tabulée*. Ph. D. thesis, Ecole Centrale Paris. (p. viii, 29, 113, 144, 160, 164)
- Bourgouin, J.-F., J. Moeck, D. Durox, T. Schuller, and S. Candel (2013). Sensitivity of swirling flows to small changes in the swirler geometry. *C. R. Méc.* 341(1-2), 211 – 219. (p. 43)
- Brauner, T., W. Jones, and A. Marquis (2016). Les of the cambridge stratified swirl burner using a sub-grid pdf approach. *Flow, Turbulence and Combustion* 96(4), 965–985. (p. 4)
- Breda, P., J. Zips, and M. Pfitzner (2018). A non-adiabatic flamelet approach for non-premixed o₂-ch₄ combustion. In *Proceedings of the 3rd World Congress on Momentum, Heat and Mass Transfer (MHMT@18)*. (p. 76)
- Brübach, J., C. Pfitsch, A. Dreizler, and B. Atakan (2013). On surface temperature measurements with thermographic phosphors: A review. *Prog. Energy Combust. Sci.* 39(1), 37 – 60. (p. 36)
- Bunce, N. A., B. D. Quay, and D. A. Santavicca (2013). Interaction between swirl number fluctuations and vortex shedding in a single-nozzle turbulent swirling fully-premixed combustor. *J. Eng. Gas Turbines Power* 136(2), 021503. (p. 62)
- Candel, S., D. Durox, T. Schuller, J.-F. Bourgouin, and J. P. Moeck (2014). Dynamics of swirling flames. *Annu. Rev. Fluid Mech.* 46(1), 147–173. (p. 7)
- Candel, S., T. Schmitt, and N. Darabiha (2011). Progress in transcritical combustion : experimentation, modeling and simulation. *Proc. 23rd ICERS, Irvine USA, 2011*. (p. 24)
- Charlette, F., C. Meneveau, and D. Veynante (2002a). A power-law flame wrinkling model for LES of premixed turbulent combustion. Part II: Dynamic formulation. *Combust. Flame* 131, 181 – 197. (p. 28)
- Charlette, F., C. Meneveau, and D. Veynante (2002b). A power-law flame

- wrinkling model for {LES} of premixed turbulent combustion part i: non-dynamic formulation and initial tests. *Combust. Flame* 131, 159 – 180. (p. 28)
- Charlette, F., C. Meneveau, and D. Veynante (2002c). A power-law flame wrinkling model for les of premixed turbulent combustion part i: non-dynamic formulation and initial tests. *Combustion and Flame* 131(1), 159–180. (p. 56, 74, 87)
- Chatelier, A., T. Guiberti, R. Mercier, N. Bertier, B. Fiorina, and T. Schuller (2019). Experimental and numerical investigation of the response of a swirled flame to flow modulations in a non-adiabatic combustor. *Flow, Turbulence and Combustion*, 1–29. (p. viii, 164)
- Chatelier, A., V. R. Moureau, N. Bertier, and B. Fiorina (2019). Large eddy simulation of a spray jet flame using filtered tabulated chemistry. In *AIAA Scitech 2019 Forum*, pp. 2144. (p. viii, 164)
- Choi, J. (2011). A quasi global mechanism of kerosene combustion for propulsion applications. In *47th AIAA/ASME/SAE/ASEE Joint Propulsion Conference & Exhibit*, pp. 5853. (p. 6)
- Chong, L. T. W., T. Komarek, M. Zellhuber, J. Lenz, C. Hirsch, and W. Polifke (2009). Influence of strain and heat loss on flame stabilization in a non-adiabatic combustor. In *Proc. Of European Comb. Meeting*. (p. 8, 76)
- Colin, O., F. Ducros, D. Veynante, and T. Poinso (2000). A thickened flame model for large eddy simulations of turbulent premixed combustion. *Physics of Fluids* 12(7), 1843–1863. (p. 82)
- Coriton, B., J. H. Frank, and A. Gomez (2013). Effects of strain rate, turbulence, reactant stoichiometry and heat losses on the interaction of turbulent premixed flames with stoichiometric counterflowing combustion products. *Combust. Flame* 160(11), 2442 – 2456. (p. 47)
- Cousteix, T. C. J. (2005). *Modeling and computation of boundary-layer flows*. Springer. (p. 21)
- Cutler, C. (2019). How does a turbofan engine work? <https://www.boldmethod.com/learn-to-fly/aircraft-systems/how-does-a-jet-engine-turbofan-system-work/>. Accessed: 2019-05-05. (p. 1, 2)
- Dagaut, P. and M. Cathonnet (2006). The ignition, oxidation, and combustion of kerosene: A review of experimental and kinetic modeling. *Progress in energy and combustion science* 32(1), 48–92. (p. 5)
- Darabiha, N. (1992). Transient behaviour of laminar counterflow hydrogen-air diffusion flames with complex chemistry. *Combustion science and technology* 86(1-6), 163–181. (p. 85)
- de la Puente, F., L. Sanders, and F. Vuillot (2014). On lagoon nose landing gear cfd/caa computation over unstructured mesh using a zdes approach. In *20th AIAA/CEAS Aeroacoustics Conference*, pp. 2763. (p. 5)
- Deardorff, J. W. (1970). A numerical study of three-dimensional turbu-

- lent channel flow at large reynolds numbers. *Journal of Fluid Mechanics* 41(2), 453–480. (p. 17)
- Deck, S. (2005). Zonal-detached-eddy simulation of the flow around a high-lift configuration. *AIAA journal* 43(11), 2372–2384. (p. 19)
- Deck, S. (2012). Recent improvements in the zonal detached eddy simulation (zdes) formulation. *Theoretical and Computational Fluid Dynamics* 26(6), 523–550. (p. 5, 19, 20, 127)
- Deck, S., F. Gand, V. Brunet, and S. B. Khelil (2014). High-fidelity simulations of unsteady civil aircraft aerodynamics: stakes and perspectives. application of zonal detached eddy simulation. *Phil. Trans. R. Soc. A* 372(2022), 20130325. (p. 19)
- Deck, S. and R. Laraufie (2013). Numerical investigation of the flow dynamics past a three-element aerofoil. *Journal of Fluid Mechanics* 732, 401–444. (p. 20)
- Deck, S., N. Renard, R. Laraufie, and P. Sagaut (2014). Zonal detached eddy simulation (zdes) of a spatially developing flat plate turbulent boundary layer over the reynolds number range $3 \cdot 10^5 \leq Re \leq 14 \cdot 10^6$. *Physics of Fluids* 26(2), 025116. (p. 5, 19)
- Deck, S., P.-É. Weiss, M. Pamiès, and E. Garnier (2011). Zonal detached eddy simulation of a spatially developing flat plate turbulent boundary layer. *Computers & Fluids* 48(1), 1–15. (p. 18, 19)
- Donini, A., S. Martin, R. Bastiaans, J. van Oijen, and L. de Goey (2013). Numerical simulations of a premixed turbulent confined jet flame using the flamelet generated manifold approach with heat loss inclusion. *Proc. ASME Turbo Expo (2013)*. (p. 6)
- Dorey, L.-H. (2012). *Modélisation des phénomènes couplés combustion-formation des suies-transferts radiatifs dans les chambres de combustion de turbine à gaz*. Ph. D. thesis, Ecole Centrale Paris. (p. 113)
- Durox, D., T. Schuller, and S. Candel (2005). Combustion dynamics of inverted conical flames. *Proc. Combust. Inst.* 30(2), 1717 – 1724. (p. 60, 62)
- Fiorina, B., R. Baron, O. Gicquel, D. Thévenin, S. Carpentier, and N. Darabiha (2003). Modelling non-adiabatic partially-premixed flames using flame prolongation of ildm. *Combust. Theory Modell.* 7(3), 449–470. (p. 23, 26)
- Fiorina, B., O. Gicquel, L. Vervisch, S. Carpentier, and N. Darabiha (2005). Approximating the chemical structure of partially premixed and diffusion counterflow flames using fpi flamelet tabulation. *Combustion and flame* 140(3), 147–160. (p. 159)
- Fiorina, B., R. Mercier, G. Kuenne, A. Ketelheun, A. Avdić, J. Janicka, D. Geyer, A. Dreizler, E. Alenius, C. Duwig, et al. (2015). Challenging modeling strategies for les of non-adiabatic turbulent stratified combustion. *Combustion and Flame* 162(11), 4264–4282. (p. 8)
- Fiorina, B., R. Mercier, G. Kuenne, A. Ketelheun, A. Avdic, J. Janicka,

- D. Geyer, A. Dreizler, E. Alenius, C. Duwig, P. Trisjono, K. Kleinheinz, S. Kang, H. Pitsch, F. Proch, F. C. Marincola, and A. Kempf (2015). Challenging modeling strategies for les of non-adiabatic turbulent stratified combustion. *Combust. Flame In press*. (p. 7)
- Fiorina, B., D. Veynante, and S. Candel (2015). Modeling combustion chemistry in large eddy simulation of turbulent flames. *Flow, Turbulence and Combustion* 94(1), 3–42. (p. 6)
- Fiorina, B., D. Veynante, and S. Candel (2015). Modeling combustion chemistry in large eddy simulation of turbulent flames. *Flow Turbul. Combust.* 94, 3–42. (p. 6)
- Fiorina, B., D. Veynante, and S. Candel (2015). Modeling combustion chemistry in large eddy simulation of turbulent flames. *Flow, Turbulence and Combustion* 94(1), 3–42. (p. 23)
- Fiorina, B., R. Vicquelin, P. Auzillon, N. Darabiha, O. Gicquel, and D. Veynante (2010a). A filtered tabulated chemistry model for les of premixed combustion. *Combustion and Flame* 157(3), 465 – 475. (p. 6, 56, 86)
- Fiorina, B., R. Vicquelin, P. Auzillon, N. Darabiha, O. Gicquel, and D. Veynante (2010b). A filtered tabulated chemistry model for {LES} of premixed combustion. *Combust. Flame* 157(3), 465 – 475. (p. 25, 32)
- Foust, M. J., D. Thomsen, R. Stickles, C. Cooper, and W. Dodds (2012). Development of the ge aviation low emissions taps combustor for next generation aircraft engines. *AIAA Paper 936*, 2012. (p. 111)
- Franzelli, B., B. Fiorina, and N. Darabiha (2013). A tabulated chemistry method for spray combustion. *Proceedings of the Combustion Institute* 34(1), 1659–1666. (p. 27, 76, 83)
- Franzelli, B., E. Riber, M. Sanjosé, and T. Poinso (2010). A two-step chemical scheme for kerosene–air premixed flames. *Combustion and Flame* 157(7), 1364–1373. (p. 6)
- Franzelli, B., A. Vié, M. Boileau, B. Fiorina, and N. Darabiha (2016). Large eddy simulation of swirled spray flame using detailed and tabulated chemical descriptions. *Flow, Turbulence and Combustion*, 1–29. (p. 82)
- Fureby, C. (2005). A fractal flame-wrinkling large eddy simulation model for premixed turbulent combustion. *Proceedings of the Combustion Institute* 30(1), 593 – 601. (p. 8)
- Gallot Lavallee, S., D. Noh, W. Jones, S. Navarro-Martinez, A. Verdier, J. Marrero Santiago, G. Cabot, and B. Renou (2017). Experimental and numerical study of turbulent flame structures of a spray jet flame. In *European Combustion Meeting*. Combustion Institute. (p. 82)
- Galpin, J., A. Naudin, L. Vervisch, C. Angelberger, O. Colin, and P. Domingo (2008). Large-eddy simulation of a fuel-lean premixed turbulent swirl-burner. *Combustion and Flame* 155(1-2), 247–266. (p. 29)
- Germano, M., U. Piomelli, P. Moin, and W. H. Cabot (1991). A dynamic subgrid-scale eddy viscosity model. *Physics of Fluids A: Fluid Dynamics* 3(7), 1760–1765. (p. 4)

- Gicquel, O., N. Darabiha, and D. Thévenin (2000). Liminar premixed hydrogen/air counterflow flame simulations using flame prolongation of ildm with differential diffusion. *Proceedings of the Combustion Institute* 28(2), 1901–1908. (p. 23)
- González-Tello, P., F. Camacho, J. Vicaria, and P. González (2008). A modified nukiyama–tanasawa distribution function and a rosin–rammler model for the particle-size-distribution analysis. *Powder Technology* 186(3), 278–281. (p. 84)
- Goodwin, D. G., H. K. Moffat, and R. L. Speth (2017). Cantera: An object-oriented software toolkit for chemical kinetics, thermodynamics, and transport processes. <http://www.cantera.org>. Version 2.3.0. (p. 24)
- Gritskevich, M. S., A. V. Garbaruk, J. Schütze, and F. R. Menter (2012). Development of ddes and iddes formulations for the k - ω shear stress transport model. *Flow, turbulence and combustion* 88(3), 431–449. (p. 18)
- Guedot, L. (2015). *Développement de méthodes numériques pour la caractérisation des grandes structures tourbillonnaires dans les brûleurs aéronautiques: application aux systèmes d'injection multi-points*. Ph. D. thesis, Rouen, INSA. (p. 84, 99)
- Guiberti, T. F., D. Durox, P. Scouffaire, and T. Schuller (2015a). Impact of heat loss and hydrogen enrichment on the shape of confined swirling flames. *Proc. Combust. Inst.* 35(2), 1385–1392. (p. 6, 32, 33, 34, 35, 36, 37, 40, 43, 45, 46, 47, 50)
- Guiberti, T. F., D. Durox, P. Scouffaire, and T. Schuller (2015b). Impact of heat loss and hydrogen enrichment on the shape of confined swirling flames. *Proceedings of the Combustion Institute* 35(2), 1385–1392. (p. 8, 60, 76)
- Guiberti, T. F., D. Durox, L. Zimmer, and T. Schuller (2015). Analysis of topology transitions of swirl flames interacting with the combustor side wall. *Combust. Flame.* (p. 6, 54)
- Gupta, A. K., D. G. Lilley, and N. Syred (1984). *Swirl flows*. Tunbridge Wells, Kent, England, Abacus Press, 488p. (p. 6)
- Hall, J. M. and E. L. Petersen (2006). An optimized kinetics model for oh chemiluminescence at high temperatures and atmospheric pressures. *International journal of chemical kinetics* 38(12), 714–724. (p. 62)
- Han, X. and A. S. Morgans (2015). Simulation of the flame describing function of a turbulent premixed flame using an open-source les solver. *Combustion and Flame* 162, 1778–1792. (p. 7, 8, 9)
- Hannebique, G., P. Sierra, E. Riber, and B. Cuenot (2012). Large eddy simulation of reactive two-phase flow in an aeronautical multipoint burner. *Flow, turbulence and combustion*, 1–21. (p. 113)
- Hawkes, E. R. and J. H. Chen (2004, 8). Direct numerical simulation of hydrogen-enriched lean premixed methane–air flames. *Combust. Flame* 138(3), 242–258. (p. 50)
- Hermeth, S., G. Staffelbach, L. Gicquel, V. Anisimov, C. Cirigliano, and

- T. Poinso (2014). Bistable swirled flames and influence on flame transfer functions. *Combustion and Flame* 161(1), 184–196. (p. 7)
- Heye, C., V. Raman, and A. R. Masri (2015). Influence of spray/combustion interactions on auto-ignition of methanol spray flames. *Proceedings of the Combustion Institute* 35(2), 1639 – 1648. (p. 82)
- Hirschfelder, J. O., C. F. Curtiss, R. B. Bird, and M. G. Mayer (1954). *Molecular theory of gases and liquids*, Volume 26. Wiley New York. (p. 26)
- Huang, Y. and V. Yang (2009a). Dynamics and stability of lean-premixed swirl-stabilized combustion. *Prog. Energy Combust. Sci.* 35(4), 293 – 364. (p. 6)
- Huang, Y. and V. Yang (2009b). Dynamics and stability of lean-premixed swirl-stabilized combustion. *Prog. Energy Combust. Sci.* 35(4), 293 – 364. (p. 7)
- Iudiciani, P. and C. Duwig (2011). Large eddy simulation of the sensitivity of vortex breakdown and flame stabilisation to axial forcing. *Flow, Turbulence and Combustion* 86, 639–666. (p. 7)
- Jaegle, F. (2009). *Large eddy simulation of evaporating sprays in complex geometries using Eulerian and Lagrangian methods*. Ph. D. thesis, Institut National Polytechnique de Toulouse-INPT. (p. 113, 114)
- Jaegle, F., J.-M. Senoner, M. Garcia, F. Bismes, R. Lecourt, B. Cuenot, and T. Poinso (2011). Eulerian and lagrangian spray simulations of an aeronautical multipoint injector. *Proceedings of the Combustion Institute* 33(2), 2099–2107. (p. 113)
- Jaravel, T., E. Riber, B. Cuenot, and G. Bulat (2017). Large eddy simulation of an industrial gas turbine combustor using reduced chemistry with accurate pollutant prediction. *Proceedings of the Combustion Institute* 36(3), 3817–3825. (p. 6)
- Jaravel, T., E. Riber, B. Cuenot, and P. Pepiot (2018). Prediction of flame structure and pollutant formation of sandia flame d using large eddy simulation with direct integration of chemical kinetics. *Combustion and Flame* 188, 180–198. (p. 23)
- Jenny, P., D. Roekaerts, and N. Beishuizen (2012). Modeling of turbulent dilute spray combustion. *Progress in Energy and Combustion Science* 38(6), 846–887. (p. 82)
- Jones, W. and R. Lindstedt (1988). Global reaction schemes for hydrocarbon combustion. *Combustion and flame* 73(3), 233–249. (p. 23)
- Jones, W., A. Marquis, and K. Vogiatzaki (2014). Large-eddy simulation of spray combustion in a gas turbine combustor. *Combustion and Flame* 161(1), 222 – 239. (p. 82)
- Jones, W. P., A. J. Marquis, and D. Noh (2017). An investigation of a turbulent spray flame using large eddy simulation with a stochastic breakup model. *Combustion and Flame* 186(Supplement C), 277 – 298. (p. 82)
- Kedia, K., H. Altay, and A. Ghoniem (2011). Impact of flame-wall interaction on premixed flame dynamics and transfer function characteristics. *Proc.*

- Combust. Inst.* 33, 1113–1120. (p. 9)
- Kedia, K. and A. Ghoniem (2015). The response of a harmonically forced premixed flame stabilized on a heat-conducting bluff-body. *Proceedings of the Combustion Institute* 35, 1065–1072. (p. 9)
- Keppeler, R., M. Pfitzner, L. T. W. Chong, T. Komarek, and W. Polifke (2012). Including heat loss and quench effects in algebraic models for large eddy simulation of premixed combustion. In *Proceedings of ASME Turbo Expo*, pp. 457–467. (p. 8)
- Ketelheun, A., G. Kuenne, and J. Janicka (2013). Heat transfer modeling in the context of large eddy simulation of premixed combustion with tabulated chemistry. *Flow Turbul. Combust.* 91(867-893). (p. 7)
- Kim, K. T., J. G. Lee, H. J. Lee, B. D. Quay, and D. A. Santavicca (2010). Characterization of forced flame response of swirl-stabilized turbulent lean-premixed flames in a gas turbine combustor. *J. Eng. Gas Turbines Power* 132(4), 041502. (p. 6, 49)
- Klarmann, N., T. Sattelmayer, G. Weiqung, and F. Magni (2016). Flamelet generated manifolds for partially-premixed, highly-stretched and non-adiabatic combustion in gas turbines. *AIAA Paper* (2016-2120). (p. 76)
- Komarek, T., L. T. W. Chong, M. Zellhuber, A. Huber, and W. Polifke (2008). Modeling the effect of heat loss on flame stabilization in shear layers. In *Int. Conf. on Jets, Wakes and Separated Flows, Technical University of Berlin*. (p. 8)
- Komarek, T. and W. Polifke (2010). Impact of swirl fluctuations on the flame response of a perfectly premixed swirl burner. *Journal of Engineering for Gas Turbines and Power* 132(6), 061503. (p. 55)
- Kraushaar, M. (2011). *Application of the compressible and low-Mach number approaches to large eddy simulation of turbulent flows in aero-engines*. Ph. D. thesis, Université de Toulouse. (p. 16)
- Krediet, H., C. Beck, W. Krebs, S. Schimek, C. Paschereit, and J. Kok (2012). Identification of the flame describing function of a premixed swirl flame from les. *Combustion Science and Technology* 184(7-8), 888–900. (p. 7)
- Kuenne, G., A. Ketelheun, and J. Janicka (2011). Les modeling of premixed combustion using a thickened flame approach coupled with fgm tabulated chemistry. *Combustion and Flame* 158(9), 1750–1767. (p. 27)
- Kuenne, G., F. Seffrin, F. Fuest, T. Stahler, A. Ketelheun, D. Geyer, J. Janicka, and A. Dreizler (2012). Experimental and numerical analysis of a lean premixed stratified burner using 1d raman/rayleigh scattering and large eddy simulation. *Combust. Flame* 159(8), 2669 – 2689. Special Issue on Turbulent Combustion. (p. 7)
- Kumar, K., J. Freeh, C. Sung, and Y. Huang (2007). Laminar flame speeds of preheated iso-octane/o₂/n₂ and n-heptane/o₂/n₂ mixtures. *Journal of propulsion and power* 23(2), 428–436. (p. 86)
- Lartigue, G., U. Meier, and C. Bérat (2004). Experimental and numerical investigation of self-excited combustion oscillations in a scaled gas turbine

- combustor. *Applied thermal engineering* 24(11), 1583–1592. (p. 4)
- Lavedrine, J. (2008). *Simulations aux grandes échelles de l'écoulement diphasique dans des modèles d'injecteur de moteurs aéronautiques*. Ph. D. thesis, Institut National Polytechnique de Toulouse. (p. 113)
- Legier, J.-P., T. Poinso, and D. Veynante (2000). Dynamically thickened flame les model for premixed and non-premixed turbulent combustion. In *Proc. of the summer program*, pp. 157–168. Citeseer. (p. 8, 27, 82)
- Lindstedt, P. (1997). 12 month progress report 1, tech. rep. tr-96 009. Technical report, Brite Euram Program Project BRPR950056. (p. 27)
- Lipatnikov, A. and J. Chomiak (2005). Molecular transport effects on turbulent flame propagation and structure. *Prog. Energy Combust. Sci.* 31(1), 1–73. (p. 50)
- Luche, J., M. Reuillon, J.-C. Boettner, and M. Cathonnet (2004). Reduction of large detailed kinetic mechanisms: application to kerosene/air combustion. *Combustion science and technology* 176(11), 1935–1963. (p. 6)
- Mejia, D., L. Selle, R. Bazile, and T. Poinso (2015). Wall-temperature effects on flame response to acoustic oscillations. *Proceedings of the Combustion Institute* 35, 3201–3208. (p. 9)
- Menter, F. and M. Kuntz (2004). Adaptation of eddy-viscosity turbulence models to unsteady separated flow behind vehicles. In *The aerodynamics of heavy vehicles: trucks, buses, and trains*, pp. 339–352. Springer. (p. 18)
- Menter, F., M. Kuntz, and R. Bender (2003). A scale-adaptive simulation model for turbulent flow predictions. In *41st aerospace sciences meeting and exhibit*, pp. 767. (p. 18)
- Mercier, R. (2015). *Turbulent combustion modeling for Large Eddy Simulation of non-adiabatic stratified flames*. Ph. D. thesis, Ecole Centrale Paris. (p. vii, 25, 163)
- Mercier, R., P. Auzillon, V. Moureau, N. Darabiha, O. Gicquel, D. Veynante, and B. Fiorina (2014a). Les modeling of the impact of heat losses and differential diffusion on turbulent stratified flame propagation: Application to the tu darmstadt stratified flame. *Flow, Turbulence and Combustion* 93(2), 349–381. (p. 6, 56)
- Mercier, R., P. Auzillon, V. Moureau, N. Darabiha, O. Gicquel, D. Veynante, and B. Fiorina (2014b). Les modeling of the impact of heat losses and differential diffusion on turbulent stratified flame propagation: Application to the tu darmstadt stratified flame. *Flow Turbul. Combust.* 93(2), 349–381. (p. 7, 25, 26, 27, 32)
- Mercier, R., T. Guiberti, A. Chatelier, D. Durox, O. Gicquel, N. Darabiha, T. Schuller, and B. Fiorina (2016a). Experimental and numerical investigation of the influence of thermal boundary conditions on premixed swirling flame stabilization. *Combustion and Flame* 171, 42–58. (p. vii, 6, 163)
- Mercier, R., T. Guiberti, A. Chatelier, D. Durox, O. Gicquel, N. Darabiha, T. Schuller, and B. Fiorina (2016b). Experimental and numerical inves-

- tigation of the influence of thermal boundary conditions on premixed swirling flame stabilization. *Combustion and flame* 171, 42–58. (p. 8, 76)
- Mercier, R., T. Schmitt, D. Veynante, and B. Fiorina (2015a). The influence of combustion sgs submodels on the resolved flame propagation. application to the les of the cambridge stratified flames. *Proceedings of the Combustion Institute* 35(2), 1259–1267. (p. 4)
- Mercier, R., T. Schmitt, D. Veynante, and B. Fiorina (2015b). The influence of combustion {SGS} submodels on the resolved flame propagation. application to the {LES} of the cambridge stratified flames. *Proc. Combust. Inst.* 35(2), 1259–1267. (p. 26, 28, 32)
- Meyers, J. and P. Sagaut (2006). On the model coefficients for the standard and the variational multi-scale smagorinsky model. *Journal of Fluid Mechanics* 569, 287–319. (p. 17)
- Miller, R., K. Harstad, and J. Bellan (1998). Evaluation of equilibrium and non-equilibrium evaporation models for many-droplet gas-liquid flow simulations. *International Journal of Multiphase Flow* 24(6), 1025–1055. (p. 105)
- Mongia, H. (2003). Taps: a fourth generation propulsion combustor technology for low emissions. In *AIAA International Air and Space Symposium and Exposition: The Next 100 Years*, pp. 2657. (p. 111)
- Montgomery, C., S. Cannon, M. Mawid, and B. Sekar (2002). Reduced chemical kinetic mechanisms for jp-8 combustion. In *40th AIAA Aerospace Sciences Meeting & Exhibit*, pp. 336. (p. 6)
- Moureau, V., P. Domingo, and L. Vervisch (2011a). Design of a massively parallel cfd code for complex geometries. *Comptes Rendus Mécanique* 339(2), 141–148. (p. 15, 54)
- Moureau, V., P. Domingo, and L. Vervisch (2011b). Design of a massively parallel cfd code for complex geometries. *C. R. Méc.* 339(2-3), 141–148. (p. 39)
- Nambully, S., P. Domingo, V. Moureau, and L. Vervisch (2014). A filtered-laminar-flame PDF sub-grid scale closure for LES of premixed turbulent flames. part i: Formalism and application to a bluff-body burner with differential diffusion. *Combust. Flame* 161(7), 1756–1774. (p. 26)
- Nicoud, F. and F. Ducros (1999). Subgrid-scale stress modelling based on the square of the velocity gradient tensor. *Flow, turbulence and Combustion* 62(3), 183–200. (p. 4)
- Nicoud, F., H. B. Toda, O. Cabrit, S. Bose, and J. Lee (2011a). Using singular values to build a subgrid-scale model for large eddy simulations. *Physics of Fluids* 23(8), 085106. (p. 4, 17, 84)
- Nicoud, F., H. B. Toda, O. Cabrit, S. Bose, and J. Lee (2011b). Using singular values to build a subgrid-scale model for large eddy simulations. *Phys. Fluids* 23(8), -. (p. 39)
- Nogenmyr, K.-J., H. J. Cao, C. K. Chan, and R. K. Cheng (2013). Effects

- of confinement on premixed turbulent swirling flame using large eddy simulation. *Combust. Theory Modell.* 17(6), 1003–1019. (p. 6, 7, 46)
- Noiray, N., D. Durox, T. Schuller, and S. Candel (2008). A unified framework for nonlinear combustion instability analysis based on the flame describing function. *Journal of Fluid Mechanics* 615, 139–167. (p. 55)
- Oberleithner, K., S. Schmiek, and C. Paschereit (2015). Shear flow instabilities in swirl-stabilized combustors and their impact on the amplitude dependent flame response: A linear stability analysis. *Combustion and Flame* 162, 86–99. (p. 60, 61, 62)
- Oijen, J. A. V., A. Donini, R. J. M. Bastiaans, J. H. M. T. Boonkamp, and L. P. H. D. Goey (2016). State-of-the-art in premixed combustion modeling using flamelet generated manifolds. *Progress in Energy and Combustion Science* 57, 30–74. (p. 6)
- Oijen, J. v. and L. d. Goey (2000). Modelling of premixed laminar flames using flamelet-generated manifolds. *Combustion Science and Technology* 161(1), 113–137. (p. 23)
- Palies, P., D. Durox, T. Schuller, and S. Candel (2010a). The combined dynamics of swirler and turbulent premixed swirling flames. *Combustion and Flame* 157(9), 1698–1717. (p. 38, 55, 56, 62)
- Palies, P., D. Durox, T. Schuller, and S. Candel (2010b, September). The combined dynamics of swirler and turbulent premixed swirling flames. *Combust. Flame* 157(9), 1698–1717. (p. 35, 43)
- Palies, P., D. Durox, T. Schuller, and S. Candel (2011). Acoustic-convective mode conversion in an airfoil cascade. *Journal of Fluid Mechanics* 672, 545–569. (p. 55)
- Palies, P., T. Schuller, D. Durox, L. Gicquel, and S. Candel (2011). Acoustically perturbed turbulent premixed swirling flames. *Physics of Fluids* 23(037101), (15 pages). (p. 7, 62)
- Passot, T. and A. Pouquet (1987). Numerical simulation of compressible homogeneous flows in the turbulent regime. *J. Fluid Mech.* 181, 441–466. (p. 39)
- Paulhiac, D. (2015). *Modélisation de la combustion dâ€™un spray dans un brûleur aéronautique*. Ph. D. thesis. (p. 82)
- Pepiot-Desjardins, P. and H. Pitsch (2008). An efficient error-propagation-based reduction method for large chemical kinetic mechanisms. *Combustion and Flame* 154(1-2), 67–81. (p. 23)
- Philip, M., M. Boileau, R. Vicquelin, T. Schmitt, D. Durox, J.-F. Bourgoïn, and S. Candel (2014). Ignition sequence of an annular multi-injector combustor. *Physics of Fluids (1994-present)* 26(9), 091106. (p. 5)
- Piomelli, U. (1999). Large-eddy simulation: achievements and challenges. *Progress in Aerospace Sciences* 35(4), 335–362. (p. 4)
- Piomelli, U. and J. R. Chasnov (1996). Large-eddy simulations: theory and applications. In *Turbulence and transition modelling*, pp. 269–336. Springer. (p. 4)

- Pitsch, H. (2006). Large-eddy simulation of turbulent combustion. *Annu. Rev. Fluid Mech.* 38, 453–482. (p. 8)
- Poinsot, T. (2017). Prediction and control of combustion instabilities in real engines. *Proceedings of the Combustion Institute* 36, 1–28. (p. 7)
- Poinsot, T. and D. Veynante (2005). *Theoretical and numerical combustion*. RT Edwards, Inc. (p. 8)
- Pons, L., N. Darabiha, S. Candel, G. Ribert, and V. Yang (2009). Mass transfer and combustion in transcritical non-premixed counterflows. *Combust. Theory Modell.* 13(1), 57–81. (p. 24)
- Pope, S. B. (2013). Small scales, many species and the manifold challenges of turbulent combustion. *Proceedings of the Combustion Institute* 34(1), 1–31. (p. 5)
- Preetham, S. Hemchandra, and T. Lieuwen (2008). Dynamics of laminar premixed flames forced by harmonic velocity disturbances. *Journal of Propulsion and Power* 24(6), 1390–1402. (p. 60)
- Proch, F., P. Domingo, L. Vervisch, and A. M. Kempf (2017). Flame resolved simulation of a turbulent premixed bluff-body burner experiment. part i: Analysis of the reaction zone dynamics with tabulated chemistry. *Combustion and Flame* 180, 321–339. (p. 4)
- Proch, F. and A. Kempf (2015). Modeling heat loss effects in the large eddy simulation of a model gas turbine combustor with premixed flamelet generated manifolds. *Proc. Combust. Inst.* 35(3), 3337 – 3345. (p. 6, 7)
- Ranzi, E., A. Frassoldati, A. Stagni, M. Pelucchi, A. Cuoci, and T. Faravelli (2014). Reduced kinetic schemes of complex reaction systems: fossil and biomass-derived transportation fuels. *International Journal of Chemical Kinetics* 46(9), 512–542. (p. 85, 86)
- Refloch, A., B. Courbet, A. Murrone, P. Villedieu, C. Laurent, P. Gilbank, J. Troyes, L. Tessé, G. Chaineray, J. Dargaud, et al. (2011). Cedre software. *AerospaceLab* (2), p-1. (p. 16)
- Robinson, S. K. (1991). The kinematics of turbulent boundary layer structure. *NASA STI/Recon Technical Report N 91*. (p. 5)
- Rutland, C. (2011). Large-eddy simulations for internal combustion engines—a review. *International Journal of Engine Research* 12(5), 421–451. (p. 5)
- Saengkaew, S., V. Bodoc, G. Lavergne, and G. Grehan (2013). Application of global rainbow technique in sprays with a dependence of the refractive index on droplet size. *Optics Communications* 286, 295–303. (p. 83)
- Sagaut, P. (2006). *Large eddy simulation for incompressible flows: an introduction*. Springer Science & Business Media. (p. 4)
- Sainte-Rose, B., N. Bertier, S. Deck, and F. Dupoirieux (2008). Delayed detached eddy simulation of a premixed methane-air flame behind a backward-facing step. *AIAA Paper 5134*, 2008. (p. 5)
- Sainte-Rose, B., N. Bertier, S. Deck, and F. Dupoirieux (2012). Numerical simulations and physical analysis of an overexpanded reactive gas flow in a planar nozzle. *Combustion and Flame* 159(9), 2856–2871. (p. 5)

- Sanjosé, M., E. Riber, L. Gicquel, B. Cuenot, and T. Poinso (2010). Large eddy simulation of a two-phase reacting flow in an experimental burner. In *Direct and Large-Eddy Simulation VII*, pp. 345–351. Springer. (p. 4)
- Santiago, J. M., A. Verdier, G. Godard, A. Vandel, G. Cabot, M. Boukhalfa, and B. Renou (2016). Experimental study of laser ignition probability, kernel propagation and air and fuel droplet properties in a confined swirled jet-spray burner. In *18th International Symposium on the Application of Laser and Imaging Techniques to Fluid Mechanics*, pp. 84. (p. x, 165)
- Schlichting, H. and K. Gersten (2016). *Boundary-layer theory*. Springer. (p. 5, 133)
- Schmitt, T., M. Boileau, D. Veynante, and V. Moureau (2013). Flame wrinkling factor dynamic modeling for large eddy simulations of turbulent premixed combustion. In *8th International Symposium On Turbulence and Shear Flow Phenomena*. (p. 28)
- Schuller, T., D. Durox, and S. Candel (2003). A unified model for the prediction of laminar flame transfer functions : comparisons between conical and v-flame dynamics. *Combustion and Flame* 134, 21–34. (p. 60, 68)
- Shashank, E. Knudsen, and H. Pitsch (2011). Spray evaporation model sensitivities. *Annual Research Briefs, Centre for Turbulence Research* (1998), 213–224. (p. 102)
- Shaw, J. and C. Peddie (2004). Nasa ultra efficient engine technology project overview. In *NASA Conference Proceedings*, Volume 212963. (p. 111)
- Shum-Kivan, F. (2017). *Simulation des Grandes Echelles de flammes de spray et modélisation de la combustion non-prémélangée*. Ph. D. thesis, Institut National Polytechnique de Toulouse (INP Toulouse). (p. x, 96, 165)
- Shum-Kivan, F., J. M. Santiago, A. Verdier, E. Riber, B. Renou, G. Cabot, and B. Cuenot (2016). Experimental and numerical analysis of a turbulent spray flame structure. *Proceedings of the Combustion Institute*. (p. 82, 83, 84, 86, 96)
- Shur, M., P. Spalart, M. Strelets, and A. Travin (1999). Detached-eddy simulation of an airfoil at high angle of attack. In *Engineering Turbulence Modelling and Experiments 4*, pp. 669–678. Elsevier. (p. 18)
- Sierra Sánchez, P. (2012). *Modeling the dispersion and evaporation of sprays in aeronautical combustion chambers*. Ph. D. thesis. (p. 105)
- Simpson, R. L. (1996). Aspects of turbulent boundary-layer separation. *Progress in Aerospace Sciences* 32(5), 457–521. (p. 133)
- Smagorinsky, J. (1963). General circulation experiments with the primitive equations: I. the basic experiment. *Monthly weather review* 91(3), 99–164. (p. 4, 17)
- Spalart, P. and S. Allmaras (1992). A one-equation turbulence model for aerodynamic flows. In *30th aerospace sciences meeting and exhibit*, pp. 439. (p. 17, 18)
- Spalart, P., W. Jou, M. Strelets, S. Allmaras, et al. (1997). Comments on the

- feasibility of les for wings, and on a hybrid rans/les approach. *Advances in DNS/LES 1*, 4–8. (p. 5, 18)
- Spalart, P. R., S. Deck, M. Shur, K. Squires, M. K. Strelets, and A. Travin (2006). A new version of detached-eddy simulation, resistant to ambiguous grid densities. *Theoretical and computational fluid dynamics* 20(3), 181–195. (p. 5, 18, 19)
- Spalding, D. B. (1953). The combustion of liquid fuels. In *Symposium (international) on combustion*, Volume 4, pp. 847–864. Elsevier. (p. 14)
- Tay-Wo-Chong, L., S. Bomberg, A. Ulhaq, T. Komarek, and W. Polifke (2012). Comparative validation study on identification of premixed flame transfer function. *Journal of Engineering for Gas Turbines and Power* 134(2), 021502. (p. 7)
- Tay Wo Chong, L., T. Komarek, R. Kaess, S. Föllner, and W. Polifke (2010). Identification of flame transfer functions from les of a premixed swirl burner. In ASME (Ed.), *Proceedings of the ASME Turbo Expo 2010*, Number GT2010-22769. ASME Turbo Expo 2010 : Power for Land, Sea and Air, June 14-18, 2010, Glasgow, UK. (p. 8)
- Tay Wo Chong, L., T. Komarek, M. Zellhuber, C. Hirsch, and W. Polifke (2016). Combined influence of strain and heat loss on turbulent premixed flame stabilization. *Flow, Turbulence and Combustion* 97, 263–294. (p. 8, 32, 76)
- Tay Wo Chong, L., T. Komarek, M. Zellhuber, J. Lenz, C. Hirsch, and W. Polifke (2009). Influence of strain and heat loss on flame stabilization in a non-adiabatic combustor. *Proc. Eur. Combust. Meeting, Vienna, Austria, April 14-17 (2009)*, 1–6. (p. 6, 7, 46)
- Tay-Wo-Chong, L. and W. Polifke (2013). Large eddy simulation-based study of the influence of thermal boundary condition and combustor confinement on premix flame transfer functions. *Journal of Engineering for Gas Turbines and Power* 135(2), 021502. (p. 7)
- Tay Wo Chong, L. and W. Polifke (2013). Large eddy simulation-based study of the influence of thermal boundary condition and combustor confinement on premix flame transfer functions. *Journal of Engineering for Gas Turbine and Power* 135, 021502 (9 pages). (p. 8)
- Tay Wo Chong, L., A. Scarpato, and W. Polifke (2017). Les combustion model with stretch and heat loss effects for prediction of premix flame characteristics and dynamics. In *GT2017-63357 in Proceedings of ASME Turbo Expo 2017: Turbomachinery Technical Conference and Exposition GT2017 June 26-30, 2017, Charlotte, NC, USA*. (p. 8, 32, 76)
- Tay-Wo-Chong, L., M. Zellhuber, T. Komarek, H. G. Im, and W. Polifke (2015). Combined influence of strain and heat loss on turbulent premixed flame stabilization. *Flow Turbul. Combust.*, 1–32. (p. 47)
- Terhaar, S., K. Oberleithner, and C. O. Paschereit (2014). Impact of steam-dilution on the flame shape and coherent structures in swirl-stabilized combustors. *Combust. Sci. Technol.* 186(7), 889–911. (p. 6)

- Tomlin, A. S., T. Turányi, and M. J. Pilling (1997). Mathematical tools for the construction, investigation and reduction of combustion mechanisms. In *Comprehensive chemical kinetics*, Volume 35, pp. 293–437. Elsevier. (p. 23)
- Trisjono, P., K. Kleinheinz, H. Pitsch, and S. Kang (2014). Large eddy simulation of stratified and sheared flames of a premixed turbulent stratified flame burner using a flamelet model with heat loss. *Flow Turbul. Combust.* 92(1-2), 201–235. (p. 7)
- Turkeri, H., X. Zhao, S. B. Pope, and M. Muradoglu (2019). Large eddy simulation/probability density function simulations of the cambridge turbulent stratified flame series. *Combustion and Flame* 199, 24–45. (p. 4)
- Valorani, M., F. Creta, D. A. Goussis, J. C. Lee, and H. N. Najm (2006). An automatic procedure for the simplification of chemical kinetic mechanisms based on csp. *Combustion and Flame* 146(1-2), 29–51. (p. 23)
- Van Driest, E. R. (2003). Turbulent boundary layer in compressible fluids. *Journal of spacecraft and rockets* 40(6), 1012–1028. (p. 22)
- Verdier, A., J. M. Santiago, A. Vandell, S. Saengkaew, G. Cabot, G. Grehan, and B. Renou (2016). Experimental study of local flame structures and fuel droplet properties of a spray jet flame. *Proceedings of the Combustion Institute*. (p. 82, 83, 84, 94)
- Vicquelin, R., B. Fiorina, S. Payet, N. Darabiha, and O. Gicquel (2011). Coupling tabulated chemistry with compressible cfd solvers. *Proceedings of the Combustion Institute* 33(1), 1481–1488. (p. 29)
- Vreman, A., J. van Oijen, L. de Goeij, and R. Bastiaans (2009). Direct numerical simulation of hydrogen addition in turbulent premixed bunsen flames using flamelet-generated manifold reduction. *Int. J. Hydrogen Energy* 34(6), 2778 – 2788. (p. 26)
- Wang, G., M. Boileau, and D. Veynante (2011). Implementation of a dynamic thickened flame model for large eddy simulations of turbulent premixed combustion. *Combust. Flame* 158(11), 2199 – 2213. (p. 28)
- Weiss, P. and S. Deck (2013). Numerical investigation of the robustness of an axisymmetric separating/reattaching flow to an external perturbation using zdes. *Flow, turbulence and combustion* 91(3), 697–715. (p. 5)
- Zettervall, N., C. Fureby, and E. Nilsson (2016). Small skeletal kinetic mechanism for kerosene combustion. *Energy & Fuels* 30(11), 9801–9813. (p. 6)

Titre : Questions de modélisation pour les simulations numériques de chambres de combustion aéronautiques

Mots clés : Simulation aux Grandes Échelles, Simulation Zonale des Échelles Détachées, Combustion turbulente, Chimie tabulée, Dynamique de flamme, Modèle F-TACLES, Flamme diphasique.

Résumé : La conception de chambres de combustion aéronautiques requiert un compromis entre les différents phénomènes physiques présents, comme les interactions entre la flamme et la turbulence, les pertes thermiques, la dynamique de flamme ou l'évaporation du carburant et son mélange. De nombreux outils numériques existent dans la littérature pour prédire ce genre d'écoulements réactifs turbulents. Les modèles de turbulence instationnaires, par exemple SGE (Simulation aux Grandes Échelles), sont un excellent compromis pour la prédiction du mélange dans des configurations réalistes. L'approche de chimie tabulée représente un équilibre attrayant entre coût de calcul et précision pour la prédiction de structure de flamme. Dans cette thèse, des modèles de turbulence avancés et de chimie tabulée sont appliqués à des configurations complexes afin d'évaluer leur capacité à prédire la structure de flammes turbulentes. La prédiction de la FDF (Flame Describing Function) par le modèle F-TACLES (Filtre-

red TABulated Chemistry for Large Eddy Simulations) est comparé à des données expérimentales pour une flamme swirlée, prémélangée et non-adiabatique. La FDF est bien prédite pour une large plage de fréquences et deux niveaux de fluctuations de vitesse. L'origine des différences est analysée. La première application du modèle F-TACLES à un brûleur diphasique est proposée. Le brûleur choisi est la flamme jet diphasique KIAI, récemment étudié au CORIA. Une comparaison détaillée avec l'expérience est faite et montre que F-TACLES est capable de prédire la bonne forme de flamme. Le modèle ZDES (Simulation Zonale des Échelles Détachées) est étudié dans la configuration TLC, un injecteur aéronautique réaliste. En non-réactif, la ZDES est validée par rapport aux mesures de vitesse expérimentales et comparée à des résultats de LES. En conditions réactives, la prédiction des profils de température dans la chambre de combustion est grandement améliorée en ZDES.

Title : Modeling questions for numerical simulations of aeronautical combustors

Keywords : Large Eddy Simulation, Zonal Detached Eddy Simulation, Turbulent combustion, Tabulated chemistry, Flame dynamics, F-TACLES model, Two-phase flame.

Abstract : The design of aeronautical combustion chambers requires a precise balance between the different physical phenomena involved, such as flame-turbulence interaction, heat losses, flame dynamics or fuel evaporation and mixing. Numerous numerical tools exist in the literature to predict these kinds of turbulent reacting flows. The unsteady turbulence models, for example LES (Large Eddy Simulation), represent an excellent compromise for the prediction of the mixing in realistic configurations. The tabulated chemistry approach is an attractive trade-off between computation cost and accuracy for predicting the structure of flames. In this thesis, advanced turbulence and tabulated chemistry models are applied to complex configurations in order to assess their ability to predict the structure of turbulent flames. The prediction of the FDF (Flame Describing Function) by the F-TACLES (Filtered TABulated Chemistry for Large

Eddy Simulations) model is compared to experimental data for a non-adiabatic premixed swirled flame. The FDF is well predicted for a wide range of frequencies and two velocity fluctuation levels. The origin of the discrepancies is analyzed. The first application of the F-TACLES model in a two-phase burner is proposed. The chosen burner is the KIAI spray jet flame, recently studied at CORIA. A detailed comparison with the experiments is performed and shows that F-TACLES is able to predict the correct flame shape. The ZDES (Zonal Detached Eddy Simulation) model is studied in a realistic aeronautical injector, the TLC configuration. In cold conditions, the ZDES is validated against velocity measurements and compared to LES results. In reacting conditions, the prediction of temperature profiles in the combustion chamber is greatly improved in the ZDES.



